In silico radiobiological investigations for the advancement of novel RT techniques

Thongchai Masilela

université PARIS-SACLAY

In silico radiobiological investigations for the advancement of novel RT techniques

Enquêtes radiobiologiques in silico pour l'avancement de nouvelles techniques de RT

Thèse de doctorat de l'université Paris-Saclay

École doctorale n° 576 - Particules, Hadrons, Énergie et Noyau : Instrumentation, Imagerie, Cosmos, et Simulation (PHENIICS)
Spécialité de doctorat : Physique et Chimie pour la Santé
Graduate School : Physique. Référent : Faculté des sciences d'Orsay

Thèse préparée dans l'unité de recherche **Signalisation radiobiologie et cancer (Université Paris-Saclay, Inserm, CNRS)**, sous la direction de **Yolanda PREZADO**, directrice de recherche

Thèse soutenue à Paris-Saclay, le 23 novembre 2023, par

Thongchai MASILELA

Composition du jury

Membres du jury avec voix délibérative

Elias KHAN Professeur, Université Paris-Saclay	Président
Stephen MCMAHON Professeur, Queen's University Belfast	Rapporteur & Examinateur
Niels BASSLER Professeur, Aarhus University	Rapporteur & Examinateur
Morgane DOS SANTOS Ingénieur de recherche, IRSN	Examinatrice

THESE DE DOCTORAT

NNT : 2023UPASP166

université PARIS-SACLAY

ÉCOLE DOCTORALE
Particules, hadrons, énergie et noyau : instrumentation, imagerie, cosmos et simulation (PHENIICS)

Titre : Enquêtes radiobiologiques in silico pour l'avancement de nouvelles techniques de RT

Mots clés : radiothérapie, traitement du cancer, protonthérapie, dosimétrie, mini-faisceaux, radiobiologie

Résumé : Le cancer est responsable d'un décès sur quatre en Europe. La radiothérapie (RT) a un rôle clé dans le traitement du cancer; environ la moitié de tous les patients atteints de cancer recevront une RT à un moment pendant leur maladie. Malgré des avancées technologiques importantes, le traitement de certaines tumeurs radiorésistantes et cancers pédiatriques est toujours compromis par la tolérance aux radiations des tissus normaux. Afin de réduire encore l'effet toxique des radiations sur les tissus normaux tout en maintenant, ou même en améliorant, la probabilité de mort de tumeurs, de nouvelles techniques RT sont à l'étude qui contredisent des caractéristiques traditionnelles du faisceau, c'est à dire: les mêmes schémas temporels, les faibles débits de dose, le type de particules de faisceau (photons) et les distributions spatiales (principalement homogènes).

Donc, deux postes de doctorat ont été mis en place dans le cadre du projet PhD conjoint Imperial College London-CNRS. L'objectif était d'étudier de nouvelles techniques de RT comme la radiothérapie à mini-faisceaux (MBRT), la thérapie avec des électrons à très haute énergie (VHEE), et la RT FLASH, en exploitant le lien entre la physique et la biologie en RT. La thérapie VHEE a été proposée comme modalité de traitement alternative des tumeurs profondes en raison de leurs divers avantages dosimétriques, et les thérapies MBRT et FLASH ont déjà montré une augmentation significative de l'indice thérapeutique des gliomes de haut grade. Cependant, les mécanismes biologiques sont encore mal connus. Finalement, les investigations sur ces nouvelles techniques devaient être utilisées afin d'optimiser la conception de LhARA, l'accélérateur hybride laser pour les applications radiobiologiques.

Dans ce context là, la branche CNRS de ce projet conjoint a eu lieu dans l'équipe «Nouvelles approches en radiothérapie (NARA)» de l'Institut Curie, qui explore la vaste «terra incognita» des mécanismes par lesquels la réponse biologique aux rayonnements ionisants est modulée par les caractéristiques physiques du faisceau.

Le travail de cette thèse de doctorat se concentre sur les simulations Monte Carlo des effets de la thérapie VHEE et de la MBRT. Dans la première partie de ce travail, les considérations de radioprotection dans une salle de traitement délivrant des VHEEs ont été évaluées, et l'effet radiobiologique de ces faisceaux a été calculé théoriquement. Ce travail a montré que l'effet biologique des VHEEs était similaire à celui de la RT conventionnelle avec des photons. De plus, ils ont démontré qu'ils étaient probablement comparables à la protonthérapie conventionnelle du point de vue de la radioprotection. Ces résultats donnent des preuves en faveur de l'application clinique de cette technique.

Dans la deuxième partie de ce travail, des simulations microdosimétriques de Monte Carlo ont été réalisées pour étudier la production de radicaux libres dans les régions de forte dose (pic) et de faible dose (vallée) de la MBRT avec des particules différentes. Ces radicaux libres sont impliqués à la fois dans les dommages traditionnels (l'ADN) et dans des idées plus nouvelles telles que les effets non ciblés. Les résultats de ce travail ont montré qu'en fonction de la particule, on obtient une production différentielle de radicaux libres entre les pics et les vallées. Cela pourrait avoir des implications biologiques en aval qui doivent encore être étudiées.

En conclusion, les travaux in silico réalisés dans le cadre de cette thèse font progresser notre compréhension actuelle des nouvelles techniques de RT et mettent en lumière des pistes possibles.

université PARIS-SACLAY

ÉCOLE DOCTORALE
Particules, hadrons, énergie et noyau : instrumentation, imagerie, cosmos et simulation (PHENIICS)

Title : In silico radiobiological investigations for the advancement of novel RT techniques

Keywords : radiotherapy, cancer treatment, proton therapy, dosimetry, minibeams, radiobiology

Abstract : Cancer is responsible for one out of four deaths in Europe. Radiotherapy (RT) has a key role in cancer treatment, with roughly half of all cancer patients receiving RT at some point during their illness. While significant technological advances have been made, the treatment of some radioresistant tumours and paediatric cancers is still compromised due to the radiation tolerance of normal tissue. In view of further decreasing the toxic effect of radiation on normal tissue, while maintaining or even enhancing the tumor-kill probability, novel RT techniques are being investigated which go against the traditional beam characteristics, namely: the same few temporal schemes, low dose rates, beam-particle type (photons) and spatial distributions (predominantly homogenous).

Therefore, two PhD posts were made available as part of the Imperial College London-CNRS joint PhD programme. By exploiting the close bond between physics and biology in RT, the objective was to investigate novel RT techniques such as minibeam radiation therapy (MBRT), very high energy electron (VHEE) therapy, and FLASH RT. VHEE therapy has been proposed as an alternative treatment modality for deep-seated tumors owing to their various dosimetric advantages, and both MBRT and FLASH RT have already shown a significant increase of the therapeutic index for high-grade gliomas, however the exact biological mechanisms are still not well known. Ultimately, investigations on these novel techniques were to be used to optimise the design of LhARA, the Laser-hybrid Accelerator for Radiobiological Applications.

In this context, the CNRS arm of this joint project took place in the "New Approaches in Radiotherapy (NARA)" team of Institut Curie, which explores the vast "terra incognita" of the mechanisms by which the biological response to ionizing radiation is modulated by the physical characteristics of the beam.

The work of this PhD thesis focuses on the Monte Carlo simulations of the effects of VHEE therapy and MBRT. In the first part of this work, the radioprotection considerations within a treatment room delivering VHEEs was evaluated, and the radiobiological effect of these beams was theoretically calculated. This work highlighted how the biological effect of VHEEs was similar to conventional photon RT. Furthermore it demonstrated that it was likely comparable to conventional proton therapy from a radioprotection point of view. These results gave evidence in favour of the clinical translation of this technique.

In the second part of this work, microdosimetric Monte Carlo simulations were performed investigating the production of free radicals in the high dose (peak) and low dose (valley) regions of MBRT with different particles. These free radicals are implicated in both the traditional DNA damage, and more novel ideas such as non-targeted effects. The results of this work showed that depending on the particle, a differential production of free radicals in the peaks and valleys is obtained. This could have downstream biological implications which still needs to be investigated.

In conclusion, the in silico work performed in this PhD advances our current understanding of novel RT techniques, and sheds light on possible avenues forward.

Dedicated to Masilela, Thanomsak,
and Sangkrom.

Acknowledgements

A common thread in the reviewer comments of this thesis was its length, particularly the introduction. In keeping with the same spirit, the length of these acknowledgements should come as no surprise, in which I hope you'll permit me the latitude to hijack this section, wax sentimental, and not only express my gratitude to the people I've met along the journey, but also selfishly reflect nostalgically on the past few years.

I suppose it makes the most sense to work our way through chronologically, starting in 2018 when I left South Africa to pursue a master's degree in France. Who could've predicted that I would only return 4 years later due to the Covid-19 pandemic. With that, I'd like to first and foremost thank all my **friends and family back in South Africa**, particularly my **mom** and **dad**. The love, support, and sacrifices you've made throughout the years has allowed me to make it as far as I have and remains a motivator for me to push forward. I was fortunate to have family members in both South Africa and Thailand who embraced the cultural differences of their counterpart, allowing me to grow up with a wholly accepting, and unique perspective of the world.

It seems to me that it was on the back of the family's forced exile to flee Apartheid South Africa that the very human, instinctual relationship with the idea of *home* was broken down, and there was an instilling of this need to find one's own path in life, thereby redefining and rebuilding this concept for oneself. From our fathers and mothers, this seems to have been transferred to the youngest generation of the family, and it is no surprise that we are scattered all over the world. Consequently, I want to express my gratitude for all the time spent with my extended family members, particularly my **cousins in South Africa, USA, Germany, South Korea, and Thailand** (sorry for not naming you all and relegating you to the collective *cousins*... As soon as I start, a new name inevitably pops up and I find it difficult to decide when to stop). I would also like to thank my aunts and uncles (**Ntongela, Aubrey, and Godfrey**) for their financial and moral support over the years; some of whom were present at the start of this journey, but were not able to see me complete this PhD.

While in France I was fortunate to still have family members nearby, namely my sister, **Don**, and **Kevin**. Don has always been the more rebellious and daring sibling, who's mind you'll be hard pressed to change once made up. After a brief stint in Cape Town, she made the decision to pursue a bachelor's in Fashion Marketing in the capital of fashion - Paris - and I still remember the more than 15 hour journey from Pretoria to Cape Town by car that my dad and I had to undertake to help her move out of her apartment. She arrived in France a year before me, met Kevin towards the end of that year, and sometimes worked two jobs while completing her bachelor's/master's, which highlights her hard-working and resilient nature. I would like to thank both of you for giving me a semblance of *home away from home* these past 5 years!

My first 2 years in France were spent in the city of Nantes in the Loire Atlantique, where it often rains horizontally. Since the university and its halls of residence were located out in the sticks, nature was not far away. I am filled with nostalgia thinking about the chilly misty morning runs in the picturesque *Parc de la Chantrerie* (throwback to a time where I lived a more balanced lifestyle), or contemplative bus rides on the C6 into the city

centre of Nantes. Most importantly, I am grateful to all my **international friends**, from Nantes and Mirepoix, with whom I shared the experience of leaving home in pursuit of something greater.

The most mentally and physically taxing period of the master's was the second year, in which I specialised in the medical applications of ionising radiation which was only offered in French. In spite of its difficulty, this second year was particularly formative, as it would end up serving as an important foundation for the following 3 years of my life. I would therefore like to thank professors **Jean-Pierre Cussonneau** and **Abdesselam Abdelouas** for agreeing to be my references while applying for internships. Their assistance ultimately led to me getting an internship at Institut Curie, which I thought to be an impossibility for some random *mec* from South Africa.

The internship at Institut Curie introduced me to **Yolanda Prezado**, who at the time was setting up a new team in a new lab. I wanted to travel the world and gain work experience outside of academia, and as such I wasn't too interested in starting a PhD. I distinctly remember telling this to Yolanda, but she seems to have a special knack of convincing people, and so in a few short months I would sign a contract to begin my PhD with Yolanda as my supervisor. While the 3 years of the PhD were not without difficulties, it was always reassuring to know that you had my best interests at heart. I am thankful not only for your trust and confidence in my abilities, but also in the fact that you were always available despite your busy schedule. I would also like to thank **Rachel Delorme** who in our brief interactions was always very kind and, in addition to Yolanda, was one of my main co-authors.

This PhD was performed in collaboration with Imperial College London, and despite not being able to spend a lot of time in London due to the global pandemic, I was fortunate to be introduced to **Kenneth Long** and **Josie McGarrigle**. The CNRS-Imperial College London collaboration was thus comprised of the two supervisors Kenneth and Yolanda, and the two PhD students myself and Josie. My gratitude goes to Kenneth, with whom I always had pleasant interactions due to his calm demeanour. Josie, I want to thank you for warmly welcoming me in London and making my stay enjoyable. Your positive outlook despite the adversity you faced while starting the PhD is inspiring, and I wish you all the best for the last stretch of your PhD.

If you, the reader, are currently reading this, it means that I have successfully defended my thesis. With that, I am grateful to all the members of jury, not only for reading the thesis and providing comments aimed at improving it, but also for taking the time to come to Orsay in person. Thank you to **Morgane Dos Santos**, **Elias Khan**, **Stephen McMahon**, and **Niels Bassler**.

Now moving on to the lifeblood of the NARA team of Institut Curie, namely its members. When I first arrived the team was quite small. In addition to Yolanda, you had **Annaïg** and **Cristèle** who are the only two who are still part of the team. I am grateful to both of you for being constants in my day to day life at Curie over the past 3 and a half years. Not only is Annaïg extremely hard working, but her kindness was exemplified when she took the time to organise zoom coffee meetings for us international members of the team during Covid, who were largely isolated alone in our apartments in a foreign country. For that, I'd like to express my appreciation to you. At the time, **Tim** was finishing up his PhD and was in the process of leaving the team. You would often hear whispers of his name within the team, always in reference to how good of a PhD thesis he produced. We

both seem to have a masochistic tendency of obsessing for literal hours over how a sentence doesn't look *quite right*. Thank you for all your guidance and advice over the years.

The team would later be joined by **Marjorie** and **Julie**. While we never had the chance to work together, I want to express my appreciate to both of you for our daily interactions, which were always positive, as well as the opportunity to maintain my level of French, which has unfortunately depreciated significantly. Throughout the years, various interns and short term members joined NARA. I would thus like to take a moment to thank **Laura**, **Roberto**, **Maria**, and **Angela** for the injection of new energy into the team. Angela completed her internship and decided to stay on for a PhD. As the senior PhD student, it should have been my responsibility to provide help, guidance, and advice when needed - however with Angela this was often not necessary as she is extremely capable. She truly comes alive at conferences, and has no qualms about approaching people she doesn't know - something I myself need to work on. Thanks for everything, and good luck with the rest of the PhD!

The most recent members of the team are **Célia**, **Alfredo**, **Vidhula**, **Robert**, and **Miriam**. Given that I have been largely MIA the past 6 months due to the thesis, I haven't had the opportunity to spend as much time with all of you. Nevertheless, I am grateful that our paths have crossed. Thanks to Alfredo for his readiness in letting me hijack his desk/computer over the past few months. Célia , I've heard from the rest of the team about the immense amount of work you have already accomplished and wish you luck for the remainder of your PhD. Vidhula is the only other member of the team coming from outside of the EU, and so I appreciate the camaraderie born out of our shared struggles in dealing with visa issues. I first met Robert when he came to France for a workshop on particle minibeams, and he later ended up joining the team on sabbatical. Thank you for your encouragement as I closed out my PhD and thank you for the shot glass from Arkansas. Although the newest in the team, I had the pleasure of meeting Miriam last year over a shared Paella in the Spanish House of *Cité Universitaire*. From the brief time we have spent together I can already tell that she has a great sense of humour. Thanks for the music recommendations, and good luck in your post-PhD life!

In concluding my acknowledgements of the NARA team members, I would like to warmly thank **Lorea**, **Sarah**, **Marios**, and **Ramon** - with whom I had the pleasure of sharing an office with over the past 3 years. Lorea (don't mention chatGPT around her) started a post-doc in the team about a year after I started the PhD. In an alternate universe, we could very well have been twins. I say this not only because we share similar sensibilities, but because 30 years ago, on Friday the 12th of November, we were respectively born in South Africa and Spain. It's dizzying to think of the paths our lives took, starting at separate ends of the world, which could have been significantly diverted at any point, but ultimately crossing for this brief moment at Curie. Though quite reserved when you first started, I have seen you grow to become more comfortable with the team - revealing more of your wonderful personality. All the best for the years to come!

Sarah, similarly to Angela, started as a master's intern but ended up beginning a PhD within the team. I was happy to learn that you would be staying within the team as a PhD student, and even happier to learn that we would be sharing an office as it gave me an excuse to spend more time with you. As soon as it hits 3 PM Sarah becomes a chemist, her desk becomes a mini-laboratory, and you can find her preparing her *special* pink drink in order to get her through the afternoon. My impression was that we both shared similar stresses/anxieties which were rarely externalised. On the contrary, your positive attitude,

permanent smile, and infectious laugh made me look forward to coming into the office and enduring the hell of the RER B. I have seen first hand how intelligent and hard working you are - good luck with the rest of your PhD, I am sure you will do well!

Marios joined the team as a post-doc a couple of months before my arrival at Curie, and throughout the 2 years remained as cool and mysterious as when I first met him. When I first started, it seemed to me that Marios had an answer for everything. Thank your for all the physics and Monte Carlo advice you provided over the years.

Ramon was the first PhD student that Yolanda hired after setting up the new lab at Curie, and he arrived a few months before I began my master's internship. If we think of Yolanda's PhD students at Curie as her adopted children, then Ramon is the eldest brother and he very much played that role throughout our time together (even though by age he is still a youngster while I am now an old man). One of my memories from the first day of the internship was Ramon explaining to me how to cut, scan, and analyse films (a rite of passage that all physicists of the team have to go through). Ask anyone in the team, and they will without fail tell you how positive and helpful Ramon is. I greatly appreciate all the help and advice you gave me, not only during the 6 months of the internship, but throughout the first 2 years of the PhD. I fondly remember the late evenings in the office, where whatever work we were busy with at the time gradually transformed into existential conversations about life. I would say good luck for the future - but I'll see you in San Francisco!

And last but not least, I would like to extend my most heartfelt thanks to all family and friends who weren't explicitly named, who before 2018, were part of my day-to-day life at **Waterkloof**, **St Alban's**, **Tuks**, and **EB**. These acknowledgements have to come to an end at some point, and so I apologize for not naming you. I will instead express my gratitude in person, when I see you in a few weeks time down in South Africa. In the meantime however, know that you contributed to the myriad aspects of my life that has allowed me to get to where I am today. And for that, I am grateful.

Abstract

The field of radiotherapy (RT) plays a vital role in the treatment of cancer, with approximately half of all patients receiving RT over the course of their illness. Despite the significant advances that were made throughout the 1900s and early 2000s, normal tissue toxicity to radiation remains one of the major hurdles to be overcome. Radioresistant tumors such as high grade malignant gliomas still have a poor prognosis due to the prohibitively high doses required for curative treatments, which would entail significant normal tissue damage.

This vision of improved tumor control while still sparing normal tissues is fundamental to the field of RT. It is in this context that the very cutting edge of RT lies in the investigation of new approaches - such as very high energy electron (VHEE) therapy, FLASH radiotherapy, and minibeam radiation therapy (MBRT) - which aim to improve patient outcomes through an expansion of the type of particle typically used, as well as the spatio-temporal aspects of the radiation. In conjunction, technological progress made in the machinery capable of delivering these novel beams in a flexible manner, such as the Laser-hybrid Accelerator for Radiobiological Applications (LhARA), further facilitates the development of these novel techniques.

Correspondingly, the work performed in this thesis aimed to advance our understanding of novel RT techniques through in silico Monte Carlo (MC) investigations in view of contributing to their implementation, firstly at research facilities such as LhARA, then eventually in clinical centres. It is split into two parts, with each of the parts tackling a different RT modality.

The first part of the thesis was related to VHEEs, and detailed the potential radioprotection concerns within a treatment room delivering VHEEs, as well as an evaluation of the relative biological effectiveness (RBE) of these beams from a microdosimetric point of view. Both studies provided evidence in favour of the more widespread adoption of this technique.

The second part of the thesis dealt with MBRT, and focused on the production and diffusion of reactive oxygen species (ROS) between the peak and valley regions. These studies highlighted how the differential production of ROS between peaks and valleys, depending on the type of particle, could be implicated in some of the novel underlying mechanisms thought to be responsible for the efficacy of MBRT.

Ultimately this thesis advanced our understanding of some of the radiobiological implications of these novel beams and provided a basis for which future biological experiments could be carried out.

Table of Contents

List of Acronyms

ATP adenosine triphosphate
BB broad beam
BEDR Bragg-peak-to-entrance dose ratio
BER base excision repair
CBB carbon broad beam
CBCT cone beam computed tomography
CCAP Centre for the Clinical Application of Particles
CH condensed history
CLEAR (French) Accélérateur linéaire d'électrons du CERN pour la recherche
CLEAR CERN Linear Electron Accelerator for Research
CMBRT carbon minibeam radiation therapy
CNRS le Centre National de la Recherche Scientifique
CT computed tomography
DC direct current
DDR DNA damage response
DSB double strand break
DUOX dual oxidase
EBR (French) efficacité biologique relative
EBRT external beam radiotherapy
ER endoplasmic reticulum
ETC electron transport chain
EUD equivalent uniform dose
EV (French) vésicule extracellulaire
EV extracellular vesicle
FFAG fixed-field alternating gradient accelerator
FSUs functional subunits
GJIC gap junction intercellular communication
GPX glutathione peroxidase
HDI Human Development Index
HR homologous recombination
HeBB helium broad beam
HeMBRT helium minibeam radiation therapy
ICD immunogenic cell death
ICPO Institut Curie Proton Therapy Centre
ICRP International Commission on Radiological Protection
ICRU International Commission on Radiation Units and Measurements
IGRT image-guided radiotherapy
ILS increased lifespan
IMRT intensity-modulated radiotherapy
IR (French) rayonnements ionisants
IRT independent reaction time
IR ionising radiation
LET linear energy transfer

LINAC (French) accélérateur linéaire de particules
LINAC linear particle accelerator
LQ linear quadratic
LRT lattice radiotherapy
LhARA Laser-hybrid Accelerator for Radiobiological Applications
MBRT (French) radiothérapie par mini-faisceau
MBRT minibeam radiation therapy
MB minibeam
MCS multiple Coulomb scattering
MC Monte Carlo
MDSC myeloid-derived suppressor cells
MKM (French) modèle cinétique microdosimétrique
MKM microdosimetric kinetic model
MLC multileaf collimator
MPO myeloperoxidase
MPTP mitochondrial permeability transition pore
MRI magnetic resonance imaging
MRT (French) radiothérapie par micro-faisceaux
MRT microbeam radiation therapy
NARA New Approaches in Radiotherapy
NHEJ non-homologous end-joining
NOX NADPH oxidase
NTCP normal tissue complication probability
OER oxygen enhancement ratio
PBS pencil beam scanning
PDD percentage depth dose
PET positron emission tomography
PHASER Pluridirectional High-Energy Agile Scanning Electron Radiotherapy
PS phase space
PVDR peak to valley dose ratio
RBE relative biological effectiveness
RF radiofrequency
RGS respiratory gating system
RIBE radiation-induced bystander effect
ROS (French) espèces réactives de l'oxygène
ROS reactive oxygen species
RT (French) radiothérapie
RT radiotherapy
SARRP Small Animal Radiation Research Platform
SBS step-by-step
SFRT spatially fractionated radiotherapy
SI stereotactic irradiation
SOD superoxide dismutase
SRS stereotactic radiosurgery
SRT stereotactic radiotherapy
SSBR single-strand break repair

SSB single strand break
SSD source to surface distance
TCP tumor control probability
TEL (French) transfert d'énergie linéaire
TEPC (French) compteur proportionnel équivalent au tissu
TEPC tissue-equivalent proportional counter
TNSA target normal sheath acceleration
TS track structure
VHEE (French) électron de très haute énergie
VHEE very high energy electron
VMAT volumetric-modulated arc therapy
ctc centre-to-centre distance
pBB proton broad beam
pMBRT proton minibeam radiation therapy
xBB x-ray broad beam
xMBRT x-ray minibeam radiation therapy

Chapter 1

Context of the thesis

The term *cancer* is used to define a group of diseases, all characterised by the abnormal growth of mutated cells. Under normal conditions, all cells grow and undergo cell division through a process known as mitosis, in which the DNA contained within those cells is replicated and passed down to the next generation. However, the mutations of cancerous cells leads to changes in gene expression, which alters the balance of cell proliferation and cell death to favour the growth of a tumor cell population [Ruddon, 2007]. While some tumors are benign, malignant tumors are able to spread to distant sites (metastasis) through the bloodstream or lymphatic system, and are the primary cause of cancer morbidity and mortality [Seyfried and Huysentruyt, 2013].

With an estimated 19.3 million new cancer cases and 10 million cancer deaths occurring in 2020 alone, the disease is one of the leading causes of death worldwide. Current projections estimate that by the year 2040, the number of global cases is expected to have increased by 47% [Sung et al., 2021b]. The extent to which cancer positions itself as the primary cause of premature deaths on a national level has been attributed to a variety of risk factors. These factors range from environmental and behavioural (smoking, alcohol consumption, obesity, exposure to ionising radiation) to those associated with the socio-economic development of a modernising, ageing, and growing population [Sung et al., 2021b, Tran et al., 2022, Omran, 2005]. While the former can largely be tackled through educational programs on cancer prevention strategies, the latter represents a more systemic and fundamental consequence of factors such as globalisation. The link between socio-economic development and cancer is plain to see in Figures 1.1 and 1.2.

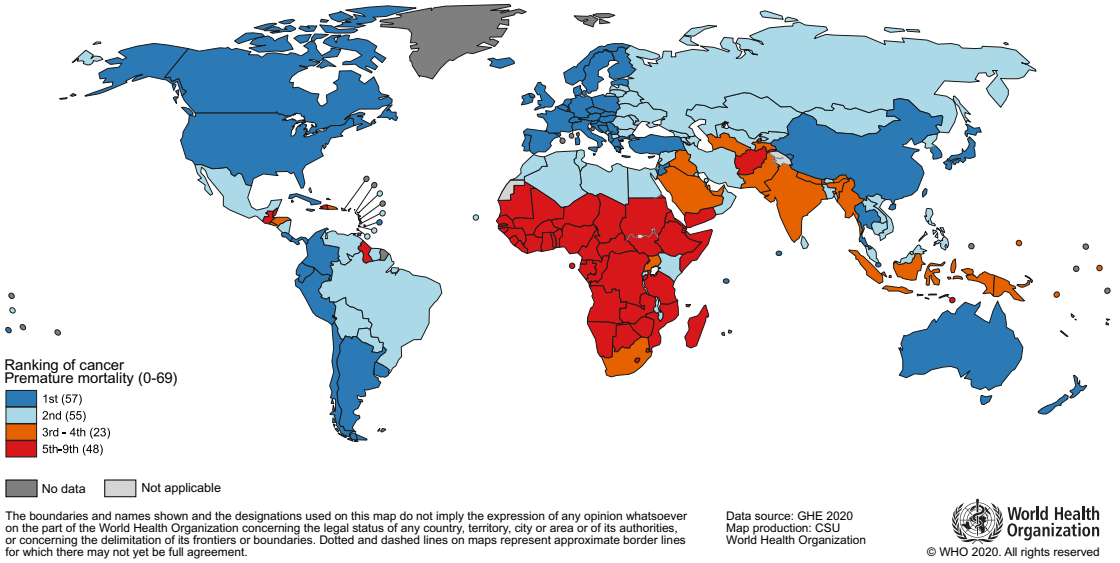

Figure 1.1: National rankings of cancer as the cause of premature (< 70 years old) deaths as of 2019. Taken from [Sung et al., 2021b].

While Fig. 1.1 depicts the national prevalence of cancer as the primary cause of premature deaths, Fig. 1.2 depicts the 4-tier Human Development Index (HDI) of each country according to the United Nations [UNDP, 2019]. This index is used to assess the development of a country where, broadly speaking: developing countries are classified as low/medium HDI, while developed countries are classified as high/very high HDI.

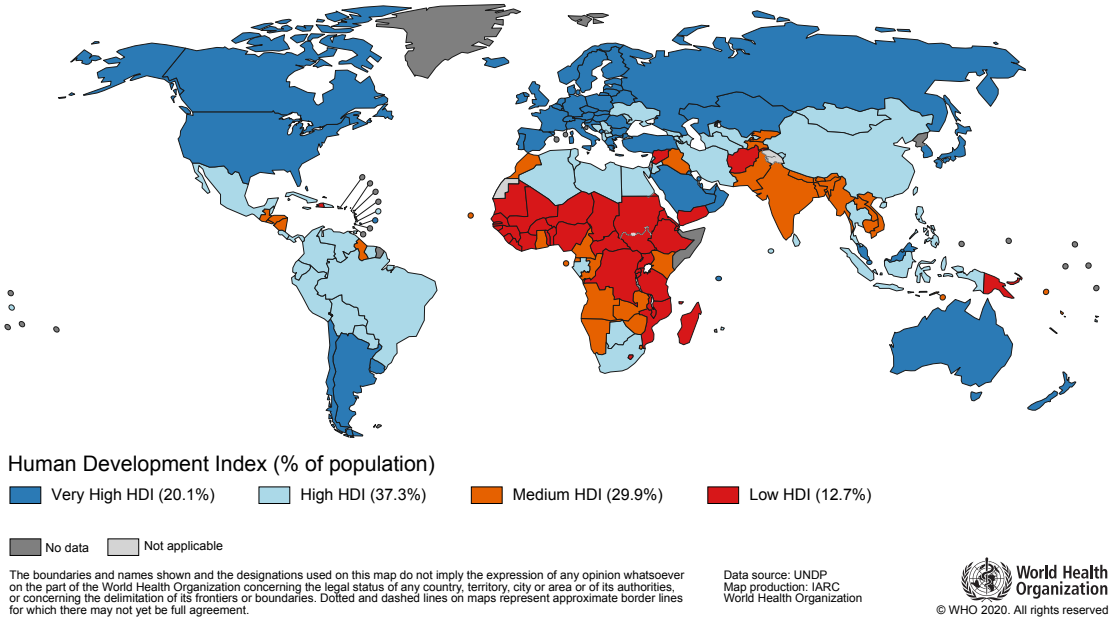

Figure 1.2: The HDI of each country as of 2019. Taken from [Sung et al., 2021b].

It is evident that the ranking of cancer as the cause of premature death within a country is strongly related to that country's HDI, with cancer ranking highly in developed countries but lowly in developing countries, particularly those in Africa. This can be attributed to the increased mortality due to malnutrition, perinatal conditions, or preventable diseases such as malaria, tuberculosis, and HIV/AIDS within these developing countries [WHO, 2023], thereby decreasing the national ranking of cancer as the cause of premature deaths. While these premature cancer deaths are foreseen to remain prevalent in high HDI countries (due to an ageing and growing population), the transition of low/medium HDI countries into developed countries is expected to lead to a reduction in the prevalence of preventable disease/conditions, therefore giving rise to a corresponding transition of cancer into the pre-eminent cause of premature deaths within these countries [Sung et al., 2021b].

With the benefit of hindsight, we are able to foresee that current advancements in the techniques used to treat cancer need to focus not only on overcoming the various biological and technical challenges we are currently facing, but also on overcoming the socio-economic limitations of low/medium HDI countries through the development of cost-effective, small scale technologies to better serve the projected cancer burden of these countries.

With this in mind, the overarching philosophical goal of this thesis was to ***investigate the impact of novel radiotherapy techniques*** *in view of better handling the global cancer burden.*

Since the discovery of radiation at the tail end of the 19th century, there have been

steady advancements made in terms of the theoretical basis surrounding its application to the treatment of cancer. As the field of RT grew, auxiliary and associated technologies were developed to better harness radiation in view of providing the best possible treatments for cancer patients. In this context, the field of RT spread its roots, leading to the situation we are in today in which ideas are constantly being drawn from various branches of science. Consequently, *multidisciplinarity* is an important aspect in the development of new cancer treatments and has been recognized as such by many leading scientific societies [Borras et al., 2015]. Marie Skłodowska-Curie, who won two Nobel prizes in different scientific fields is emblematic of the importance of this multidisciplinarity. Together with Claudius Regaud, she created one of the first interdisciplinary institutes - the *Institut du Radium*, later renamed *Institut Curie* [Rockwell, 2003], which is the institute at which this PhD has been performed.

In terms of the physics, it all started off with the discovery of x-rays by Röntgen in 1895. Since then, we have learnt how to better generate beams of these particles in a clinical context, and how to properly harness their physical properties. We have come to understand the importance of different charged particles such as electrons and protons, and how in certain situations they may be the better option to treat cancer. More recently, there has been a rise in the number of treatments using heavier ions such as carbon [Durante et al., 2021]. Development of auxiliary fields such as mechanical engineering and accelerator physics has further enhanced the efficacy of cancer treatments by providing more complex, robust, and flexible accelerator technologies capable of delivering beams of these particles, representing promising potentials for the use of these technologies in the future [Cirrone et al., 2013, Manti et al., 2017, Aymar et al., 2020].

In terms of the biological response to radiation, throughout the mid 1900's *target theory* models were predominantly used to predict cell survival as a response to radiation, where the targets (or *sensitive volumes*) were thought to be the components of a cell [Bodgi et al., 2016]. Since then, damage to the DNA molecule and the ability of radiation, through this damage, to disrupt biological functions, has been elucidated, with the linear quadratic (LQ) model being the most frequently used model to describe the probability of cell survival after exposure to ionising radiation (IR) [McMahon, 2018]. Even more recently, there is an increased importance being placed on non-targeted effects, vascular effects, and an activation of the immune system [Boustani et al., 2019].

Chemically speaking, the production of ROS contributes to the level of DNA damage through the indirect effect, however in line with the aforementioned advancements highlighting the importance of effects other than DNA damage, these ROS have been implicated therein, with evidence for their role in cell signalling and the bystander effect [Mothersill and Seymour, 1997, Azzam et al., 2002, Widel et al., 2012], vascular development and angiogenesis [Zhou et al., 2013], and both innate and adaptive immunity [Yang et al., 2013]. Consequently, further investigations on this front are warranted.

If we consider physics, biology, and chemistry as the three main ingredients of the metaphorical RT *pie*, then computer simulations can be thought of as the *utensils* used to probe each of those ingredients. The increased capability of computers and computer simulations has been essential in investigating radiation's effect on the human body by enabling predictions without the strict requirement of performing experiments. The use of MC simulations in particular has increased exponentially since the 1970's [Andreo, 2018] and their use through tools such as TOPAS [Perl et al., 2012, Faddegon et al., 2020] and TOPAS-nBio [Schuemann et al., 2018a] has allowed us to not only probe the physical interactions of IR, but also make predictions about the resulting biological and chemical ramifications through experimentally validated models [Incerti et al., 2010]. Further

advancements in these codes is expected to allow us to overcome challenges linked with the wide range of temporal scales over which the physical, chemical, and biological effects of radiation are observed.

Given all the aforementioned advancements, and given the close links between physics and biology, the forefront of RT is now in the midst of a paradigm shift in which we are carefully considering how changes in the physical parameters of the irradiation impact the biological response and resulting treatment outcome. Leading the charge at this frontier are techniques such as VHEE therapy [DesRosiers et al., 2000]: where previously unthought-of energies in the hundreds of MeV are being used. FLASH [Favaudon et al., 2014]: which drastically alters the speed at which the dose is delivered. And MBRT [Dilmanian et al., 2006]: where highly heterogeneous dose distributions are used over the conventional homogeneous fields, and effective treatments in single temporal fractions [Bertho et al., 2021] make it a potentially attractive and cost-effective technique for use in low/medium HDI countries. The adoption of these techniques could lead to radically different outcomes for the treatment of cancers with historically poor prognoses, however more work needs to done to elucidate their underlying radiobiological mechanisms.

It is important to note that in the context of the field of RT, the branches of science representing the physical, biological, and chemical consequences of the irradiation are not distinct from one another, and in fact significantly overlap in certain areas. **It is in these overlapping areas that this thesis makes its home**. The vast *terra incognita* of the radiobiological mechanisms underpinning the aforementioned novel RT techniques exists in these areas. It became evident that in order to systematically investigate the biological consequences of changes to the physical characteristics of these novel beams, dedicated platforms capable of generating multiple different types of particles, in a variety of temporal, spatial, and spectral fractionation schemes was needed. This led to the conceptualisation of the LhARA facility, which aims to fulfil these needs [Aymar et al., 2020].

Consequently, this PhD thesis has been framed within the context of the collaboration between le Centre National de la Recherche Scientifique (CNRS) and Imperial College London's Centre for the Clinical Application of Particles (CCAP) - the entity behind LhARA. Two PhD posts were made available at the end of 2020, and while I myself was hosted by the New Approaches in Radiotherapy (NARA) team of Institut Curie, a second PhD student was hosted by Imperial College London. Both students were expected to contribute to the joint CCAP-CNRS project, which entailed investigations of how to better understand the micro-biophysical processes that determine the response of living tissue to IR. The student associated to Imperial primarily worked on the creation of a searchable online database of preclinical FLASH data, aiming to correlate a physical characteristic of the irradiation with a biological response. I, on the other hand was focused on VHEEs and MBRT. While LhARA itself is not being designed to deliver VHEEs, this novel RT technique has been an auxiliary interest of the NARA team since 2015 and laser based accelerators have been touted as one of the ways to overcome the logistical challenges of generating VHEEs in a clinical context [Nakajima et al., 2015, Labate et al., 2020, Svendsen et al., 2021]. MBRT is the primary interest of the NARA team, and previous MC simulations of the LhARA facility have shown that beam sizes sufficiently small enough to deliver MBRT irradiations in flexible conditions without mechanical collimation was possible [Schneider, 2020, Aymar et al., 2020]. There was therefore an interest in investigating the impact of different beam parameters and radiobiological consequences of MBRT with protons and other ion species relevant to LhARA. While MBRT has already been implemented at clinical facilities and is close to clinical trials, the work performed on VHEE therapy represents a more medium-long term investment.

Ultimately, this thesis aimed to use powerful MC codes to investigate two novel RT techniques, namely VHEE therapy and MBRT, through the calculation of various radiobiological endpoints. More specifically, the technical goals of this thesis were to investigate the ***radioprotection concerns and potential increased biological efficacy of using VHEEs****, and investigate whether the different parameters of the LhARA beams (particle type, spatial distribution) would have an impact* on the **production and diffusion of cytotoxic ROS between the minibeam peaks and valleys.**

Chapter 2

Introduction

In order to place the field of RT into context, fundamental ideas are described in section 2.1. This is followed by an introduction to the physical consequences of IR (section 2.2), the initial production of cytotoxic chemical species through water radiolysis (section 2.3), the resulting biological consequences (section 2.4), and mathematical models of this biological response (section 2.5). Subsequently, radioprotection considerations (section 2.6) and particle accelerators (section 2.7) are discussed. And the final two sections describe the two novel RT techniques of VHEE therapy (section 2.8) and spatially fractionated radiotherapy (SFRT) (section 2.9).

2.1 The landscape of radiotherapy: from fundamentals, to current techniques

The philosopher R. Pirsig wrote: "*Definitions are the foundation of reason. You can't reason without them.*" And so to start, a definition:

Definition 1

Radiotherapy refers to a treatment technique characterized by the clinical use of IR to eradicate cancerous tumor cells, with either curative or palliative intent [Zeman et al., 2020].

The trio of surgery, chemotherapy, and RT, form the main established treatment options for cancer. While surgery has the longer history and is the primary form of treatment for a slew of early, non-metastatic cancers, RT is almost entirely used for the treatment of malignant disease[1], and represents a more localized form of cancer treatment compared to chemotherapy, which is the more systemic, and aggressive option. In order to improve the therapeutic outcome for patients, these techniques are routinely combined with one another depending on the type and stage of cancer, and approximately 50% of all patients will receive a round of RT over the course of their treatment [Joiner et al., 2018].

2.1.1 Fundamental concepts

One of the core tenets of cancer treatment through radiotherapy lies in the exploitation of the DNA damaging capabilities of the aforementioned IR. While it is inevitable that some portion of non-tumor tissue may be irradiated over the course of the treatment, given their mutated nature, cancerous cells are less capable of repairing themselves than normal cells, thereby leading to cell death [Gerber and Chan, 2008]. One of the commonly used experimental techniques for determining the survival of irradiated cells is the clonogenic

[1] RT also has a small role to play in the treatment of benign diseases of the heart, soft tissue and muscle-skeletal disorders, and neurological disorders such as epilepsy [Nardone et al., 2022].

cell survival assay, which determines the degree to which a cell has retained its reproductive ability (thereby its ability to form a large colony) enabling it to proliferate indefinitely [Franken et al., 2006]. Consequently, the extinction of these clonogenic tumor cells are used as the endpoint to determine the level of tumor control exerted by a specific amount of IR. This tumor control can be modelled using a sigmoidal function of the dose, otherwise known as the tumor control probability (TCP), while the level of normal tissue damage is modelled using a similar function, resulting in a curve known as the normal tissue complication probability (NTCP) [Bentzen, 2018].[2]

While the TCP is defined as the probability of clonogenic cell extinction after a specific dose [Munro and Gilbert, 1961] the NTCP is indicative of the tolerance of normal tissue to the dose, and describes the probability of normal tissue complications [Bloomer and Hellman, 1975]. The gap between these two curves is representative of a qualitative concept known as the *therapeutic window*. Figure 2.1 depicts both an optimal, and unfavourable therapeutic window. The therapeutic strategy at the heart of RT is to deliver a treatment with as wide a therapeutic window as possible, thereby increasing the likelihood of tumor control while simultaneously reducing the likelihood of normal tissue complications.

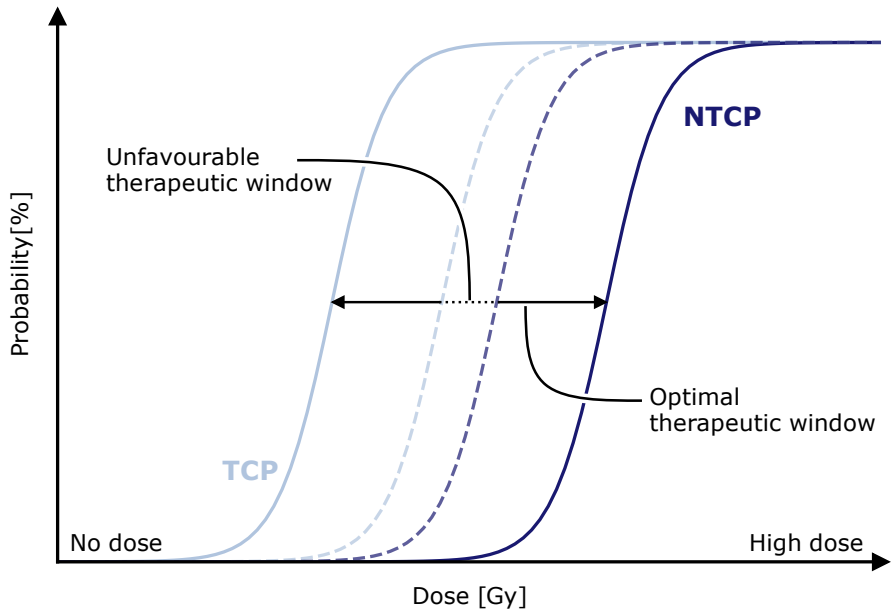

Figure 2.1: Graphical representation of the TCP (light blue) and NTCP (dark blue) curves as a function of dose, for an optimal (solid line) and unfavourable (dashed line) therapeutic window.

For a treatment modality with an optimal therapeutic window, escalation of the dose to achieve complete tumor control is possible given that the doses required do not incur a significant risk of normal tissue complications. On the other hand, for a narrow therapeutic window, dose escalation strategies no longer become viable given that the doses required would result in adverse normal tissue effects. While some state of the art strategies for widening the therapeutic window involves the use of molecularly targeted radiation sensitisers or nanoparticles, historically this widening was achieved through delivering the RT in temporally fractionated sessions, which remains the standard of care

[2] Various radiobiological models may be used for TCP modelling (see section 2.5). NTCP modelling, on the other hand, is more complicated owing to various factors such as the numerous organs at risk and will not be discussed in this thesis. For a more detailed description refer to [Gulliford and El Naqqa, 2022].

in most conventional RT treatments [Reda et al., 2020]. The rationale for this temporal fractionation is based on the *6 Rs of radiotherapy*, which is described in more detail in section 2.4.

This constant *toeing the line* between dose escalation for tumor control while avoiding normal tissue complications is a cornerstone of modern-day RT. It highlights one of the fundamental challenges with the use of IR for cancer treatment, namely developing effective treatments for various radioresistant tumors. One example is the treatment of high grade malignant gliomas, which still have a poor prognosis [Bleeker et al., 2012] and whose exact mechanisms of radioresistance are not fully defined [Ali et al., 2020].

In view of achieving a better dose conformality to the tumor (thereby allowing an escalation of the dose while sparing nearby healthy tissues), different RT modalities have been developed to better treat the various types of cancers. These modalities can be classified as either *internal* or *external*, to describe the origin of the source of radiation. The main internal techniques are brachytherapy and radiometabolic therapy (or systemic radiotherapy/radiopharmaceutical therapy), while external beam radiotherapy (EBRT) is the primary technique in RT [Gerber and Chan, 2008]. Each technique has its own sub-techniques with different use-cases. These are described briefly in the following subsections.

2.1.2 Internal radiotherapy

Brachytherapy

While globally not as common in the modern day landscape of RT as it was in the past, brachytherapy refers to a treatment technique in which sealed radioactive sources are placed either within, or directly adjacent to the tumor. The most common sources used are ^{192}Ir, ^{60}Co, ^{125}I, and ^{103}Pd. Sharp radiation dose gradients are the main advantage of brachytherapy, which allows it deliver very high doses locally, while benefiting from the rapid dose fall-off at distances from the source to spare the surrounding normal tissue, thereby minimizing the NTCP [Chargari et al., 2019].

According to the International Commission on Radiation Units and Measurements (ICRU), brachytherapy can be categorised as three different types depending on the activity of the radioactive source used. Dose rates of 0.4 - 1 Gy/h are classified as low dose rate, 1 - 12 Gy/h as medium dose rate, and anything greater than 12 Gy/h as high dose rate [ICRU, 2013]. The dose rate, and level of permanence of the brachytherapy implant depends both on the indication to be treated, as well as whether or not the indication is to be treated solely using brachytherapy (monotherapy) or as a boost to EBRT. Typically, permanent implants are used for indications such as prostate cancer, whereas temporary implants are the standard for breast cancer or gynaecological malignancies [Gerber and Chan, 2008, Chargari et al., 2019].

In high HDI countries such as the US, the invasiveness of the technique, high level of expertise required (with fewer procedures being performed by resident physicians), and recent developments in EBRT allowing for easier to implement treatments, has lead to a steady decline in the use of brachytherapy over the past 20 years [Zaorsky et al., 2017]. However, the economic favourability of brachytherapy over EBRT, coupled with the geographic and socio-economic barriers of low/medium HDI countries, means that it is still a preferred method of treating certain cancers within these countries [Grover et al., 2017].

Radiometabolic therapy

Similarly to brachytherapy, radiometabolic therapy makes use of radioactive isotopes to deliver radiation to a tumor. The main difference comes from the fact that the sources used in radiometabolic therapy are not sealed, but are rather attached to some kind of carrier agent (nanoparticles, antibodies, peptides, or small molecules) which have an affinity for cancerous cells, thereby selectively delivering the dose and reducing the NTCP [Sgouros, 2019].

These *radiopharmaceuticals* are administered orally or intravenously, and are primarily used for the treatment of metastasised cancers. In the case of metastatic thyroid cancer or benign causes of hyperthyroidism, the most common radioisotope is the γ-emitter ^{131}I [Gudkov et al., 2015], while for the treatment of bone metastases two common isotopes are the β-emitter ^{186}Re or α-emitter ^{223}Ra [Rubini et al., 2014]. Compared to brachytherapy or EBRT however, radiometabolic therapy is not effective for the treatment of solid tumors as it is not able to overcome the resilience of the tumor cells to IR owing to the fact that the radiopharmaceuticals accumulate in the periphery of the tumor body, resulting in an uneven distribution of the dose [Gudkov et al., 2015].

2.1.3 External beam radiotherapy

With almost 90% of all RT treatments being some variation of EBRT, this technique is undoubtedly the pre-eminent form of cancer treatment using radiation [Gerber and Chan, 2008]. Given its importance to the two central works of this thesis, this subsection will detail: some fundamental principles, which have been present since the very early days of the technique, advancements made over the past half-century in an attempt to improve patient outcomes, and finally an introduction to state of the art techniques.

Fundamental ideas behind conventional EBRT

The discovery of x-rays by Röntgen in 1895 was a monumental moment as it allowed physicians to see *inside* the patient in a non-invasive manner for the very first time. When transmitted through the human body and onto photographic plates, these x-rays generated images (later referred to as *radiographs*) which became a widespread diagnostic tool [Cherry et al., 2012a].

It was not long afterwards that x-ray generating technology was applied to cancer therapy. Initially, orthovoltage (100 - 500 kV) x-rays were predominantly used, but with the development of the modern medical linear particle accelerator (LINAC) megavoltage x-rays ($\geq$ 1 MV) became ubiquitous in the modern day landscape of RT. These higher energy x-rays have a deeper penetration range which is favourable for the treatment of deep-seated tumors (see section 2.2). These LINACs are also able to operate in electron irradiation mode, which filled the gap left by the move from orthovoltage to megavoltage x-rays, namely the irradiation of superficial tumors. The typical photon/electron energies offered by the machines are 6 - 25 MV[3] and 4 - 25 MeV respectively [Podgorsak, 2005]. Figure 2.2 depicts a typical medical LINAC treatment head with both irradiation modes.

The source of electrons is generated using an *electron gun*, which is primarily comprised of a heating element, cathode, and anode, all contained within a vacuum tube. Upon the application of an electric potential (voltage), the heating element heats up the negatively

[3] While electrons are accelerated at discrete energies, the photons are produced as a spectra. Therefore the convention is to report the voltage V used for their generation as opposed to their energy in eV.

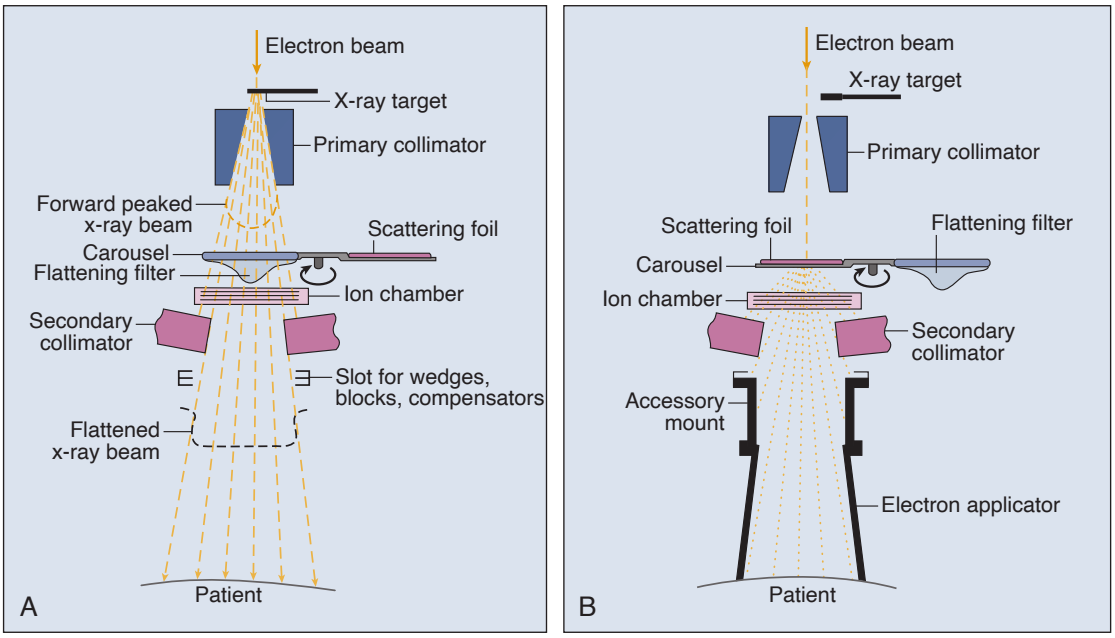

Figure 2.2: Schematic representation of the treatment head of a modern medical LINAC. Panel **A** depicts the machine in x-ray irradiation mode, while panel **B** is representative of the electron irradiation configuration. Taken from [Zeman et al., 2020].

charged cathode thereby liberating electrons through a process known as thermionic emission. These electrons are then accelerated towards the positively charged anode, drift towards the accelerating waveguide, and are accelerated once again using radiofrequency (RF) waves [Podgorsak, 2005].

As depicted in Fig. 2.2, the fundamental difference between photon and electron irradiation configurations is the presence of a target (most commonly tungsten). For photon generation, the target is placed in front of the electron beam and photons are generated through a process known as *Bremsstrahlung* (see section 2.2). This target is removed when in electron irradiation mode, and in both cases multiple filters and beam shaping elements are used to obtain the desired distribution of photons/electrons [Zeman et al., 2020]. One of the older techniques for generating megavoltage photons is the use of radioactive ^{60}Co placed directly within the treatment head. While this technique represents a technically and practically inferior alternative to modern LINACs, it is expected that their use will continue (particularly in the developing world) due to their low relative installation and maintenance costs [Podgorsak, 2005].

The three central principles for an effective treatment in the context of conventional RT, are a homogeneous dose coverage of the tumor volume (95 - 107% of the prescribed dose), delivery of moderate doses per fraction (1.8 - 2 Gy), with fractions sufficiently separated in time to allow for adequate normal tissue recovery (typically 4 to 7 weeks total treatment time). These classical *dogmas* were set out in ICRU report 62 [ICRU, 1999] for conventional EBRT with beams of photons, and are still at the foundation of most treatments in the present day and age. Nevertheless, the incremental technological developments of dose delivery methods over the years, combined with new biological evidence for the immunomodulatory effects and vascular impact of EBRT, are gradually leading to a reconsideration of these dogmas [Zhang et al., 2022, Khalifa et al., 2021].

Advancements in EBRT treatment techniques

Various technological advancements over the past few decades have engendered the concept of *precision radiotherapy*. Some of these advancements include better imaging technologies, the use of different particles, new beam generation and delivery techniques, and novel insights into the radiobiological consequences thereof. These are highlighted in brief below.

Imaging One of the first important advances has been better imaging technologies to more accurately pinpoint the tumor. Due to better imaging technologies, one is able to better target the tumor volume. Up until the 1980's radiation treatment plans made using radiography did not allow for direct visualisation of the tumor. Consequently, generous margins were needed to be used [Gerber and Chan, 2008]. Today we have techniques such as computed tomography (CT), magnetic resonance imaging (MRI), cone beam computed tomography (CBCT), and positron emission tomography (PET).

IMRT By using multiple radiation fields, and splitting each of the fields through the use of a multileaf collimator (MLC) to create beamlets of varying intensity, a high degree of dose conformity to a target region can be achieved. This technique is known as intensity-modulated radiotherapy (IMRT) and has, in recent years, become a mainstay of most RT centres across the world. It represents a more advanced version of 3D-conformal RT in which multiple fields are used however the intensity of each field is not changed, and rather the apertures of the beams are tailored to the shape of the target volume [Podgorsak and Podgorsak, 2005]. The rotational form of IMRT is known as volumetric-modulated arc therapy (VMAT), in which the intensity and aperture of the fields are continuously modulated while the gantry rotates around the patient [Elith et al., 2011].

IGRT In view of reducing the systematic uncertainty arising from day-to-day variations in the patient setup, image-guided radiotherapy (IGRT) was developed. In this technique, an image of the patient anatomy is taken just before the delivery of a fraction of RT, thus allowing clinicians to have more precise knowledge of the location of the target on a daily basis [Podgorsak and Podgorsak, 2005]. Tomotherapy is a form of IGRT, and is best described as a combination of IMRT with CT scanning technology in which the patient is moved through the bore of the machine [Elith et al., 2011, Mackie, 2006].

Four-dimensional radiotherapy In this technique, a fourth dimension is taken into account - namely motion of an organ during treatment. One of the most important organ motions in this context is the movement of the thorax during respiration. By acquiring volumetric CT images that change over time (the fourth dimension), IMRT treatment plans can be created to take into account this movement [Moorrees and Bezak, 2012]. Alternatively, a simpler way to compensate for this motion is to use a respiratory gating system (RGS), which is a special accessory added on to a LINAC. For example, Varian developed an RGS in which a reflective marker is placed on the patient's chest, a video tracks the marker's motion, and a signal is sent to initiate a *beam hold* when the movement exceeds a certain threshold [Podgorsak and Podgorsak, 2005].

SI In stereotactic irradiation (SI), a focal irradiation is performed through the use of multiple non-coplanar narrow beams, delivering a prescribed dose of IR to highly localised lesions, which are generally located within the brain. In general, prescribed doses are on the order of 10 - 50 Gy, with target volumes ranging from 1 to 35 cm^3. When treatments

are delivered in a single fraction, the technique is referred to as stereotactic radiosurgery (SRS), whereas when multiple fractions are used as in conventional RT it is referred to as stereotactic radiotherapy (SRT) [Podgorsak and Podgorsak, 2005]. Commercial examples are the *Gamma Knife* and *Cyber Knife*, where the former refers to the use of several ^{60}Co sources placed inside a helmet, while the latter refers to the use of a small and lightweight (∼120 kg) LINAC mounted on to a robotic arm [Khan and Gibbons, 2014b].

The use of different particles Worldwide, treatments are carried out primarily with machines producing either x-rays or electrons, however in some specialised centres, other particles such as neutrons, protons, or heavy ions are used [Podgorsak, 2005]. The use of these particles comes with different dosimetric benefits/challenges for their implementation. Due to the different patterns of dose deposition, there are different radiobiological consequences, which will be expanded upon throughout various chapters of this thesis. To-date, it has become well recognised that protons are more preferable over photons when treating tumors close to critical structures. As an example, at Massachusetts General Hospital 90% of the paediatric patient population treated with EBRT was done so using protons [Paganetti, 2020].

For the heavier ions such as ^{12}C and ^{16}O, there is a wealth of evidence for their superior physical and biological characteristics, with the increased RBE being the primary argument put forth for their adoption [Ando and Kase, 2009, Malouff et al., 2020]. Nevertheless, the severe toxicities in normal tissue as a result of their fragmentation tail has been a concern [Durante et al., 2021]. At the time of writing, a randomized controlled phase III study is being carried out comparing RT with carbon ions, to conventional proton or photon therapy [Balosso et al., 2022].

Given that the two main topics of thesis are linked with novel EBRT techniques, the following section describes fundamental principles behind the physics of IR.

2.2 Physics of ionising radiation

As a beam of radiation passes through matter its constituent particles undergo various physical interactions causing them to impart energy to their immediate surroundings. Depending on the level of energy deposition, the incident particles may cause the orbital electrons to become *excited*, i.e. raising them to higher energy levels, or *ionised*, i.e. directly liberating them from the atom. The latter *ionising radiations* can be further classified as either *directly ionising* or *indirectly ionising*. Directly ionising radiations refer to charged particles such as electrons, protons, or ionic species, which lose energy in many small collisions[4]. Comparatively, indirectly ionising radiations lose their energy in a few large interactions from which directly ionising particles are liberated [Podgorsak, 2005].

Before going on to describe the exact mechanisms of each reaction, it is important to take note of some fundamental quantities of ionising radiation. One of these quantities, which lies at the heart of every physical interaction, is known as the *cross section*, σ, which essentially acts as a measure of the probability for a specific interaction to occur. This quantity depends on both the target material and incident particle, and is often described in terms of an amount of *barns*, where 1 barn is equivalent to 10^{-28} m^2 [Khan

[4] While the term "collision" is colloquially used, it refers to the interaction of the electromagnetic fields of the colliding particles (causing attraction or repulsion) as opposed to actual mechanical contact [Cherry et al., 2012b].

and Gibbons, 2014a]. The cross section is calculated according to Equation 2.1, where N is the mean number of particle interactions within the target and ϕ is the particle fluence in particles/m^2 [ICRU, 2011a].

$$\sigma = \frac{N}{\phi} \tag{2.1}$$

Once an interaction does occur, it typically involves some kind of energy transfer between the incident particles and the material through which they are travelling. The term *dose* (with units of J/kg) is used to describe the energy deposited ($\mathrm{d}\bar{\varepsilon}$) per unit mass ($\mathrm{d}m$), where 1 J/kg is equivalent to 1 *gray* (Gy). The ICRU defines the dose according to Equation 2.2 [ICRU, 2011b].

$$D = \frac{\mathrm{d}\bar{\varepsilon}}{\mathrm{d}m} \tag{2.2}$$

These 2 quantities of cross section and dose are ubiquitous in the field of RT. Secondary to these ideas of a probability of particle interaction, and corresponding consequence (energy deposition), are the types of interactions themselves, and the laws governing the pattern of said depositions in the spatial dimension. These will be outlined in the relevant subsections below.

2.2.1 Photon interactions

There are two defining qualitative characteristics of photon interactions with matter which differentiates them from charged particles, the first of which is that they are many times more penetrating (see Fig. 2.6). This is owing to the fact that the cross sections of the interactions, which will be described in this subsection, are much smaller than the charged particle interaction cross sections (see Fig. 2.8). Secondly, as the beam of photons passes through matter they are attenuated in intensity but not degraded in energy. This is due to the fact that the various photon interaction processes, which will be described below, are able to completely remove the photon from the beam either through absorption or scattering. Consequently those photons that remain within the beam have not undergone any interaction process and therefore retain their initial energy [Leo, 1994].

In the context of uncharged particle interactions, the previously defined cross section can be calculated according to Equation 2.3, where N_A is the Avogadro constant, M is the molar mass of the material, and the quantity μ/ρ is the known as the *mass attenuation coefficient* [ICRU, 2011a].

$$\sigma = \frac{\mu}{\rho} \cdot \frac{M}{N_A} \tag{2.3}$$

In isolation, μ is called the *linear attenuation coefficient* and describes the probability that a particle of normal incidence undergoes an interaction within a material of specific thickness. Conversely, the *mean free path* is the reciprocal of μ and describes the average length travelled by the particle without undergoing any interaction [ICRU, 2011a].

The main photon interactions are Rayleigh and Compton scattering, the photoelectric effect, and the pair production reaction. Figure 2.3 depicts the various interaction cross sections per unit mass of material as a function of incident photon energy, where the total cross section is the arithmetic sum of the individual cross sections. In accordance with

the typical medical LINAC of Fig. 2.2, graphs of water[5] and tungsten are depicted to represent x-ray and electron irradiation modes respectively.

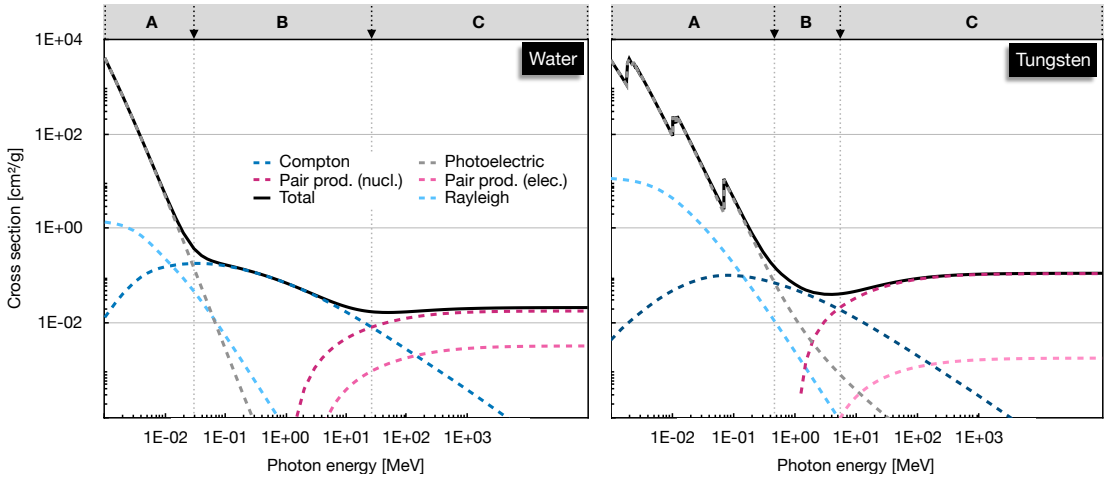

Figure 2.3: Interaction cross sections of photons in water (left) and tungsten (right). Regions **A**, **B**, and **C** depict the energies at which the photoelectric, Compton, and pair production interactions respectively dominate. Graphs were produced using data from the NIST database [Berger et al., 2010b].

As highlighted in Fig. 2.3, the most dominant interactions, depending on the energy, are the photoelectric effect, Compton scattering, and the pair production process, with Rayleigh scattering only playing a minor role at low energies. Schematic representations of each interaction are depicted in Figure 2.4, with the exact mechanisms described in the relevant subsections below.

The photonuclear (nuclear dissociation) interaction is much less common in a therapeutic setting and is not shown in either Figures 2.3 or 2.4, however it gains importance when considering certain novel RT techniques. This interaction will be introduced and discussed in more detail in section 2.8.

The Photoelectric effect

The photoelectric effect is based on the complete absorption of a photon, and corresponding ejection of an orbital electron (otherwise known as a *photoelectron*). In order for this interaction to occur, the energy of the incident photon, E_0, needs to overcome the binding energy of the orbital electron, E_{be}. Correspondingly, the energy of the emitted photoelectron is equal to the difference between the two energies: $E_{pe} = E_0 - E_{be}$. When an electron from an inner shell is ejected, a *hole* (or vacancy) is created. By losing energy through the emission of what is termed a *characteristic x-ray*, an electron in an outer shell fills that vacancy. This characteristic x-ray may then go on to be absorbed by another orbital electron leading to the emission of what is termed an *Auger electron* [Cherry et al., 2012b]. As can be seen in Fig. 2.3, this interaction process is the most dominant at low energies. When the Z of the material increases (i.e. for Tungsten) the energy range over which

[5] Most of the human body is comprised of water, with it being the major constituent (80%) in cells [Azzam et al., 2012]. Therefore for simplicity reasons, it is often used as a surrogate for biological tissue in both experimental and simulation contexts [Nikjoo et al., 2006].

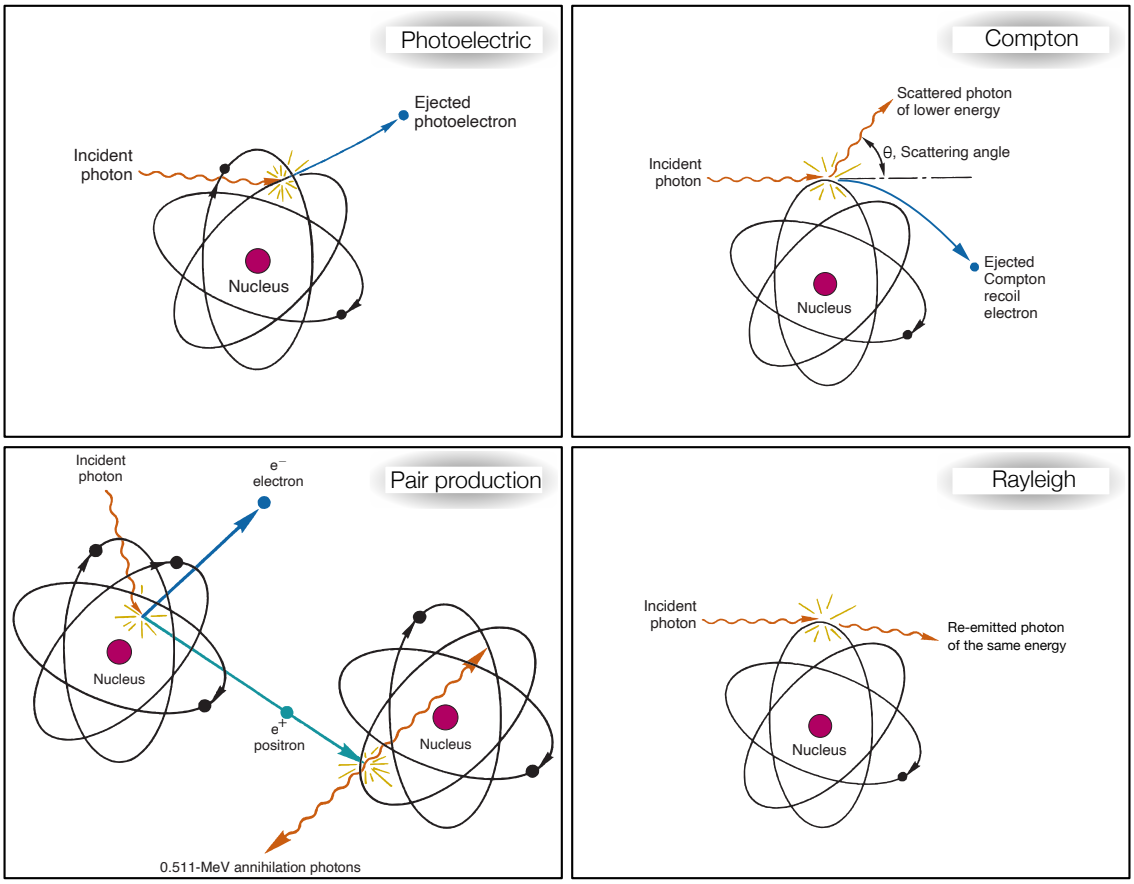

Figure 2.4: Schematic representations of the main photon interactions with matter. Adapted from [Cherry et al., 2012b].

this interaction occurs also increases, and sharp edges[6] in the cross section appear which represents the incident photon reaching a high enough energy to liberate the electrons of an inner shell.

Compton scattering

As the energy of the incident photon increases, Compton scattering becomes the most dominant interaction process over the photoelectric effect. Since the photon energy is so much higher than the binding energy of electrons, these electrons can effectively be thought of as 'free'. This interaction mechanism involves the incident photon scattering on an orbital electron, liberating it, then leaving with a new trajectory defined by the scattering angle θ, shown in Fig. 2.4. The photon scattering angle can range from 180° to 0°, where $\theta = 180°$ represents a direct hit (resulting in a backscattered photon with a forward scattered electron), while $\theta = 0°$ represents a grazing hit (resulting in a forward scattered photon with an electron scattered at right angles). Given that these electrons are 'free', the compton interaction cross section is largely independent of Z, and is instead dependent on the number of electrons per gram of material [Khan and Gibbons, 2014e]. This quantity is approximately constant for all elements and consequently leads to the

[6] The electron binding energy is directly proportional to Z. Consequently, the edges are not shown for water as they occur at very low energies [Khan and Gibbons, 2014e].

observable trend in Fig. 2.3, where the Compton cross section is largely unchanged between water and tungsten. Compton scattering is the most important interaction in the context of RT.

Pair Production

Pair production involves the interaction of an incident photon in the electromagnetic field of a charged particle. While in most cases the offending electromagnetic field is that of the atomic nucleus, it can also be that of the orbital electrons. This preference for nuclear pair production as opposed to electronic pair production is evidenced by the enhanced cross section of the former over the latter as shown in Fig. 2.3. In this interaction, the photon is completely absorbed and an electron-positron pair is created. The minimum photon energy for this interaction to occur is $E = 2m_e = 1.022$ MeV, where $m_e = 0.511$ MeV is the rest mass of both the electron and positron. For increasing photon energy, this interaction eventually overtakes the Compton interaction for the most dominant process, and any additional photon energy is imparted to both the recoil electron and positron. The positron may then go on to *annihilate* with a nearby electron, leading to the emission in opposite directions of two 0.511 MeV *annihilation photons* [Cherry et al., 2012b].

Rayleigh scattering

Rayleigh scattering (also known as coherent scattering) is an elastic process in which there is no transfer of energy. The incident photon is briefly absorbed by an orbital electron, and immediately re-emitted with the same energy with a slight angular deflection, resulting in approximately the same direction of travel. This type of photon interaction is primarily of academic as opposed to therapeutic interest for two main reasons. Firstly, no energy is deposited which means that this interaction does not contribute to the absorbed dose. Secondly, the interaction only becomes probable with photons of low energy or for high-Z materials [Khan and Gibbons, 2014e] as shown in Fig. 2.3, but it never becomes the most dominant interaction process.

2.2.2 Neutron interactions

In addition to photons, neutrons represent the other type of indirectly ionising radiation. In the majority of cases, these neutrons are not explicitly generated, but are rather a consequence of various processes (i.e. fission, fusion, space radiation interactions), each leading to the generation of neutrons of a wide range of energies. In the context of conventional RT, we are mostly concerned with the production of neutrons from the previously mentioned photonuclear interaction, which produces neutrons with a maximum energy of approximately 30 MeV [Banaee et al., 2021].

The different interaction processes for neutrons with matter are scattering (elastic or inelastic), neutron absorption, and spallation, whose various cross sections, similarly to photons, varies as a function of incident neutron energy. Elastic scattering is important up to 14 MeV, and involves the scattering of the neutron on a target nucleus, causing it to *recoil*. The dose deposited by these elastic interactions is predominantly through recoiling hydrogen nuclei (protons). While termed a 'scattering' interaction, the inelastic process actually involves brief neutron capture by the nucleus leaving it an excited state, followed by the emission of a neutron with a different energy and a γ-ray[7]. Neutron absorption is

[7] The term γ-ray is used for photons originating from the nucleus, i.e. through de-excitation events,

most dominant for low energy (*thermal*) neutrons, leading to the creation of radioactive isotopes which go on to disintegrate through the emission of γ-rays, protons, or α-particles, which themselves are major contributors to the dose. And finally, the spallation interaction only becomes relevant for energies in excess of 100 MeV and involves the capture of a neutron by a nucleus, which subsequently undergoes nuclear fragmentation [Alpen, 1997a].

Neutrons are particularly biologically effective, therefore one of the factors that needs to be considered when proposing the clinical translation of novel RT techniques is the likelihood and magnitude of secondary neutron production within a treatment room. These considerations are explored in more detail in sections 2.4 and 2.6 respectively.

2.2.3 Charged particle interactions

Charged particle interactions in matter are particularly important since the principal mechanism by which energy is finally deposited in a biological environment is through the interaction of electrons with the surrounding medium. Regardless of the mass of the charged particle, this energy loss is primarily through coulombic interactions (forces of attraction/repulsion) between the electric field of the charged particle, and those of the nuclei/electrons of the matter through which they are travelling [Alpen, 1997a]. The energy transfer of these charged particle interactions is inversely proportional to the squared velocity of the incident particle. This relation was highlighted by both Bethe [Bethe, 1930] and Bloch [Bloch, 1933], leading to the Bethe-Bloch formulation for charged particle energy loss, shown in Equation 2.4. The consequence of this inverse proportionality is that the energy loss per unit length, dE/dx, along the particle trajectory drastically increases as the particle slows down. This can be seen in Fig. 2.6 in which the trend in energy deposition in depth for different particles is compared.

$$-\frac{dE}{dx} = 2\pi N_A {r_e}^2 m_e c^2 \rho \frac{Z}{A}\frac{z^2}{\beta^2}\left[\ln\left(\frac{2m_e\gamma^2 v^2 W_{\max}}{I^2}\right) - 2\beta^2 - \delta - 2\frac{C}{Z}\right] \tag{2.4}$$

The terms r_e and m_e are constants for the electron radius and mass respectively. The speed of light is given by c, and the incident particle is described through its charge z and velocity v, where $\beta = v/c$ and the Lorentz factor $\gamma = 1/\sqrt{1-\beta^2}$. The absorbing material is taken into account through its density ρ, atomic number Z, and atomic weight A. $W_{\max}$ and I are terms describing the maximum energy in a single collision and mean excitation potential respectively, and δ and C are the density and shell correction terms which become important at high and low energies respectively [Leo, 1994].

The coulombic interactions of charged particles lead to energy losses that are classified as either elastic or inelastic, with the latter being depicted in Fig. 2.5. These inelastic interactions can be further classified as *collisional losses* or *radiative losses*.

While collisional losses are characterised by atomic excitation or ionisation[8] of an orbital electron due to coulombic forces, radiative losses occur when an incident charged particle interacts with the atomic nucleus. These radiative losses are characterised by an incident particle being subjected to the strong electric forces of the nucleus, leading to its deflection, rapid deceleration, and subsequent emission of a photon (known as a *Bremsstrahlung* photon) [Cherry et al., 2012b].

whereas x-rays originate from outside of the nucleus [Khan and Gibbons, 2014a].

[8] If the energy transferred to the ionised electron is sufficiently high it may go on to cause secondary ionisation events. These secondary electrons are known as δ-rays [Leo, 1994].

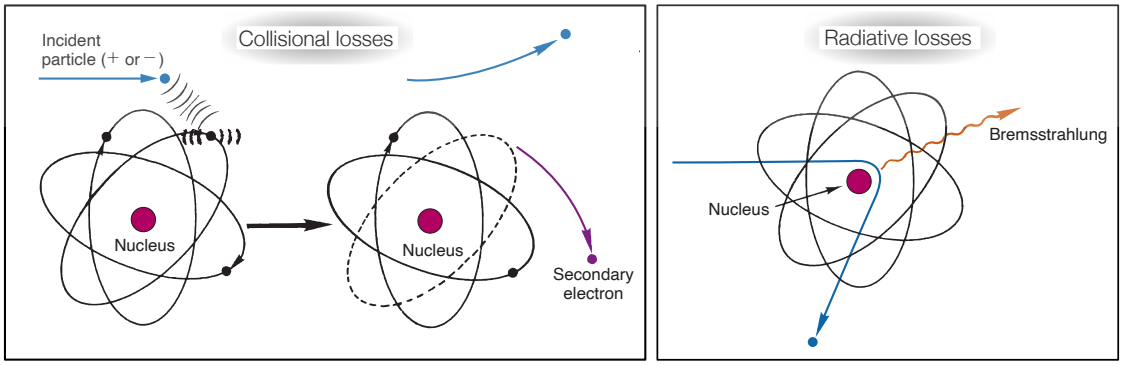

Figure 2.5: Schematic representations of the main charged particle interactions with matter. Adapted from [Cherry et al., 2012b].

In addition to the above inelastic interactions, charged particles suffer repeated elastic interactions - primarily with the atomic nucleus - in a process known as multiple Coulomb scattering (MCS). These repeated scatterings at small angles causes the incident particle to follow a zigzag pattern, with the cumulative effect being a net deflection from the particle's original trajectory [Leo, 1994]. It is at this point that it makes sense to distinguish the preferred interactions of *light charged particles* such as electrons and positrons, from those of *heavy charged particles* such as protons and alphas or heavier. These are detailed in the subsections below.

Heavy charged particles

As would intuitively be expected, the net angular deflection due to MCS for heavy charged particles is much less than that of light charged particles owing to their mass. Correspondingly, the incident particle remains largely undeflected over its range. This is one of the assumptions of the Bethe-Bloch formula of Equation 2.4. In fact, for heavy charged particles, Equation 2.4 as it is shown is largely accurate to within a few percent for relativistic particles down to $\beta \approx 0.1$ and can be decreased even further by adding other correctional terms [Leo, 1994]. Other interaction processes such as nuclear reactions or Cherenkov radiation are possible but rare, and are often not considered in the context of RT treatments. Finally, given that the magnitude of Bremsstrahlung losses are inversely proportional to the square of the incident particle mass, these radiative losses are largely negligible for heavy charged particles [Baker, 2012].

Light charged particles

The Bethe-Bloch equation, as it relates to light charged particles such as electrons or positrons needs additional correctional terms for two main reasons. Firstly, given its small mass it is greatly deflected during the collision process thereby invalidating the assumption of undeflected trajectory inherent in Equation 2.4. Secondly, the incident colliding electrons and deflected orbital electrons are identical and therefore indistinguishable [Leo, 1994]. An additional consequence of the small mass of the electrons is that the influence of Bremsstrahlung is no longer negligible, particularly at high energies as shown in Fig. 2.8. Consequently, their total energy loss per unit length becomes a summation of the collisional and radiative losses as shown in Equation 2.5 [Leo, 1994].

$$\left(\frac{dE}{dx}\right)_{\text{tot}} = \left(\frac{dE}{dx}\right)_{\text{coll}} + \left(\frac{dE}{dx}\right)_{\text{rad}} \tag{2.5}$$

This knowledge about how charged and uncharged particles interact with matter allows one to have a theoretical foundation upon which investigations into their consequences in a clinical setting can be built. These consequences will be discussed in the remainder of this section and are primarily: variations in the longitudinal depth of penetration of a particle beam, the extent of its lateral spread from the central beam axis, and how clustered/dispersed the points of energy deposition are.

2.2.4 Dosimetric quantities

As mentioned earlier, energy deposited by various particle interactions are interpreted through the lens of *dose* which is ubiquitous in the field of RT. Consequently, quantities related to said dose can be defined as follows:

Definition 2

Dosimetric quantities are those which describe the results of processes by which particle energy is converted and finally deposited in matter. They are used to provide a physical measure of, and correlate, the actual or potential effects of ionising radiation in the human body [ICRU, 2011b].

Dose deposition in depth

The depth that an ionising particle reaches in matter is often described in terms of its percentage depth dose (PDD), which is the ratio between the measured dose at a particular depth, $D(d)$ and the maximum dose deposited over the entire range $D(d_{max})$:

$$\text{PDD} = \frac{D(d)}{D(d_{max})} \times 100 \tag{2.6}$$

A typical MV photon beam is very penetrating, and retains a high relative level of dose deposition ($\gtrsim 70\%$) across the majority of its range. The first few centimetres of the material is referred to as the *dose build-up region*. As shown in Fig. 2.3, the Compton interaction dominates at this energy level. The liberated Compton electrons do not all deposit their energy at the site of the Compton interaction but rather do so over a finite range. The build-up region is then created from *downstream* regions still receiving energy depositions from electrons created upstream, up to a point where the number of electrons entering upstream is equal to those leaving downstream. This condition is known as *charged particle equilibrium* [Baker, 2012].

As was previously mentioned, the interaction mechanisms of photons in matter are able to completely remove the photon from the beam path, leading to the beam being attenuated in depth. This exponential[9] attenuation is responsible for the decrease observed

[9] The intensity of the photon beam is reduced according to the equation $N = N_0 e^{-\mu x}$ which has the same mathematical form as the equation describing radioactive decay [Baker, 2012].

beyond 1 cm in Fig. 2.6. Nevertheless doses still remain high beyond the point of charged-particle equilibrium, which is detrimental for the sparing of healthy tissue behind the tumor. Neutron PDD is similar to that of photons in that there is an initial build-up region followed by an exponential decrease.

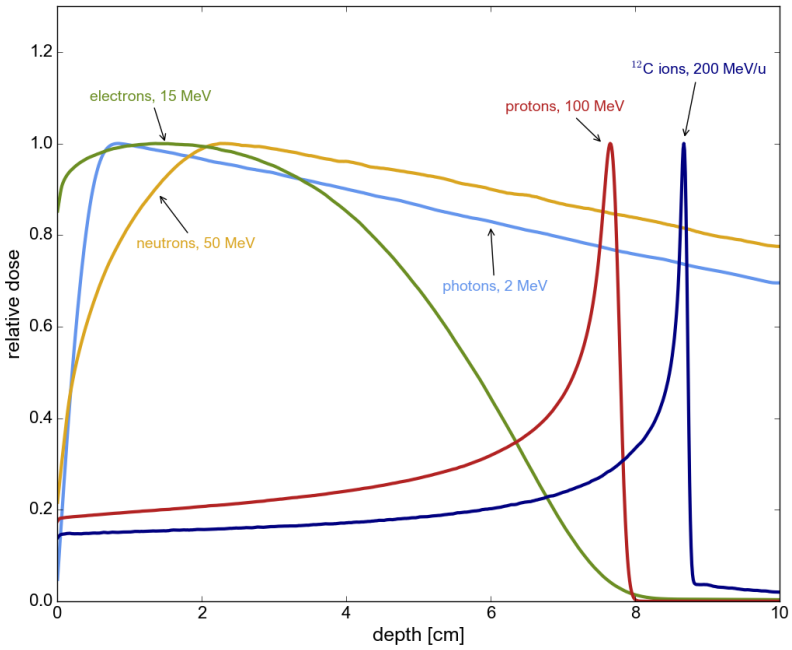

Figure 2.6: Percentage depth dose curves for beams of different particles in a water phantom. Each curve was normalised to the maximum dose. Taken from [Schneider, 2020].

The PDD curves for charged particles represent a marked change in the behaviour of dose deposition events in depth, with a further distinction being visible for light charged particles such as electrons compared to the heavier charged particles of protons or carbon ions. For electrons, the relatively high entrance dose is followed by a steady fall off as the electrons lose energy to their surroundings at an approximately continuous rate [Baker, 2012]. These low energy electrons are most useful for treating superficial tumors, however by increasing their energy up to hundreds of MeV the steepness of the drop off decreases and a deeper penetration depth is possible [DesRosiers et al., 2000]. These VHEEs are therefore more suited to the treatment of deep-seated tumors and will be expanded upon in section 2.8.

Protons and Carbon ions exhibit relatively low entrance doses, followed by a sharp rise in the dose deposited near the end of their range, known as a *Bragg peak*, followed by a sharp dose drop off. This peak is due to the inverse proportionality of the rate of energy deposition in depth with incident particle velocity, as can be seen in Equation 2.4. This idea of a very localised high dose is important in the context of RT as it enables the sparing of normal tissue both in front of, and behind the tumor [Baker, 2012]. The consequence of using heavier ions such as carbon is that one is able to obtain an even sharper Bragg peak, however this comes at the cost of a non-negligible dose beyond the drop-off. This *fragmentation tail* is due to an increased contribution by nuclear fragments to the dose, which becomes even more prevalent as the size of the incident charged particle increases [Baker, 2012].

Lateral scattering

The PDD curves of Fig. 2.6 only show one part of the picture when it comes to how the dose is distributed. These curves show the on-axis dose deposition, however as was highlighted when describing the various charged and uncharged particle interactions, there are some interaction mechanisms which cause the incident particle or the recoiling nucleus/electron (or both) to be deflected at some angle from the original incidence. The *lateral scattering* is then a measure of the degree to which ionising radiation has deviated from the central axis of the beam. This lateral scattering forms what is known as a beam *penumbra*. The ICRU defines this penumbra as the lateral cross section, at a specific depth, in which the dose decreases from 80% of the maximum dose down to 20% [ICRU, 2007]. A comparison of the different penumbras associated with the use of different particles is shown in Fig. 2.7.

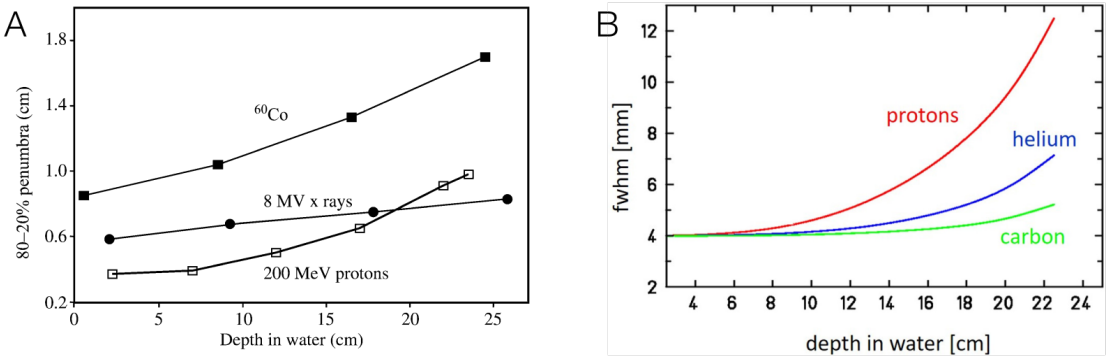

Figure 2.7: Comparison of the penumbras of different particle beams. Panel **A** was taken from [ICRU, 2007], while panel **B** was taken from [Jäkel, 2020].

Linear energy transfer and stopping power

For charged particles, the mass stopping power (S/ρ) describes the pattern of energy deposition events and is given by Equation 2.7 with units of $J \cdot m^2 kg^{-1}$:

$$\frac{S}{\rho} = \frac{1}{\rho}\frac{dE}{dl} \tag{2.7}$$

This equations describes the mean energy dE lost by charged particles traversing a distance dl in a material of density ρ. Consequently S denotes the linear stopping power [ICRU, 2011a]. The total mass stopping power can be expressed as the sum of three separate quantities: energy loss due to electron ionisation or excitation from Coulomb collisions (electronic/collision stopping power), Bremsstrahlung losses (radiative stopping power), and the transfer of energy to recoiling atoms through elastic Coulomb interactions (nuclear stopping power). The contribution of each quantity to the total stopping power for incident electrons, protons and alpha particles is shown in Fig. 2.8.

While Bremsstrahlung is theoretically possible for protons or light/heavy ions, in the context of RT it is negligible at the typical therapeutic energies and is only important for electrons [Khan and Gibbons, 2014e]. As can be seen in Fig. 2.8, radiative losses becomes the most dominant energy loss mechanism for incident electrons at higher energies, while for protons and heavier energy losses are predominantly in the form of Coulomb collisions with orbital electrons.

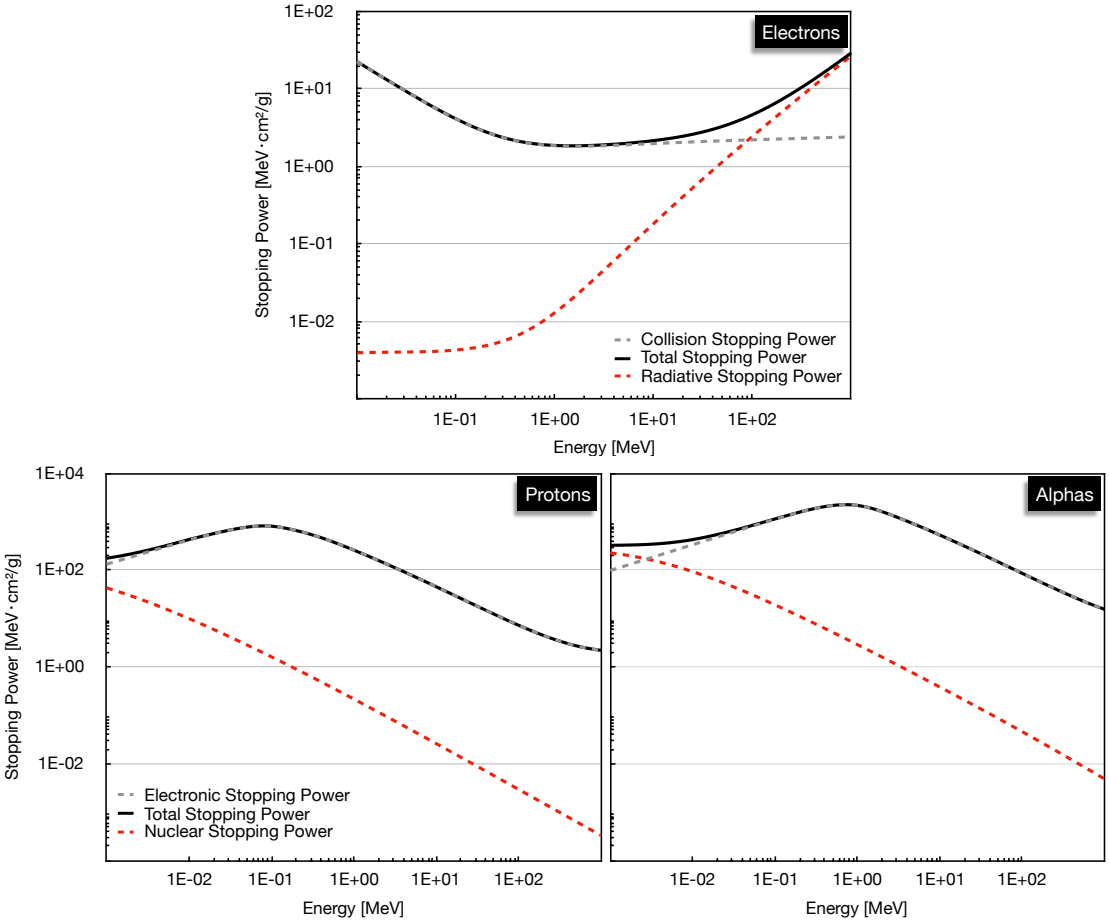

Figure 2.8: Total mass stopping powers for incident electrons, protons, and alpha particles in liquid water. Produced using data from the NIST *ESTAR*, *PSTAR*, and *ASTAR* databases respectively [Berger et al., 2017].

While the stopping power considers the total amount of energy lost by a charged particle, the restricted linear energy transfer (LET) only takes into account local energy losses and does not consider energy transfers responsible for the creation of δ-rays. The ICRU defines the restricted LET as the mean energy lost dE_Δ by charged particles due to electronic interactions while travelling a distance dl, minus the sum of the kinetic energies of all electrons (δ-rays) having a kinetic energy greater than Δ (and thus not depositing their energy locally) [ICRU, 2011a]:

$$LET = \frac{dE_\Delta}{dl} \tag{2.8}$$

One can view this Δ as being a radial distance around the particle track. If no energy cutoff is specified, the unrestricted LET is then exactly equivalent to the electronic stopping power S_{el}, given by dE/dl in Equation 2.7 [ICRU, 2011a]. Equation 2.8 is only valid for monoenergetic beams, however in a more realistic scenario each constituent particle of a clinical beam of IR may have its own LET. Consequently, two *flavours* of LET are typically reported - the track-averaged LET, or the dose-averaged LET. In the former, a frequency distribution of LETs within the beam is used as a weight, while in the latter the reported LET is weighted by the absorbed dose. The dose-averaged LET can be calculated

deterministically by Equation 2.9,

$$LET_d(z) = \frac{\int_0^\infty S_{el}(E)D(E,z)dE}{\int_0^\infty D(E,z)dE} \tag{2.9}$$

where $S_{el}(E)$ is the electronic stopping power, and $D(E,z)$ is the absorbed dose contributed by primary charged particles with kinetic energy E at location z [Guan et al., 2015]. In the context of RT, dose-averaged LET is typically reported as it is the better correlating quantity to the biological damage to tissues [Granville and Sawakuchi, 2015]. Calculation of both the track- and dose-averaged LET in the context of particle tracking MC simulations is extensively discussed elsewhere [Kalholm et al., 2021, Cortés-Giraldo and Carabe, 2015, Granville and Sawakuchi, 2015, Guan et al., 2015, Shin, 2020].

Lineal energy While the LET is a macroscopic quantity, its microscopic equivalent is the *lineal energy* y, defined as the ratio of ε_s to $\bar{l}$, where ε_s is the energy imparted to a given volume by a single energy deposition event, and $\bar{l}$ is the mean chord length of that volume [ICRU, 2011a]:

$$y = \frac{\varepsilon_s}{\bar{l}} \tag{2.10}$$

The lineal energy is expressed in units of $keV/\mu m$, and the mean chord length is given by $4V/A$ where A is the surface area and V is the volume [ICRU, 2011a]. Given that the lineal energy is a stochastic quantity, it is useful to describe it in terms of the probability density function $f(y)$. As stated in ICRU report 36, the expectation value of this probability density is then termed the *frequency-mean lineal energy* ($\bar{y}_F$) and is given by [ICRU, 1983]:

$$\bar{y}_F = \int_0^\infty y f(y) dy \tag{2.11}$$

This quantity is the first moment of $f(y)$ and can be considered to be the microdosimetric analogue to the track-averaged LET. The *dose-mean lineal energy* ($\bar{y}_D$), on the other hand, is the second moment[10] of $f(y)$, therefore describing the variance of energy depositions within the sensitive volume. It can be considered to be the microdosimetric analogue to the dose-averaged LET and is calculated as follows [ICRU, 1983]:

$$\bar{y}_D = \int_0^\infty y d(y) dy = \frac{1}{\bar{y}_F} \int_0^\infty y^2 f(y) dy \tag{2.12}$$

The quantity $yd(y)$ in Equation 2.12 is known as the dose-weighted lineal energy distribution, and $d(y)$ is related to $f(y)$ through the following equation [ICRU, 1983]:

$$d(y) = \frac{y}{\bar{y}_F} f(y) \tag{2.13}$$

Both $\bar{y}_F$ and $\bar{y}_D$ are used to characterize radiation quality, and, as will be shown in section 2.5 can be used to accurately predict the survival of irradiated human cell lines

[10] In mathematical terms, the first moment of a probability density is the expected value, while the second moment is its variance.

[Kase et al., 2006, Kase et al., 2013].

In summary, this section spoke about the physical interactions mechanisms of incoming beams of IR as well as the liberated secondary particles, the consequences thereof, and related concepts. However what about the atom/molecule of the biological medium which was left in either an excited or ionised state? This is where water radiolysis comes in, as detailed in the following section. Beyond the physical interactions, it represents the next step in the chain linking the physics of the irradiation to the resulting biological response.

2.3 Water radiolysis

The mechanism of DNA damage caused by IR is categorised as either *direct action* or *indirect action*, depending on its target. In both cases it leads to the induction of single-strand breaks, double-strand breaks, or base damages to the DNA molecule. The biological ramifications of these damages will be expanded upon in section 2.4. In the direct action, the IR interacts directly with the DNA molecule, thereby splitting the chemical bonds. In the latter, IR interacts with an H_2O molecule in the vicinity of DNA, leading to the production of chemical species known as *free radicals*. This generation of free radicals occurs through a process called *water radiolysis* [Hall and Giaccia, 2012a]. The most important free radical in the context of indirect DNA damage induction is the hydroxyl radical ($^{\bullet}OH$) [von Sonntag, 2006].

Given the pattern of energy deposition of a single radiation track, the associated DNA damage occurs in clusters, where increasing particle LET leads to more complex, less repairable DNA damage [Hill, 2018]. This shift to higher LET is also associated with a shift towards a dominance for direct damage as opposed to indirect damage. 70% of all DNA damage induced by sparsely ionising x-rays is due to the indirect action [Roots and Okada, 1975] whereas the higher the LET of the particle, the more densely packed the energy deposition events, leading to a greater probability for direct damage. Various studies over the years have shown a decreasing contribution of the indirect action for increasing particle LET [Hirayama et al., 2009]. Both the direct and indirect actions are depicted in Fig. 2.9.

Given that other molecules within the cellular environment are susceptible to IR induced chemical transformations, why is it that DNA has long been accepted as the critical target molecule for IR? The difference between the loss of biologic activity of other molecular species within a cell compared to the loss of biologic activity of DNA is that the former can more often than not be sustained without any significant adverse consequences, due to the cell continually replacing important biological molecules. The latter, on the other hand, leads to biologically important changes in cell survival owing to the fact that the total genome[11] within a cell is unique. This lack of redundant information means that irreversible damage leads to loss of cellular function [Alpen, 1997b].

2.3.1 General overview of water radiolysis processes

From a holistic point of view, the free radical induced DNA damage as a consequence of water radiolysis is important as it represents a vital link in the chain connecting the physical parameters of the irradiation to the eventual biological response. A definition is therefore important:

[11] The genome refers to the entire set of DNA instructions found within a cell [Green, 2023].

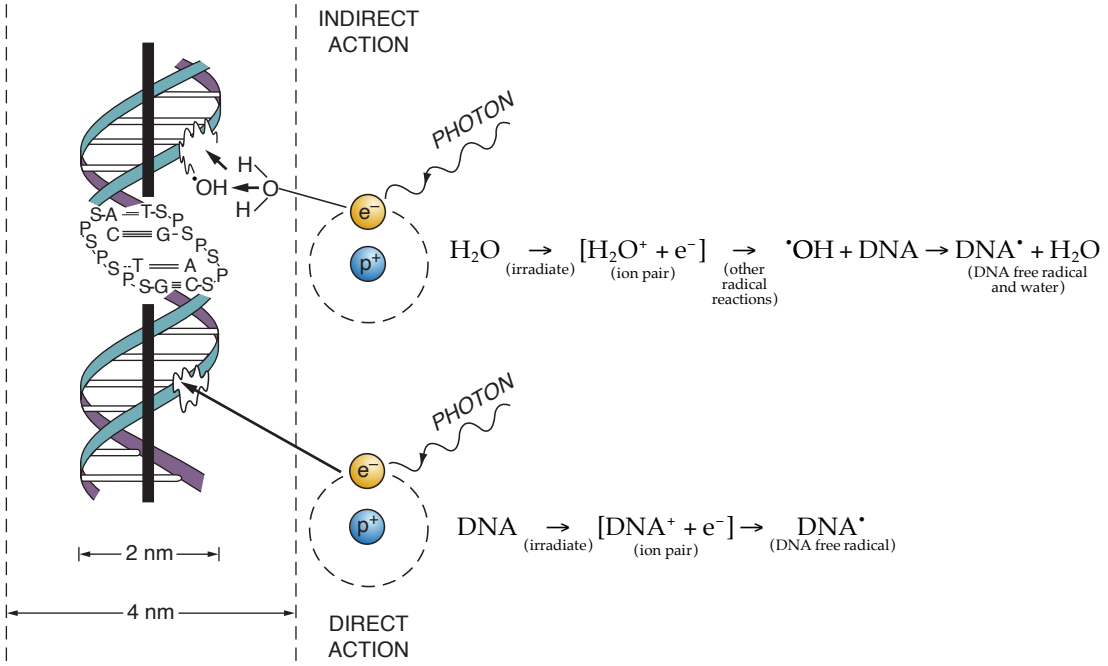

Figure 2.9: Mechanisms of DNA damage induction by IR. In the direct action, there is a direct interaction within the DNA molecule, whereas in the indirect action the damage is caused by free radicals generated through water radiolysis. Adapted from [Hall and Giaccia, 2012a] and [Zeman, 2016].

Definition 3

Water radiolysis is defined as the process by which molecules of water, having been ionised or excited by IR, decompose into either radical or molecular chemical species. This decomposition occurs in four, more or less distinct temporal stages, namely: the *physical*, *physicochemical*, *chemical*, and in a physiologic system, the *biological* stage [Azzam et al., 2012].

The term *free radicals* refers to molecules that are characterised by their unpaired valence electron, therefore making them highly unstable (i.e. highly reactive), and ROS are a subset of free radicals which contain oxygen [Pham-Huy et al., 2008]. These ROS can be further classified as either free oxygen radical ROS and the nonradical, where the former are representative of typical free radicals with an unpaired electron in the outer molecular orbit, while the latter lacks unpaired electrons but still remains reactive. The most widely studied free oxygen radical and nonradical ROS are $^{\bullet}OH$ and hydrogen peroxide (H_2O_2) respectively [Gupta et al., 2012].

As stated in Definition 3, the main stages of water radiolysis are the physical, physicochemical, chemical, and biological stage. Broadly speaking, the physical stage occurs up to approximately 1 fs, where the physical interactions of the incident IR leads to a collection of electrons (e^-) and water molecules which are ionised (H_2O^+) or excited (H_2O^*). Numerous processes occur in the physicochemical stage (10^{-15} – 10^{-12} s), leading to an initial creation of chemical species. This is followed by the chemical stage (10^{-12} – 10^{-6} s), where these initially created species diffuse and react with one another [Le Caër, 2011]. And finally in the biological stage ($\sim 10^{-3}$ s or longer), cells respond to the damages caused

by chemical species produced in the preceding stages [Azzam et al., 2012].

As early as 1905, various pioneering works in the field of radiation chemistry showed that irradiation by α-rays caused water to smoothly decompose into hydrogen gas and oxygen gas, with some of the oxygen combining with water to form hydrogen peroxide [Allen, 1948]:

$$H_2O \xrightarrow{\alpha\text{-irradiation}} H_2,\ O_2,\ H_2O_2 \tag{2.14}$$

It was later shown that when using x-rays instead of α-rays to irradiate aqueous solutions of water, the molecules of water decomposed into hydrogen and hydroxyl radicals [Risse, 1929, Weiss, 1944, Fricke et al., 1938].

$$H_2O \xrightarrow{x\text{-irradiation}} H^{\bullet},\ {}^{\bullet}OH \tag{2.15}$$

This dependence of the decomposition products on the LET of the incident particle was first described by Allen, who also put forward the concept of chemical *spurs* occurring along the track of the ionising particle [Allen, 1948]. The main ideas of his work were that molecular decomposition products (such as H_2O_2) were produced by radical-radical reactions within the high radical concentration spur, and that there exists a constant competition between the reactions of these radicals and their escape into the bulk liquid [Buxton, 2004]. Significant advances have since been made, and water radiolysis is now well understood both experimentally and theoretically. The entire process can be summarised as follows[12] [Le Caër, 2011]:

$$H_2O \xrightarrow{\text{ionising radiation}} e^-_{aq},\ {}^{\bullet}OH,\ H^{\bullet},\ HO_2^{\bullet},\ H_3O^+,\ OH^-,\ H_2O_2,\ H_2 \tag{2.16}$$

The creation of these species in space, and their associated yield, is detailed in the following subsection.

2.3.2 Radiolytic yield

All along the radiation track, chemical species are created in clusters which are differentiated by the local density of reactive species which themselves are created in accordance with the energy deposited in that locality. These clusters are referred to as *spurs* (0 - 100 eV), *blobs* (100 - 500 eV), and *short tracks* (500 - 5000 eV), with their relative ratio depending on the type of incident particle and its energy [Mozumder and Magee, 1966]. Taking 1 MeV electrons as an example, 65% of its energy is deposited in isolated spurs, 15% in blobs, and 20% in short tracks [Mozumder and Magee, 1966]. These clusters are depicted in Fig. 2.10.

The yield of chemical species at various points throughout the process of water radiolysis are referred to as *G-values* [Burton, 1947], which are typically reported as a number of species per 100 eV:

[12] Depending on the author/publication/study, the hydronium ion H_3O^+ is sometimes replaced with the hydrogen ion H^+ in chemical reactions [Frongillo et al., 1998]. Nevertheless, the two are equivalent, with the former simply representing the hydrated version of the latter.

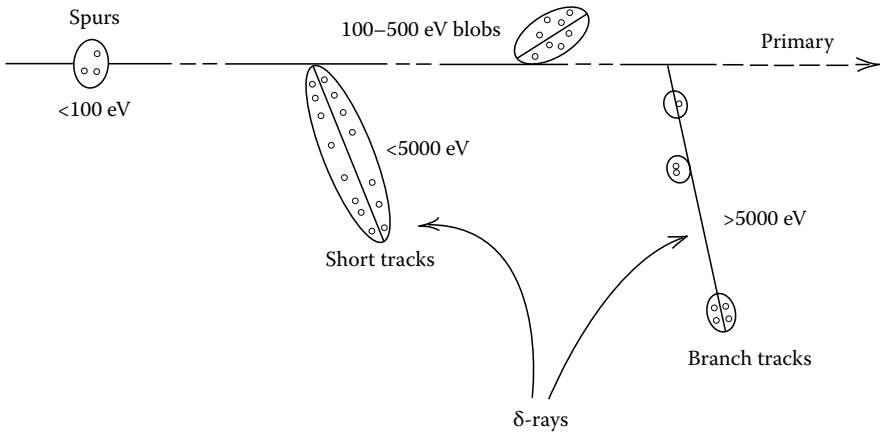

Figure 2.10: Classification of chemical species created along a particle track. Spurs are approximately spherical, blobs are approximately spherical or ellipsoidal, and short tracks are approximately cylindrical. Both short and branch tracks are characteristic of δ-rays. Taken from [Meesungnoen and Jay-Gerin, 2011].

$$\text{G-value (species/100 eV)} = \frac{\text{number of species produced or consumed}}{\text{100 eV of energy deposited}} \tag{2.17}$$

At the end of the chemical stage (approximately 10^{-6} s) the created species are assumed to be homogeneously distributed and the G-value at this point is now referred to as the *primary yield*. The framework within which water radiolysis occurs is quite well understood both experimentally and theoretically, and it is now generally agreed upon that for low LET radiation such as x-rays, γ-rays, and fast electrons, the primary yields resulting from water radiolysis in pure liquid water can be approximated as follows [Buxton, 2004]:

$$4.2\,H_2O \xrightarrow{\text{ionising radiation}} 2.7\,e^-_{aq},\ 0.6\,H,\ 2.7\,OH,\ 0.45\,H_2,\ 0.7\,H_2O_2,\ 2.7\,H^+ \tag{2.18}$$

Nevertheless these yields relate to conventional RT for only a specific set of particles. Therefore in the context of novel RT techniques, there is a real interest in the investigation of the radiochemical consequences of the physico-chemical and chemical stages of water radiolysis, which may be involved in potential novel radiobiological mechanisms.

2.3.3 Scheme of water radiolysis

The entire water radiolysis scheme is depicted in Fig. 2.11, which details the approximate timescales for each stage, as well as the main processes associated to each stage. The chemical stage can be further classified as corresponding either to heterogeneous chemistry or homogeneous chemistry, where in the former, chemical species diffuse and react with one another in the spur, whereas in the latter, these species are assumed homogeneously distributed and react with the bulk water. As mentioned earlier, the transition between the stages occurs at more or less distinct time points. This fact is depicted in Fig. 2.11 with each stage being strictly separated. However it should be noted that changes in the

local environment may cause a stage to occur at a different point in time. Taking the transition from heterogeneous to homogeneous chemistry as an example, it has been shown that parameters such as acidity, temperature, and pressure will cause this transition to occur either earlier or later [Kanike et al., 2017].

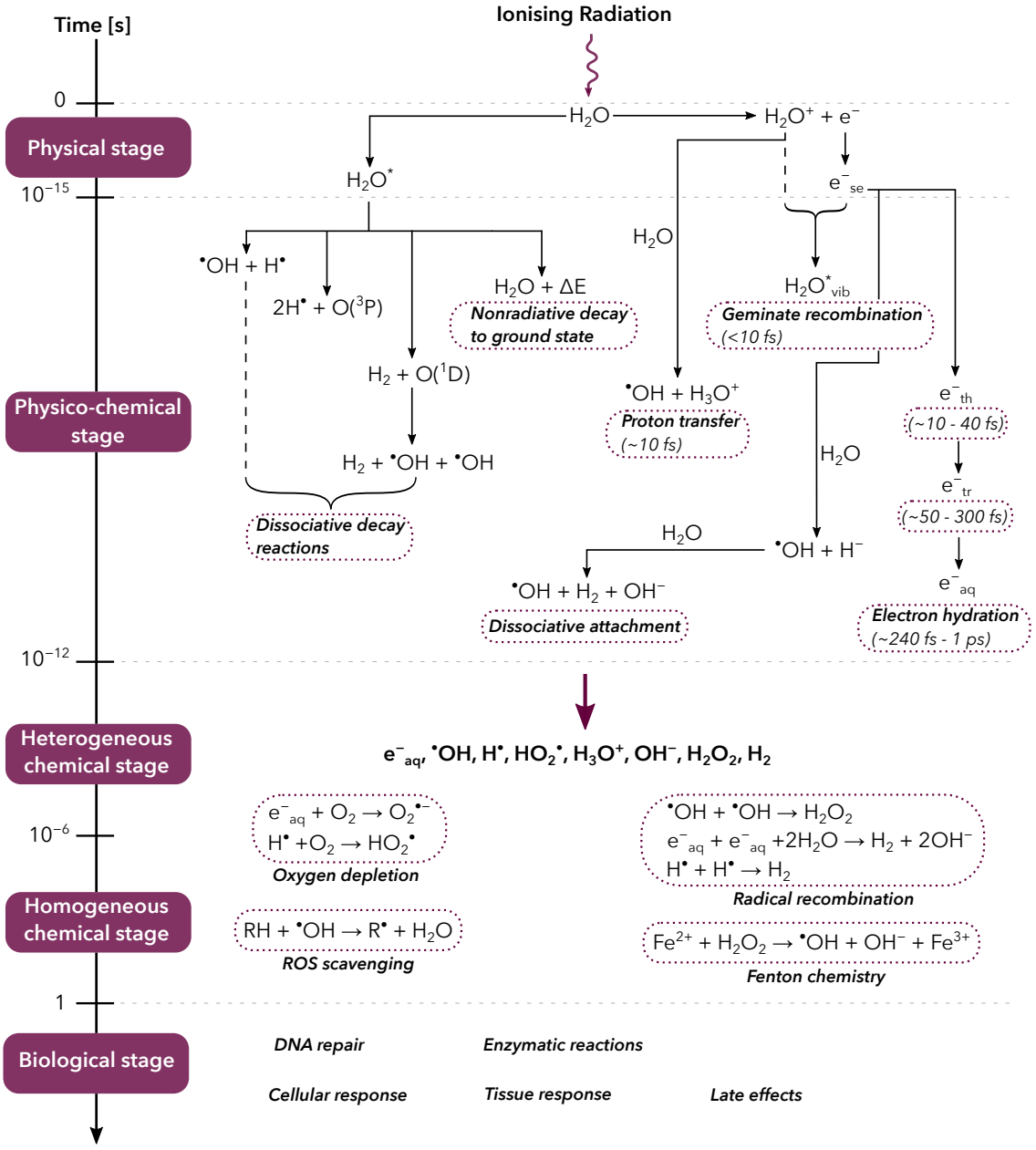

Figure 2.11: Schematic depiction of all 4 stages of water radiolysis along with the main processes involved in each stage. Adapted from: [Le Caër, 2011, Meesungnoen and Jay-Gerin, 2011, Baikalov et al., 2022].

Another thing to note, is that the progression of each stage of water radiolysis is characterized by the final event of one stage being the initial triggering event of the next stage. For example, the final event in the physical stage is the creation of three distinct species: an excited water molecule (H_2O^*), an ionised water molecule (H_2O^+), and

subexcitation electrons (e^-_{se})[13] [Platzman, 1955], from which all physico-chemical processes stem. The final event in the physico-chemical stage is the creation of various chemical species, which is then fed into the chemical stage. And the location/concentration of species at the end of the chemical stage directly relates to the observed biological effect.

2.3.4 Physico-chemical stage

While the sequence of events in the physico-chemical stage are still not well characterized experimentally [Plante, 2010], the main processes are known to consist of ion-molecule/electron reactions, dissociative relaxation, auto-ionisation of excited states, thermalisation of subexcitation electrons (otherwise known as electron solvation), and hole diffusion [Le Caër, 2011].

Fate of ionised water molecules, H_2O^+

There are three main pathways that describe the fate of H_2O^+: the ion-molecule reaction (otherwise known as the proton transfer reaction), the ion-electron reaction, and hole diffusion (or hole migration/electron transfer). The proton transfer reaction is shown in Reaction R1.1. It occurs very early on in the physico-chemical stage ($\sim$ 10 fs) [Azzam et al., 2012] and is important in the context of RT as it produces the $^{\bullet}OH$ species:

$$H_2O^+ + H_2O \longrightarrow {}^{\bullet}OH + H_3O^+ \tag{R1.1}$$

The ion-electron reaction involves the recombination of subexcitation electrons with H_2O^+ to form water molecules in high vibrational levels of their electronic ground state [Buxton, 2004]:

$$H_2O^+ + e^-_{se} \longrightarrow H_2O^*_{vib} \tag{R1.2}$$

And hole diffusion involves the migration of H_2O^+ over a few molecular diameters [Buxton, 2004]:

$$H_2O^+ + H_2O \longrightarrow H_2O + H_2O^+ \tag{R1.3}$$

In early water radiolysis studies, Reaction R1.1 was considered the dominating reaction, whereas Reaction R1.2 was completely neglected [Kaplan et al., 1990]. However recent evidence points to Reaction R1.2 occurring faster than R1.1, as well as there existing certain situations whereby Reaction R1.2 may in fact compete with R1.1 [Ma et al., 2018]. In the context of RT this has important practical consequences as a preference of one reaction

[13] The initially ejected electron usually has enough energy to further ionise/excite other water molecules. This process continues until the electron energy is lower than the minimum energy required to electronically excite a water molecule (7.4 eV) - hence the term *subexcitation electron*. The remaining energy is lost through vibrational losses (Reaction R1.2) dissociative attachment (Reaction R1.9) or thermalisation (Equation 2.19) [Buxton, 2004]

over the other would lead to differences in pH and $^{\bullet}OH$ yield. Given the extremely transient nature of the existence of H_2O^+, a full understanding of the competing/complementary nature of Reactions R1.1-R1.3 remains a challenging subject of radiation chemistry [Ma et al., 2018].

Fate of excited water molecules, H_2O^*

Both the electronically excited (H_2O^*) and vibrationally exited ($H_2O^*_{vib}$) water molecules are able to dissociate under three different decay channels [Buxton, 2004]. These channels are shown below:

$$H_2O^* \longrightarrow {}^{\bullet}OH + H^{\bullet} \tag{R1.4}$$

$$H_2O^* \longrightarrow H_2 + O(^1D) \longrightarrow H_2 + {}^{\bullet}OH + {}^{\bullet}OH \tag{R1.5}$$

$$H_2O^* \longrightarrow 2\,H^{\bullet} + O(^3P) \tag{R1.6}$$

The terms $O(^3P)$ and $O(^1D)$ in Reactions R1.5 and R1.6 refer to atomic oxygen in its singlet and triplet states respectively[14]. Depending on the availability of chemical species in the specific MC code one is using, atomic oxygens produced during the dissociation process may not explicitly be simulated. In such situations, the dissociative decay of excited oxygen shown in Reaction R1.6 is neglected, and the intermediate step of Reaction R1.5 is skipped completely, which results in the immediate creation of H_2 and $2\,^{\bullet}OH$ [Kreipl et al., 2009b]. The two other dominant processes experienced by excited water molecules are auto-ionisation and relaxation to the ground state, as shown below:

$$H_2O^* \longrightarrow H_2O^+ + e^-_{se} \longrightarrow {}^{\bullet}OH + H_3O^+ + e^-_{aq} \tag{R1.7}$$

$$H_2O^* \longrightarrow H_2O + \Delta E \tag{R1.8}$$

The auto-ionisation process of Reaction R1.7 involves the spontaneous ionisation of an excited water molecule, which is then effectively entirely equivalent to an initially ionised molecule [Cobut et al., 1998, Ballarini et al., 2000]. Correspondingly, the ionised water molecule undergoes proton transfer to yield $^{\bullet}OH$ and H_3O^+, the ejected electron becomes a subexcitation electron through the physical interaction mechanisms already described, and the subexcitation electron thermalises to yield aqueous (or hydrated/solvated) electrons (e^-_{aq}). This thermalisation is described in the following subsection. The final process available to excited water molecules is relaxation to the ground state. This involves the transfer of energy (ΔE) to the surrounding medium, typically in the form of heat loss [Plante, 2010].

Fate of subexcitation electrons, e^-_{se}

In addition to Reaction R1.2, subexcitation electrons are able to undergo dissociative attachment to H_2O according to Reaction R1.9 [Buxton, 2004].

[14] Singlet and triplet states are quantum mechanical concepts which refer to systems with fully paired, and two unpaired electrons respectively. The ground electronic state of most molecules is a singlet state [Phillips, 2016].

$$e^-_{se} + H_2O \longrightarrow {}^{\bullet}OH + H^- \longrightarrow {}^{\bullet}OH + H_2 + OH^- \tag{R1.9}$$

Those subexcitation electrons which escape Reactions R1.2 and R1.9 are further slowed down through collisions with molecules of the medium, resulting in rotational excitations, or elastic scattering, until they are in thermal equilibrium with the material [Inokuti, 1991]. This process of continuous energy loss until thermal equilibrium is reached is known as *thermalisation*, and the various energy domains an electron goes through to become *thermalised* is depicted in Fig. 2.12.

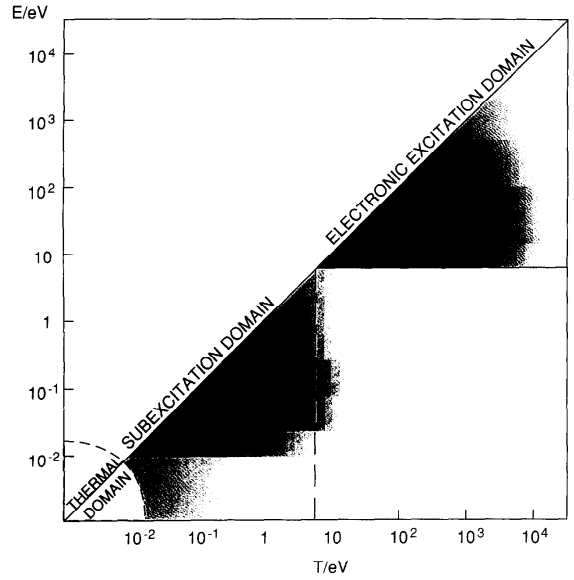

Figure 2.12: Schematic diagram depicting the electronic excitation, subexcitation, and thermal domains of electron energy. The horizontal axis represents the electron kinetic energy, while the vertical axis represents the energy loss in a single collision. Taken from [Inokuti, 1991].

By interacting with the dipoles of the surrounding water molecules, these electrons become *trapped*, occupying a cavity in the structure of liquid water. Ultimately, within this cavity the trapped electron forms hydrogen bonds with up to six surrounding water molecules, thereby becoming hydrated and behaving like a chemical species. The electron fate, from ejection by ionisation, to thermalisation, is depicted below.

$$e^- \ (> 7.4 \text{ eV}) \longrightarrow e^-_{se} \ (0.025 - 7.4 \text{ eV}) \longrightarrow e^-_{th} \ (\sim 0.025 \text{ eV}) \longrightarrow e^-_{tr} \longrightarrow e^-_{aq} \tag{2.19}$$

The *cavity model* used to describe the structure of aqueous electrons was subject to scrutiny over the past few years, however the evidence overwhelmingly points to this interpretation of the aqueous electron being the correct one [Herbert, 2019].

2.3.5 Chemical stage

After the pre-chemical stage there is a very high concentration of ${}^{\bullet}OH$, $H^{\bullet}$, and e^-_{aq} in the spurs. These species then go on to diffuse and react with one another within the spur (and

depending on the incident particle LET, with chemical species from other spurs) in what is known as the heterogeneous chemical stage. Typically these species react within 1 μs to form molecular products such as H_2O_2, after which the chemical species are typically sufficiently diffused to be considered homogeneously distributed in what is known as the homogeneous chemical stage [Buxton, 2004].

Whereas Fig. 2.11 only depicts the main chemical species resulting from the chemical stage as well as some select chemical reactions, a more comprehensive list of reactions in pure liquid water is shown in Table 2.1.

Table 2.1: List of chemical reactions used by the MC code TRACIRT to simulate the radiolysis (chemical stage) of pure neutral liquid water. Reactions taken from: [Frongillo et al., 1998], in which H^+ is used in place of H_3O^+.

List of chemical stage reactions during water radiolysis		
$H + H \rightarrow H_2$	$H \rightarrow e_{aq}^- + H^+$	$OH + O^- \rightarrow HO_2^-$
$H + OH \rightarrow H_2O$	$OH + OH \rightarrow H_2O_2$	$OH + O_3^- \rightarrow O_2^- + HO_2$
$H + H_2O_2 \rightarrow OH + H_2O$	$OH + H_2O_2 \rightarrow HO_2$	$H_2O_2 + e_{aq}^- \rightarrow OH + OH^-$
$H + e_{aq}^- \rightarrow H_2 + OH^-$	$OH + H_2 \rightarrow H + H_2O$	$H_2O_2 + OH^- \rightarrow HO_2^- + H_2O$
$H + OH^- \rightarrow e_{aq}^- + H_2O$	$OH + e_{aq}^- \rightarrow OH^-$	$H_2O_2 + O(^3P) \rightarrow OH + HO_2$
$H + O_2 \rightarrow HO_2$	$OH + OH^- \rightarrow O^- + H_2O$	$H_2O_2 + O^- \rightarrow HO_2 + OH^-$
$H + HO_2 \rightarrow H_2O_2$	$OH + HO_2 \rightarrow O_2 + H_2O$	$H_2 + O(^3P) \rightarrow H + OH$
$H + O_2^- \rightarrow HO_2^-$	$OH + O_2^- \rightarrow O_2 + OH^-$	$H_2 + O^- \rightarrow H + OH^-$
$H + O(^3P) \rightarrow OH$	$OH + HO_2^- \rightarrow HO_2 + OH^-$	$e_{aq}^- + e_{aq}^- \rightarrow H_2 + 2\ OH^-$
$H + O^- \rightarrow OH^-$	$OH + O(^3P) \rightarrow HO_2$	$e_{aq}^- + H^+ \rightarrow H$
$e_{aq}^- + O_2 \rightarrow O_2^-$	$H^+ + O_3^- \rightarrow OH + O_2$	$O_2^- + H_2O \rightarrow HO_2 + OH^-$
$e_{aq}^- + HO_2 \rightarrow HO_2^-$	$OH^- + HO_2 \rightarrow O_2^- + H_2O$	$HO_2^- + O(^3P) \rightarrow OH + O_2^-$
$e_{aq}^- + O_2^- \rightarrow H_2O_2 + 2\ OH^-$	$OH^- + O(^3P) \rightarrow HO_2^-$	$HO_2^- + O^- \rightarrow OH^- + O_2^-$
$e_{aq}^- + HO_2^- \rightarrow O^- + OH^-$	$O_2 + O(^3P) \rightarrow O_3$	$HO_2^- + H_2O \rightarrow H_2O_2 + OH^-$
$e_{aq}^- + O^- \rightarrow 2\ OH^-$	$O_2 + O^- \rightarrow O_3^-$	$O(^3P) + O(^3P) \rightarrow O_2$
$e_{aq}^- + H_2O \rightarrow H + OH^-$	$HO_2 + HO_2 \rightarrow H_2O_2 + O_2$	$O(^3P) + H_2O \rightarrow\ 2OH$
$H^+ + OH^- \rightarrow H_2O$	$HO_2 + O_2^- \rightarrow O_2 + HO_2^-$	$O^- + O^- \rightarrow H_2O_2 + 2\ OH^-$
$H^+ + O_2^- \rightarrow HO_2$	$HO_2 + O(^3P) \rightarrow O_2 + OH$	$O^- + O_3^- \rightarrow 2O_2^-$
$H^+ + HO_2^- \rightarrow H_2O_2$	$HO_2 \rightarrow H^+ + O_2^-$	$O^- + H_2O \rightarrow OH + OH^-$
$H^+ + O^- \rightarrow OH$	$O_2^- + O^- \rightarrow O_2 +\ 2\ OH^-$	$O_3^- \rightarrow O^- + O_2$

The enormous complexity of this stage of water radiolysis can be attributed to the sheer amount of chemical reactions occurring. However, many of the reaction products are of little importance in the context of RT [Alpen, 1997b], and as such the more modern MC codes use a significantly reduced list of chemical reactions (as will be seen in section 3.1).

The most important species for RT are $^{\bullet}OH$, H_2O_2, and e_{aq}^-. The exact physical/chemical properties which make them pertinent will be described in section 2.4.2, however in brief $^{\bullet}OH$ is primarily responsible for the indirect portion of DNA damage [von Sonntag, 2006], H_2O_2 has a role to play in cell signalling [Forman et al., 2014] and may contribute to the bystander effect [Azzam et al., 2002], and e_{aq}^- has an impact on the level of oxygenation as it reacts with dissolved oxygen leading to its depletion [Boscolo et al., 2020].

2.3.6 LET and pH considerations

LET

For particles of low LET, the primary yields of the superoxide anion radical ($O_2^{\bullet -}$)[15] and the hydroperoxyl radical ($HO_2^{\bullet}$) are often neglected given that they account for less than 1% of the primary radiolytic species [Meesungnoen and Jay-Gerin, 2011]. As the LET of the incident particle increases, the distance between spurs decreases owing to the higher ionisation density. The structure of isolated spurs which is characteristic of low LET radiation transitions into a dense cylindrical concentration of species along the particle track, formed by overlapping spurs. This transition occurs at approximately 3 eV/nm [LaVerne, 2004]. Due to these overlapping spurs, the production of molecular species (H_2 or H_2O_2) are favoured over the production of radical species ($H^{\bullet}$, $^{\bullet}OH$, e_{aq}^-) due to an increase in radical-radical reactions [Baldacchino et al., 2019]. Despite this increase in radical-radical reactions, the previously neglected $O_2^{\bullet -}$ and $HO_2^{\bullet}$ then become the major radical species surviving the spur/track expansion [Meesungnoen and Jay-Gerin, 2011]. Although the exact mechanisms accounting for their increased formation is not fully understood, one of the pathways that has been postulated is through Reaction R1.11.

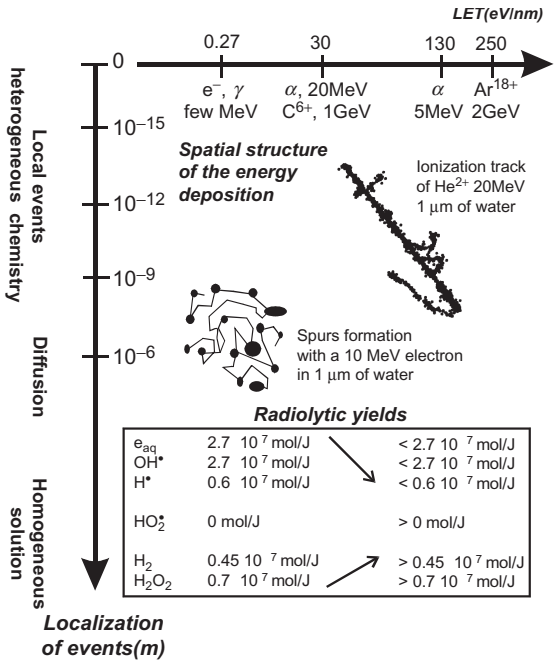

Figure 2.13: Schematic depiction of the impact of increasing particle LET on radiolytic yields. Taken from [Baldacchino and Katsumura, 2010].

Interestingly, the increase in molecular yields does not scale *ad infinitum* with increasing LET. In fact, it has been suggested that the G-values for heavy ions begins to decrease in the very high LET regions [Wasselin-Trupin et al., 2002, Meesungnoen and Jay-Gerin, 2011]. This decrease was hypothesised to occur as a result of an increase in Reactions R1.10 and R1.11, leading to a smaller concentration of H_2O_2 escaping the spur.

[15] The superoxide anion radical $O_2^{\bullet -}$ always exists in a pH-dependent equilibrium with $HO_2^{\bullet}$ [Bielski et al., 1985]

$$e^-_{aq} + H_2O_2 \longrightarrow OH^- + {}^\bullet OH \quad \text{(R1.10)}$$
$${}^\bullet OH + H_2O_2 \longrightarrow H_2O + HO_2^\bullet \quad \text{(R1.11)}$$

One of the other radiochemical consequences of high LET particles is the so-called *oxygen in the tracks* hypothesis [Alper and Bryant, 1974], which states that the passage of a heavy ion through a cellular environment generates molecular oxygen (O_2) *in situ* which then sensitises cells to radiation induced damages. This hypothesis is one of a handful of explanations for the decrease in the oxygen enhancement ratio (OER) observed for high LET radiations [Meesungnoen and Jay-Gerin, 2009] (the importance of oxygen in the context of RT will be expanded upon in section 2.4). The three possibilities for the formation of oxygen are shown in Reactions R1.11-R1.13.

$$HO_2^\bullet + HO_2^\bullet \longrightarrow H_2O_2 + O_2 \quad \text{(R1.12)}$$
$${}^\bullet OH + HO_2^\bullet \longrightarrow H_2O + O_2 \quad \text{(R1.13)}$$

Reaction R1.11 is relatively slow and Reactions R1.12 and R1.13 both necessitate the presence of $HO_2^\bullet$. In recent years, the multiple ionisation model [Meesungnoen and Jay-Gerin, 2005] has emerged as the most probable model to explain the oxygenation effect of high LET particles, first through the production of $HO_2^\bullet$ through Reactions R1.14 and R1.15, from which O_2 can consequently be produced [Baldacchino et al., 2019].

$$H_2O^{2+} + 2\,H_2O \longrightarrow 2\,H_3O^+ + O \quad \text{(R1.14)}$$
$$O + HO^\bullet \longrightarrow HO_2^\bullet \quad \text{(R1.15)}$$

These multiple ionisations of a single water molecule have been shown to cause a progressive reduction in the H_2O_2 yields for LET values above approximately 100 eV/nm [Baba et al., 2021].

pH

The pH of a medium is a representation of how acidic (low pH) or basic (high pH) it is, with the former corresponding with a higher concentration of H^+ (or H_3O^+) ions while the latter corresponds with a higher concentration of OH^- ions. For low LET radiation, the primary yields of ${}^\bullet OH$, H_2O_2, and e^-_{aq} all remain approximately constant for a pH > 3. However for a pH < 3, there is a decrease in the primary yield of e^-_{aq} and an increase in the primary yields of ${}^\bullet OH$ and H_2O_2 [Buxton, 2004].

In contrast to the inherent pH of a solution, an interesting phenomenon is that of an explicit change in the pH due to the chemical species generated along the particle track. The so-called transient *acid-spike*, is a term used to describe the rendering of the spur/particle track temporarily more acidic than its surroundings due to the generation of H_3O^+. For low LET radiation this acid spike response to radiation is most prevalent at times shorter than ∼1 ns and results in a local pH of ∼3.3, whereas for high LETs the pH decreases to approximately 0.5 over a timescale of ∼100 ps after the initial ionising radiation [Kanike et al., 2015]. This variation in pH is shown in Fig. 2.14.

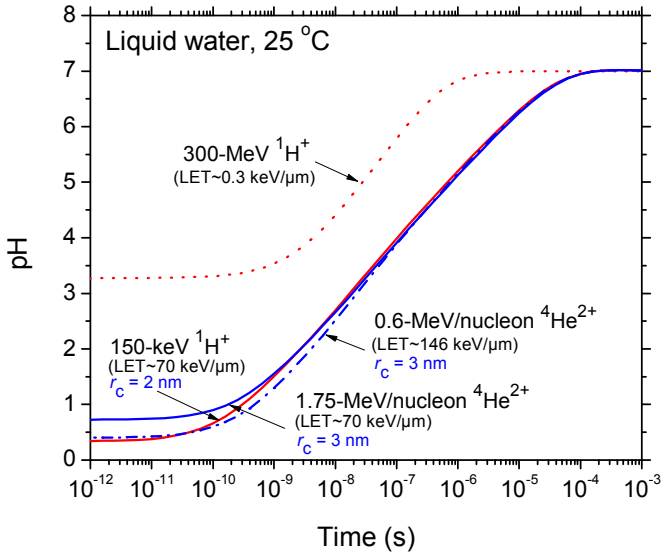

Figure 2.14: Variation in pH as a function of time for protons (300 MeV and 150 keV) and ^{4}He ions (0.6 MeV/nucleon and 1.75 MeV/nucleon). The radius r_c[16] is indicative of the radius of the physical track core. Taken from [Kanike et al., 2015].

The radiobiological ramifications of this early, transient, and highly acidic region within the spur are still not fully understood, however it certainly merits further investigations given the dependence of many cellular processes on the pH [Putnam, 2012]. In the context of RT it provokes the questions of whether this unphysiological pH could have an impact on the level of DNA damage, and could these local changes in acidity trigger bystander responses [Kanike et al., 2015]. With regards to FLASH RT, in which the induced radiochemical changes are already widely studied, these spikes in pH could further elucidate the fundamental mechanisms involved in the enhanced normal tissue sparing effect [Jay-Gerin, 2020, Sultana et al., 2022].

The next logical link in the chain, following on from the initial physical and chemical consequences of ionising radiation, are the resulting biological effects. These will be expanded upon in the following section.

2.4 Radiobiological consequences

For the average person receiving a round of RT, the biological consequences of radiation's effect on the human body are what we first *experience*. They are the tangible manifestations of the processes described in this thesis up until this point, primarily due to the matching of the time scale in which they act and the time scale of our perception, and thus these biological effects act as a compass which ultimately guides the advancement of the field of RT.

[16] The pH was calculated by taking the negative base 10 logarithm of $[H_3O^+]$, where $[H_3O^+](t) = G(H_3O^+)(t) \times \frac{\text{LET}}{\pi r(t)^2}$, and $r(t)^2 = r_c^2 + 4Dt$ [Kanike et al., 2015].

Definition 4

Radiobiology is a field of science that exists at the intersection between physics and biology. It is the study of the effects of ionising radiation on biological systems, ranging from simple or complex cellular organisms, to mammalian cells in culture, to the constituent tissue, tumors, and organs of animals or humans [Zeman, 2016].

As already mentioned, DNA is touted as the critical target for radiation. Given that the DNA molecule is one of the pre-eminent components of a cell, the basic functioning of a cell and its response to ionising radiation induced damages is of utmost importance.

2.4.1 Cell and tissue biology fundamentals

The cell is the fundamental building block of living matter, and consists primarily of: a nucleus where all the genetic information is stored, the cytoplasm which contains various organelles (sub-cellular structures) each carrying out different activities within the cell, and a cell (plasma) membrane, which encloses the cell [Saha, 2013].

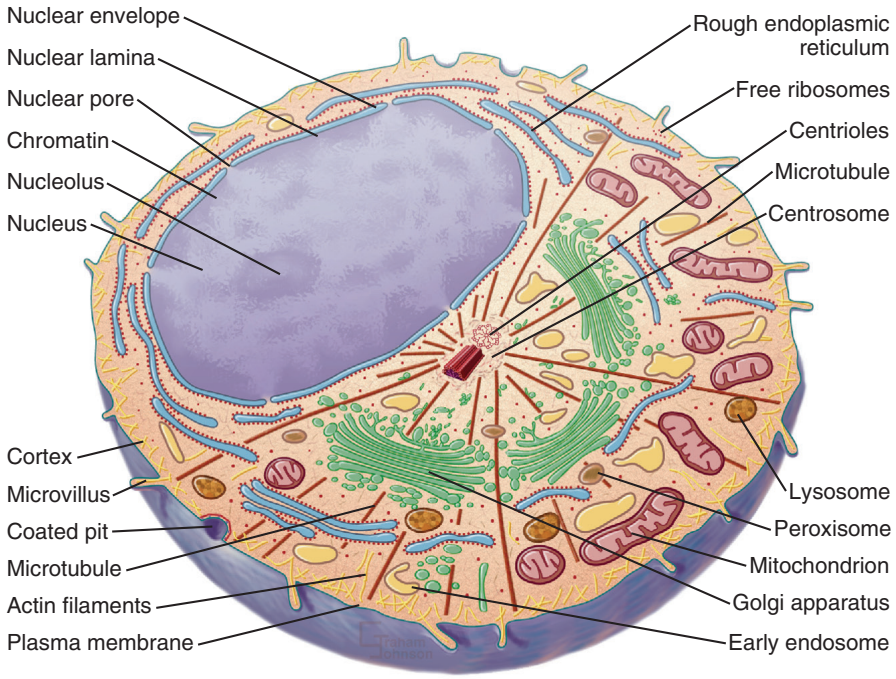

Figure 2.15: Schematic representation of the cross section of a cell, showing all its internal components. Taken from [Pollard et al., 2017].

While Fig. 2.15 highlights the many different cellular components, the main components of interest in the context of RT are described by the brief glossary of terms below:

- The **nucleus** is composed of chromosomes - which are essentially just long DNA molecules which have been wrapped around histones, and packed into chromatin fibers. These chromosomes store the genetic information required for cellular growth, multiplication, and function [Pollard et al., 2017]. While a small proportion of IR

induced DNA damage occurs within the mitochondria, the majority occurs within the nucleus [Kim et al., 2019].

- The **plasma membrane** selectively permits or prohibits the passage of all substances entering and leaving the cell [Saha, 2013]. It is composed of a lipid bilayer containing proteins which have various functions, such as: anchoring the membrane to the extracellular matrix, forming connections with receptors on other cells, acting as pumps that create ion concentration gradients across the lipid bilayer, or carrying nutrients into the cell thanks to these concentration gradients. While largely impermeable, ions and other water-soluble molecules are able to traverse this membrane due to these proteins [Pollard et al., 2017]. In the context of RT, when the plasma membrane is exposed to IR or IR induced ROS it can undergo lipid peroxidation [Kim et al., 2019], consequently disrupting the membrane's permeability and transport capabilities [Wong-Ekkabut et al., 2007].

- The major function of the **endoplasmic reticulum** is the synthesis and folding[17] of the aforementioned proteins present in the lipid bilayer of the cell membrane. If the proteins are not destined for the plasma membrane, they are transported to their appropriate destination [Schwarz and Blower, 2016]. Furthermore, the endoplasmic reticulum is a source of intracellular ROS [Gupta et al., 2012]. Interestingly, direct or indirect (ROS) IR induced endoplasmic reticulum stress has been associated with tumor cell survival and enhanced radioresistance [Kim et al., 2019].

- **Mitochondria** are the principal source of energy for the cell. Through a process known as *cellular respiration*, shown in Equation 2.20, glucose (sugar, or chemically: $C_6H_{12}O_6$) is oxidized and converted into adenosine triphosphate (ATP), which is an organic compound used to fuel other cellular processes [Alberts et al., 2019a].

$$C_6H_{12}O_6 + 6\,O_2 \longrightarrow 6\,CO_2 + 6\,H_2O + ATP \tag{2.20}$$

  The final step in cellular respiration involves the electron transport chain (ETC). In the most simplest terms, as a result of preceding processes in cellular respiration, electrons are donated to the ETC, which is essentially just a chain of proteins, located on an inner membrane of the mitochondria that transports electrons through redox reactions. As the electrons move along the ETC, energy is lost to *proton pump* proteins which use this energy to pump protons (H^+) from the mitochondrial matrix to the intermembrane space (the space between the inner membrane and the mitochondrial membrane). These protons travel back into the mitochondrial matrix through an enzyme known as ATP synthase which generates ATP [Alberts et al., 2019a]. Leakage of these electrons from the ETC during ATP synthesis results in the reduction of molecular oxygen (O_2) to superoxide ($O_2^{\bullet-}$) as can be seen in Fig. 2.17 [Gupta et al., 2012, Averbeck and Rodriguez-Lafrasse, 2021]. Consequently, mitochondria also function as a source of intracellular ROS.

- Similarly to mitochondria, **peroxisomes** are organelles containing proteins and enzymes which participate in oxidative reactions. They are also serve as sources of

[17] Proteins need to be folded into specific three-dimensional structures in order to properly function [Sharma, 2013].

ROS within the cell, however they do not contribute to ATP synthesis [Gupta et al., 2012, Pollard et al., 2017].

- Vesicles are small cellular structures enclosed by a lipid bilayer, containing a variety of proteins and nucleic acids (such as DNA and RNA). These structures can be secreted by the cells into the extracellular space, thereby becoming **extracellular vesicles**. The three main types of extracellular vesicle (EV) are exosomes, microvesicles, and apoptotic bodies and they are responsible for cell-cell communication [Doyle and Wang, 2019]. EVs are generated in response to RT, and there is emerging evidence that these radiation induced EVs (particularly exosomes) play a vital role in both radioresistance and the radiation-induced bystander effect (RIBE) [Yang et al., 2022b], which will be expanded upon in section 2.9.5.

While DNA is indeed the fundamental genetic material for carrying information from one generation to the next, its effects on the characteristics of the cell first require it to undergo a set of processes, as shown in Fig. 2.16, before a specific biological activity is obtained [Dale and von Schantz, 2008].

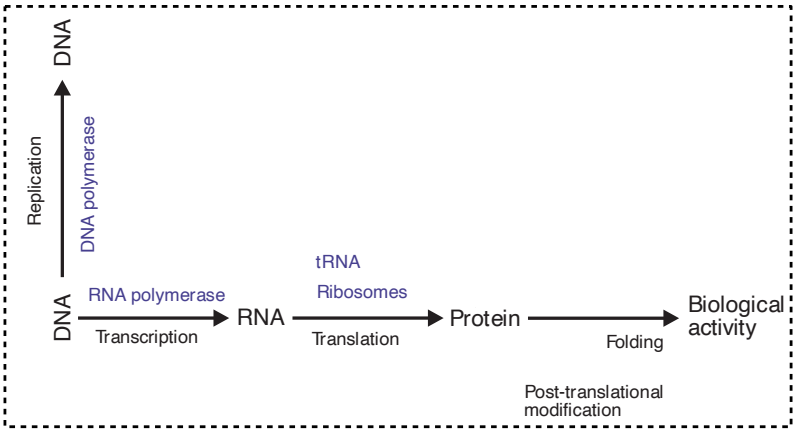

Figure 2.16: Genetic information flow required for gene expression. Adapted from [Dale and von Schantz, 2008].

In brief, the DNA is first copied into RNA through a process known as *transcription*. This RNA is either directly functional or acts as the intermediate template for a protein [Orgogozo et al., 2016]. In the case of the former, this RNA is the final product of a gene, whereas in the latter case, the RNA is then *translated* into a protein. After undergoing various processes such as protein folding (see footnote 17), the final biological function is manifested [Dale and von Schantz, 2008]. This flow of information resulting in the creation of proteins is what ultimately dictates cell function.

Cells then clump together to form tissues, which make up the organs of a body. The arrangement of tissue within an organ is characterised by the arrangement of functional subunits (FSUs), which can be considered anatomical structures and are defined as the largest volume of cells capable of being regenerated from a surviving clonogenic cell without losing their function [Withers et al., 1988]. FSUs are organised in either *serial* or *parallel*, leading to serial (i.e. the spinal cord) or parallel (i.e. the lung) organs respectively. While the loss of function of a parallel organ only occurs after the damage or loss of function of a critical number of these FSUs, serial organs fail in their entirety from the loss of a single one of these FSUs [Withers et al., 1988, Dörr and van der Kogel, 2018].

2.4.2 Free radicals in the context of a biological environment

As highlighted in section 2.3, ROS can be produced by IR through water radiolysis. These ROS are considered exogenously produced due to their origination from an external source. Alternatively, ROS can also be produced endogenously from within the cell itself, and IR, in addition to the ROS produced from water radiolysis, can destabilize certain cellular components causing changes in the level of intracellular ROS [Gupta et al., 2012]. These ideas were broached in section 2.4.1, and this section expends upon those initial discussions through a detailing of the production and fate of ROS within the cell. The major sources of ROS within a tumor cell are depicted in Fig. 2.17.

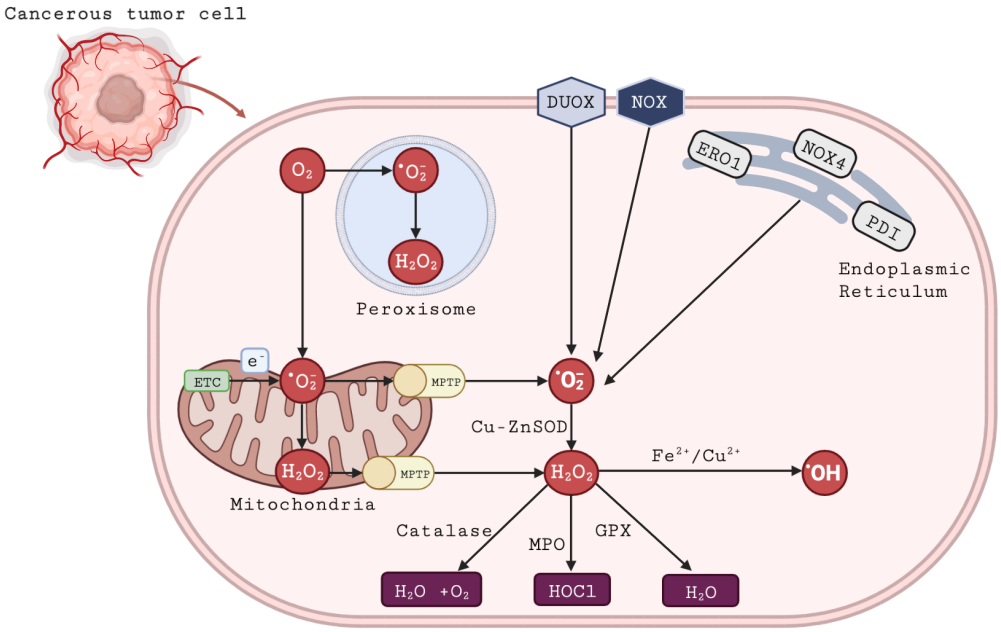

Figure 2.17: Major sources of ROS within a tumor cell. Adapted from [Gupta et al., 2012] using BioRender.

The process for the creation of $O_2^{\bullet-}$ within the mitochondria was detailed in section 2.4.1. This superoxide within the mitochondria is dismutated to H_2O_2 through Mn-superoxide dismutase (SOD) and both $O_2^{\bullet-}$ and H_2O_2 are then able to leak out of the mitochondrial permeability transition pore (MPTP) into the cytoplasm. The destabilisation of these mitochondria due to IR leads to increased ROS generation for the cell [Widel et al., 2012]. Peroxisomes are the other major sites of superoxide and H_2O_2 within the cell, and both the endoplasmic reticulum (ER) and NADPH oxidase (NOX)/dual oxidase (DUOX) contribute to the increased presence of $O_2^{\bullet-}$ within the cytoplasm [Gupta et al., 2012].

Within the cytoplasm, superoxide is dismutated through Cu-Zn-SOD to form intracellular H_2O_2. Cells are endowed with multiple antioxidant defences against H_2O_2, namely catalase, myeloperoxidase (MPO), and glutathione peroxidase (GPX) [Winterbourn, 2013], where they effectively work to scavenge H_2O_2 resulting in the conversion of H_2O_2 into water (H_2O), oxygen (O_2), or hypochlorous acid (HOCl), as depicted in Fig. 2.17. H_2O_2 is a strong two-electron oxidant with a standard reduction potential of 1.32 V, however compared with other highly oxidizing species such as hypochlorous acid (1.28 V) or peroxynitrite (1.20 V), it reacts poorly or not at all with most biological molecules. Its most favoured reactions are with transition metals or scavengers such as catalase and GPX [Winterbourn, 2013].

At low physiological levels, H_2O_2 can contribute to non-targeted (bystander) effects through redox-sensitive cell signalling cascades [Azzam et al., 2002, Gough and Cotter, 2011], while at high physiological levels it can trigger cell death [Gough and Cotter, 2011]. Furthermore, studies have shown that it can act as second messengers for certain signalling pathways [Forman et al., 2014, Gough and Cotter, 2011], which may contribute to the bystander effect [Azzam et al., 2002]. There is some evidence that the anti-tumor immune response triggered by immunogenic cell death (ICD) is weakened for elevated levels of H_2O_2 due to the oxidation of HMGB1, an important mediator of inflammation and immunity, thereby neutralizing its biologic activity [Lennicke et al., 2015, Deng et al., 2020].

Reactions of H_2O_2 with transition metals such as iron or copper are known as Fenton reactions which lead to the generation of a hydroxyl ($^{\bullet}OH$) radical as shown in reactions R1.16 and R1.17 [Plante, 2010, Meesungnoen and Jay-Gerin, 2011]:

$$H_2O_2 + Fe^{2+} \longrightarrow {}^{\bullet}OH + OH^- + Fe^{3+} \tag{R1.16}$$

$$H_2O_2 + Cu^{+} \longrightarrow {}^{\bullet}OH + OH^- + Cu^{2+} \tag{R1.17}$$

The hydroxyl radical is an important species in the context of RT since it is primarily responsible for the indirect portion of DNA damage [von Sonntag, 2006], which itself accounts for approximately 70% of all DNA damage induced by low LET irradiations [Roots and Okada, 1975]. Furthermore, this free radical has been shown to be the primary mediator of the oxygen enhancement effect [Hirayama et al., 2013].

2.4.3 Dose-volume effects

Dose-volume effects in RT refer to the phenomenon whereby the smaller the volume to be irradiated, the higher the tolerance of absorbed dose to induce damage to normal tissue. This effect was first observed by Zeman and Curtis in their studies of deuteron beams [Zeman et al., 1959, Zeman et al., 1961, Curtis, 1967], and an example of the effect is shown in Fig. 2.18, which depicts the histologic[18] examination of brain tissue.

It was shown that for beams with widths of 1 mm, 75 μm, and 25 μm, cavitation[19] occurred at 250 Gy, 750 Gy, and 10000 Gy respectively. While panel A of Fig. 2.18 depicts the cavitation of a 1 mm wide deuteron beam in which the surrounding tissue is devoid of nerve cells, panel B highlights the seemingly normal appearance of vessels within the beam track. It was observed that at 4000 Gy for the 25 μm beam, there was a death of nerve and glial cells, however there was no permanent damage to blood vessels or the overall tissue architecture, whereas the same level of destruction for the 1 mm beam was obtained at 140 Gy [Zeman et al., 1961]. This effect was later exploited by Slatkin *et al.* which thus led to the birth of microbeam radiation therapy (MRT) [Meyer et al., 2019, Slatkin et al., 1992], which will be discussed in section 2.9.3.

2.4.4 Temporal fractionation

Historically speaking, both the energy (dose) and time (fractionation) have long been the two central paradigms of RT treatments. From treatments at the previously named

[18] Histology refers to the microscopic analysis of the structure and function of tissues. Tumor tissue is assigned a *histological grading* depending on its degree of differentiation and estimated growth rate [Ruddon, 2007].

[19] This refers to the creation of a *cystic cavity*, or air-filled regions of the tissue [Kim and Han, 2012].

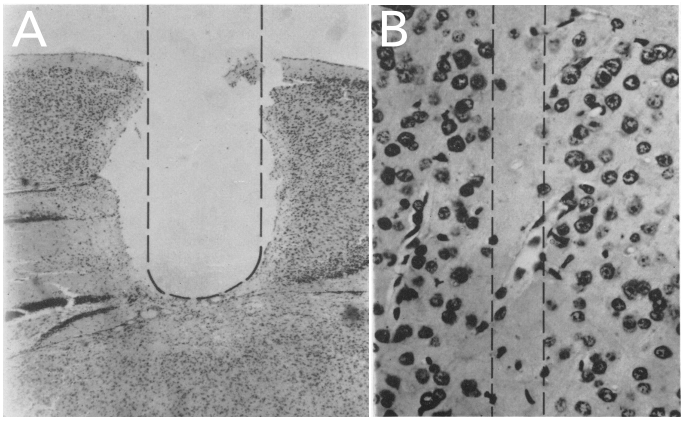

Figure 2.18: Histological analysis of mouse brain tissue after exposure to a 1 mm 280 Gy deuteron beam (panel **A**), and a 25 μm 4000 Gy deuteron beam (panel **B**). Taken from [Zeman et al., 1961].

Fondation Curie in 1934 it was shown that for certain cancers better patient outcomes were achievable by decreasing the daily dose fractions - from 750 rad/day (7.5 Gy/day) to 375 rad/day (3.75 Gy/day) - and increasing the duration of the treatment from 6 to 12 days while maintaining the same total delivered dose [Coutard, 1934]. In today's context, most RT treatments with photons are delivered over 4 to 7 weeks, with doses of 1.8 - 2 Gy per fraction, and only a single fraction per day optimising normal tissue recovery [ICRU, 1999, Suntharalingam et al., 2005]. The biological basis for this temporal fractionation is explained by the *Rs of radiobiology*, which is described in the following section (2.4.5).

Other fractionation regimens exist, notably *hyperfractionated* and *hypofractionated* RT treatments. While hyperfractionated regimens consist of doses as low as 0.5 Gy, delivered in 2 fractions per day, with a total of 2-5 treatment days over 2-4 weeks, the hypofractionated regimen involves much higher (up to 20 Gy) single fractions per day [Prasanna et al., 2014]. The biological rationale of hyperfractionation lies in the exploitation of the differential between tumors and late responding normal tissue, allowing overall total dose-escalation aimed at improving tumor control without increasing the risk of late complications [Baumann and Grégoire, 2018]. On the other hand, hypofractionated regimens appear to be more well suited in view of eliciting an anti-tumor immune response [Ngwa et al., 2018, Boustani et al., 2019].

2.4.5 The Rs of radiobiology

This list of Rs refers to the most important biological factors influencing the response of both normal and tumor tissue to radiation, and is depicted in the figure below.

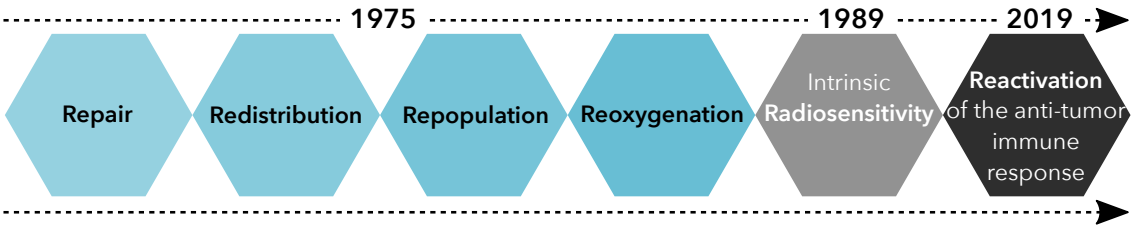

Figure 2.19: The 6 Rs of radiobiology.

The first four Rs of *Repair*, *Redistribution*, *Repopulation*, and *Reoxygenation* were

first described in 1975 [Withers, 1975]. This list was later appended with *intrinsic Radiosensitivity* in 1989 [Steel et al., 1989]. Finally, given the advent of immunotherapy for cancer treatment, and a better understanding of the link between anti-tumor immunity and RT, the 6th R of *Reactivation of the anti-tumor immune response* was proposed in 2019 [Boustani et al., 2019].

Repair

As previously mentioned, IR induces damage to the DNA molecule either through the direct or indirect effect. Given that permanent DNA damage is often lethal for the cell, various repair pathways exist to cope with the different types of DNA damage. In the context of RT, single strand break (SSB) or damage to DNA bases is repaired through the closely related single-strand break repair (SSBR) and base excision repair (BER) respectively. Alternatively, a DNA double strand break (DSB), which is the most complex and lethal type of damage, is repaired through homologous recombination (HR) and non-homologous end-joining (NHEJ) [Wouters and Begg, 2018].

The DNA damage response (DDR) of a cell is a highly complex system composed of a group of interrelated signalling pathways which ultimately control the fate of the cell. In brief, a group of proteins act as sensors of DNA damage, which then signal to the cell to activate specific repair pathways aimed at repairing the DNA, activate programmed cell death pathways to kill the cells, or activate cell cycle checkpoints which block or slow the progression of the cell into the next phase of the cell cycle (expanded upon in the following subsection) [Wouters and Begg, 2018]. One of the earliest responses to DNA damage is the recruitment of proteins to the site of damage. In the case of DSBs for example, a protein called H2AX is recruited to the site of damage, becomes phosphorylated[20] within a few minutes, and can then be used as a marker of DNA DSB presence/repair [Stucki and Jackson, 2006, Kuo and Yang, 2008].

As previously mentioned, normal cells are more capable of repairing DNA damage since tumor cells may have mutations affecting the DDR of a cell [Gerber and Chan, 2008]. Nevertheless, some tumor cells are either intrinsically radioresistant or can acquire radioresistance after repeated irradiations, which seems to be particle-dependant [Sato et al., 2019]. Figure 2.20 shows how radioresistance may be acquired through DNA repair pathways, thereby enabling the survival of cancer. The upregulation of certain genes/proteins involved in different repair pathways allows the cancerous tumor cell to effectively repair the damages [Carlos-Reyes et al., 2021].

Some of the strategies employed to be able to overcome the acquired radioresistance of upregulated DNA repair pathways involves the use of higher LET particles, thereby inducing more complex DNA damages which are more difficult for the cell to repair [Wilkinson et al., 2023], or making use of DNA repair inhibitors to block certain repair pathways, effectively sensitising the tumor to IR [Biau et al., 2019].

Redistribution

Cells do not exist in a static state but instead control their growth and division through what is known as the *cell cycle*, as shown in Fig. 2.21. This cycle consists of four stages: In the G1 phase the cell grows in size, replication of the cell's DNA occurs in the S phase,

[20] The term *foci* is used to describe the regions of protein recruitment, and the phosphorylation (attachment of a phosphate group to the molecule/ion) of H2AX results in the formation of γH2Ax which can be observed under a microscope [Hall and Giaccia, 2012b].

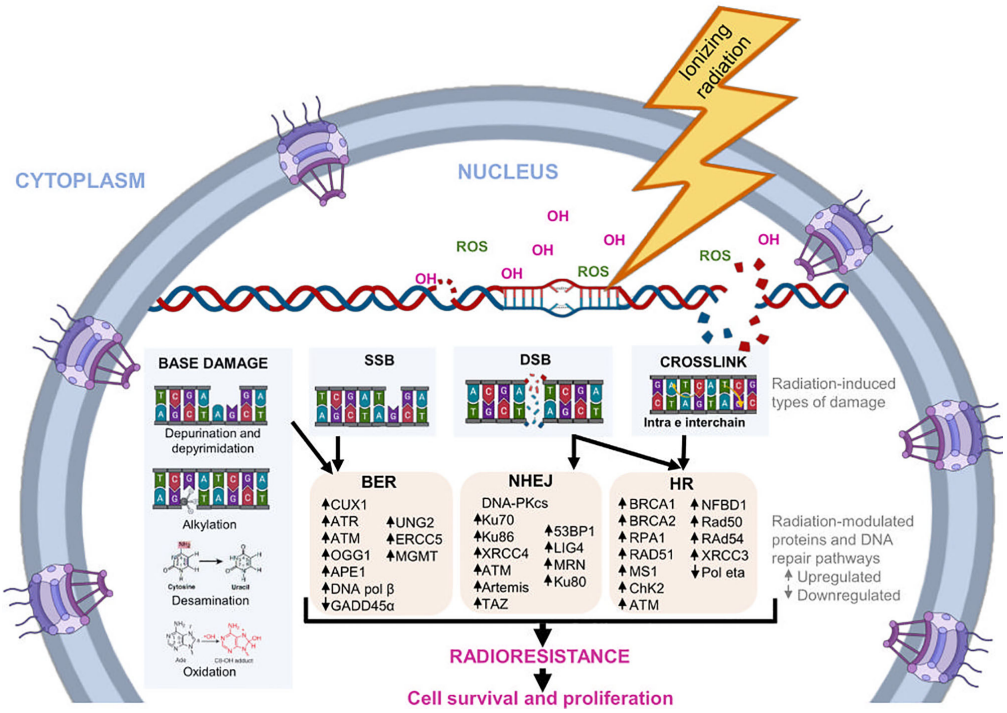

Figure 2.20: Acquired radioresistance, and subsequent tumor cell survival, through biological adaptations in the form of upregulated DNA repair pathways after IR induced damages. Taken from [Carlos-Reyes et al., 2021].

the G2 phase consists of checks for proper completion of DNA replication, and the process of cell division (mitosis) occurs in the M phase [Pollard et al., 2017].

This *redistribution* of cells into different phases of the cell cycle are important in the context of RT as the sensitivity of the cells vary depending on which phase it is in, with the G2 and M phases being the most sensitive [Withers, 1975]. Temporally fractionated treatments therefore aim to give cells time to transit into the more sensitive phases of the cell cycle. DNA damage induction by IR may activate cell cycle checkpoints through the previously mentioned DDR, thereby causing delays in the transition of the cells between phases. The G1 phase is particularly important as once it has passed this point a cell usually continues all the way through the rest of the cell cycle [Alberts et al., 2019b]. DNA damage in this G1 phase blocks the cell from replicating its DNA, and causes an increase in the concentration of p53 which is an important signalling protein and can induce cell death through *apoptosis* [Alberts et al., 2019b]. Apoptosis due to this G1 arrest is one of the mechanisms of early cell death as shown in Fig. 2.22.

Successful repair of DNA damage, or irradiation during a more radioresistant phase of the cell cycle may lead to mitosis which can ultimately lead to clonogenic survival. In most cases cells die only after attempting mitosis (*mitotic catastrophe*) and early cell death (after several hours) only occurs in a small minority of cases, depending primarily on the type of cell [Wouters, 2018].

Repopulation

As the name suggests, both normal and tumoral cells receiving fractionated doses of IR have the ability to repopulate through proliferation. Since the repopulation of surviving tumor cells after IR may counteract the cell killing effect, effective suppression of tumor

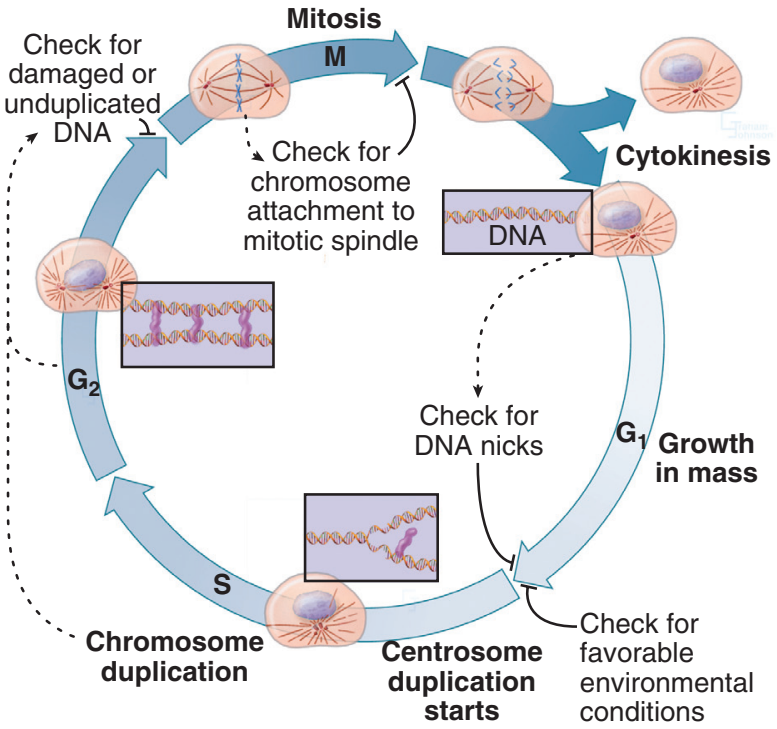

Figure 2.21: The four phases, G1, S, G2, and M, of the cell cycle. Checkpoints halt the progression of the cell cycle until successful completion of the preceding phase. Taken from [Pollard et al., 2017].

cell repopulation is essential for the success of a RT treatment [Ng et al., 2013]. On the other hand, the repopulation of normal cells is beneficial for the sparing of healthy tissue, highlighting the idea that a balance needs to be struck. Ultimately, the reduction of tumor control due to repopulation is dependent on the repopulation kinetics of the surviving tumor cells, which itself varies substantially between the different tumor types [Bleddyn and G, 2007].

Reoxygenation and the role of oxygen

Oxygen is known to be one of the most potent modifiers of radiation sensitivity, and hypoxic cells are known to be more radioresistant than oxic cells [Pajonk et al., 2010]. Specifically for low LET radiation such as x-rays, the proportion of hypoxic to oxic cells in the tumor after a fractionated RT regimen is the same as in an untreated tumor, highlighting the fact that some hypoxic cells become oxygenated over the course of the treatment [Hall and Giaccia, 2012c]. This phenomenon is depicted in Fig. 2.23, in which there is a continuous cycle of preferential cell killing of aerated cells due to their increased radiosensitivity, followed by an oxygenation of hypoxic cells before the following fraction of IR.

Through fractionated RT, a portion of the tumor cells is allowed to become reoxygenated, thus improving the efficacy of the treatment. This efficacy can be quantified by the OER which is defined as the ratio of doses administered under hypoxic to normoxic conditions needed to achieve the same biologic effect [Hall and Giaccia, 2012c], as shown in Equation 2.21.

$$\mathrm{OER} = \frac{\text{Dose to produce a given effect without oxygen}}{\text{Dose to produce the same effect with oxygen}} \tag{2.21}$$

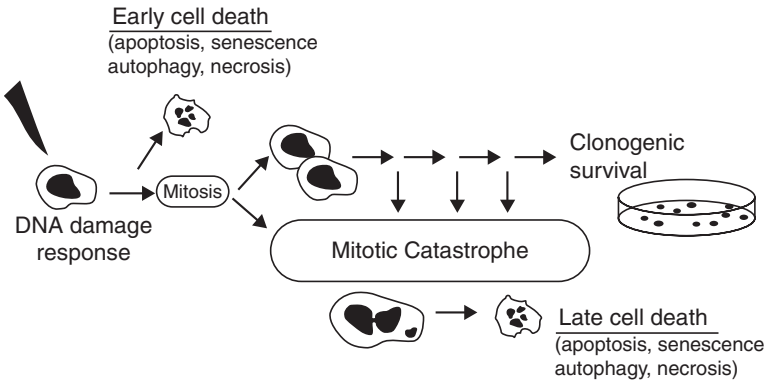

Figure 2.22: Schematic diagram depicting either cell death, or survival, after the induction of DNA damage by ionising radiation. Taken from [Wouters, 2018].

The general trend is that the OER decreases for increasing particle LET. For low LET particles such as photons, the presence of oxygen has a large impact, resulting in an OER between 2.5 and 3, while for high LET particles the OER can range from 2.5 down to unity (complete independence from the presence/absence of oxygen) [Hirayama, 2014]. This OER value reflects the relative importance of direct vs. indirect DNA damage, and is higher for low LET particles due to the creation of free radicals through water radiolysis whereas high LET particles induce more direct DNA damages.

The mechanism of the enhanced effect of radiation for low LET particles is commonly referred to as the *oxygen fixation* hypothesis, in which the presence of oxygen *fixes* (or stabilises) the chemical composition change of the target DNA molecule induced by the IR. Subsequently, this damage can be recognized through the DDR of a cell [Joiner, 2018]. An alternative mechanism has been proposed for high LET particles, and is known as the *oxygen in the track* hypothesis [Meesungnoen and Jay-Gerin, 2009], and was discussed in section 2.3.6. Nevertheless, this hypothesis is still controversial and definite conclusions remain to be drawn [Meesungnoen and Jay-Gerin, 2011].

Intrinsic Radiosensitivity

In view of the fact that tumor responses to RT are modulated by many factors other than those explained by the aforementioned four Rs, the 5$^{\text{th}}$ R of *intrinsic Radiosensitivity* was defined by Steel *et al.* as the inherent difference in the radiosensitivity of cells from different types of tumors, which becomes even more apparent at low dose rates [Steel et al., 1989]. This intrinsic radiosensitivity can be evaluated through the steepness of the cell survival curve where a steeper initial slope is obtained from tumor cell lines which are clinically responsive to RT [Steel et al., 1989].

Reactivation of the anti-tumor immune response

In recent years there has been an increased recognition of the importance of the immune system in the response to RT, thus prompting the addition of a 6$^{\text{th}}$ R of radiobiology, namely the *Reactivation of the anti-tumor immune response*, which can be both local and systemic (abscopal) [Boustani et al., 2019]. For a long time, the only observable immunologic effect of IR was the killing of immune cells, thus leading to an immunosuppressive tumor microenvironment. However, it is now well known that RT can also cause ICD which is

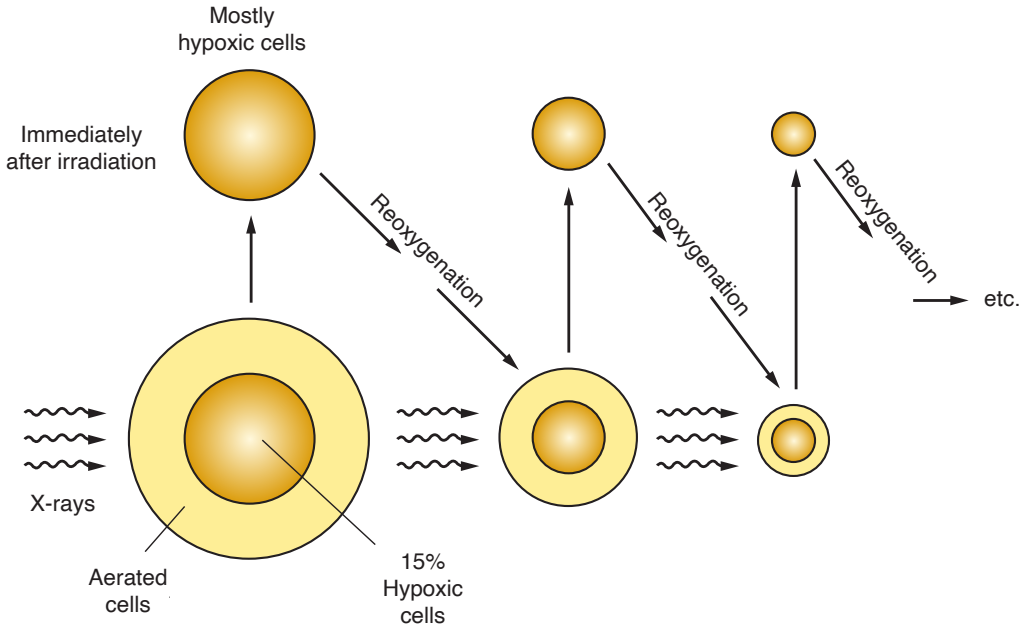

Figure 2.23: The process of reoxygenation during fractionated RT treatments. Adapted from [Hall and Giaccia, 2012c].

a prominent pathway for the activation of the immune system against cancer [Rückert et al., 2021, Kroemer et al., 2013]. Nevertheless, reliably eliciting an immune response in conventional RT is difficult due to the effects of IR being both immune promoting and suppressing [Rückert et al., 2021]. While the novel technique of SFRT could potentially be used to more reliably induce an immune response (see section 2.9.5), in conventional RT it is essential that an appropriate fractionation regimen is set [Boustani et al., 2019], as highlighted in Fig. 2.25.

Broadly speaking, Fig. 2.25 indicates that lower doses given in more fractions correlates with a greater proportion of myeloid-derived suppressor cells (MDSC), while higher doses given in a shorter period of time correlates with a higher proportion of T cells. These MDSC promote immunosuppressive mechanisms, while T cells promote immunostimulatory mechanisms [Boustani et al., 2019]. As previously noted, the 5 Rs of radiobiology, together with the newly recognized sixth R, form the foundation upon which temporally fractionated conventional RT treatments are given.

2.4.6 Relative biological effectiveness

The relative biological effectiveness is a quantity that takes into account the fact that different types of IR depositing the same dose do not produce the same biological response [Hall and Giaccia, 2012d]. It is defined as the ratio of the dose required by a reference radiation (often ^{60}Co γ-rays) to produce a given biological effect, to the dose required by the test radiation to produce the same effect, as shown in Equation 2.22.

$$\text{RBE} = \frac{\text{Dose from reference radiation to produce a given biological effect}}{\text{Dose from test radiation to produce the same biological effect}} \tag{2.22}$$

While the RBE varies with the type of cell/tissue, the biological effect under investigation, dose, dose rate, and fractionation, it is most commonly compared against

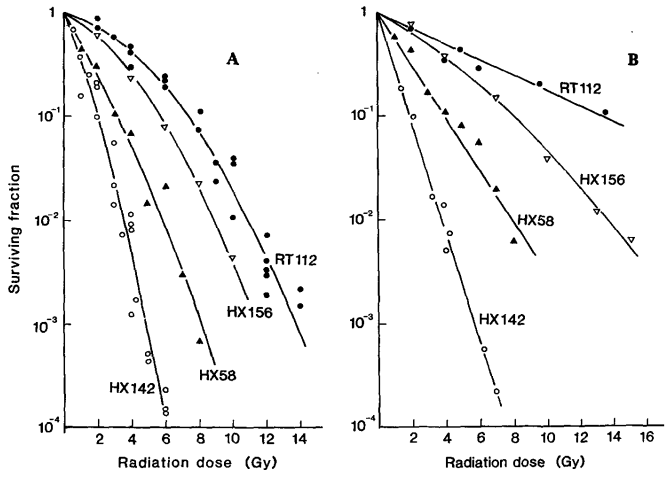

Figure 2.24: Cell survival curves for four human cell lines irradiated at 150 cGy/min (panel **A**) and 2 cGy/min (panel **B**). Taken from [Steel et al., 1989].

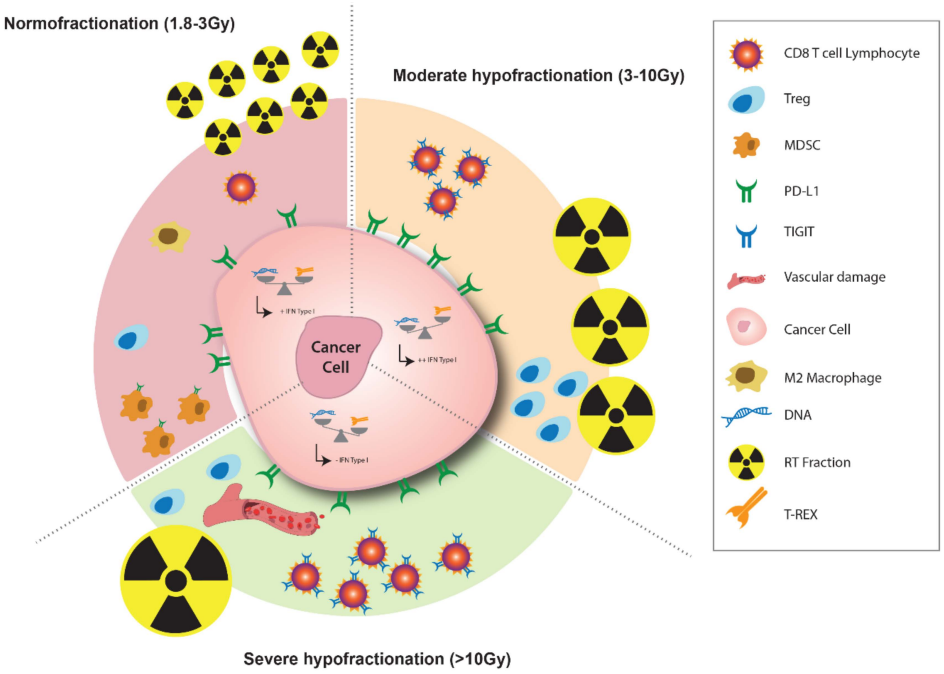

Figure 2.25: The dependence of the type of immune cell and the fractionation regimen in conventional RT. Taken from [Boustani et al., 2019].

the particle LET [Suntharalingam et al., 2005]. As a general rule, the RBE increases with increasing LET as shown in Fig. 2.26. However this increase only occurs up to a point, beyond which a decrease in the RBE begins.

The drop off in the RBE is representative of the *overkill* effect. The optimum LET being located at approximately 100 keV/μm is indicative of the fact that this density of ionisation corresponds with ionisation events being separated by approximately 2 nm, which is the diameter of a DNA double helix, thus being the value of LET which is most likely to cause a DSB [Hall and Giaccia, 2012d].

As shown in Fig. 2.27, even though the very high 200 keV/μm LET produces the same two ionisation events in the DNA double helix, some energy is *wasted* since the ionisation

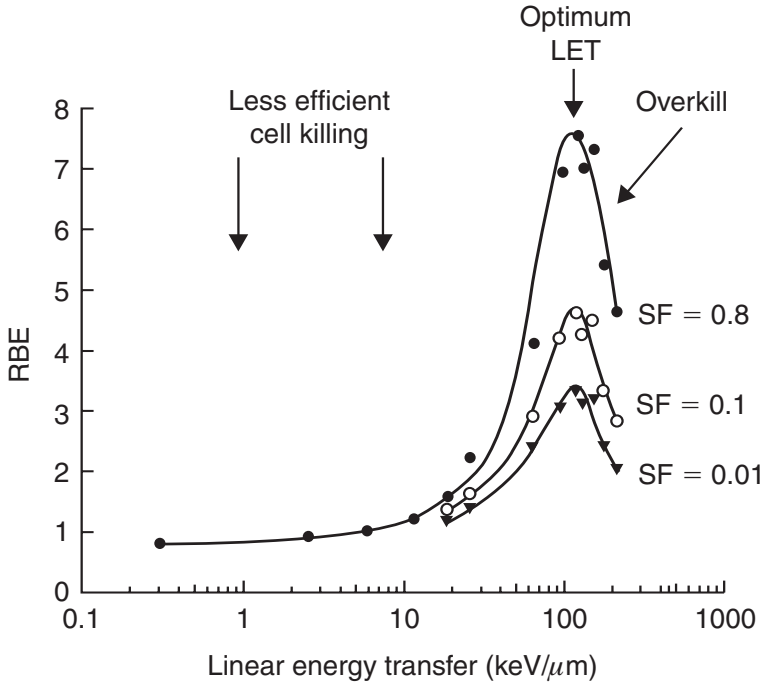

Figure 2.26: Graph of RBE as a function of LET, depicting the onset of an overkill effect for very high LET radiations. Taken from [Joiner, 2018].

events are too close together, thus resulting in the overkill effect, and subsequent drop off depicted in Fig. 2.26.

2.4.7 Non-targeted effects

Contrary to the ideas of direct DNA damage due to incident IR, or indirect DNA damage induced by cytotoxic ROS in the vicinity of the DNA as a result of water radiolysis, the past few decades have been marked by an increasing number of studies showing the importance of non-DNA targets such as lipids and proteins, as well as non-targeted effects [Pouget et al., 2018]. These non-targeted effects can be further classified as either *bystander*, *cohort*, or *abscopal* effects, as depicted in Fig. 2.28.

The two local effects are the bystander effect, or RIBE, and cohort effects. RIBEs were identified by Nagasawa and Little in 1992, where they observed a biological response in 20 - 40% of cultured cells while only 0.1 - 1% of the cells were traversed by an α-particle [Nagasawa and Little, 1992]. It can be thought of as the response of unirradiated cells within the irradiated volume to signals emanating from irradiated neighbour cells. These neighbour cells communicate radiobiologically manifested damages to the otherwise healthy cells which were not directly targeted by the radiation [Blyth and Sykes, 2011, Desouky et al., 2015]. Interestingly, cell-to-cell contact is not a strict requirement of these RIBEs. In the case where these bystander signals are in fact transferred through cell-to-cell contact, they are mediated by gap junction intercellular communication (GJIC), where gap junctions are specialised protein channels allowing communication between two neighbouring cells [Azzam et al., 2001]. Alternatively, these bystander signals can also be transferred through the release of diffusible (soluble) factors such as ROS or cytokines from irradiated cells into the medium [Mothersill and Seymour, 1997].

The cohort effect, on the other hand, is characterised by an enhanced radiobiological

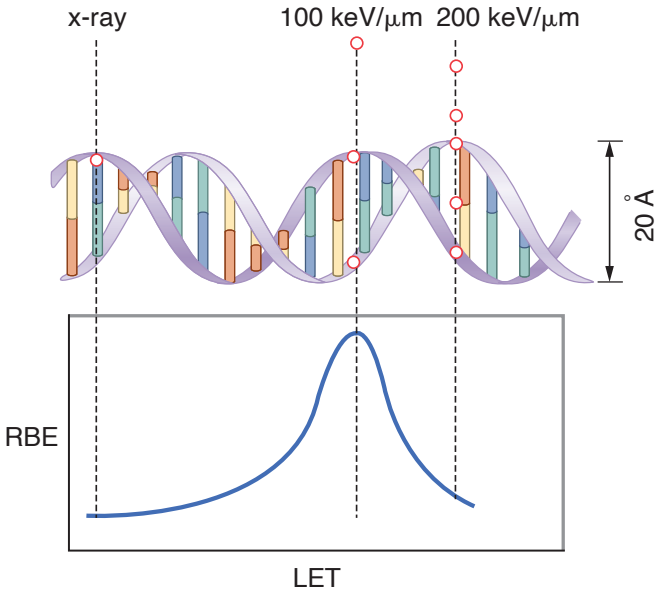

Figure 2.27: Diagram illustrating the coincidence of a 100 keV/μm beam of radiation with the diameter of a DNA double helix. Taken from [Hall and Giaccia, 2012d].

effect than what is to be expected in cells receiving low dose. This results from the interaction between low- and high-dose-irradiated cells within a heterogeneously irradiated volume [Daguenet et al., 2020, Grass et al., 2016].

In contrast to the bystander and cohort effects which are both local, the abscopal effect is distant and systematic, and can be defined as the communication of damages from irradiated tissues to unirradiated tissues outside of the irradiation volume [Pouget et al., 2018]. In recent years, there has been accumulating evidence of the immune system being a major determinant in the mediation of abscopal effects [Demaria et al., 2004, Daguenet et al., 2020, Griffin et al., 2020] and absolute T lymphocyte counts have been associated with the presence of abscopal effects [Nabrinsky et al., 2022].

With these radiobiological consequences in mind, the following section briefly introduces some models often used to characterise radiation's (physics) effects on the body (biology).

2.5 Radiobiological models

The LQ model describes the relationship between delivered dose and cell survival, and in its most simplest form is given by Equation 2.23 where the parameters α and β describe the sensitivity of the cell. Qualitatively, it can be said that α is representative of lethal damage caused by a single incident particle, while β corresponds to multiple-hit cell death [McMahon, 2018].

$$S = e^{-\alpha D - \beta D^2} \tag{2.23}$$

The degree of curvature of the curves in Fig. 2.29 is defined in terms of its α/β ratio, where high α/β ratios are associated with approximately constant rates of cell killing with dose [McMahon, 2018]. To date, the LQ model is the most frequently used model in radiobiology and RT and dominates all other models due to its robustness and simplicity [Bodgi et al., 2016].

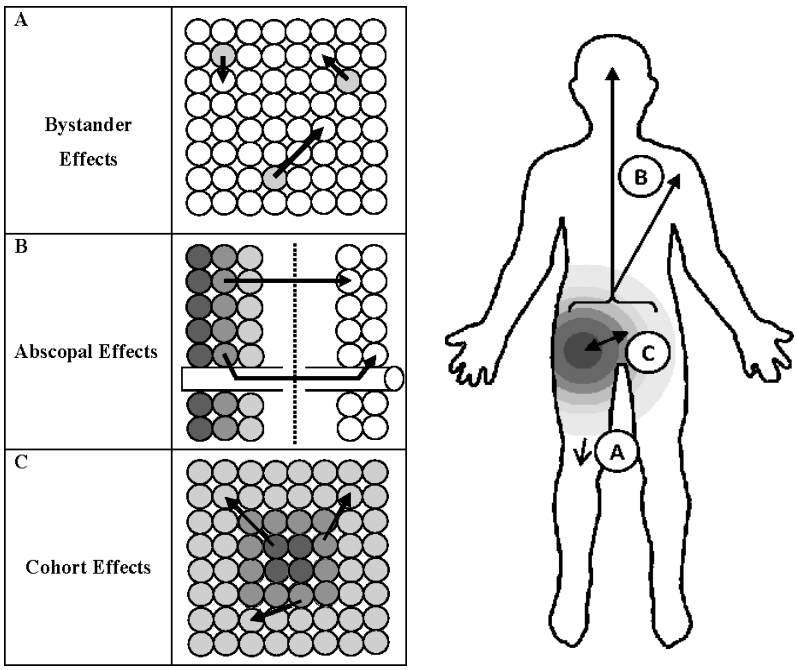

Figure 2.28: Classes of non-targeted effects, with the bystander, abscopal, and cohort effects depicted by **A**, **B**, and **C** respectively. The level of irradiation is indicated by the shading, where the white cells receive "no dose". Adapted from [Blyth and Sykes, 2011].

The microdosimetric kinetic model (MKM) is a variant of the LQ model, and relates α to the microdosimetric quantity of lineal energy [Debrot et al., 2018]. It was originally developed by Hawkins *et al.* in the 90's, who theorised that the effect of varying LET on cell survival can be attributed to random variations of the dose to small volumes within the nucleus [Hawkins, 1994, Hawkins, 1996]. The MKM was later modified by Kase *et al.*, to account for a saturation in the RBE due to cell-overkill effects at high LET [Kase et al., 2006], and has since been shown to accurately calculate cell survival and RBE when compared to *in vitro* measurements for proton and helium ion beams [Kase et al., 2013, Mairani et al., 2017]. The cell survival S in the modified MKM is calculated as follows [Kase et al., 2013]:

$$S = e^{\left(-\left(\alpha_0 + \frac{\beta}{\rho \pi r_d^2} y^*\right) D - \beta D^2\right)} \tag{2.24}$$

The lone parameters of Equation 2.24 that depends on the physical characteristics of the particle beam are the absorbed dose D and y^*, which represents the saturation-corrected dose-mean lineal energy [Kase et al., 2013]. The other parameters ($\alpha_0 = 0.13$ Gy^{-1}, $\beta = 0.05$ Gy^{-2}, and $r_d = 0.42$ μm) are biological constants for human salivary gland tumor cells and $y_0 = 150$ keV/μm is the saturation correction parameter [Kase et al., 2006, Kase et al., 2011]. The density of tissue ρ is assumed to be 1 g/cm^3, and y^* is calculated as follows [Kase et al., 2013]:

$$y^* = \frac{{y_0}^2 \int 1 - e^{-\left(\frac{y}{y_0}\right)^2} f(y) dy}{\int y f(y) dy} \tag{2.25}$$

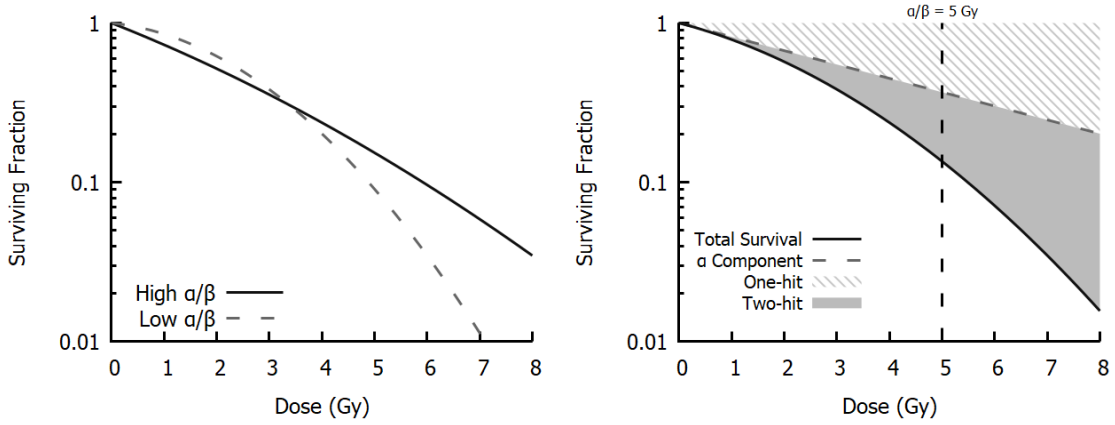

Figure 2.29: Illustration of cell survival curves. Taken from [McMahon, 2018].

Consequently, these microdosimetric spectra, which are often measured using a tissue-equivalent proportional counter (TEPC) (described in section 5.2.1) can be used as an input to the modified MKM to calculate the cell survival and RBE for a beam of IR.

Given the scattered radiation from EBRT treatments posing a risk of secondary cancers, radioprotection considerations need to be taken into account. Consequently, a brief introduction to radiation protection is provided in the following section.

2.6 Radioprotection considerations

In order to quantify the effect that ionising radiation has on the human body, the International Commission on Radiological Protection (ICRP) defined protection quantities (organ absorbed dose, equivalent dose, effective dose) to act as limitation and optimisation guidelines [Endo, 2016]. The equivalent dose takes into account the fact that different types of IR depositing the same dose may result in different degrees of biological damage. In other words, the equivalent dose takes into account the quality of the radiation and is measured in Sievert (Sv). The equivalent dose for a particular type of radiation is obtained by multiplying the absorbed dose in Gy by a dimensionless parameter known as the *radiation weighting factor* (W_R) which is dependent on the particle LET [Dunn, 2012]. The list of weighting factors set out by the ICRP is shown in Table 2.2, which compares the previous weighting factors from ICRP 60 to the current recommendations. The main changes were the fact that the proton weighting factor was reduced, and the neutron weighting factor should now be sampled from a continuous distribution, as shown in Fig. 2.30.

The effective dose takes into account the effect that IR would have on a specific organ, and the full list of factors can be found elsewhere [ICRP, 2003]. Given the difficulty at measuring the aforementioned protection quantities, operational quantities were originally defined in ICRU reports 39 [ICRU, 1985] and 43 [ICRU, 1988] to provide estimates for the related protection quantity. The enhanced biological effectiveness and highly penetrating nature of neutrons are a concern, and given their capability to scatter throughout the treatment room, stray neutrons could potentially reach the patient and deposit an unwanted dose. Therefore area monitoring operational quantities such as the ambient dose equivalent, given by $H^*(d)$, which acts as an estimate of the effective neutron dose, have often been

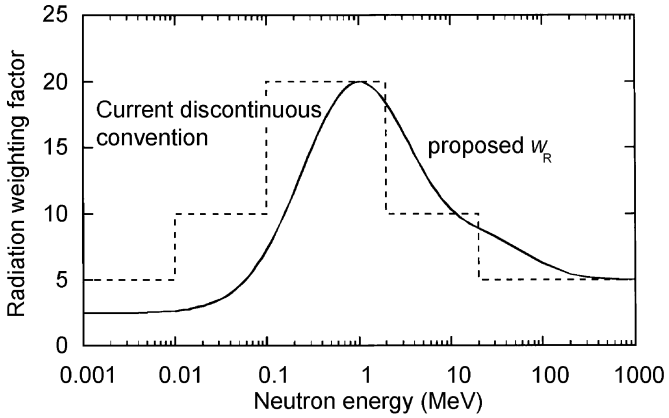

Figure 2.30: Weighting factors for neutrons as a function of neutron energy. Taken from [ICRP, 2003].

used to evaluate the degree of the presence of neutrons at various locations in a treatment room for both conventional photon and proton treatments [Yücel et al., 2016, Jakubowska et al., 2016]. It is defined as the dose equivalent at a point in a radiation field that would be produced by the corresponding expanded and aligned field in the ICRU sphere at a depth, d, on the radius opposing the direction of the aligned field, with 10 mm being the recommended depth to consider for penetrating radiations [Pelliccioni, 2000].

Table 2.2: A comparison of previous weighting factors W_R and the current recommendations by the ICRP. Taken from [ICRP, 2003].

Type and energy range of incident radiation		Radiation weighting factor (w_R)	
		Publication 60	Proposed[c]
Photons, all energies		1	1
Electrons and muons (all energies)[a]		1	1
Protons (incident)		5	2
Neutrons, energy	< 10 keV	5	
	10 keV–100 keV	10	Use the proposed w_R function in Fig. 1 below
	> 100 keV–2 MeV	20	
	> 2 MeV–20 MeV	10	
	> 20 MeV	5	
Alpha particles, fission fragments, and heavy ions[b]		20	20[d]

[a] Exclude Auger electrons from emitters localising to cell nucleus/DNA- special treatment needed.
[b] Use Q-LET relationships of *Publication 60* for unspecified particles.
[c] Changes for neutron energies < 1 MeV are required to account for gamma contribution to internal organs (see text).
[d] ICRP Committee 4 Task Group on Radiological Protection in Space Flight to consider w_R for high energy neutrons and heavy ions of LET > 200 keV/µm.

The ambient neutron dose equivalent can be calculated according to equation 2.26 where Φ_i is the neutron fluence for the ith energy bin, and $h^*(10)_i$ is the corresponding

fluence to dose equivalent conversion coefficient for that energy bin [Charyyev and Wang, 2020].

$$H^*(10) = \sum_{i=1}^{n} h^*(10)_i \times \Phi_i \tag{2.26}$$

Sets of fluence to dose equivalent conversion coefficients were first outlined in ICRP publication 74 [ICRP, 1996] and ICRU report 57 [ICRU, 1998], and M. Pelliccioni expanded this initial set of conversion coefficients to cover higher energies in view of better servicing the new and emerging RT modalities at the time [Pelliccioni, 2000]. The most recent publication detailing the set of recommended fluence to dose equivalent conversion coefficients is provided in ICRU report 95 [ICRU, 2020], which also outlines an alternative definition of the ambient dose equivalent, as the previous definition using an ICRU sphere resulted in an underestimation of the neutron dose equivalent for energies higher than 40 MeV [Pelliccioni, 2000, ICRU, 2020].

Accelerators are essential in the landscape of RT and their continued development opens up the possibility of exploring even more ways of delivering the radiation. The following section provides an overview of the main types of accelerators.

2.7 Accelerators

The modern medical LINAC, as shown in Fig. 2.2, has become the mainstay in RT treatments delivering beams of 6 - 25 MV photons and and beams 4 - 25 MeV electrons depending on the irradiation mode of the device [Podgorsak, 2005]. However, these devices aren't suited for the delivery of protons or heavier ions, primarily due to their increased mass. Consequently, this section briefly presents the different methods of generating different beams of IR.

2.7.1 LINAC

A detailed depiction of each of the components of a modern medical LINAC is shown in Fig. 2.31 where the part of the figure which is outlined in red corresponds to the treatment head of the device as was discussed in section 2.1.3 and Fig. 2.2.

Each of the components of Fig. 2.31 can be grouped into six classes, the injection system, RF power generation system, accelerating waveguide, auxiliary system, beam transport system, and beam collimation and beam monitor system [Podgorsak, 2005]. Broadly speaking, A *power supply* supplies direct current (DC) power to the *modulator*, from which high voltage flat-topped DC pulses of a few μs in duration are emitted. These pulses are delivered simultaneously to the *magnetron/klystron* (these devices are used to generate microwaves) and the electron gun. In order to match the RF waves originating from the magnetron/klystron, electrons produced by the electron gun, are pulse injected into the *accelerator waveguide*. Analogous to the idea of a *surfer*, electrons gain energy from the sinusoidal electric field within the waveguide before being delivered to the *beam transport system* and entering into the treatment head of the machine as was shown in Fig. 2.2 [Khan and Gibbons, 2014d].

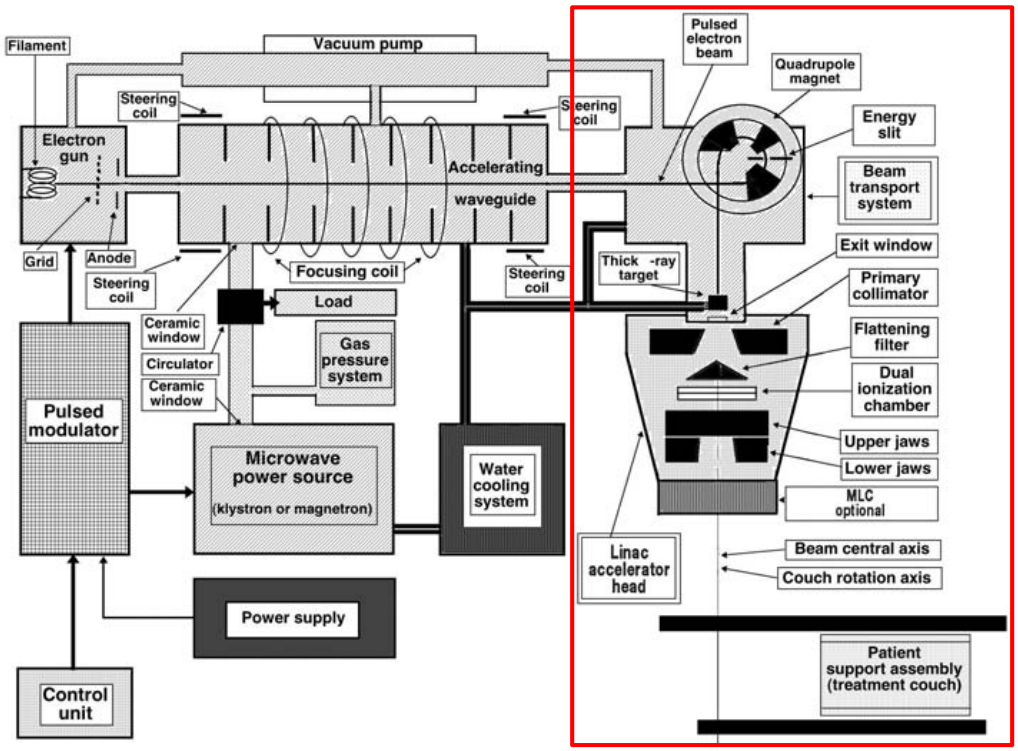

Figure 2.31: Components of a typical modern medical LINAC. Adapted from [Podgorsak, 2005].

2.7.2 Cyclotron

In contrast to a LINAC, particles in a cyclotron are accelerated along a spiral trajectory. In order to generate beams of protons, both cyclotrons or synchrotrons are generally used, while heavy ions are produced predominantly by synchrotrons or synchrocyclotrons. These devices will be discussed in the following subsections. As shown in the left panel of Fig. 2.32 the RF system of a cyclotron consists of two to four electrodes (each electrode is referred to as a *dee*) connected to an RF generator supplying a constant frequency. These dees are placed between magnetic poles. The direction of the electric field between successive dees is horizontal, while the direction of the magnetic field outside of the dees is vertical. When a proton crosses from a dee to a grounded region (shown in the right panel of Fig. 2.32) it experiences an acceleration due to the electric field between the oppositely charged dees. While inside the electrode the polarity of the applied electric field is changed in order for the proton to continue being accelerated in the gap between dees. The magnetic field bends the trajectory of the protons and the orbiting radius increases with the particle's kinetic energy. Once the radius of the particle is sufficiently large that it reaches the edge of the magnet, it is extracted and can then be transported to the end user [Schippers, 2020].

This type of system enables the acceleration of protons up to a maximum of 250 MeV, beyond which the increase in mass of the protons due to relativistic effects no longer allows it to be accelerated. Given the inverse relationship between cyclotron frequency and the Lorentz factor, devices known as *synchrocyclotrons* were created, where instead of keeping the cyclotron frequency constant, it is modified in order to counteract the increase in the Lorentz factor due to relativistic effects. This enables the production of higher energy protons [Schippers, 2020].

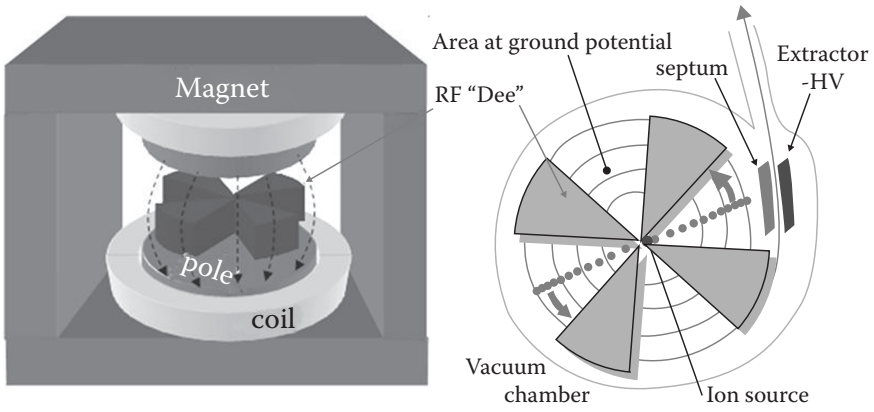

Figure 2.32: Schematic representation of a typical cyclotron, where the left panel shows the magnet and the RF system, while the right panel shows the extraction elements. Taken from [Schippers, 2020].

2.7.3 Synchrotrons

Synchrotrons work by accelerating the charged particles within a ring-like enclosed structure, referred to as a *lattice*, as shown in Fig. 2.33. This ring contains quadrupole focusing and defocusing magnets, as well as sextupole magnets, which work together to both focus the beam and correct chromatic aberrations. Bending and acceleration of the beam is achieved through the use of dipole magnetics and RF cavities respectively, and the strength of the magnetic and electric fields employed are increased in synchrony with the increasing particle energy [Khan and Gibbons, 2014c].

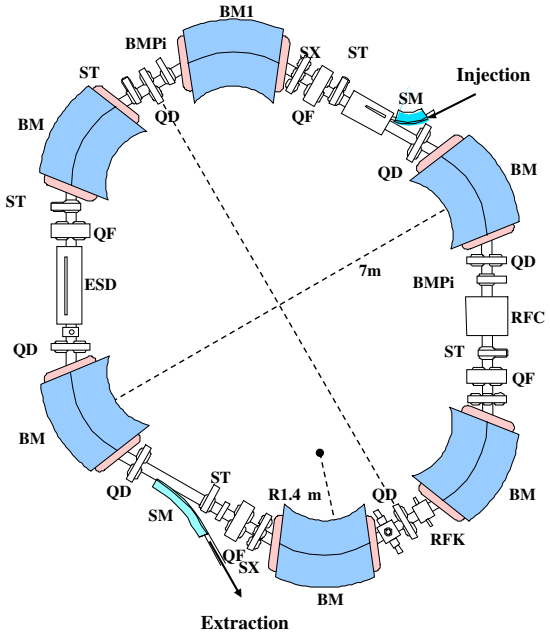

Figure 2.33: Schematic depiction of the lattice structure of a Hitachi synchrotron. Taken from [Hiramoto et al., 2007].

In contrast to cyclotrons, the beam of particles does not originate from within the synchrotron structure but instead needs to be injected from a pre-acceleration system

which fills the synchrotron lattice with bunches of particles [Schippers, 2020].

2.7.4 Laser-driven ion acceleration

One of the main limitations on RF-driven accelerators is the large space requirements owing to the fact that the accelerating field strength is on the order of magnitude of approximately 1 MV/cm. This leads to the situation whereby in order to accelerate proton or ion species to sufficiently high enough energies to be used in a clinical context, a large accelerating path is required. In order to combat this large size limitation, laser-driven acceleration has been proposed as an alternative and has been shown to be able to produce accelerating fields on the order of tens or hundreds of GeV/cm [Badziak, 2018].

The concept of laser-driven acceleration is based on the idea that a short pulse of a high intensity laser beam interacting with a thin target produces a plasma, in which the electrons are separated from the ions by the laser, resulting in a very strong electric field which can then be used to accelerate your particle [Badziak, 2018]. Examples of laser-based acceleration techniques are target normal sheath acceleration (TNSA) [Macchi et al., 2013], skin-layer ponderomotive acceleration [Badziak et al., 2011], and radiation pressure acceleration [Macchi et al., 2013], with TNSA representing the technique with which the most experience has been obtained [Schippers, 2020].

As set out in chapter 1.1, this thesis was performed within the framework of the CNRS-CCAP collaboration in which the goal was to aid in the design of LhARA. The use of a laser source allows LhARA to aim for a shot-to-shot stability of less than 1% and overcome some of the *space charge* effects which significantly limits the instantaneous dose rates at conventional facilities [Aymar et al., 2020]. At this point in time, the LhARA facility is being developed in two stages. In the first stage, the laser-driven beam will be captured and transported using plasma lenses and bending magnets to produce protons of 15 MeV to serve the *in vitro* investigations of the radiobiology programme. In the second stage, the beam will be accelerated using a fixed-field alternating gradient accelerator (FFAG) to produce 127 MeV protons to serve the *in vitro* and *in vivo* experiments. Ion beams up to and including ^{12}C will also be made available. A schematic depiction of the LhARA beam lines is shown in Fig. 2.34.

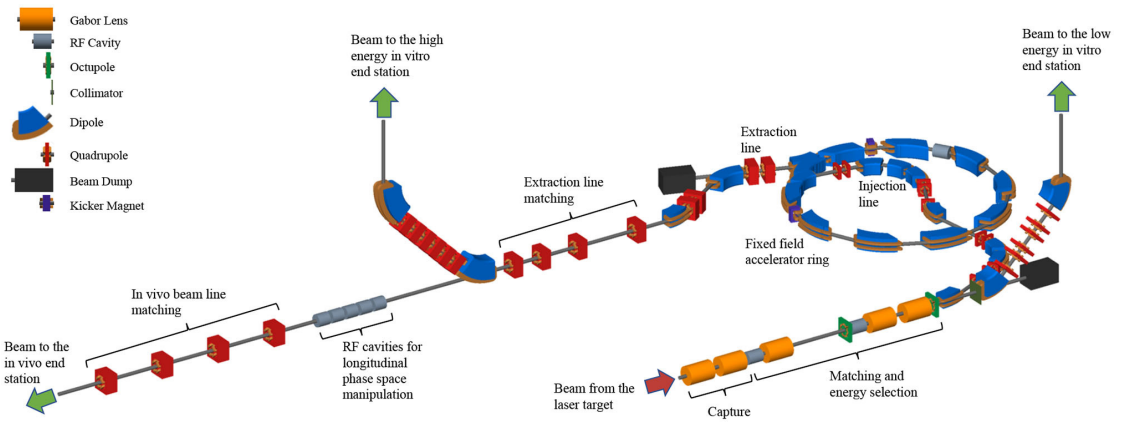

Figure 2.34: Schematic representation of the LhARA beamline, depicting all the beamline elements and the three end stations. Taken from [Aymar et al., 2020].

Consequently, two central aspects in the design of LhARA are the generation of beams via TNSA, and the subsequent acceleration using FFAG. These concepts will be explained

a bit further in the following subsections.

Target normal sheath acceleration

The use of TNSA has been shown to be effective at accelerating protons and light ions [Clark et al., 2000], and can be summarised by Fig. 2.35.

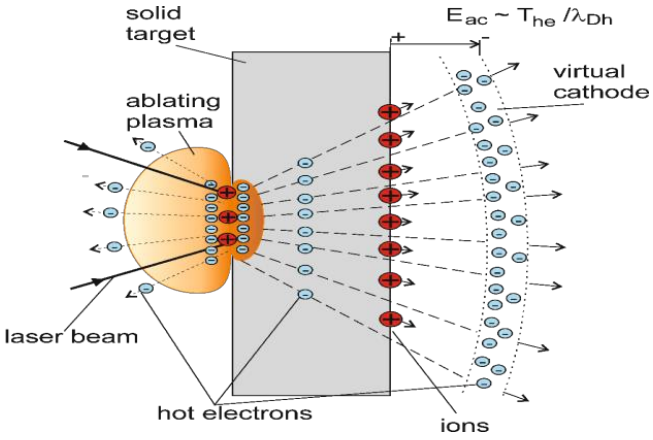

Figure 2.35: Fundamental ideas behind TNSA. Taken from [Badziak, 2018].

In brief, a laser pulse interacts with the front surface of the target producing a plasma and hot electrons between 0.1 - 10 MeV. The electrons then penetrate through the target and at a distance of 10 - 50 μm from the rear surface they form what is known as a *virtual cathode*. Consequently, the electric field induced by the cathode ionises atoms at the rear surface and accelerates those ions, in an approximately normal direction, over the distance between the rear surface and the cathode. As stated, this technique enables the generation of extremely high accelerating fields, thus dramatically reducing the size requirements of the installation [Badziak, 2018].

Fixed-field alternating gradient accelerator

The FFAG concept is not exclusive to laser-driven ion acceleration, and in fact has also been explored as an alternative to conventional cyclotron and synchrotron accelerated protons [Schippers, 2020]. It can be summarised by Fig. 2.36

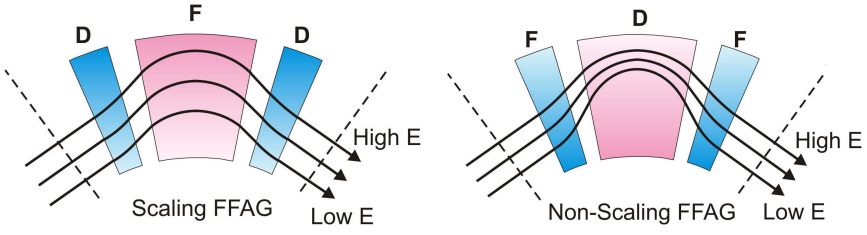

Figure 2.36: Schematic depictions of a scaling (left) and non-scaling (right) FFAG, where D denotes a defocusing effect and F denotes a focusing effect. Adapted from [Craddock and Symon, 2008].

Similar to synchrotrons, FFAGs consist of a closed loop of various elements. However, the novelty lies in the fact that the magnets are broken into sectors with strong radial field

gradients to account for the fact that magnetic fields in the bending magnets are kept constant (as opposed to being ramped up to account for the increase in particle energy) [Craddock and Symon, 2008]. In scaling FFAGs, orbits are kept the same shape, whereas in non-scaling FFAGs the shape of the particle orbits are allowed to vary. Both types of FFAG require an approximately 10 MeV injection system [Schippers, 2020]. Consequently, the main properties of FFAGs are that they offer much higher acceptances and repetition rates than synchrotrons, they provide higher beam intensities, however they come at the cost of more complicated magnet and RF cavity design [Craddock and Symon, 2008].

It is at this point in the thesis in which I believe to have sufficiently covered the theoretical and technical ideas behind conventional RT treatments. The remaining sections of this introduction will be dedicated to VHEE therapy and MBRT, which form the two central works of this thesis.

2.8 Very high energy electron therapy

Conventional RT treatments using electrons of 4 to 25 MeV can be used to treat superficial tumors due to the nature of their dose deposition in depth. Although these characteristics are well suited for these superficial tumors, their short penetration depth and significant lateral scattering make them unsuitable for the treatment of deep-seated tumors [Baskar et al., 2012]. Consequently, the use of VHEEs was proposed to overcome some of these challenges.

2.8.1 Physical and dosimetric advantages and disadvantages

In contrast to low energy electrons, VHEE beams of 150 to 250 MeV have been proposed as an alternative treatment modality for deep-seated tumors owing to their various dosimetric advantages [DesRosiers et al., 2000]. Among those advantages is the increased inertia of VHEEs, resulting in an increase in their practical range, and a narrowing of the beam penumbra at depth - both of which becomes more severe with increasing beam energy [DesRosiers et al., 2000, Papiez et al., 2002]. Resultingly, the dose distributions of VHEEs are favourable compared to those of photon beams. This increased range is depicted in Fig. 2.37.

As can be seen in both panels of Fig. 2.37, as the electron energy increases, the dose profile becomes approximately homogeneous in depth, leading to one of the drawbacks which is the high entrance doses and exit doses. One of the ways to overcome this is through the use of magnetic focusing lenses. Kokurewicz *et al.* demonstrated that magnetic focussing could be used as a way to overcome the high entrance and exit doses, and in fact localise the dose into small volumetric elements [Kokurewicz et al., 2019]. They focused beams of 200 MeV and 2 GeV VHEEs at different f-numbers, which are calculated as the ratio of the focal length (distance between the focusing element and the target) to the diameter of the beam. The reduction in entrance and exit doses is shown by the curves (g) and (h) in panel B of Fig. 2.37. Fig. 2.38 also depicts the differences between f-numbers of 1.2 and 11.5, in which a clear lateral focusing effect can be observed for the smallest f-number.

An additional advantage of VHEEs is the fact that they have been shown to be relatively insensitive to tissue heterogeneities [Papiez et al., 2002, Moskvin et al., 2010], experiencing a less than 15% dose deviation in the central plane of the beam. This is compared to therapeutic proton and photon beams, which can experience a deviation of

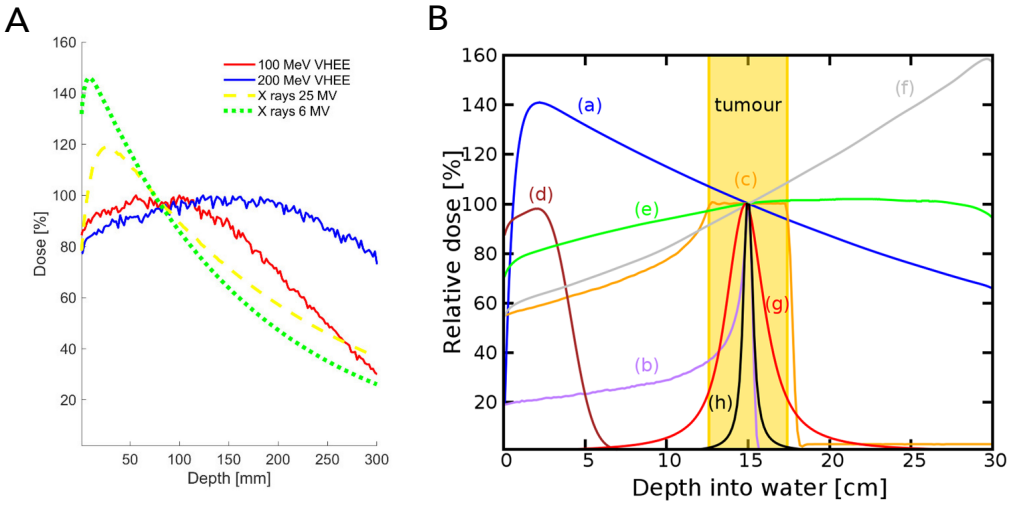

Figure 2.37: Comparison of VHEE depth dose profiles. Panel **A** is from [Ronga et al., 2021], while panel **B** is from [Kokurewicz et al., 2019] where the particles are (a) 6 MV photons, (b) 147 MeV protons, (c) SOBP protons, (d) 10 MeV electrons, (e) 200 MeV electrons, (f) 2 GeV electrons, (g) focused 200 MeV electrons, and (h) focused 2 GeV electrons.

up to 100% and 74% respectively when cuboid inserts of 0.001 - 2.2 g/cm^3 are embedded in the water phantom [Lagzda et al., 2020]. Fig. 2.39 depicts the difference incurred in PDD curves for a 150 MeV VHEE beam compared to a 150 MeV proton beam.

Furthermore, the capability of VHEEs to be electromagnetically scanned opens them up to the possibility of their use in conjunction with SFRT techniques [Martínez-Rovira et al., 2015, Dos Santos et al., 2020]. Despite these advantages, the high energy photons produced from these beams have been pinpointed as one of the potential areas of concern due to their high biological effectiveness. In fact, before the advent of VHEE therapy, there was an interest in determining the RBE due to Bremsstrahlung photons produced in the treatment head of a LINAC for conventional electron therapy. While the contribution to absorbed was found to be between 0.5% and 8% for beams up to 50 MeV, this contribution is highly machine dependent [Sorcini et al., 1996]. Consequently, in order to advance the field investigations to this end are still needed.

2.8.2 Consequences of neutron production on radioprotection and biological effectiveness

In the context of VHEEs, the main channels of neutron production are through the reactions (γ, xn)[21], (γ, p), and (γ, pn) [DesRosiers et al., 2000, Subiel et al., 2014]. Their production is predominantly through the giant dipole resonance (γ, xn), which causes the nucleus to emit neutrons through de-excitation events after a photon has imparted a sufficient amount of energy to the nucleus. With an upper threshold of approximately 30 MeV, this production of neutrons through the giant dipole resonance on light nuclei targets occurs from approximately 10 to 19 MeV up to the threshold. For heavy ions, this occurs from 4 to 6 MeV up to the threshold [Subiel et al., 2014, IAEA, 1979]. Above this giant dipole resonance, neutrons can also be produced through the *quasi-deuteron effect*[22]

[21] In this reaction x denotes a variable number of neutrons.

[22] In this interaction mechanism the photon interacts with a neutron-proton pair within the nucleus [IAEA, 1979].

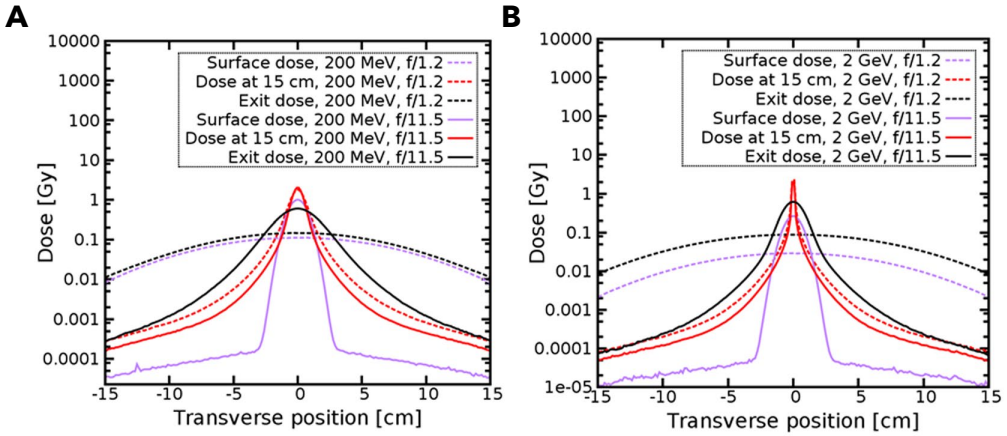

Figure 2.38: Doses at the entrance, 15 cm, and at the exit as a function of the transversal distance from the central beam axis. Focusing strength is depicted by *f*, where panel **A** is for the 200 MeV beam and panel **B** is for the 2 GeV beam. Adapted from [Kokurewicz et al., 2019].

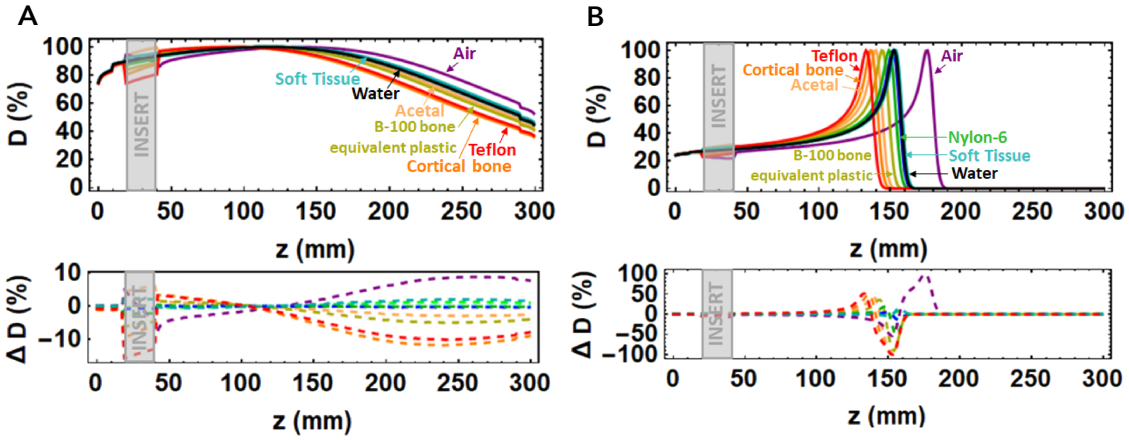

Figure 2.39: Simulated PDD profiles for a 150 MeV VHEE beam (panel **A**) and a 150 MeV proton beam (panel **B**) along with differences δD to the respective dose profile in pure water. Adapted from [Lagzda et al., 2020].

(γ, pn) for photons between 50 and 300 MeV [IAEA, 1979]. At even higher energies ($>$ 140 MeV) neutrons are generated $(\gamma, n$ and $\gamma, p)$ through photopion production processes, with a maximum cross-section at approximately 300 MeV. Nevertheless, these higher energy neutron production reactions have cross sections which are approximately at least an order of magnitude lower than the giant dipole resonance (γ, xn) [IAEA, 1979, DesRosiers et al., 2000].

Early studies on the RBE of 50 MeV Bremsstrahlung photons produced in the treatment head of a LINAC found values between 1.1 and 1.2 and therefore concluded that they could have non-negligible biological consequences [Zackrisson et al., 1991, Tilikidis et al., 1996]. Specific to VHEEs however, DesRosiers *et al.* observed only a 0.2% increase in the dose due to neutrons, and through the application of a quality factor of 10, hypothesised that an RBE of 1.02 should be used for dose prescription in VHEE therapy [DesRosiers et al., 2000]. Subiel *et al.* evaluated the neutron fluence within and in the immediate vicinity of a water phantom for a 165 MeV beam and found a neutron yield on the order of 10^{-5} neutrons/cm^2 per incident electron, which they concluded contributed negligibly to the neutron dose equivalents surrounding the water phantom [Subiel et al.,

2014]. Despite these findings, there was still an interest in performing complementary studies, using different configurations in order to more concretely conclude on these matters.

Therefore, given the concern, primarily with the production of high energy photons and neutrons, and to a lesser degree the production of protons through some the aforementioned reactions, one of the central works of this thesis was to explicitly evaluate the expected increase in their RBE from a microdosimetric point of view, and investigate the neutron dose equivalents beyond the irradiated volume within a treatment room.

Given its role as one of the other central works of this thesis, the following section will provide an overview of SFRT.

2.9 Spatially fractionated radiotherapy

2.9.1 Fundamental ideas behind SFRT techniques

In comparison to conventional RT in which the tumor is covered by a homogeneous dose [ICRU, 1999], SFRT represents a departure from this dogma by making use of several spatially fractionated narrow beamlets, thereby creating alternating regions of high and low dose, and consequently leading to highly heterogeneous dose distributions [Prezado, 2022]. SFRT techniques are typically categorised as one of four types: GRID, lattice radiotherapy (LRT), MRT, and MBRT [Butterworth et al., 2023]. The main differences between these techniques is the size and spacing of each of the individual beamlets, leading to variations in the degrees of spatial fractionation, and resultantly variations in the therapeutic doses and dose rates delivered. Typical lateral dose profiles of the different techniques, along with corresponding spatial distributions of the radiation are shown in Fig. 2.40.

Given the divergence of SFRT techniques from conventional RT, some new terms needed to be coined in order to more accurately describe the spatial distribution of the doses delivered. Standardization of the definition of these terms, and ubiquity of their use-cases are important to the advancement of the field of SFRT in view of having a *common language* to effectively communicate, collaborate, and collate the works of different teams, in different parts of the world, who may be approaching the field from different scientific disciplines. To this end, an extensive glossary has recently been published aiming to achieve just that [Meyer et al., 2023]. A non-exhaustive list of the most important dosimetric and geometric parameters are summarised below:

- The **average dose**, similarly to conventional RT, is the arithmetic mean dose delivered by the irradiation field to a target.
- The **peak dose** is the maximum dose along the central axis of a beamlet.
- The **valley dose** describes the region of low dose occurring at the midpoint between two adjacent beamlets.
- The **beamlet width**, is used to describe the size of the beamlet. This could be a width or a diameter, depending on the type of SFRT.
- The centre-to-centre distance (**ctc**), or **beam spacing**, refers to the lateral distance between the central axes of adjacent beamlets.

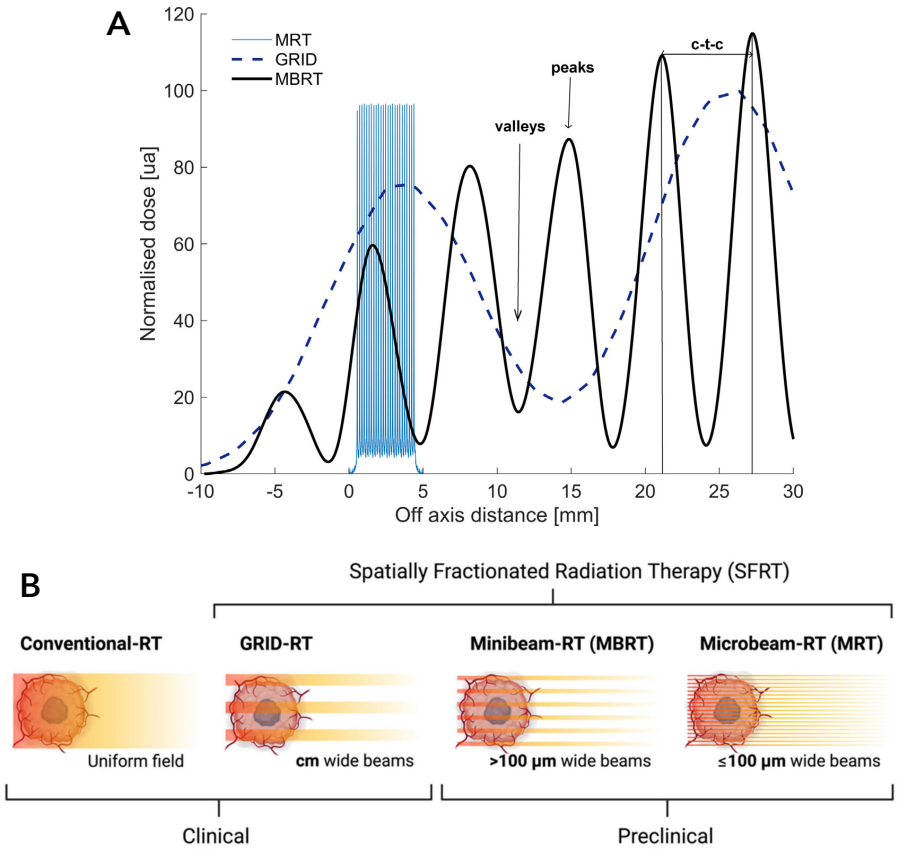

Figure 2.40: Lateral dose profiles for GRID, MRT, and MBRT, showing some of the important parameters (panel **A**), along with an illustration (panel **B**), indicating the different spatial distributions of the radiation for each of the techniques. Taken from [De Marzi et al., 2019] and [Fernandez-Palomo et al., 2022] respectively.

- The peak to valley dose ratio (**PVDR**) is a quantity commonly used to describe the degree of spatial fractionation[23], and is given by the ratio between the peak (D_{peak}) and valley (D_{valley}) doses:

$$\text{PVDR} = \frac{D_{peak}}{D_{valley}} \tag{2.27}$$

The different SFRT techniques, in ascending order according to beamlet width, are: MRT < MBRT < GRID/LRT. As highlighted in panel B of Fig. 2.40 and Table 2.3, the techniques with the largest beam sizes are prevalent in a clinical context (primarily for palliative care), whereas the use of MRT and MBRT is still only limited to preclinical studies, but are promising candidates for clinical translation and curative treatments of radioresistant tumors.

[23] In a clinical context, the *dose prominence* was put forth as an alternative to the average or integral dose, and describes the degree of spatial fractionation using the dose *difference* between a peak and its lowest contour on a treatment plan [Lansonneur et al., 2020].

Table 2.3: Main differences between the different SFRT techniques. Taken from [Prezado, 2022].

Technique	Beamlet width	Beam spacing	Typical pattern	Typical therapeutic (peak) dose	Dose gradient/spatial modulation (PVDR)	Application
GRID therapy	1–2 cm	2–4 cm	2D-grid of pencil shaped beamlets	10–15 Gy	Low (2–5)	Mainly palliative
LATTICE therapy	1–2 cm	2–4 cm	High-dose region ('vertices') in the tumour	10–15 Gy	Low (2–5)	Mainly palliative
MBRT	0.5–1 mm	1–4 mm	Arrays of planar beamlets	50–100 Gy	Medium (10–20)	Preclinical (potentially radical treatments)
MRT	50–100 µm	200–400 µm	Arrays of planar beamlets	300–600 Gy	High (>50)	Preclinical (potentially radical treatments)

One of the challenges with performing a comprehensive comparison between conventional RT and SFRT techniques, as well as between the different SFRT techniques, is that there is still a lack of dedicated biological experiments investigating these differences. Consequently, there is still no generally accepted formalism for reporting SFRT doses [Meyer et al., 2017]. It still remains difficult to truly elucidate the link between the physical parameters of the irradiation and the resulting biological response, however some attempts to shed light on this link from existing preclinical data was performed by Fernandez-Palomo *et al.* [Fernandez-Palomo et al., 2022], as will be discussed below.

The earliest form of SFRT was GRID therapy [Mohiuddin et al., 1990]. The work of Mayr *et al.* highlighted that in GRID therapy, the dose was predominantly prescribed to the 3D gross tumor volume without an additional margin in 62.5% of the cases, and to the maximum dose (however not to a gross tumor volume with a margin or to a defined prescription point in depth) in 37.5% of the cases [Mayr et al., 2023]. Similarly, the work of Grams *et al.* showed that in their institute, dose prescription for brass GRID collimators was to the maximum dose along the central axis [Grams et al., 2023]. Dose prescription in LRT on the other hand was to the peak dose covering 95% of the volume of the vertices and covering 1% to 10% of the gross tumor volume [Grams et al., 2023].

The preclinical work from Rivera *et al.* evaluated the influence of different dosimetric parameters in a variety of different radiation spatial distributions in a rat fibrosarcoma model. They found that in fact the average and peak doses correlated the least with tumor response, whereas the best correlating dosimetric parameters were the tumor equivalent uniform dose (EUD) and the valley dose [Rivera et al., 2020]. The importance of the valley dose was also remarked by Fernandez-Palomo *et al.*. They evaluated a total of eighteen studies in which tumor-bearing animals were treated with either MRT or MBRT and found that the valley dose was the dosimetric parameter which best correlates with increased lifespan (ILS) [Fernandez-Palomo et al., 2022].

The common denominator between these SFRT techniques, and one of their main draws, is the fact that they have all shown a propensity for enhanced normal tissue sparing despite the high/extremely high peak doses [Laissue et al., 2012, Mohiuddin et al., 1990, Mohiuddin et al., 1996, Wu et al., 2010, Amendola et al., 2019, Slatkin et al., 1992, Bräuer-Krisch et al., 2010, Dilmanian et al., 2006, Prezado et al., 2015]. While the tumor control in SFRT is thought to be a latent consequence of the highly heterogeneous dose distribution [Griffin et al., 2020, Johnsrud et al., 2020, Prezado et al., 2019, Lamirault et al., 2020a], the relative contribution of the different underlying radiobiological mechanisms is still not fully understood. Before diving into the physical consequences and potential radiobiological mechanisms of the different techniques, a brief historical overview is provided in the following section in order to give more context to the development of the field of SFRT.

2.9.2 A brief historical overview of SFRT

The first instance of SFRT dates back to 1909 when A. Köhler proposed the use of a perforated steel grid, placed at the exit of the x-ray tube, in order to create interspersed areas of high and low dose [Laissue et al., 2012]. The use of this technique, which later came to be known as GRID therapy, was motivated by the desire to reduce skin toxicities when treating deep-seated tumors with orthovoltage x-rays, which given their low energy, necessitated massive doses to the skin in order to achieve curative doses in the tumor. Eventually, by changing the material to lead-rubber to limit the amount of secondary rays, and empirically establishing a 40/60 ratio of open to closed areas, the technique was successfully used up until the 1950's - at which point the prevailing belief was that sparing of the skin was achieved due to the reduction in the volume of tissue irradiated [Marks, 1952].

This technique was successfully used up until the 1950's, but then fell into obscurity due to the advent of megavoltage x-ray sources and the very first medical LINACs [Thwaites and Tuohy, 2006], thus eliminating the use of orthovoltage x-rays for deep seated tumors. Ultimately, this marked the beginning of the megavoltage era as shown in Fig. 2.41.

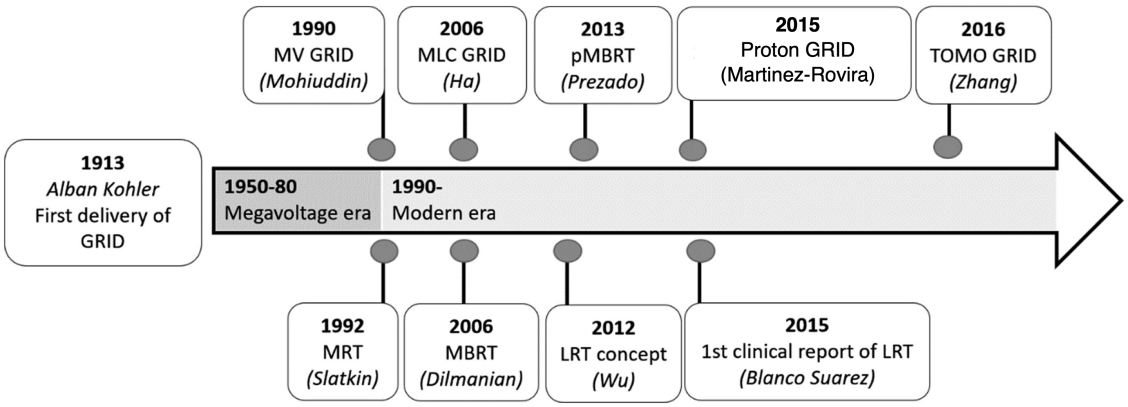

Figure 2.41: Timeline of major events in SFRT, from its discovery to the present day. Adapted from [Butterworth et al., 2023].

There were no new GRID therapy developments for approximately two decades, however in the 1970's it was rediscovered, and consequently applied to megavoltage photons through its use in conjunction with Co-60 machines [Barkova and Kholin, 1971, Muth et al., 1977] and eventually modern medical LINACs [Mohiuddin et al., 1990]. Up until this point, the delivery of GRID therapy treatments was performed solely with photons, and with physical perforated blocks as shown in panel A of Fig. 2.42. However developments in the technique have demonstrated the feasibility of delivering GRID treatments (1) using MLCs [Ha et al., 2006], (2) in conjunction with helical tomotherapy [Zhang et al., 2016], or (3) with protons instead of photons [Martínez-Rovira et al., 2015].

The other SFRT technique employing ∼cm size beamlets is LRT, which was first proposed as 3-D alternative to 2-D GRID treatments in which focused high dose volumes were generated within the tumor [Wu et al., 2010]. Similarly to GRID therapy, this technique has been successfully translated to the clinic [Blanco Suarez et al., 2015].

Going back to the 90's and we have the first formal definition of MRT, which refers to the use of parallel micrometer sized beams [Slatkin et al., 1992], thereby taking advantage of the dose-volume effects first observed by Zeman and Curtis [Zeman et al., 1959, Zeman et al., 1961, Curtis, 1967]. This technique was born in large synchrotron facilities, capable of

delivering beams of photons at very high dose rates [Slatkin et al., 1992, Slatkin et al., 1995]. These high dose rates are necessary in order to deliver the beams in a fraction of a second so as to avoid the blurring of the beam caused by cardiosynchronous pulsations in the brain [Manchado de Sola et al., 2018, Duncan et al., 2020] or organ motion [Grotzer et al., 2015], which could compromise the radiobiological efficacy of the technique. Interestingly, MRT is the only SFRT technique which is predominantly delivered with high dose rates, similar to those used in FLASH in which normal tissue sparing effects are also observed. A combination of SFRT and FLASH-RT could have the potential to further increase the therapeutic index [Schneider et al., 2022].

In order to overcome some of the technical challenges associated with MRT while still benefiting from the dose-volume effect, an alternative technique (MBRT) using submillimetric sized beams was proposed [Dilmanian et al., 2006]. By using larger beams, beam blurring is avoided, thereby eliminating the requirement of very high dose-rates, and consequently enabling the implementation of MBRT in more cost-effective machinery [Prezado et al., 2017a]. The use of protons in conjunction with MBRT was first proposed by Prezado and Fois who showed that the marriage of SFRT and particle beams could yield higher or similar PVDRs compared to traditional x-rays [Prezado and Fois, 2013]. Consequently, it was also shown that by specifically tuning the beam parameters one is able to obtain a heterogeneous distribution in the normal tissues, while achieving a homogeneous dose coverage of the tumor, thereby avoiding the dose bath which would have otherwise been received by the organs at risk when conventional x-rays are used [Prezado and Fois, 2013].

It is evident that significant advances to the field of SFRT has been made over the past 20 years. These techniques represent radically different ways of delivering the dose, and while both GRID and LRT have seen clinical use, MRT and MBRT have major potential for widespread clinical implementation in the years to come, with great potential to achieve curative treatments of radioresistant tumors. Consequently, these techniques should be regarded as important signifiers of the paradigm shift we are currently experiencing in RT [Griffin et al., 2020, Prezado, 2022].

2.9.3 Types of SFRT techniques

GRID therapy

As previously mentioned, GRID is the earliest form of SFRT and consequently it is the most commonly reported SFRT dose pattern and has the greatest body of clinical evidence [Billena and Khan, 2019]. In the seminal paper by Mohiuddin *et al.*, a physical GRID block collimator made of Cerrobend was used, with holes spaced in such a way as to take into account the divergence of the photon beam, and resulting in a 50:50 ratio between the open and closed areas. An example of such a GRID block, when mounted on to the end of a LINAC head, is shown in panel A of Fig. 2.42. In this study, 10 - 15 Gy was prescribed to the peaks (open areas of the GRID) in view of providing palliative treatment of bulky tumors, ranging in size of 6×5 cm^2 to 25×25 cm^2 [Mohiuddin et al., 1990].

As with all SFRT techniques, modification of the physical/technical parameters of these GRID blocks results in modifications of the delivered dose distributions and consequent treatment outcome. For example, the use of a commercially available Cerrobend GRID block with hole diameter of 1.43 cm and centre-to-centre distance (ctc) of 2.11 cm was shown to yield similar dose profiles for both 6 and 18 MV x-ray beams. While the doses in the valleys remained approximately constant, the peak doses decreased in depth, therefore resulting in a reduction in the peak to valley dose ratio (PVDR) with depth [Meigooni

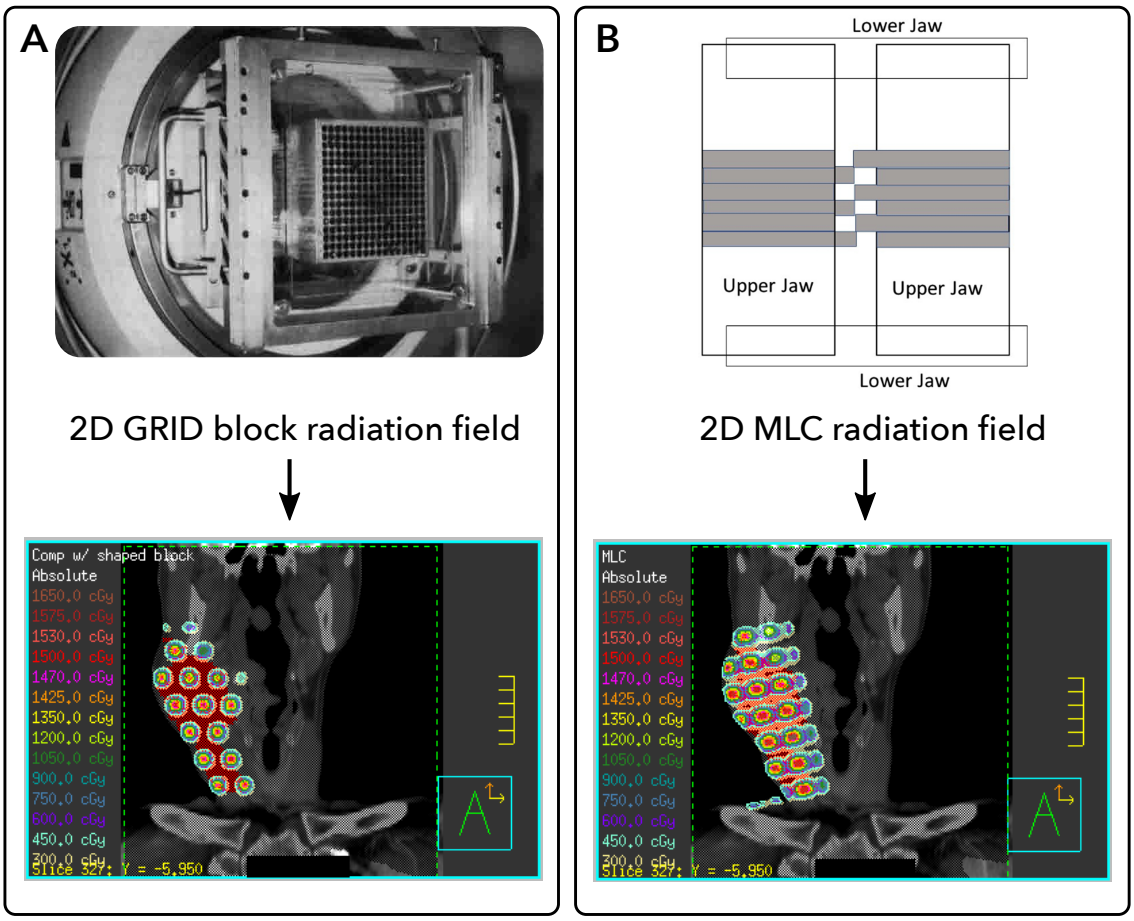

Figure 2.42: Panel **A** depicts a typical 2D GRID collimator block mounted on to the end of the LINAC head - as would be used for clinical treatments - along with and example sagittal view of the resulting isodose distribution. A schematic diagram of a single GRID field using a MLC is shown in panel **B**, together with an example of the sagittal view of its resulting isodose distribution. Taken from: [Mohiuddin et al., 1996, Buckey et al., 2010, Zhang, 2023].

et al., 2006]. A similar dosimetric behaviour was observed when using a commercially available brass block (1 cm hole diameter and 2 cm ctc) instead of Cerrobend, however use of the latter results in a higher PVDR [Buckey et al., 2010, Zhang, 2023]. In order to maximise the therapeutic ratio, MC simulations were carried out in which it was reported that the optimal hole sizes are between 1 - 1.25 cm with a spacing of 1.7 - 1.8 cm [Gholami et al., 2017].

One of the alternatives involves the use of a MLC as shown in panel B of Fig. 2.42. While the use of either blocks or MLCs has various advantages and disadvantages (i.e. treatment time, flexibility, cost), and despite the differences in the open:closed ratio (31% for MLCs compared to 50% for GRID blocks [Neuner et al., 2012]) in a clinical setting the two techniques were found to be comparable in terms of treatment outcome [Ha et al., 2006, Neuner et al., 2012, Billena and Khan, 2019].

While single fraction GRID therapy delivered in combination with conventional EBRT has historically been used with great success for palliative treatments of a variety of bulky tumors [Billena and Khan, 2019, Yan et al., 2020], there have been a small number of cases in which GRID therapy, with peak doses of 15 - 20 Gy, was used in conjunction with either EBRT, surgery, or chemotherapy with curative intent. The use of this technique

with curative intent was primarily in the context of squamous cell carcinomas of the head and neck. GRID therapy was combined with: a conventional course of EBRT, leading to local control rates[24] between 44 and 93% [Huhn et al., 2006, Edwards et al., 2015, Choi et al., 2019] - a conventional course of EBRT and surgery (neck dissection), leading to control rates of 92% [Huhn et al., 2006] - and a course of chemoradiotherapy (combined administration of both chemotherapy and RT), with a control rate of 79 % [Peñagarícano et al., 2010].

Finally, given the 2D nature of GRID blocks or GRID with MLCs, one of the limitations is the dose conformality to the target. Of the two main methods to overcome this, one is through the exploitation of the physical characteristics of protons, namely a reduced dose to proximal organs [Henry et al., 2017, Gao et al., 2018]. The second is through an implementation with helical tomotherapy [Zhang et al., 2016] or VMAT [Grams et al., 2021]. This 3D implementation of GRID was first performed in the context of LRT, as will be described in the following subsection. It was also shown that the implementation of GRID therapy in the context of flattening filter-free accelerators could enable the use of thinner beams, thereby potentially leading to a widening of the therapeutic window due to the increased tissue tolerances of the smaller beams, thereby enabling higher and potentially curative doses to be delivered. [Martínez-Rovira et al., 2017b].

Lattice radiotherapy

LRT is a technique whereby multiple beams are locally converged in order to create spherical volumes (vertices) of high dose within the tumor, while limiting the dose to the surrounding normal tissues or proximal organs at risk [Wu et al., 2010]. It has primarily been used as a palliative treatment in combination with either conventional RT, chemotherapy, or immunotherapy, and since 2010 it has been used to treat over 150 patients with late-stage bulky tumors [Wu et al., 2020]. Figure 2.43 depicts an example dose distribution from a LRT treatment plan.

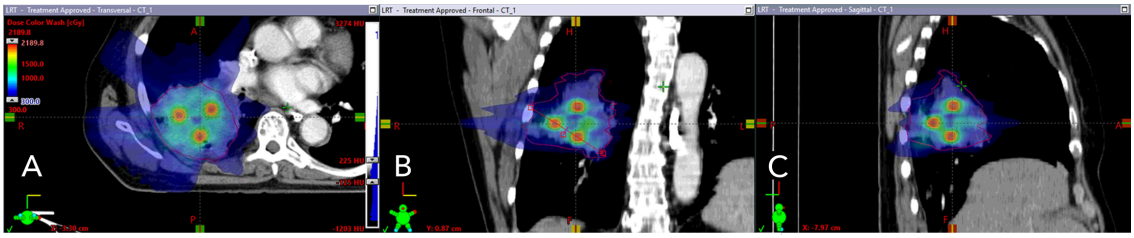

Figure 2.43: Axial (**A**), coronal (**B**), and sagittal (**C**) views of a LRT treatment plan, where red indicates the high dose vertices, while blue indicates the low dose regions. Taken from: [Amendola et al., 2019, Amendola et al., 2023].

The number of vertices, their size, and their spacing depends on the size, shape, and location of the tumor with respect to normal structures or critical organs. In general, the high dose vertices range in size from 0.5 to 1.5 and are usually separated by 2 to 5 cm [Amendola et al., 2019, Amendola et al., 2023]. The two most prominent clinical centers delivering LRT treatments are the Innovative Cancer Institute in Miami and the Fujian Union Hospital in China, where the vertex doses are between 2.4 - 18 Gy and 8 - 20 Gy

[24] The *control rate* represents the percentage of patients with advanced cancer whose therapeutic intervention has led to a complete or partial response, or stabilised the disease [Delgado and Guddati, 2021].

per fraction respectively. Doses to the tumor periphery are typically < 3 Gy, and valley doses are thought to generally not be important in palliative treatments as long as toxicity control can be ensured [Wu et al., 2020]. Finally, as with GRID therapy, the feasibility of using LRT in conjunction with charged particles has recently been demonstrated [Yang et al., 2022a].

Microbeam radiation therapy

MRT was first proposed by Slatkin *et al.* in 1992 [Slatkin et al., 1992]. Representative of the most radical form of SFRT, the use of micrometer size beams in this technique diverges from GRID and LRT not only due to the size of beams, but also in their use, which has predominantly been with curative as opposed to palliative intent [Dilmanian et al., 2002]. Typically, these spatially fractionated fields are characterised by narrow (25 - 100 μm), quasi-parallel, planar beams, with ctcs between 100 and 400 μm [Bräuer-Krisch et al., 2010]. However, depending on the collimation technique, cylindrical microbeams may also be generated to produce an array of beams similar to GRID therapy, as shown in Fig. 2.44.

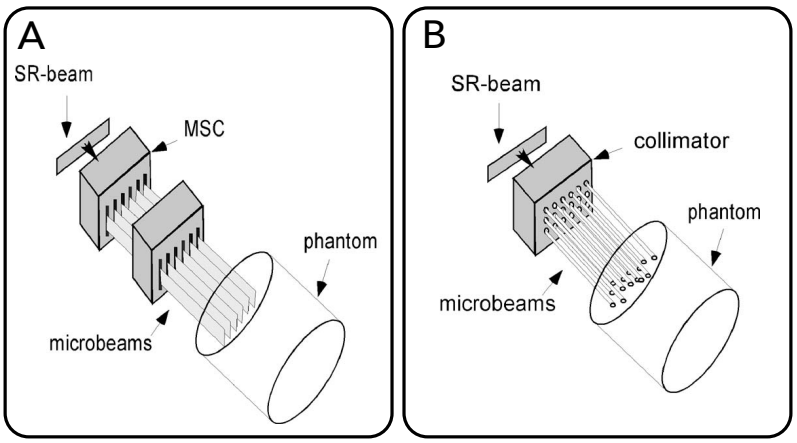

Figure 2.44: Examples of two different MRT irradiation modalities. Panel **A** depicts the use of a multislit collimator to create planar beams, while panel **B** depicts the creation of cylindrical beams. Taken from [Siegbahn et al., 2006].

The term *SR* in Fig. 2.44 refers to the synchrotron radiation (as was briefly detailed in section 2.7) of large synchrotron facilities, which provide the necessary physical beam parameters to create optimal MRT peak-valley dose distributions [Slatkin et al., 1992]. The physical characteristics of these synchrotron generated MRT beams are: **(1)** small beam divergences constraining the high dose peaks to a small volume, thereby taking advantage of the dose-volume effect to deliver large doses of 100 - 1000 Gy without incurring deleterious effects in the normal tissue [Bartzsch et al., 2020]. **(2)** Delivery of x-rays in the keV energy range resulting in a minimal lateral scattering and a preservation of the sharp beam penumbra [Siegbahn et al., 2006, Prezado et al., 2009, Smyth et al., 2019]. **(3)** Low valley doses and high (20 - 50) PVDR values [Regnard et al., 2008, Serduc et al., 2009a, Schültke et al., 2018] as a result of **(1)** and **(2)**, which has been shown to be essential for normal tissue sparing [Dilmanian et al., 2002]. And **(4)** very high dose rates of hundreds of Gy/s to overcome the effect of cardiosynchronous pulsations or organ motion [Manchado de Sola et al., 2018, Duncan et al., 2020, Grotzer et al., 2015].

As has already been highlighted, the earliest advantage associated with the use of MRT was the observed enhanced normal tissue sparing. From the early work of Slatkin

et al. it was shown that delivering single fraction MRT to rat brains with entrance doses between 1250 and 10000 Gy resulted in a loss of neuronal and astrocytic nuclei. Of the four rats receiving 10000 Gy entrance dose only two developed brain tissue necrosis, and for entrance doses up to 625 Gy all the brain tissue slices remained normal [Slatkin et al., 1995]. Heterogeneity of the dose within the tumor is a characteristic of MRT that goes directly against one of the main guiding principles of conventional RT - namely covering the tumor volume with a homogeneous dose. Despite this contradiction, various preclinical studies have demonstrated the capability of such heterogeneous dose distributions to achieve tumor control for various tumor types such as gliomas [Bouchet et al., 2016], squamous cell carcinomas [Miura et al., 2006], and melanomas [Potez et al., 2019]. Furthermore, critical structures such as the spinal cord are able to tolerate the high peak doses associated with the technique [Laissue et al., 2013].

While the original pioneering work on MRT was performed using single arrays and single fractions, the technical feasibility and biological interest of interlacing the arrays (i.e. single arrays of microbeams with different ports of entry) or temporally fractionating the treatment was demonstrated by various authors [Laissue et al., 1998, Serduc et al., 2009b, Bräuer-Krisch et al., 2013]. The biological basis for delivering MRT over multiple days is based on the Rs of radiobiology and its benefits are well known in conventional RT (see section 2.4.5). By interlacing the beams the normal tissue still benefits from spatial fractionation while the percentage of the tumor volume receiving peak doses is higher. It has been hypothesised that this leads to an an enhanced anti-tumoral effect [Fernandez-Palomo et al., 2020].

Over the years, various factors contributing to the biological efficacy of MRT have been elucidated, however their relative contribution to the full picture of the radiobiological mechanisms at the heart of MRT are still not fully understood. These mechanisms will be further described in section 2.9.5. MRT has been implemented at large synchrotron facilities in North America, Europe, Japan, and Australia, however its development, and translation into a clinical context has been hampered by: the cost associated with the use of large synchrotron facilities - necessitated by the high dose rates required to overcome beam blurring, precise patient positioning, and a challenging dosimetry. One of the main limitations of MRT is that it is only performed with low energy x-rays, thus restricting its potential clinical use to the treatment of superficial tumors. From an experimental point of view, a reduction in normal tissue damage was observed when using 20 MeV proton microbeams with a ctc of 500 μm and widths of 10 μm and 50 μm [Zlobinskaya et al., 2013]. However, MC investigations showed that the heterogeneity characterized by high PVDR values would only be maintained over the first 25 - 35 mm in depth before eventually homogenising, thereby still limiting its potential implementation to superficial targets [Kłodowska et al., 2015]. While these challenges and potential solutions are reviewed elsewhere [Bartzsch et al., 2020], one of the effective alternatives is MBRT, which is detailed in the following section.

2.9.4 Minibeam radiation therapy

As previously noted, the motivation for the development of MBRT lay in the desire to continue exploiting dose volume effects while overcoming the aforementioned technical difficulties linked with MRT [Dilmanian et al., 2006]. By using larger beams with a width between 300 μm and 1 mm, separated by ctc distances between 600 μm and several millimetres, PVDR values are only reduced by at most 10 % as a result of cardiosynchronous pulsations compared to a static case [Manchado de Sola et al., 2018]. The wider beam

spacing employed in MBRT compared to MRT also lifted the stringent requirements on x-ray energy. Given that the beams are not as closely packed, higher energy x-rays may be used, thereby further sparing the skin. A consequence of this higher energy with more separated beams is that the normal tissue PVDRs are not as susceptible to being reduced due to lateral scattering from the beamlet [Prezado et al., 2009]. Consequently, this paved the way for a move away from synchrotron generated minibeams [Dilmanian et al., 2006, Prezado et al., 2015] to its implementation at the more practical and cost-effective small animal irradiators [Prezado et al., 2017a, Bazyar et al., 2017]. Nevertheless, one of the limitations with the use of these kV x-rays is that one would be limited to the treatment of superficial tumors in a clinical setting. Consequently, there is an interest in combining MBRT with MV photons, or other charged particles.

With respect to MV photons, the work of Kundapur *et al.* used 1 mm thick 6 MV photon MBs for the irradiation of pet dogs with de-novo brain tumors [Kundapur et al., 2022]. Conventional broad beam (BB) irradiations were delivered in 3 fractions of 9 Gy, while the minibeam (MB) irradiations were given in single fractions of 26 Gy mean dose. Ultimately, the MB irradiation was observed to be superior to the BB irradiation and a complete pathological remission in 71% of the dogs treated with MBs was found. Furthermore, structural damage to the brain tissue was not observed in the beam path outside of the target region [Kundapur et al., 2022].

Prezado and Fois showed that combining protons with MBs could yield higher PVDRs compared to the use of photons, and at the time suggested that there could be a potential gain in healthy tissue sparing with the use of this technique [Prezado and Fois, 2013]. Furthermore, the use of protons at appropriate energies would allow the treatment of deep seated tumors, thereby overcoming the restriction of superficial treatments using kV x-rays. The dosimetric benefits of protons will be further discussed in section 2.9.4.

Beyond protons, there is also an interest in using other ion species to take advantage of their reduced lateral scattering, sharper Bragg peak, and increased RBE, among various other factors. To this end, first studies on ^{4}He ions [Schneider et al., 2021, Schneider et al., 2019] ^{12}C and ^{16}O ions [González et al., 2017, Martínez-Rovira et al., 2017a] and ^{20}Ne ions [Prezado et al., 2021]. The ability to make use of different particle beams highlights the flexibility of the technique.

Consequently, the remainder of this subsection is dedicated to further exploring the technical, physical, biological, and chemical factors associated with the implementation of MBRT. By detailing these different factors, I hope to further familiarise, and situate the reader within the current landscape of the field of MBRT, hopefully providing a clear vantage point of the way forward.

Minibeam generation

As depicted in Fig. 2.45, the three main methods of generating MBs are through mechanical collimation, dynamic collimation, or magnetic focusing. In the context of MBRT with photons, mechanical collimation is the only option, whereas charged particles benefit from having all three options available to them.

Mechanical collimation typically involves placing a physical block of some collimating material at the end of the beamline, as shown in panel A of Fig. 2.45. The very early studies of photon MBRT at synchrotron facilities made use of mechanical collimators positioned between the source and the animal to create interlaced MBs [Dilmanian et al., 2006, Deman et al., 2012]. These mechanical collimators represent the most straightforward and easy to implement method of MB generation, however they are inflexible and need

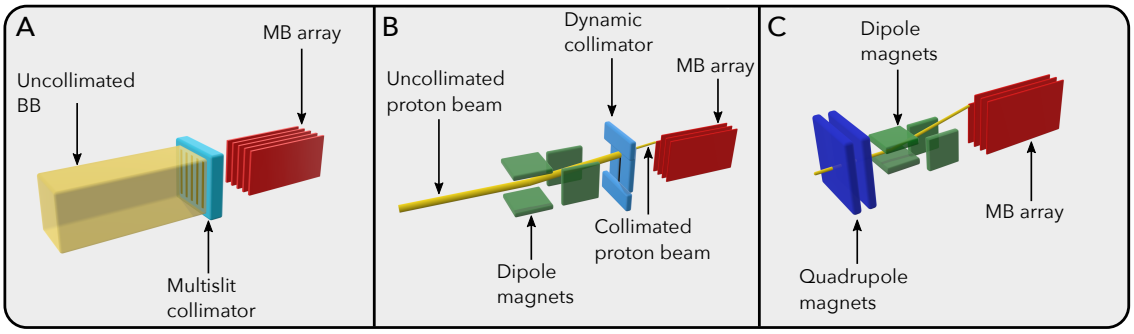

Figure 2.45: Schematic depiction of the three mechanisms for generating a MB array. Panel **A** depicts a multislit collimator performing mechanical collimation of a broad beam, while panels **B** and **C** are representative of the use of a dynamic scanning collimator and magnetic focusing respectively. Adapted from [Ortiz, 2022].

to be adapted to each treatment machine. In the work of Prezado *et al.*, in which a successful implementation of the technique at a small animal irradiator was carried out, divergent brass collimators were designed to compensate for the large divergence (20°) of the beam [Prezado et al., 2017a]. This collimator allowed the generation of MBs with similar dosimetric features (beam width and PVDR) to the collimated synchrotron beams. In a later study, different collimator geometries were investigated in the evaluation of x-ray MBs for the treatment of ocular tumors [Schneider et al., 2023]. The successful collimation of beams from a small animal irradiator was also shown by Bazyar *et al.*, however lead was used instead of brass [Bazyar et al., 2017].

The first implementation of proton minibeam radiation therapy (pMBRT) was performed with a mechanical collimator at the passive beamline of the Institut Curie Proton Therapy Centre (ICPO) in France [Peucelle et al., 2015b], and was also later implemented in conjunction with the same centre's pencil beam scanning (PBS) system [De Marzi et al., 2018a]. While various studies have investigated the optimal parameters for MB generation with collimators, the broad range of collimator parameters (ctc, slit width, collimator thickness) along with irradiation parameters (type of particle, beam divergence, dose rate) means that these types of studies are quite complex and depend heavily on factors such as the available facilities/equipment, the type of particles to be used, and the goal of ones study. In general, it could be said that the PVDR (and by consequence the normal tissue sparing effect) could be maximised by decreasing the slit width, increasing the ctc, ensuring that the collimator is sufficiently thick and that the air gap between the exit of the collimator and the target surface is limited [Lee et al., 2016, Guardiola et al., 2017, Tobola-Galus et al., 2018, Charyyev et al., 2020]. In view of limiting the activation of treatment equipment while maintaining the best dosimetric characteristics, brass collimators were found to offer the best compromise for the generation of proton MBs, and the biologically effective neutron dose within a patient being was found to be below 1% [Guardiola et al., 2017]. The use of physical collimators was found to increase the neutron dose equivalent ten-fold compared to when no collimator was used, however these dose equivalents are still low compared to conventional passively scattered BBs [Charyyev and Wang, 2020]. Currently, all experiments with protons and ions at clinically relevant energies have been done using planar beams [Meyer et al., 2019], which have various dosimetric benefits over pencil beams, as will be highlighted in section 2.9.4.

Without a mechanical collimator, it was deemed unlikely that PBS nozzles in their current state would be able to directly generate MBs [Schneider et al., 2020]. Consequently,

with the goal of foregoing rigid mechanical collimation blocks, thereby avoiding some of the aforementioned technical limitations, two novel MB generation methods were proposed, namely a dynamic scanning collimator (panel B of Fig. 2.45) [Sotiropoulos and Prezado, 2021] and a novel nozzle design to generate magnetically focused MBs (panel C of Fig. 2.45) [Schneider et al., 2020]. To date, only one research facility has implemented magnetically focused pMBRT [Girst et al., 2016], however the energy of the beam (20 MeV) is too low for most clinical applications. Nevertheless some theoretical studies have demonstrated methods of feasibility implementing magnetically focused pMBRT at clinically relevant energies [Schneider et al., 2020, Mayerhofer et al., 2021].

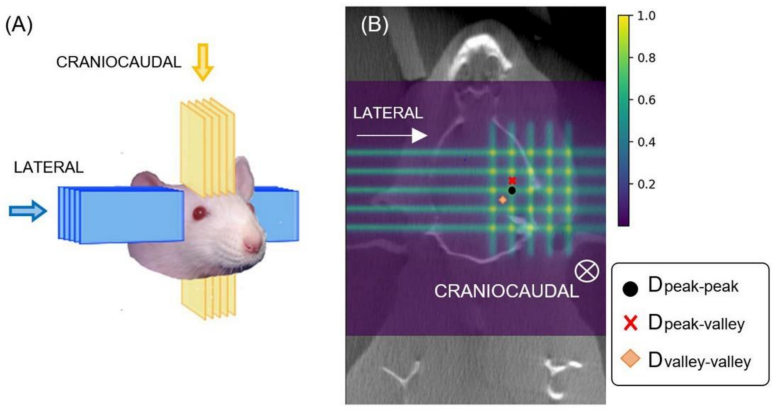

Figure 2.46: Schematic example of the crossfiring technique, where panel **A** depicts a crossfire irradiation geometry in pMBRT, while panel **B** depicts the resulting 2D dose map. Taken from [Bertho et al., 2021].

Similarly to the early studies of photon MBRT at synchrotron facilities [Dilmanian et al., 2006, Deman et al., 2012], proton MBs can also be delivered in an interlaced/crossfired geometry, as shown in Fig. 2.46. Given the mechanical tolerances required for interlacing microbeams, one of the initial interests was to use thicker beams which would be easier to accurately interlace from a mechanical point of view [Dilmanian et al., 2006]. Obtaining a homogeneous dose coverage within the tumor with x-rays requires these interlaced configurations [Dilmanian et al., 2006, Deman et al., 2012, Prezado et al., 2012], and while this homogenisation can be achieved without interlacing by using protons instead of x-rays [Prezado and Fois, 2013, Martínez-Rovira et al., 2015], various studies have demonstrated that tissue sparing can be further enhanced by crossfiring proton MBs [Bertho et al., 2021, Sammer et al., 2021] or interlacing carbon MBs [Dilmanian et al., 2012]. Furthermore, it has recently been demonstrated that generating MBs in an arc may also lead to a net reduction in the doses to normal tissues [Ortiz et al., 2021]. Ultimately the manner in which the MBs are generated, in addition to the type of particle and its energy, determines the way in which the dose is deposited. These dosimetric aspects are discussed in the following section.

Dosimetric considerations

The capability of pMBRT to deliver homogeneous doses to a target is shown in Fig. 2.47, which depicts MC calculated dose distributions for standard proton therapy compared to pMBRT for the treatment of meningioma [Lansonneur et al., 2020].

Panel B of Fig. 2.47 depicts the dose distribution resulting from the use of a 6 mm ctc, and panels C and D highlight that an even greater degree of tumor dose homogeneity

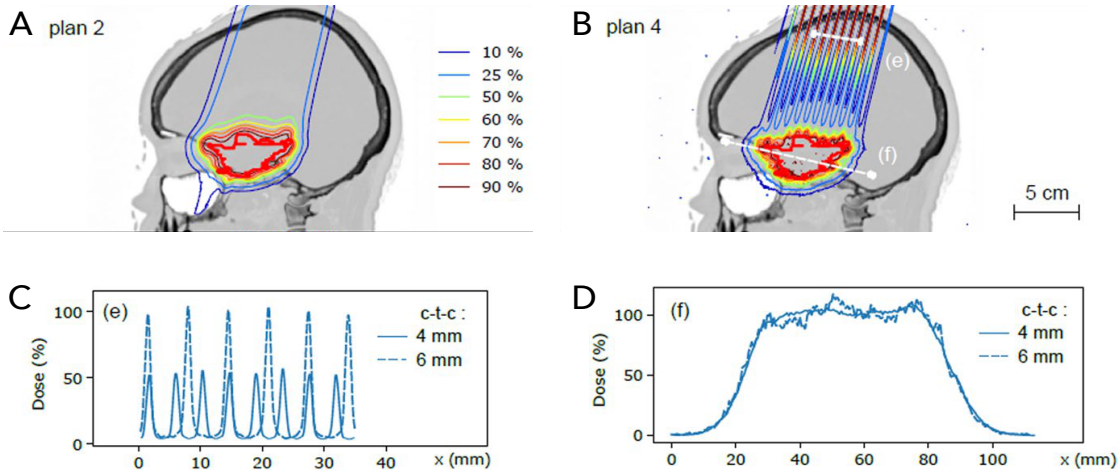

Figure 2.47: Dose distributions for standard BB proton therapy (panel **A**) and pMBRT (panel **B**) along with the lateral dose distributions in the entrance (panel **C**) and in the target (panel **D**). Adapted from [Lansonneur et al., 2020].

could be achieved by decreasing the ctc to 4 mm. However this comes at the cost of a reduced spatial fractionation in the normal tissues. It was found that standard proton therapy and pMBRT gave similar dose volume histograms for deep seated organs at risk such as the brain stem, while pMBRT benefited from lower average doses in shallower organs such as the eyes, highlighting the idea that equivalent, or even better treatment plans could be obtained with pMBRT for the treatment of brain tumors, owing to the fact that very little optimisation would be needed to achieve a homogeneous dose in the target, and normal tissues would be spared by the spatial fractionation [Lansonneur et al., 2020]. Furthermore, the microdosimetric MC study of Dos Santos *et al.* showed that pMBRT, in comparison to MBRT with electrons or photons, exhibited lower amounts of DNA strand breaks in the entrance region, while exhibiting a higher degree of complex DNA damages in the Bragg peak (tumor location). This highlighted the pMBRT shows great potential for both the sparing of healthy tissue, as well as tumor control [Dos Santos et al., 2020].

One facet of MBRT dose distributions that is not immediately obvious is the divergence in the behaviour of the dose/LET in depth along the peak and valley axes compared to conventional BB irradiations. This is partially visible in panel B of Fig. 2.47 in which there appears to be higher doses in the entrance, which decreases in depth, then increases again in the target. This effect is better visualised in Fig. 2.48.

Along the central beam axis (MB peak) there is a high entrance dose, which initially decreases before eventually increasing again near the Bragg peak. This behaviour in depth is not at all similar to what one would expect in the context of conventional proton BBs[25], in the sense that for the case of proton MBs there is a reduction in the Bragg-peak-to-entrance dose ratio (BEDR), which becomes more pronounced as the size of the MB decreases [Martínez-Rovira et al., 2015, Peucelle, 2016]. This effect is a direct by-product of the heterogeneity of the irradiation field. As the depth increases, protons are continuously scattered away from the central axis of the MB, leading to a reduction in the on-axis fluence, and a resulting drop off of the dose deposited. In the conventional BB case, this

[25] It should be noted that taking the integral dose of the entire MB array would lead to a PDD similar to that of conventional proton therapy.

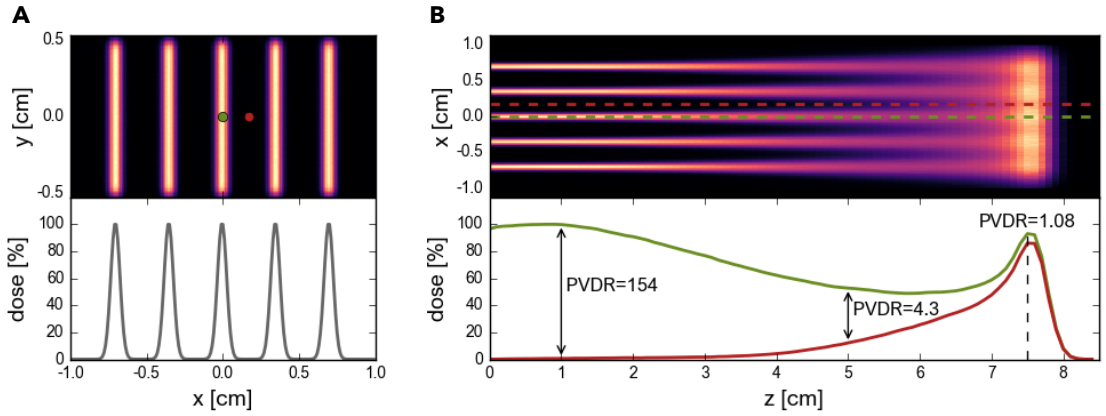

Figure 2.48: Lateral (panel **A** and PDD (panel **B**) distributions for 100 MeV planar proton MBs with a width of 0.7 mm and a ctc of 3.5 mm. Green and red dots indicate the lateral positions where the peak and valley profiles were sampled. Taken from [Schneider, 2020].

scattering away would be compensated by the *scattering in* of protons in what would be the valley region. Consequently, this also explains one of the dosimetric advantages of planar MBs over pencil shaped MBs. The longer dimension of the planar MB essentially acts as a broad beam, thereby compensating for the particles scattered away from the centre of the peak, leading to less degraded peak dose distributions and higher BEDRs compared to pencil shaped hexagonal/square MBs [Schneider, 2020]. It has been shown that at shallow depths, the valleys of proton MBs are filled with particles of a higher LET (approximately 20 - 30% higher) than what is present in the peaks [Lansonneur et al., 2020, Schneider et al., 2019]. This is attributed to the fact that the valleys are composed primarily of scattered and secondary particles which have a lower energy, and thus a higher LET as can be seen in Equation 2.4.

From a dosimetric point of view, it has been shown through MC simulations that light ions such as ^{4}He could be used in a similar vein as protons, taking advantage of the reduced lateral scattering in normal tissues and local dose deposition offered by the Bragg peak to spare proximal tissues [Dilmanian et al., 2015, Schneider et al., 2019], while yielding higher PVDRs and a more favourable BEDR [Schneider et al., 2021]. For the heavier ions such as ^{12}C, ^{16}O, and ^{20}Ne, several MC studies have highlighted the potential for a reduced NTCP due to the high degree of spatial fractionation incurred in the normal tissues [González et al., 2017, Martínez-Rovira et al., 2017a, Peucelle et al., 2015a, González and Prezado, 2018]. Although these results still need to be validated through biological experiments for the use of lighter ions such as ^{4}He, heavy ions such as neon have already been been used experimentally [Prezado et al., 2021].

Gonzalez *et al.* performed a preliminary MC investigation into the composition of the radiation field of carbon and oxygen MBs of varying ctc. They found that there were no significant physical differences between the two particles. In both cases, when a narrow ctc of 910 μm and 980 μm for oxygen and carbon respectively was used, a quasi-homogeneous dose distribution in the target was obtained, and the MB valleys were predominantly composed of scattered primary particles - thus implying a similar LET between peaks and valleys. When the ctc was increased to 3500 μm, extremely high PVDR values ($>$ 50) were obtained in the normal tissue, which is favourable for normal tissue sparing, and the dose distribution in the target remained heterogeneous. Interestingly, as shown in Fig. 2.49, nuclear fragments were the major contributors to the dose in the valleys,

and light nuclear fragments such as protons and neutrons dominated at shallow depths while heaver fragments were dominant in the valleys of the target depth. The authors hypothesised that this could be one of the contributing factors for tumor control despite the dose heterogeneity when using heavy ions [González et al., 2017].

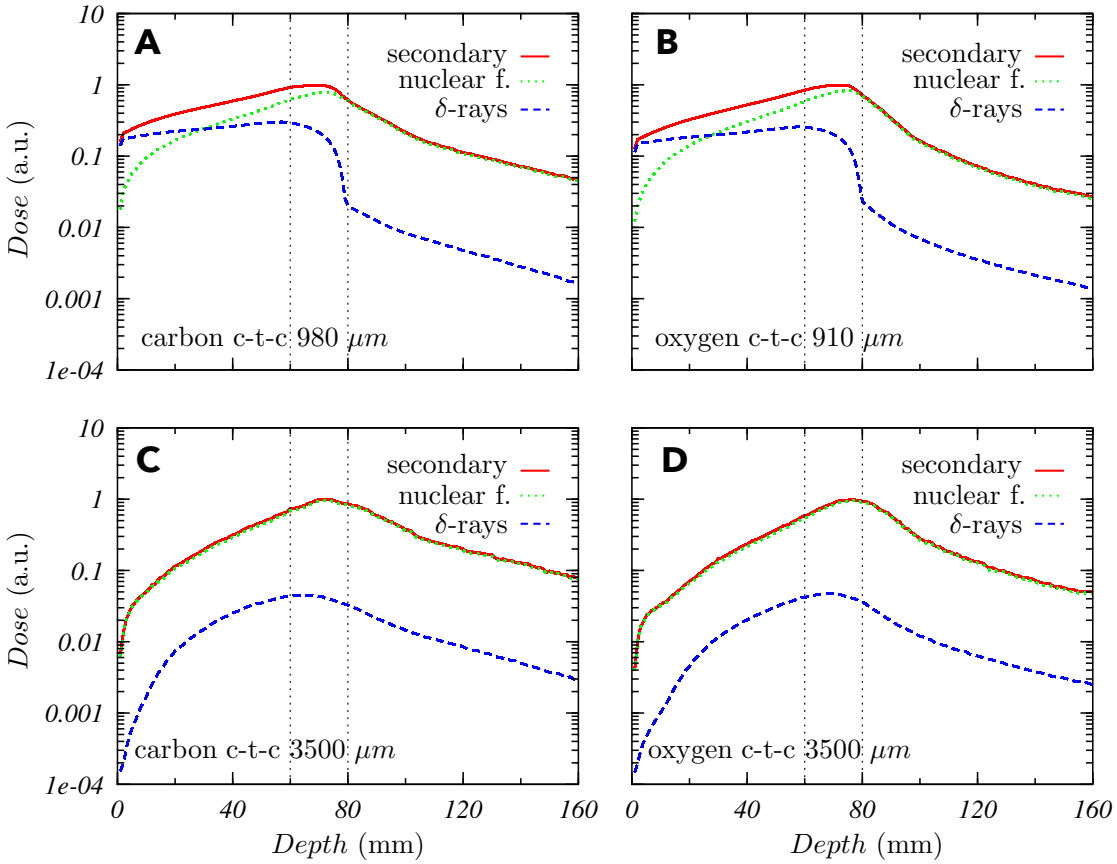

Figure 2.49: Contribution of different secondary particles to the dose deposited in the valleys for carbon MBRT (panels **A** and **C**) and oxygen MBRT (panels **B** and **D**). Taken from [González et al., 2017].

Experimentally measuring doses in MRT and MBRT is one of the major challenges given the spatial resolution requirements. Ionisation chambers, whose use represents the gold standard in RT, do not have the spatial resolution to resolve the peak and valley regions of SFRT beams [Meyer et al., 2019]. Consequently, in the context of MBRT relative dosimetry is often performed using radiochromic films, microdiamond detectors, or silicon diode detectors [Peucelle et al., 2015b, Guardiola et al., 2020, De Marzi et al., 2018b, Ortiz et al., 2022] according to an established two-step protocol [Prezado et al., 2011] in which absolute dosimetry is first carried out under BB conditions with the use of an ionisation chamber before performing relative dosimetry with the aforementioned detectors. Further technical challenges linked with the dosimetry of SFRT beams, such as the *quenching* effect in films in which there is an LET-dependant under-responsiveness, is explored in more detail in other review articles [Meyer et al., 2019, Bartzsch et al., 2020].

Biological evidence

There is a wealth of preclinical evidence for both the normal tissue sparing effects of MBRT, and the ability to achieve an equivalent or superior tumor control compared to conventional RT. A small selection of these studies is presented in the following subsections.

X-rays As previously stated, the early synchrotron work from Dilmanian *et al.* showed that the use of thicker beams could overcome some of the technical limitations of MRT. MBs with a width of 0.68 mm, and a ctc of 1.36 mm were interlaced and used to deliver a homogeneous dose to a cubic region of the brain. While focal damage was observed for doses between 120 - 150 Gy, normal brain tissues exhibited an increased tolerance to the dose compared to conventional RT and no apparent normal tissue damage was observed elsewhere [Dilmanian et al., 2006]. Despite the use of thicker beams than in MRT, high doses to critical structures such as the spinal cord were also well tolerated [Dilmanian et al., 2006]. While Deman *et al.* similarly investigated the normal tissue consequences of interlaced beams (600 μm width and 910 μm ctc) delivering a homogeneous dose (54 Gy) to a localised area of rat brains, they also irradiated the brains with a single array of 4 MBs covering an area of 4×4 mm^2 with a prescribed dose at 1 cm depth of 123 Gy [Deman et al., 2012]. In both cases the histological slices were perfectly normal [Deman et al., 2012]. In a later dose escalation study by Prezado *et al.*, whole brains were irradiated with single arrays (600 μm width and 1200 μm ctc) thus experiencing highly heterogeneous doses throughout. Peak doses greater than 200 Gy were not well tolerated and led to early deaths. Long term survival was observed for rats receiving 150 Gy, but significant brain damage was observed upon MRI and histopathological analyses. However peak doses up to 100 Gy were well tolerated and there were no significant deleterious effects [Prezado et al., 2015]. Furthermore, peak doses of 100 Gy are still above the doses needed to control aggressive tumor models, as shown by Sotiropolous *et al.* who achieved 60% long term survivals with 81 Gy peak dose. These works on synchrotron generated x-ray MBRT thus highlighted the normal tissue sparing capabilities of the technique despite the high peak doses, and demonstrated the feasibility of taking advantage of this normal tissue sparing in a variety of irradiation configurations.

As already highlighted, the move to thicker beams allowed the translation of the technology away from synchrotron facilities to the more practical and cost-effective small animal irradiators [Prezado et al., 2017a, Bazyar et al., 2017]. The proof of concept work of Prezado *et al.* demonstrated a successful implementation of x-ray MBRT at the Small Animal Radiation Research Platform (SARRP) [Xstrahl, 2023, Wong et al., 2008] in which standard BB RT was compared against MBRT through the irradiation of rat brains [Prezado et al., 2017a]. The same average dose (20 Gy) was delivered to the centre of the rat brains in both techniques (corresponding to a MBRT peak dose of 58 Gy at 1 cm depth in a water phantom), and while histopathological analysis revealed severe damage in the BB case, no substantial damage was observed for MBRT despite irradiation of the entire brain [Prezado et al., 2017a]. Similar conclusions were reached by Bazyar *et al.* who found that normal mouse skins well tolerated up to 150 Gy peak doses [Bazyar et al., 2017]. In contrast to the aforementioned studies which have all been with planar MBs, Sammer *et al.* showed that mouse ears well tolerated up to 60 Gy peak dose from pencil-shaped MBs generated at a SARRP as long as the beam sizes were kept below 3 mm, with the best results being for the smallest beam sizes of 0.5 and 1 mm, thus taking advantage of dose-volume effects [Sammer et al., 2019]. An in silico study of x-ray MBRT from a SARRP also found that in comparison to previous normal tissue sparing studies, similar

dose distributions in CT images of a human head could be obtained, thus highlighting the potential to benefit from this normal tissue sparing while treating ocular tumors [Schneider et al., 2023].

In terms of the tumor control characteristics of synchrotron x-ray MBRT, using the aforementioned interlaced MB configuration of the study of Deman *et al.*, F98 glioma bearing rats received a quasi-homogeneous dose of 54 Gy in the tumor, resulting in an ILS of 210% compared to the untreated rats, which is comparable with other RT techniques [Deman et al., 2012]. Another study corroborated this level of tumor control for 9L gliosarcoma bearing rats, in which interlaced MBs delivering a quasi-homogeneous dose of 70 Gy and 100 Gy to the tumor led to an ILS of 100% and 215% respectively [Prezado et al., 2012]. One of the first studies demonstrating the transfer of x-ray MBRT into small animal irradiators showed that the use of higher energy orthovoltage MBs could leverage the increased beam divergence to achieve a quasi-homogeneous dose distribution within deep-seated brain tumors [Prezado et al., 2017a]. In subsequent *in vitro* studies, it was shown that these SARRP x-ray MBs could induce a significant amount of clonogenic cell death in radioresistant F98 rat, and U87 human glioma cell lines [Guardiola et al., 2018]. Furthermore, clonogenic assays of two different irradiated murine cell lines (B16-F10 and TRP) highlighted the increased capability of MBRT to induce cell death over conventional BB irradiations [Bazyar et al., 2017]. From an *in vivo* point of view, it was shown that heterogeneously irradiated rats displayed an increased survival (60% long term survivals) compared to the controls [Sotiropoulos et al., 2021] - thus directly going against the dogmas from conventional RT that a homogeneous dose is necessary. The most recent study of tumor control from SARRP-generated x-ray MBs highlighted the participation of T-cells in the mechanism of tumor control after MBRT, suggesting a very effective anti-tumoral immune response [Bertho et al., 2022a]. These results will be further expanded upon in one of the following subsections looking at the *underlying radiobiological mechanisms*.

This wealth of biological evidence for the normal tissue sparing and tumor control capabilities of x-ray MBRT at both synchrotrons and small animal irradiators well situates the technique as an an effective alternative to conventional RT. As the dosimetric benefits of using protons has already been discussed, the following subsection puts forth the biological evidence for the efficacy of their use.

Protons Similarly to x-ray MBRT, there is a large amount of biological evidence for both the normal tissue sparing and tumor control capabilities of pMBRT. As previously discussed, one of the initially hypothesised advantages of the technique was the ability to retain dose heterogeneity in the normal tissue, while simultaneously depositing a quasi-homogeneous dose in the tumor [Prezado and Fois, 2013].

Starting with pMBRT irradiations of single fractions, using single arrays (uni-directional), various *in vivo* studies have demonstrated the gain in normal tissue sparing compared to conventional BB irradiations [Prezado et al., 2017b, Girst et al., 2016, Lamirault et al., 2020b, Prezado et al., 2018]. From the works of the NARA team of Prezado, a preferential normal tissue sparing effect of pMBRT (n=8)[26] over conventional proton BBs (n=8) was observed in Fischer 344 rat brains when exposed to whole brain irradiations of the same average dose (25 Gy) [Prezado et al., 2017b]. The use of a multislit collimator (henceforth referred to as the ICPO collimator) to generate 400 μm wide MBs separated by 3200 μm, resulted in no significant tissue damage despite the high peak doses (57 Gy) in the brain, while the BB irradiation resulted in extensive brain damage. This

[26] In this context, n denotes the total number of rats being irradiated in the associated configuration.

work highlighted the capability of pMBRT to offer a reduction of normal tissue toxicity while providing doses high enough to sterilize glioma [Prezado et al., 2017b]. A later study from our team was performed in which normal Fischer 344 rats were irradiated with the same ICPO collimator, delivering pMBRT with an average dose of 30 Gy (n=9). They remarked that no skin damage developed, and no tissue damage was observed in the MRI images of irradiated normal rat brains after 6 months [Prezado et al., 2018]. Furthermore, Lamirault *et al.* evaluated the effects of pMBRT on motor, emotional, and cognitive function and concluded that no significant impacts could be observed [Lamirault et al., 2020b].

Similar normal tissue sparing effects were observed in the study of Girst *et al.* from a German team. Mouse ears were irradiated with 20 MeV protons in either a BB, or MB configuration. It was shown that for the same average dose of 60 Gy, there was an approximately four fold increase in the size of the ears having received BB irradiations, and histological analysis revealed significant edema, erythema, and desquamation for the BB configuration which was not the case for pMBRT irradiation [Girst et al., 2016]. This study highlighted the idea that there was a reduction in adverse effects when using pMBRT over a conventional BB of protons. Compared to the aforementioned normal tissue sparing studies which were all *in vivo*, an *in vitro* study was performed by the same German-based team. This *in vitro* work of Zlobinskaya *et al.* showed that there was decreased inflammatory responses and genetic damage in a human skin model when using pMBRT compared to conventional BB irradiations [Zlobinskaya et al., 2013].

Moving now to the biological evidence of tumor control, the aforecited work of Prezado *et al.* also involved irradiations of RG2 glioma-bearing rats [Prezado et al., 2018]. The same irradiation conditions were used, leading to highly heterogeneous doses within the tumor. It was observed that there was significant tumor control and tumor eradication in 22% of the cases (n=9). The combination of enhanced normal tissue sparing and tumor control from this study gave further indications that pMBRT is able to widen the therapeutic index, and homogeneous doses within the tumor may not be strictly necessary to achieve tumor control [Prezado et al., 2018].

The tumor controlling capabilities of pMBRT have also been observed through the delivery of quasi-homogeneous (PVDR of 1.2) doses within the tumor. Using the ICPO collimator, Prezado *et al.* placed a build-up material before RG2 glioma-bearing rat brains in order to position the Bragg peak within the tumor - thus resulting in an irradiation producing a quasi-homogeneous dose distribution within the tumor. An average tumor dose of 25 Gy was prescribed, and pMBRT was compared to a conventional BB of protons. It was found that there were 67% long term survivals (n=9) in the pMBRT modality - a three-fold increase over the BB modality [Prezado et al., 2019]. Using the same irradiation setup, Lamirault *et al.* now irradiated F98 glioma-bearing rats instead. The resulting survival curve for the irradiation of the tumor with quasi-homogeneous doses is depicted by the red curve in panel A of Fig. 2.50. As can be seen, the use of pMBRT delivering quasi-homogeneous doses to the tumor led to a significant increase in the mean survival time over the controls, and long term survival in 11% of the cases (n=9). This lone surviving rat is in contrast to the 6 survivors (67%) of the previous study of Prezado *et al.* [Prezado et al., 2019]. This difference was attributed to F98 being more radioresistant, thus requiring higher doses, and perhaps also being less responsive to cell signalling effects than RG2 [Lamirault et al., 2020a].

As can be seen in the green curve in panel A of Fig. 2.50, Lamirault *et al.* also studied tumor control elicited by highly heterogeneous dose distributions. While there was a significant increase in the mean survival, being approximately equivalent to the

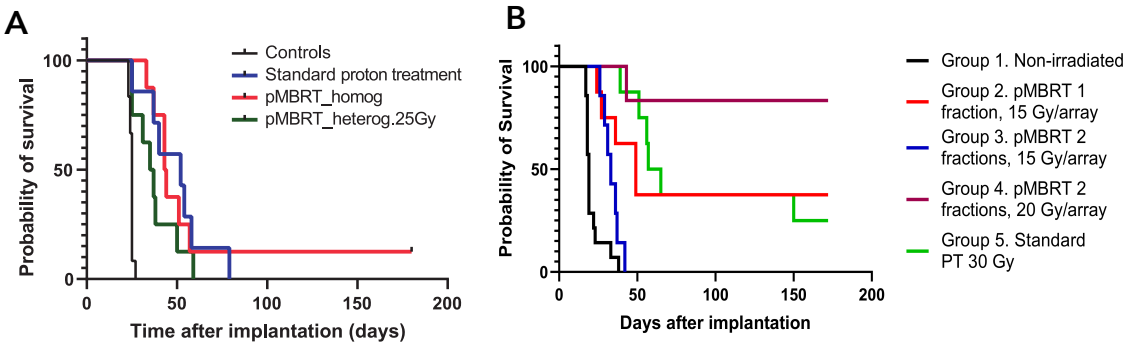

Figure 2.50: Panel **A** depicts survival curves comparing pMBRT delivering homogeneous/heterogeneous doses to the tumor, to standard BB proton therapy. The survival curves of panel **B** highlight the consequences of temporal fractionation as applied to crossfired pMBRT. Taken from [Lamirault et al., 2020a] and [Bertho et al., 2021] respectively.

conventional BB protons and quasi-homogeneous pMBRT cases, there were no long term survivals [Lamirault et al., 2020a]. This, once again is in contrast to the earlier work of Prezado *et al.* highly heterogeneous doses resulted in 2 (22%) long term survivors for RG2 glioma-bearing rats [Prezado et al., 2018], however it should be noted that not exactly the same configurations were used.

pMBRT is a particularly exciting RT modality as it been shown to diverge from, and in certain cases take advantage of the classical dogmas from conventional RT, namely homogeneous dose distribution and temporal fractionation. This was shown in the work by Bertho & Ortiz *et. al.* [Bertho et al., 2021] where tumor control was still ensured with heterogeneous doses within tumor, and in fact improved upon by temporally fractionating the treatment. This is highlighted in panel B of Fig. 2.50, which shows the main results of the work by Bertho & Ortiz *et. al.*. Through the use of a crossfire geometry, dose heterogeneity was maintained in the tumor, and by temporally fractionating treatments over 2 days, the original 67% long term survivors found in the work of Prezado *et al.* [Prezado et al., 2019] was now increased to 83% for RG2 glioma-bearing rats, the best results ever obtained [Bertho et al., 2021].

Ultimately, pMBRT has been shown to be effective at ensuring both normal tissue sparing and improved or equivalent tumor control over conventional BB irradiations with protons, particular for RG2 glioma-bearing rats. This effectiveness may be improved even further by ensuring dose heterogeneity within tumor, and spatially fractionating the pMBRT treatments [Bertho et al., 2021].

Light and heavy ions Compared to x-rays and protons, biological data to corroborate the potential dosimetric advantages highlighted by MC simulations and experimental dosimetry of light and heavy ions is still sparse, with only single studies on different ionic species having been performed [Prezado, 2022]. Eley *et al.* found that the use of ^{7}Li MBs, while substantially reducing the severity of physical damage to the skin, did not spare normal brain tissue, likely a result of the high ($\sim$ 63 Gy) peak doses used [Eley et al., 2021]. Given the increased RBE of lithium it is likely that the peak doses used were above the tolerance for minibeams [Prezado et al., 2015]. In the case of ^{12}C, only one biological experiment has been carried out by Dilmanian *et al.*, in which the damage to healthy tissue of a rat brain irradiated with 300 μm wide interleaved carbon beams was evaluated. Histological analysis revealed substantial focal damage while a sparing of the surrounding brain normal tissue was observed [Dilmanian et al., 2012]. For the heavier

^{20}Ne beams, Prezado *et al.* compared neon MBRT and neon BBs and observed significant tissue damage (necrosis) in the latter, while use of the former only resulted in dermatitis, indicating a clear normal tissue sparing effect associated with neon MBRT [Prezado et al., 2021]. These studies on ion-MBRT highlight the idea that, while promising in terms of its normal tissue sparing capabilities, further experiments need to be performed exploring their tumor control effectiveness [Prezado et al., 2021].

Despite the dosimetric and biological advantages associated with the use of the GRID, LRT, MRT, and MBRT, the exact underlying radiobiological mechanisms, and their relative contribution to the efficacy of SFRT treatments, is not fully understood. These mechanisms are discussed in the following subsection.

2.9.5 Underlying radiobiological mechanisms in SFRT

Despite the various advantages associated with the use of SFRT, the exact radiobiological mechanisms underpinning SFRT efficacy are still not fully understood. These mechanisms include, but may not necessarily be limited to [Prezado, 2022, Griffin et al., 2020, Bertho et al., 2022b]:

- Differential vascular effects.
- Cell signalling effects (bystander-like/cohort effects)
- Inflammation and immunomodulatory effects (mediating the abscopal effect)
- Stem cell proliferation and cell migration

At the heart of SFRT modalities are dose-volume effects, as described in section 2.4.3, in which the normal tissue tolerance to absorbed dose increases as the volume of the irradiation decreases [Zeman et al., 1961]. The main mechanism hypothesised to be responsible for this effect was the migration of stem cells in the unirradiated valleys to the peaks, thus aiding in the repairing of the damaged tissues along the irradiation path [Hopewell and Trott, 2000]. These effects are not fully exploited for GRID and LRT due to the large beam size, and are more relevant for MRT and MBRT. Differential vascular effects have been predominantly reported for MRT, and no robust evaluation of the effects of other SFRT modalities on vasculature has been performed [Prezado, 2022]. Non-targeted effects were introduced in section 2.4.7, however the current model for their role in SFRT is depicted in Fig. 2.51.

As described in section 2.4.7 and as depicted in Fig. 2.51, RIBEs are typically classified as occurring through cell-to-cell contact mediated by GJIC [Azzam et al., 2001] or through diffusible factors released into the medium by the irradiated cells [Mothersill and Seymour, 1997], thus allowing intercellular communication over longer distances. In the context of SFRT the term *bystander* is often used when in fact the response is better classified as a *cohort* effect[27] [Prezado, 2022]. Nevertheless, both bystander and cohort effects are local and occur in the primary tumor, while the abscopal effect, as shown in Fig. 2.51, is a distant effect, mediated by immune cells in the tumor microenvironment which have an immunomodulatory role. Evidence for the presence of these underlying radiobiological mechanisms in each SFRT technique is described in more detail in the following subsections.

[27] In an effort to remain consistent, any reference in this thesis to studies of non-targeted effects in SFRT will use the terminology of the respective study.

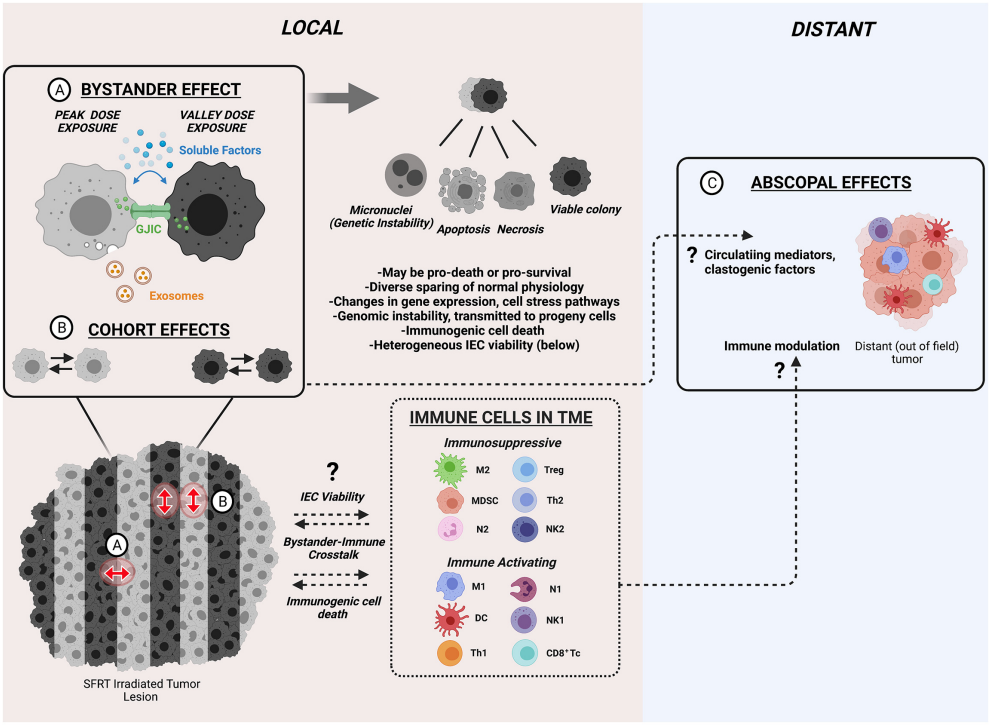

Figure 2.51: A model for local (bystander and cohort effects) and distant (abscopal effects) non-targeted effects in SFRT. Taken from [Johnsrud et al., 2023]

GRID

Starting with GRID therapy, bystander-like effects have been reported in the work of Asur *et al.* [Asur et al., 2012]. Cells were irradiated with a GRID pattern producing a 50:50 ratio of direct to bystander exposure where bystander cells were defined as receiving approximately 1 Gy scattered dose. It was observed that the survival of cells located in the GRID valleys was lower than what would be normally be expected of the scattered dose in those regions, suggesting the existence of cytotoxic bystander effects [Asur et al., 2012, Asur et al., 2015]. Earlier work by Suchowerska *et al.* showed that the non-uniformity of the radiation field affects the dose response *in vitro* only when cellular communication was not inhibited [Suchowerska et al., 2005]. In this work the authors irradiated cells contained within a single flask allowing inter-cellular communication, and cells contained within three separate flasks, where the physical barriers inhibited inter-cellular communication. In the single flask, an enhanced cell death was observed in the low dose regions, while the high dose regions exhibited reduced death compared to what would be expected of a uniform radiation of the same dose [Suchowerska et al., 2005]. This importance of intercellular communication was further highlighted by Asur *et al.* by an experiment they performed in which the medium of an irradiated culture was transferred to unirradiated cultures. These unirradiated cultures experienced significant cell killing when exposed to the irradiated medium, further suggesting bystander-like responses [Asur et al., 2012].

An exploration of these two strategies (medium transfer or cell-to-cell contact) in the context of GRID was also performed by Pakniyat *et al.* [Pakniyat et al., 2020]. One of the indications of a RIBE stress response is the formation of an elevated number of γH2Ax foci, indicating the presence of DSBs. The authors observed a 1.8 times increased frequency of γH2Ax in the cells experiencing cell-to-cell contact, thereby implying a greater bystander

effect in that configuration. They also observed that there was a greater reduction in cell survival of GRID bystander cells for a radioresistant cell line (HN5) compared to HeLa cells [Pakniyat et al., 2020]. While not explicitly correlated, these findings evoke similar ideas to that of the SBRT-PATHY (Stereotactic Body Radiation Therapy for PArtial Tumor irradiation of unresectable bulky tumors targeting exclusively their HYpoxic segment) technique, in which only the central hypoxic (and consequently most radioresistant) portion of the tumor was irradiated in order to induce non-targeted effects [Tubin et al., 2019].

The preclinical study of Johnsrud *et al.* also suggested the presence of abscopal effects in GRID RT [Johnsrud et al., 2020]. Tumors were implanted into the right and left flanks of mice, and while conventional BB irradiation of one of the tumors did not impact the growth of the unirradiated tumor, a 20 Gy peak dose GRID irradiation of one of the tumors led to an increased infiltration of immune cells into the unirradiated tumor, triggering an immune response which ultimately led to tumor growth delay [Johnsrud et al., 2020]. Furthermore, combined GRID and temporally fractioned RT for the treatment of patients with bulky tumors seemed to result in lower rates of metastasis than historical controls - implying a potential GRID abscopal effect [Edwards et al., 2015]. GRID therapy may allow for a more intact physiological response due to the retention of viable vasculature and immune cells within the low dose volumes [Griffin et al., 2020]. Contrastingly, it has been suggested that the high dose volumes induce vascular damages which reduce the blood supply to the tumor, contributing to the debulking of the tumor [Yan et al., 2020].

LRT

Similarly to GRID RT, bystander-like effects and abscopal effects in LRT have been reported in the work of Kanagavelu *et al.* [Kanagavelu et al., 2014]. Both the right and left flanks of mice were implanted with tumors, and irradiation of a single tumor with 20 Gy peak dose LRT occurred under the following configurations: (1) using a single LRT vertex covering 50% of the volume of one of the tumors, (2) using a single vertex covering 20% of the tumor volume, and (3) using two vertices of the same peak dose each covering 10% of the tumor volume. With respect to the irradiated tumor, it was observed that tumors receiving two vertices of LRT exhibited the most significant growth delay, potentially indicating the presence of intra-tumor bystander effects [Kanagavelu et al., 2014]. Concerning the unirradiated tumor, all configurations demonstrated distal effectiveness, with increased immune cell infiltration, however the single 50% vertex resulted in the maximum growth delay, thereby suggesting the presence of an abscopal effect [Kanagavelu et al., 2014]. As with GRID, this study on LRT highlighted the potentially immunomodulatory role for SFRT treatments.

These findings were further corroborated by the work of Jiang *et al.* who reported on a clinical case which demonstrated the likely synergies of LRT with immunotherapy. A patient with invasive lung adenocarcinoma was developing multiple metastases. Each of the developing metastases was treated with some form of RT with different doses and fractionation in combination with an immune checkpoint inhibitor (anti-PD-1), however only the metastasis treated with the combination of LRT and anti-PD-1 exhibited a complete local response without any side effects [Jiang et al., 2020]. It is thought that ICD occurring in the LRT vertices may provoke the release of antigens and inflammatory cytokines which could enhance the homing and activation of immune cells, by exploiting the preserved vasculature of the valleys [Iori et al., 2023].

MRT

In the context of MRT, one of the early hypotheses for the main contributors to the enhanced normal tissue sparing was the migration of stem cells in the valleys to repair the damaged tissues in the peak [Dilmanian et al., 2002]. Compared to the other SFRT modalities, a differential vascular effect was predominantly observed in MRT. Normal tissue sparing due to this differential vascular effect is thought to occur through the microbeams preferentially damaging the immature vasculature of the tumor compared to the mature vasculature of normal tissue which are promptly repaired [Dilmanian et al., 2005, Sabatasso et al., 2011, Bouchet et al., 2015]. The preferential damaging of tumor blood vessels may prevent the supply of oxygen, and it has been shown that MRT delivered in two orthogonal arrays (50 μm width and 200 μm ctc) of 400 Gy peak dose induces local hypoxia within the tumor [Bouchet et al., 2010, Bouchet et al., 2013a]. In the work of Griffin *et al.* single arrays (50 μm width/200 μm ctc and 500 μm width/2000 μm ctc) were used instead of two orthogonal arrays, with peak doses ranging between 75 Gy and 150 Gy. While tumor vascular damage was induced in all cases, for peak doses of 150 Gy in both irradiation geometries there was a reduction in tumor hypoxia [Griffin et al., 2012]. This contradicts the aforementioned studies suggesting an induction of local hypoxia. As stated by Bouchet *et al.*, these contradictory findings with respect to tumor oxygenation/hypoxia as a consequence of MRT vascular alterations, requires complementary studies, with different tumor models, in order to better comprehend the vascular responses to MRT [Bouchet et al., 2015]. This re-oxygenation may be one of the factors contributing to the potential of MRT to overcome tumor radioresistance [Trappetti et al., 2021].

Non-targeted effects have also been suggested to be involved in MRT and bystander-like effects have been observed to act in both a destructive [Lobachevsky et al., 2015, Lobachevsky et al., 2021] and protective [Smith et al., 2018] manner. There is also evidence that the RIBE in MRT, while mediated by both GJIC and secreted soluble factors, is particularly dependent on GJIC [Autsavapromporn et al., 2013, Autsavapromporn et al., 2022]. Interestingly, these results are similar to a previous work on GRID RT by Pakniyat *et al.*, who observed that there was an enhanced bystander effect when there was cell-to-cell contact [Pakniyat et al., 2020]. In the former work by Autsavapromporn *et al.*, cells were irradiated with microbeams of varying LET (x-rays up to argon ions) in the presence or absence of a GJIC inhibitor. While there was an increased bystander effect for the high LET microbeams in the absence of the inhibitor compared to in its presence, this difference was not observed for the x-ray microbeams - also thereby highlighting the importance of radiation quality in the RIBE [Autsavapromporn et al., 2013]. These results are in line with the work of Mothersill & Seymour, who demonstrated that cell-to-cell contact is not required for the induction of bystander responses after low LET irradiation [Mothersill and Seymour, 1997].

Finally, there are also studies implying both an abscopal effect [Fernandez-Palomo et al., 2013] and the activation of the immune system [Bouchet et al., 2013b, Bouchet et al., 2016, Potez et al., 2019, Bazyar et al., 2021] as important mechanisms behind MRT, highlighting the potential of the technique to treat metastases [Trappetti et al., 2021]. Bouchet *et al.* observed that there was a modulation of gene expression following MRT, with a predominance for genes expressed through immunological pathways [Bouchet et al., 2013b]. In a similar work was performed by Sprung *et al.*, it was shown that there was a differential gene expression between MRT and BB irradiations with a greater proportion of immunity related genes in the former [Sprung et al., 2012]. Nevertheless, gene expression analysis in isolation is insufficient to form concrete conclusions about the level of immune activation [Bertho et al., 2022b]. Potez *et al.* showed that there was a higher infiltration of

$CD4^+$ lymphocytes and natural killer cells in the tumor after irradiation with MRT over conventional BB irradiations, which was linked to the enhanced tumor grow delay of MRT [Potez et al., 2019]. Bazyar *et al.* also observed an enhanced infiltration of immune cells into the tumor [Bazyar et al., 2021]. While these studies investigated the level of infiltration of immune cells, the exact extent of their antitumor activity, as well as the origin of the infiltration is not fully known [Bertho et al., 2022b], however as stated by Johnsrud *et al.*: the quality of spatial fractionation "may create interspersed areas of intratumoral immune cell sparing and vascular access with the potential for better immune system activation" [Johnsrud et al., 2020].

MBRT

The impact of MBRT on tumor and normal tissue vasculature remains a largely unexplored area of research. Only a single study exists by Brönnimann *et al.*. In this work they amputated part of the fin of a zebrafish, which is known to have efficient regenerative properties, then irradiated the entire fin. They observed that MRT preferentially damaged the immature vasculature of the regenerated part of the fin, while the mature vasculature of the original part of the fin was unaffected. In contrast, MBRT displayed no such selective damaging based on vascular maturation [Brönnimann et al., 2016]. However, it should be noted that the MBRT peak doses employed in this study corresponded to the MRT domain, and thus were much higher than typically employed in preclinical studies [Prezado, 2022]. While not explicitly aimed at untangling a vascular effect, Price *et al.* showed that low peak dose (28 Gy) MBRT led to a 7.1-fold enhancement in the delivery of nanoparticle-based anti-cancer drugs to the tumor. A significantly reduced effect (only 2.7-fold enhancement) was observed when delivering a 7 Gy BB irradiation, and MBRT with peak and valley doses of 100 Gy and 7.5 Gy respectively (leading to the same PVDR as the 28 Gy irradiation) [Price et al., 2021]. Vascular alterations have been associated with changes to the degree of drug delivery [Price et al., 2021], and perhaps these results highlight the need for more moderate peak doses in order to observe a selective vascular damaging effect in MBRT. Nevertheless, more systematic studies still need to be performed.

While studies on the potentially immunomodulatory role of SFRT have been performed in GRID [Johnsrud et al., 2020], LRT [Kanagavelu et al., 2014], and MRT [Bouchet et al., 2013b, Potez et al., 2019], as described in the previous subsections, Bertho *et al.* investigated the potential role of the immune system in the context of MBRT in comparison to conventional BB irradiations. In this work, both immunocompetent (F344) and immunodeficient (nude) glioma bearing rats were irradiated with x-ray MBRT and x-ray BB with a prescribed mean dose of 30 Gy in both cases. Resulting survival curves are shown in Fig. 2.52.

The most interesting result is the lack of response of the nude rats to MBRT, compared to the 33% long term survivals of the F344 rats. Taken together with the response of nude rats to conventional BB radiation, these results suggest a fundamentally distinct T-cell dependant mechanism underpinning the anti-tumor immune effects of MBRT. Through immunohistochemical analysis, it was shown that MBRT provoked a faster and more efficient infiltration of T-cells into the tumor [Bertho et al., 2022a]. Furthermore, Bertho *et al.* showed that MBRT induces long term anti-tumor immunity. The rats which demonstrated a complete response to the treatment (n=4 in MBRT and n=4 in conventional BBs) were re-injected with RG2 tumor cells 3-6 months post-irradiation, and while the controls developed tumors, none of the re-injected originally irradiated rats developed any tumors. [Bertho et al., 2022a].

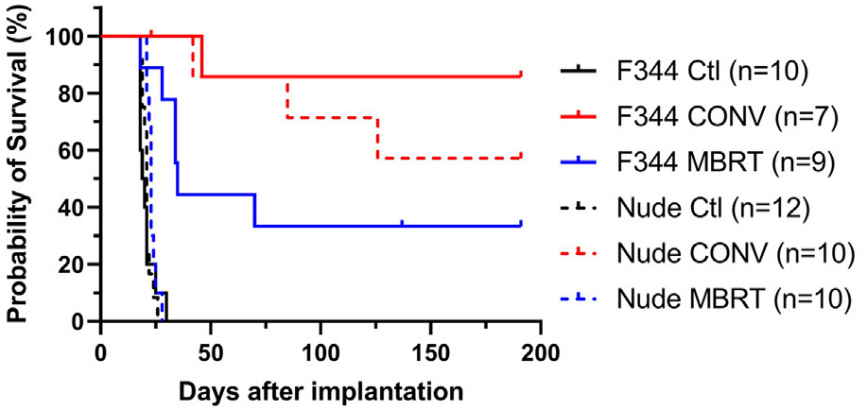

Figure 2.52: Survival curves comparing the irradiation of immunocompetent (F344) and immunodeficient (nude) rats with conventional BB x-rays and x-ray MBRT. Taken from [Bertho et al., 2022a].

In addition to these aforementioned underlying mechanisms, ROS produced through water radiolysis may have a role to play. These ideas are explored in the following subsection.

2.9.6 The role of ROS in SFRT

As highlighted in section 2.4.2, ROS have an important role to play in the biological response to IR. However, these biological responses were given in the context of conventional BB irradiations. While these *traditional* ideas are likely still relevant to SFRT, there is as of yet very little knowledge about the role that ROS play in the underlying radiobiological mechanisms discussed in the previous subsection. Even in the most recently published textbook about SFRT [Zhang and Mayr, 2023], ROS are only briefly discussed in their relation to the FLASH dose rates of MRT, in which a rapid local oxygen consumption has been thought to play a role in the underlying mechanisms [Djonov et al., 2023]. In fact to date, to the best my knowledge there are only three studies explicitly evaluating the production and distribution of ROS in MBRT [Dal Bello et al., 2020, Zhang et al., 2023, Masilela and Prezado, 2023]. The work of Dal Bello *et al.* hypothesised a potential homogeneous coverage of the tumor by H_2O_2 during beam-on time, which could be used as a chemical marker of MB efficacy [Dal Bello et al., 2020]. The second publication from the same team by Zhang *et al.* improved upon the diffusion model of the first paper by including a scavenging capacity [Zhang et al., 2023]. Nevertheless these studies have some limitations owing to the fact that a homogeneous media was assumed, as opposed to the complex, and heterogeneous biological microenvironment, and chemical reactions of the homogeneous chemical stage of water radiolysis were not considered. At this point in time, these kinds of all-in-one investigations of the physical interactions producing ROS, all the way through to the homogeneous chemistry which takes place at timescales relevant to biological processes is not possible. However, advances are steadily being made in this direction [D-Kondo et al., 2023]. The only other published work looking at the production of ROS is from Masilela & Prezado, which is one of the publications resulting from this thesis and will be expanded upon in chapter 6.

In the context of the underlying radiobiological mechanisms involved in SFRT, there is a wealth of evidence that both extracellular and intracellular ROS contribute to bystander

effects through redox-sensitive cell signaling cascades [Azzam et al., 2002]. In this work by Azzam *et al.* cell cultures were partially irradiated by a beam of α-particles, and it was shown that there were a greater number of cells than those traversed by the particle beam which responded to the radiation. This greater response was evaluated through the lens of $p21^{Waf1}$ which is a type of protein. In response to DNA damage, the signaling protein p53 upregulates $p21^{Waf1}$ which itself can suppress tumor colony growth through cell cycle arrest [El-Deiry, 2016]. Azzam *et al.* showed that there was an upregulation of $p21^{Waf1}$ in bystander cells, and said upregulation was inhibited with the addition of SOD and catalase. As noted in section 2.4.2, SOD is a scavenger of $O_2^{\bullet -}$, producing H_2O_2, and catalase is a scavenger of H_2O_2, producing water and molecular oxygen. The inhibition of $p21^{Waf1}$ upregulation through the addition of SOD and catalase led to the hypothesis proposed by Azzam *et al.* that $O_2^{\bullet -}$ and H_2O_2 are important mediators of the bystander response [Azzam et al., 2002].

Alexandre *et al.* specifically singled out H_2O_2 as being primarily responsible for the bystander effect [Alexandre et al., 2007]. In their work, cancer cells treated with paclitaxel, a type of chemotherapy drug, generated a large amounts of extracellular ROS which caused lethal damage to bystander cells not exposed to the drug. Through the addition of SOD it was observed that this bystander response was enhanced, and the scavenging of H_2O_2 through the addition of catalase led to an abolishment of these bystander responses [Alexandre et al., 2007].

Bystander effects can be bidirectional, i.e. non-irradiated cells not only respond to signals emitted by irradiated cells, but can also themselves send signals to the irradiated cells. Such bidirectional bystander effects can modulate the response to radiation, and have been observed to produce a *rescue*, or protective effect - mitigating the damage in directly irradiated cells [Widel et al., 2012, Chen et al., 2011]. This radioprotective effect has been observed in response to MRT with both x-rays [Smith et al., 2018] and protons [Desai et al., 2014], and there are a few studies identifying ROS as being involved in the underlying mechanisms of this inverse bystander effect [Widel et al., 2012, Lam et al., 2015]. In the work of Widel *et al.*, irradiated tumor cells (Me45) were co-cultured with either non-irradiated normal cells (NHDF), non-irradiated Me45, or incubated alone, and the results are depicted in Fig. 2.53.

Using the presence of micronuclei[28] and apoptotic cells as endpoints, it was observed that there was a greater than 50% decrease in the presence of micronuclei, and a slightly lower decrease in the presence of apoptotic cells when Me45 was co-cultured with NHDF - indicating the presence of a protective bystander effect [Widel et al., 2012]. This protective effect was linked to the level of ROS. It was shown that irradiated Me45 cells incubated alone displayed a systematic increase in the level of intracellular ROS (as is to be expected after receiving a dose of IR), however this increase was significantly lower when Me45 was co-cultured with non-irradiated NHDF [Widel et al., 2012]. Lam *et al.* proposed the activation of nuclear factor κB (NF-κB)[29] as being the mechanism responsible for this protective effect given previous studies highlighting its role in modulating the intracellular ROS levels of irradiated cells [Lam et al., 2015, Morgan and Liu, 2011].

As previously noted, the RIBEs are typically classified as occurring through cell-to-cell contact mediated by GJIC [Azzam et al., 2001] or through soluble factors such as ROS

[28] Micronuclei are typically formed following genotoxic stress induced by DNA damage [Krupina et al., 2021].

[29] NF-κB proteins are a type of transcription factor that, in addition to regulating the amount of ROS in the cell, are of critical importance in inflammation and immunity [Morgan and Liu, 2011].

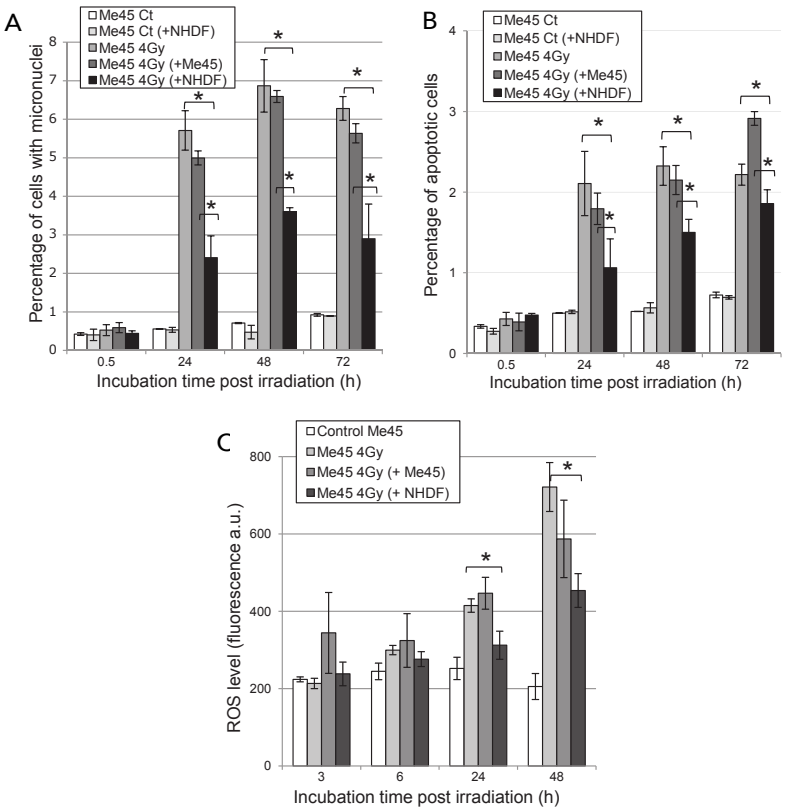

Figure 2.53: The role for ROS in the inverse bystander effect. Panels **A** and **B** depict the decrease in micronuclei and apoptotic cells for irradiated tumor Me45 tumor cells co-cultured with normal NHDF cells, while panel **C** depicts the associated drop in intracellular ROS. Adapted from [Widel et al., 2012].

released into the medium by the irradiated cells [Mothersill and Seymour, 1997]. However in recent years, there is also increasing evidence that the secretion of EVs, specifically exosomes, play an important role in RT [Doyle and Wang, 2019]. In addition to GJIC and soluble factors, exosomes in particular are now thought to be one of the mediators of not only the RIBE, but also involved in mechanisms of radioresistance [Du et al., 2020, Elbakrawy et al., 2020, Smolarz et al., 2022, Yang et al., 2022b]. With regards to cell migration, the review article of Sung *et al.* discussed the general mechanisms of this process, and how the biogenesis, and functions of EVs lend themselves to being important mediators of cell migration [Sung et al., 2021a]. As of this date, the role of exosomes in SFRT remains an unexplored avenue of research, however given the recent knowledge of their influence on RIBEs, it can be expected that some publications on the topic will come out in the years to follow. Interestingly, there are also recent studies looking into the link between exosomes and ROS [Bodega et al., 2019, Nakaoka et al., 2021, Miller et al., 2022], with the work of Nakaoka *et al.* being one of the first to demonstrate that irradiated exosomes have a radiosensitizing effect on neighbouring cancer cells by increasing the level of intracellular ROS [Nakaoka et al., 2021].

And finally, ROS have been shown to play a regulatory role in vascular development and angiogenesis [Zhou et al., 2013], and there is also evidence that ROS have important functions to play in both innate and adaptive immunity, as highlighted in the review paper by Yang *et al.* [Yang et al., 2013]. It has been shown that the anti-tumor immune response triggered by immunogenic cell death is weakened for elevated levels of H_2O_2

due to the oxidation of HMGB1, an important mediator of inflammation and immunity, thereby neutralizing its biologic activity [Lennicke et al., 2015, Deng et al., 2020]. It has also been shown that decreasing the levels of extracellular ROS increased the infiltration of T lymphocytes, which play an essential role in the immune system [Deng et al., 2020]. This highlights the idea that ROS modulation is important in prolonging the survival of T cells [Chen et al., 2016].

Therefore, given the importance of ROS to both conventional RT, and them being potentially involved in the underlying radiobiological mechanisms of SFRT, as discussed above, one of the central works of this thesis was an investigation into the relative production of ROS between MBRT peaks and valleys.

Chapter 3

Materials and methods

This chapter details the materials and methods used in this PhD thesis. The MC methods of Geant4, GATE, TOPAS, and TOPAS-nBio are introduced in section 3.1, and details about the high performance computing clusters used are provided in section 3.2.

3.1 Monte Carlo methods, a general introduction

The aptly named computational techniques known as *Monte Carlo* (MC) methods come from the casino of the same name in Monaco, given the inherently *random* nature of the different quantities used by this method. While there is no clear-cut consensus on how these methods should be defined, they can be thought of as a broad range of computational techniques whereby the random sampling of a series of probability density functions is used to estimate a numerical quantity [Harrison, 2010]. Given the stochasticity of radiation's interaction with matter, these MC methods have long been used to solve problems in radiation transport. In the present day, they are widely accepted as one of the most powerful modelling tools for RT applications [Verhaegen and Seuntjens, 2003].

In the context of radiation transport simulations, an initial *primary* particle is created with a specific position, trajectory, and energy, according to user-defined distributions. The total collection of these primaries are then representative of your incident ionising radiation. The primary particle is then transported within the material through a series of simulation *steps*. The distance of travel, type of physical interaction (if any), resulting secondary products, and loss of energy of the initial primary particle are then calculated according underlying physical laws, often incorporated into the simulation through probability density functions [Schneider, 2020]. Ultimately, by simulating a large number of primary particles, the value of a specific stochastic quantity (i.e. the dose) can be approximated, and the precision of this approximation increases as the number of simulated particles increases. The various MC codes can be further split into those employing condensed history (CH) models or track structure (TS) models, as depicted in Fig. 3.1.

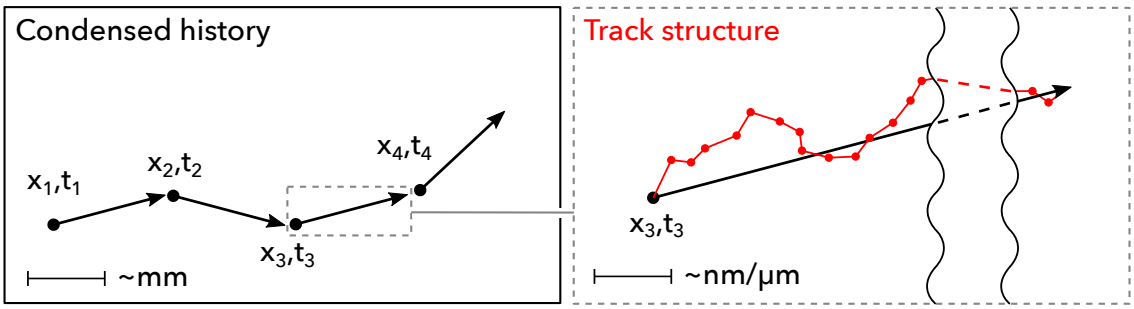

Figure 3.1: Comparison of a particle track with positions `x` and trajectories `t`, using CH models (left) and TS models (right).

CH models approximate the cumulative effect of a large number of interactions during a simulation step, therefore making them more computationally efficient, while still

providing a high degree of accuracy with respect to the macroscopic scales relevant to dose-calculations in a clinical setting [Kyriakou et al., 2019]. In these types of models, the position and trajectory (x_i and t_i in Fig. 3.1) at each simulation step is known, however there is no detailed information about the specific path the particle took between steps. Examples of these CH-based codes are PENELOPE [Baró et al., 1995], FLUKA [Ferrari et al., 2005], and Geant4 [Agostinelli et al., 2003, Allison et al., 2006, Allison et al., 2016]. On the other hand, TS codes consider all interaction events along the simulation step, as shown by the red line in Fig. 3.1. Consequently, these types of models are more accurate for micro/nanoscale applications such as calculating the level of DNA damage, however they come at the cost of being more computationally expensive [Kyriakou et al., 2019]. These TS codes can be further split into 3D codes, which are capable of simulating the distribution of physical events (ionisation, excitations, scatterings) in space, while 4D codes are capable of generating chemical species from the physical events, and simulating their distribution within the medium in time [Nikjoo et al., 2006]. Some examples of TS MC codes are PARTRAC [Dingfelder et al., 2008], RITRACKS [Plante and Cucinotta, 2009], and Geant4-DNA [Incerti et al., 2010].

In the context of this thesis, the MC codes GATE and TOPAS (derivatives of Geant4), as well as TOPAS-nBio (a derivative of Geant4-DNA) were used, as will be discussed in the following subsections.

3.1.1 Geant4

Geant4 is known as an open source *toolkit*, in which the user designs an application using C++ code. It is one of the most popular MC codes currently available, and is known as a *general purpose* MC code given its wide use in fields such as medical physics, space applications, microdosimetry, radiation protection, or high energy physics. It is the code of choice for institutions such as the LHC, ESA, and NASA [Allison et al., 2016]. A Geant4 simulation can be thought of as a C++ program which calls various sets of functions from predefined Geant4 classes.

The simplest Geant4 simulation consists of a geometry containing what's known as a *sensitive volume*, a particle source, and a *physics list* which details all the relevant physics processes to be used in the simulation. The NIST database for elements and compounds[30] is imported inside of Geant4, allowing the user to specify the exact composition of a material. For example, `G4_C` refers to elemental carbon, and `G4_WATER` refers to water with the appropriate elemental composition already defined. These materials can then be assigned to a specific geometry, which itself is designed using Geant4 *Solids*. For example, `G4_Box` can be used, which, as the name suggests, allows the user to create a 3D box by supplying a name for the geometry, and its `x`, `y`, and `z` half lengths. An extensive library of solids is already provided, however the user has the option to create their own solid class if necessary. The user then chooses the geometrical component within which to accumulate and track the quantity of interest, and assigns that component to be the sensitive volume [Geant4 Collaboration, 2023].

Geant4 provides the user with different ways of generating primary particles. One of those ways is through the `G4ParticleGun` class, which is more often than not the most suitable particle generator regardless of application. This class generates primary particles with a given trajectory and position and, as stated previously, various random distributions

[30] https://geant4-userdoc.web.cern.ch/UsersGuides/ForApplicationDeveloper/html/Appendix/materialNames.html

can be assigned from which these properties are sampled. The approach used by Geant4 to include physics processes is through the specification of a physics list which is organised into different modules, each describing various processes, i.e. electronic, hadronic, or decay processes [Geant4 Collaboration, 2023, Allison et al., 2016]. These lists then refer the simulation to quantities such as the cross-sections, stopping powers, or final states. These quantities are computed according to: (1) *parametrizations*, which are essentially heuristic formulae established on some measurements. This approach is gradually being deprecated in the newer releases of Geant4. (2) Databases, which contain large data sets of direct experimental measurements. And (3), theory driven models which are based either partly or fully on theoretical considerations/calculations. A *packaged* physics list, compiled by physicists of the Geant4 collaboration, will then have a mix of these different approaches for computing the required quantity in view of achieving the "best" or most accurate combination. [Verderi, 2023]. For example, `QGSP_BERT_EMZ` describes a physics list in which the hadronic options are specified by `QGSP` (Quark Gluon String model with the Precompound model used for nuclear de-excitation) for energies greater than 12 GeV, and `BERT` (Bertini-style Cascade) for energies below 10 GeV with the transitioning between the two being handled by the `FTF` (Fritiof) model. `EMZ` designates the electromagnetic physics options - in this case *emstandard_ opt4* [Geant4 Collaboration, 2021].

Several validation studies (a non-exhaustive list is provided here) have been performed looking at the validity of the use of Geant4 in the context of medical physics applications [Arce et al., 2021] with photons [Thiam et al., 2008], protons [Zacharatou Jarlskog and Paganetti, 2008, Grevillot et al., 2010], and heavy ions [Bolst et al., 2017]. While not directly used, Geant4 acts as the core of all other simulation codes utilised in this thesis. In other words, almost all geometries, scorers, physics processes, and chemical processes specified in the following subsections are based on/have their equivalent in Geant4.

3.1.2 GATE

GATE (Geant4 Application for Emission Tomography) is an open-source software developed by the OpenGATE collaboration, and has primarily been applied in medical imaging and RT applications [Jan et al., 2011, Sarrut et al., 2014]. Whereas a pure Geant4 simulations is coded completely in C++, GATE acts as an extension of Geant4, enabling the user to access all the functionality of Geant4 without having to code in C++.

A GATE simulation is defined through a collection of macro files - which are simply ASCII files with the .mac extension. Each line of the macro file contains commands with a specific GATE syntax. The typical convention is that a single simulation is composed of individual macro files for the geometry, physics, visualisation, source, etc. Implementing the previously mentioned `G4_WATER` first requires importing a material database:

```
/gate/geometry/setMaterialDatabase MyMaterialDatabase.db
```

Then the name, half lengths, and material of a Geant4 `G4_Box`, inserted into the virtual *World*, can be specified as follows:

```
/gate/world/daughters/name Phantom
/gate/world/daughters/insert box
/gate/Phantom/setMaterial Water
/gate/Phantom/geometry/setXLength 20.  cm
/gate/Phantom/geometry/setYLength 10.  cm
/gate/Phantom/geometry/setZLength 5.  cm
```

Using a similar syntax, a physics list can be specified, the source of primary particles defined, and *actors* can be attached to a volume, thereby allowing the user to track and collect various information such as the dose, or LET [OpenGATE Collaboration, 2023]. Although the various validation studies of Geant4 are mostly applicable to GATE given that it is built on Geant4, separate validation studies have been carried out specifically for GATE, looking at both medical imaging [Schmidtlein et al., 2006, Assié et al., 2005], and RT [Thiam et al., 2008, Padilla-Cabal et al., 2020] applications.

3.1.3 TOPAS

Similarly to GATE, TOPAS [Perl et al., 2012, Faddegon et al., 2020] acts as a wrapper of Geant4, enabling full use of its functionality. However in contrast to the use of macro files, TOPAS uses a unique parameter control system consisting of user generated .txt files containing TOPAS commands with a specific TOPAS syntax. This parameter control system streamlines the capabilities of Geant4 by allowing users to develop their own applications without needing to write their own C++ code, thereby facilitating its accessibility, and transporting its applications beyond high energy physics to domains such as medical applications. The architecture of a TOPAS simulation is depicted in Fig. 3.2.

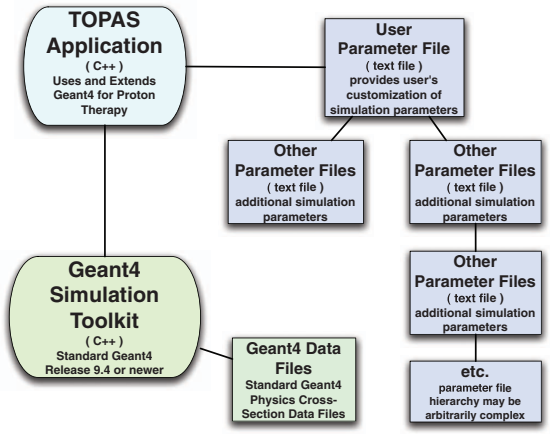

Figure 3.2: Typical framework for the creation of a TOPAS simulation using user generated .txt parameter files, which then calls the underlying Geant4 data files. Taken from [Perl et al., 2012]

Each line of the parameter file is structured as follows: `Parameter_Type: Parameter_Name = Parameter_Value`. The parameter type designates the data type of the parameter value (i.e. "`s`" for string, or "`i`" for integer), and the parameter name consists of a predefined set of prefixes, each describing a part of the code (i.e. "`Ge/`" for geometries, or "`Ph/`" for physics) [Perl et al., 2012]. The TOPAS corollary code for the creation of a box of water, as was previously shown for GATE, consists of the following:

```
s:Ge/Phantom/Parent = "World"
s:Ge/Phantom/Type = "TsBox"
s:Ge/Phantom/Material = "G4_WATER"
d:Ge/Phantom/HLX = 20.  cm
d:Ge/Phantom/HLY = 10.  cm
d:Ge/Phantom/HLZ = 5.  cm
```

In the above example `TsBox` is the TOPAS equivalent to Geant4's `G4_Box`, and the material can be directly defined from the same NIST database for elements and compounds

as used by Geant4. One can also import complex geometries in the form of CAD (computer aided design) files into TOPAS [Faddegon et al., 2020]. As opposed to the actors of GATE, or the sensitive volumes of Geant4, TOPAS makes use of *scorers* to track and accumulate the quantity of interest. The TOPAS geometries, scorers, and particle sources are all implementable using the same TOPAS specific syntax, with further details available in the TOPAS documentation [TOPAS MC Inc, 2023]. There are two types of physics lists in TOPAS: reference physics lists, which are the pre-made Geant4 physics lists such as the aforementioned `QGSP_BERT_EMZ`, or modular physics lists, in which the user can create create a completely customizable list of physics processes by including specific TOPAS modules [TOPAS MC Inc, 2023]. The latter takes the following form, in which the name of each TOPAS module has its equivalent in Geant4, i.e. `g4em-standard_opt4` in TOPAS is equivalent to `G4EMStandardPhysics_option4` in Geant4:

```
sv:Ph/Default/Modules = 2 "g4em-standard_opt4" "g4h-phy_QGSP_BIC"
```

TOPAS was initially developed for use in proton therapy, and as such it was originally validated against proton therapy measurements from the MGH (Massachusetts General Hospital) beamline [Testa et al., 2013]. Since then, there have been various other TOPAS validation studies [Shin et al., 2017, Huang et al., 2018, Liu et al., 2019], and the TOPAS collaboration plays an active role in the benchmarking of Geant4 [Faddegon et al., 2020].

3.1.4 TOPAS-nBio

In contrast to the purely physical simulations which have been described up until this point, the changes in the electronic properties of the target atom/molecule from incident IR also leads to a cascade of chemical reactions, as was highlighted in section 2.3. The indirect DNA damage induced by the resulting chemical species, together with the direct portion of DNA damage, is known to significantly contribute to cell death [Hirayama et al., 2009]. In view of grasping the full picture of the relation of micro/nanodosimetric quantities to macroscopic biologic observables, it is important to consider that one part of the picture is how the *static* physical interactions impact the biological response, while the other part of the picture is the complex, and transient chemical kinetics that takes place immediately after the physical event, during water radiolysis, which depends not only on the microenvironment, but also on the quality and type of the radiation [Karamitros et al., 2014].

While there exists various softwares capable of specifically simulating this chemical kinetics such as Smoldyn [Andrews and Bray, 2004], or VCell [Moraru et al., 2008], there are only a limited number of codes which attempt to consolidate the physical, chemical, and biological consequences of IR into a single simulation platform. The most prominent codes in this space are RADAMOL [Štepán and Davídková, 2008], PARTRAC [Friedland et al., 2011, Kreipl et al., 2009b, Kreipl et al., 2009a], and Geant4-DNA [Incerti et al., 2010]. These codes aim to unify the study of the radiobiological effects of IR by: taking into account the physical interactions at the micro- and nano-scales using TS physics, considering the aforementioned complex chemical kinetics associated with the generation, reactions, and diffusion of chemical species, and evaluating the resulting consequences on biological targets [Karamitros et al., 2014]. Geant4-DNA represents the microdosimetric extension of Geant4, and similarly to how TOPAS wraps and extends Geant4, TOPAS-nBio [Schuemann et al., 2018a] is the radiobiological extension of TOPAS which wraps and extends Geant4-DNA. The majority of the work in this thesis was performed using TOPAS-nBio version 1.0. While there are no syntactical differences between TOPAS and

TOPAS-nBio, there are some extra capabilities which are summarised below [Schuemann et al., 2018a]:

- Physical interactions are simulated using TS physics.
- The diffusion and reaction of chemical species in the chemical stage of water radiolysis is simulated by assuming Smoluchowski boundary conditions, which will be briefly described below.
- New specialised cell-specific geometries were added, including, but not limited to: different DNA models, mitochondria, lipids, or various nuclei models.
- Scorers can be used to collect information about the chemical track, such as the number and location of chemical species at a user-defined time cut, the level of DNA damage, or G-value scorers.
- And finally, users are able to interface TOPAS-nBio simulations to mechanistic models of DNA repair kinetics.

TOPAS-nBio simulates the radiolysis of liquid water in three stages. The first of the three is called the 'physical stage' ($< 10^{-15}$ s), in which the interaction of ionising radiation with matter is simulated through the application of specified physics processes. The ionisations, and electronic and vibrational excitations from this stage then give rise to an initial creation of chemical species in the 'pre-chemical stage' (10^{-15} – 10^{-12} s) through dissociative decay, relaxation, and auto-ionisation processes. Finally, the non-homogeneous 'chemical stage' (10^{-12} – 10^{-6} s) occurs, whereby the created species diffuse and react with one another [Ramos-Méndez et al., 2018]. The physics and chemical processes employed by TOPAS-nBio are briefly described in the following subsections.

Physics processes

Due to the lack of experimental data at the low-energies relevant to TS physics, the majority of the physics processes are only relevant to liquid water. There are, however, some low energy cross-sections for the interaction of electrons and protons with DNA related materials, and the interaction of electrons with solid gold (intended for nanoparticle applications) [Schuemann et al., 2018a, Geant4-DNA Collaboration, 2023]. Physics processes in liquid water are available for electrons, photons, protons, hydrogen atoms, alpha particles, and the ion species of ^{4}He through to ^{16}O, ^{28}Si, and ^{56}Fe. Using electrons as an example, depending on the user-specified physics list (*default*, *option2*, *option4*, *option6*), each interaction process (elastic scattering, electronic excitation, ionisation, vibrational excitation, or attachment) is described by a specific type of model (either analytical or interpolated from data tables) which also specifies the high and low energy limit, below which the particle is immediately killed and the energy is locally deposited [Geant4-DNA Collaboration, 2023, Incerti et al., 2018].

Chemistry of the physicochemical and non-homogeneous chemical stages

The physico-chemical processes and chemical reactions implemented in this work are shown in Table 3.1, and their use in TOPAS-nBio was validated through comparisons of simulated G-values to published experimental G-values. In general, a good agreement within the estimated uncertainty was found between the measurements and the simulation [Ramos-Méndez et al., 2018]. Table 3.1 depicts the chemical processes of the `TsEmDNAChemistry`

module, which is the default option in TOPAS-nBio v1.0. It represents the TOPAS-nBio version of Geant4-DNA's `G4EmDNAChemistry` module, however with updated and reviewed parameters [Zhu et al., 2020]. The choice of chemistry options is specified by appending the name of the module to the end of the physics list.

Table 3.1: Pre-chemical processes and non-homogeneous chemical stage reactions considered in TOPAS-nBio. Adapted from Tables 2 and 3 in Ramos-Meńdez *et al.* [Ramos-Méndez et al., 2018].

Pre-chemical stage processes			
Process			**Probability [%]**
Ionised state	Dissociative decay	$H_3O^+ + {}^\bullet OH$	100
A^1B_1 excitation	Dissociative decay	${}^\bullet OH + H^\bullet$	65
	Relaxation	$H_2O + \Delta E$	35
B^1A_1 excitation	Auto-ionisation	$H_3O^+ + {}^\bullet OH + e^-_{aq}$	55
	Auto-ionisation	${}^\bullet OH + {}^\bullet OH + H_2$	15
	Relaxation	$H_2O + \Delta E$	30
Rydberg, diffuse bands	Auto-ionisation	$H_3O^+ + {}^\bullet OH + e^-_{aq}$	50
	Relaxation	$H_2O + \Delta E$	50
Chemical stage reactions			
(1) $e^-_{aq} + e^-_{aq} \longrightarrow H_2 + 2\,OH^-$		(2) $e^-_{aq} + {}^\bullet OH \longrightarrow OH^-$	
(3) $e^-_{aq} + H^\bullet \longrightarrow H_2 + OH^-$		(4) $e^-_{aq} + H_3O^+ \longrightarrow H^\bullet$	
(5) $e^-_{aq} + H_2O_2 \longrightarrow OH^- + {}^\bullet OH$		(6) ${}^\bullet OH + {}^\bullet OH \longrightarrow H_2O_2$	
(7) ${}^\bullet OH + H^\bullet \longrightarrow H_2O$		(8) $H^\bullet + H^\bullet \longrightarrow H_2$	
(9) $H_3O^+ + OH^- \longrightarrow H_2O$			

Given the extremely short time scale, little is known about the qualitative and quantitative production of chemical species during the physicochemical stage, compared to the subsequent chemical stage. The approach generally adopted by different research groups is to first perform radical yield measurements as a function of scavenger concentration[31], then use a set of branching ratios which best matches these picosecond yields [Ballarini et al., 2000, Kreipl et al., 2009b]. TOPAS-nBio uses the dissociation scheme from Cobut *et al.* [Cobut et al., 1998], in which ionised water molecules undergo dissociation as the only possible pathway, and the revised branching ratios of Bernal *et al.* [Bernal et al., 2015].

The work of Karamitros *et al.* describes the full methodology and extensive mathematical background for the simulation of the chemical stage which will not be covered in this thesis [Karamitros et al., 2014]. In brief, the evolution of the chemical track in water is largely dependent on two parameters, the diffusion coefficient of each species (D) and the reaction rate constants of each reaction (k) [Ballarini et al., 2000]. Chemical species move by Brownian motion, which describes the random motion of particles suspended in

[31] In this type of experiment, a solute (scavenger) is added to the liquid which consumes radical species at a known rate. The yield of the scavenged radicals can then be inferred by measuring the concentration of the scavenger [Pimblott, 1992].

a medium. In Geant4-DNA (and by extension in TOPAS-nBio) the medium is assumed to be a continuum, and the brownian motion is based on the Smoluchowski model. The principal assumption of the Smoluchowski model is that two species immediately interact when they encounter one another, resulting in an immediate removal of the reactants while the products of the chemical reaction are added into the simulation at the same location. This is otherwise known as the *Smoluchowski boundary condition*, and chemical reactions modelled using this approach are said to be *totally diffusion controlled* [Karamitros et al., 2014, Bernal et al., 2015].

The extensive list of chemical reactions shown in Table 2.1 are categorised into 6 different types [Plante, 2011]:

- **Type I**: totally diffusion controlled reactions between neutral particles.
- **Type II**: partially diffusion controlled reactions between neutral particles.
- **Type III**: totally diffusion controlled reactions between charged particles.
- **Type IV**: partially diffusion controlled reactions between charged particles.
- **Type V**: reactions with a spin statistical factor.
- **Type VI**: reactions with species in the continuous background.

As is clearly evident from a comparison of Tables 3.1 and 2.1, the list of reactions used in TOPAS-nBio is significantly smaller. There are 3 main justifications for this. First of all, as previously stated, many of the reactions are of little importance in the context of RT [Alpen, 1997b] and are often neglected. Secondly, given the use of the Smoluchowski boundary condition in TOPAS-nBio, only the totally diffusion controlled reactions of type I and III are able to be simulated. The more modern Noyes boundary condition allows the simulation of partially diffusion controlled reactions however this was not implemented in TOPAS-nBio v1.0 [Karamitros et al., 2014]. Thirdly, this selection of a small portion of chemical reactions is an approach used by many different research groups. A subset of the chemical reactions (those deemed the most prominent) are chosen based on if simulated chemical yields are comparable to experimental results. Consequently, the choice of parameters in the physicochemical and chemical stage of water radiolysis are strongly dependent on the model used by that specific group [Ballarini et al., 2000]. The assumption of Smoluchowski boundary conditions results in the following set of equations to describe the step-by-step (SBS) diffusion and reaction of chemical species in TOPAS-nBio [Karamitros et al., 2014]:

$$p(\overrightarrow{r}) = \frac{4\pi r^2}{(4\pi Dt)^{3/2}} \cdot \exp\left(-\frac{r^2}{4Dt}\right) \tag{3.1}$$

Equation 3.1 is the solution to the Smoluchowski equation in three dimensions, which describes the probability density of finding a particle at some position after a time lapse of t. In order to simplify the calculation, TOPAS-nBio uses the one-dimensional form of Equation 3.1, and diffuses the particles in x, y, and z according to Equation 3.2.

$$\begin{aligned} \hat{x}(\tau) &= x_0 + \sqrt{2D \cdot \tau} \cdot \hat{\xi_x} \\ \hat{y}(\tau) &= y_0 + \sqrt{2D \cdot \tau} \cdot \hat{\xi_y} \\ \hat{z}(\tau) &= z_0 + \sqrt{2D \cdot \tau} \cdot \hat{\xi_z} \end{aligned} \tag{3.2}$$

The variable $\hat{\xi}_{x,y,z}$ is a random number from a Gaussian distribution with a mean of 0 and standard deviation of 1. The chemical species are transported some distance away from their current location according to that species' diffusion coefficient D, and the simulation time step τ. While some older MC codes used fixed time steps for chemical kinetics simulations, TOPAS-nBio uses a dynamic time step approach. At the beginning of the simulation, when the concentration of chemical species are highly localised, small time steps are used in order to increase the accuracy of the simulation. These time steps are gradually increased to reduce the computational expense, and avoid the situation whereby prohibitively small time steps are taken within which no reactions would occur [Karamitros et al., 2014]. In order to implement the immediate creation of products from totally diffusion controlled reactions, Equations 3.3 and 3.4 are used for type I and type III reactions respectively.

$$k = 4\pi N_A \cdot DR_0 \tag{3.3}$$

Equation 3.3 is referred to as the *Smoluchowski reaction theory*. The variable R_0 is the reaction radius and can be calculated for reactions with known rate constants k, where D is taken to be the sum of the diffusion coefficients of the reactants. As previously stated, the assumption of totally diffusion controlled reactions implies an immediate creation of the products upon encounter. Practically speaking, this *encounter* occurs whenever the reactants, after being diffused some time step τ, are separated by a distance smaller than R_0 [Karamitros et al., 2014].

$$k = 4\pi N_A \cdot DR_{eff} \quad \text{with, } R_{eff} = \frac{R_C}{exp(\frac{R_C}{R_0}) - 1} \tag{3.4}$$

Equation 3.4 is referred to as the *Smoluchowski-Debye reaction theory*. For these types of chemical reactions the reaction radius is R_{eff} with R_0 corresponding to the reaction radius if there were no electrostatic forces, and R_C is a constant known as the Onsager radius [Karamitros et al., 2014].

This SBS approach is a widely used MC method for the diffusion and reaction of chemical species [Kreipl et al., 2009b, Štepán and Davídková, 2008, Michalik et al., 1998]. In the context of TOPAS-nBio, it is applied history-by-history, such that the chemical events of one particle history are completely independent from another history [Ramos-Méndez et al., 2018]. While the type II and types IV-VI reactions were not able to be simulated in TOPAS-nBio v1.0, a second version of the software was recently made publicly available in which these reactions can be included. Instead of the SBS as described here, this second version of TOPAS-nBio allows the use of the independent reaction time (IRT) method which is computationally more efficient (by a factor of ∼145 [Schuemann et al., 2018a]), allows the simulation of partially diffusion controlled and background reactions, but comes at the cost of not having access to the spatio-temporal information of the chemical species [Ramos-Méndez et al., 2020a, Ramos-Méndez et al., 2020b]. The inclusion of these background reactions opens up the door to simulations potentially investigating the effect radical scavenging. An even more advanced method is the use of the Gillespie algorithm, which has recently been shown to be able to perform long time scale simulations of homogeneous chemistry [D-Kondo et al., 2023]. However this algorithm is not yet available in the publically released version of TOPAS-nBio.

A brief description of the high performance computing clusters used in this work is provided in the following section.

3.2 High performance computing clusters

All simulations were performed on either one of two high performance computing infrastructures. The work on VHEEs described in chapters 4 and 5 was performed exclusively on the Joliot Curie-SKL supercomputer[32], which uses 2×24-core Intel Skylake@2.7GHz (AVX512) CPUs, with 1656 computing nodes in total, and 48 cores per node. Full use of all 48 cores of a node had a default time limit of 24 hours, but could be increased to 72 hours by supplying the submission script with a specific option. The work on free radicals in the context of MBRT, described in chapters 6 7, was in part performed on the aforementioned Joliot Curie-SKL supercomputer. However an additional computing cluster was also used: that of HPC VEGA supercomputer[33], which uses 2×64-core AMD Epyc 7H12 CPUs, with 960 computing nodes in total and 256 cores per node. The maximum time limit of a simulation running on a single node of HPC VEGA is two days.

3.2.1 Data processing

Given that TOPAS has implemented multithreaded capability, all TOPAS simulations of this thesis took advantage of the multiple computing threads available in a single node to perform simulations of a large amount of particles in a reasonable amount of time. If more than a single computing node was needed, the parallelization of the simulations was followed by some post-processing to combine all the simulation outputs. In TOPAS, if the sum of a particulary quantity is requested, the scored quantity is simply accumulated. However if the mean, second moment, variance, or standard deviation are requested, then the accumulation occurs according to the numerically stable algorithm of D. E. Knuth [Knuth, 1997], i.e. the calculations shown below are performed in each voxel, where `data` represents the scored distribution of the quantity requested by the user [TOPAS MC Inc, 2023].

```
for x in data:
    n = n+1
    delta = x - mean
    mean = mean + delta/n
    M2 = M2 + delta*(x - mean)
sum = n * mean
variance = M2/(n - 1)
standard deviation = sqrt(variance)
```

The standard error of the mean/sum is the found by dividing/multiplying the reported standard deviation by the square root of the total number of histories simulated [Perl et al., 2012, Faddegon et al., 2020]. This normalisation by the total number of histories (i.e sample size) provides insights into the dispersion of the calculated (sample) mean around the true population mean. In the case where multiple computing nodes were used, doses in each voxel of each of the output files were simply accumulated, however standard

[32] https://www-hpc.cea.fr/tgcc-public/en/html/tgcc-public.html
[33] https://doc.vega.izum.si/

errors were propogated using the summation in quadrature method. Unless a specific methodology for calculating statistical uncertainties is detailed, all statistical uncertainties in this thesis are representative of standard errors.

Given the distinct nature of each of the works performed in this thesis, and in order to aid in the readability and comprehension of the thesis, the exact setup of each simulation (associated geometries, placement and use of scorers, and post-processing methodology) isn't provided in this chapter, but is instead described in the appropriate sections in chapters 4, 5, 6 and 7

Chapter 4

Radioprotection considerations for VHEEs

This chapter of the thesis contains the work performed looking at the potential radioprotection concerns within a treatment room delivering VHEE therapy, and has been published in *Scientific Reports* [Masilela et al., 2021]. It is split into four main parts which describe: the rationale for performing the work (section 4.1), details of the simulation (section 4.2), results (sections 4.3, 4.4, and 4.5), and final discussions and conclusions (section 4.6).

4.1 Rationale for the work

Conventional EBRT treatments with electrons have typically been performed using low energies in the range of 4 to 25 MeV to treat superficial tumors [Baskar et al., 2012]. However in the early 2000s, the use of electrons of a higher energy, so called VHEEs, was proposed due to their various dosimetric advantages [DesRosiers et al., 2000]. Among these advantages, are the increased practical range, narrowing of the beam penumbra with depth, and relative insensitivity to tissue heterogeneities [DesRosiers et al., 2000, Papiez et al., 2002, Lagzda et al., 2020] - thus resulting in dose distributions for the treatment of deep seated-tumors which are more favourable than conventional photon beams [DesRosiers et al., 2000]. Furthermore, there is an interest in performing combined FLASH + VHEE experiments, as evidenced by the recent activities of the Pluridirectional High-Energy Agile Scanning Electron Radiotherapy (PHASER) [Maxim et al., 2019] and CERN Linear Electron Accelerator for Research (CLEAR) facilities [Gamba et al., 2018]. Additionally, laser-based accelerators may represent a more effective way of producing these beams in a clinical context [Nakajima et al., 2015, Labate et al., 2020, Svendsen et al., 2021].

As detailed in section 2.8, one of the main concerns with these high energy electrons is the risk of secondary cancers from the production of neutrons, primarily through the giant dipole resonance [IAEA, 1979], however early studies concluded that the generation of these neutrons is likely negligible from the point of view of total dose deposited or neutron dose equivalent [DesRosiers et al., 2000, Subiel et al., 2014]. Nevertheless, this production of neutrons is highly dependent on the geometry of the treatment room [Banaee et al., 2021, Sorcini et al., 1996], as well as parameters related to the type of treatment machine (i.e. materials used, field size, type of collimator) which differs depending on the manufacturer (Varian, Elekta, Siemens) [Ronga et al., 2021, Naseri and Mesbahi, 2010].

In this context, the work performed in this chapter evaluated the production of neutrons and resulting ambient neutron dose equivalents for VHEE beams of 200 MeV and 2 GeV, within a treatment room surrounded by concrete walls, and in conjunction with a conventional electron applicator as the collimation system. The novelty of this work is based on the fact that: (1), previous studies only looked at neutron production in, or in the immediate vicinity of a water phantom [DesRosiers et al., 2000, Subiel et al., 2014] and a possible contribution from the concrete walls was not considered. (2), The significantly higher energy 2 GeV beam was evaluated, which was shown to have possible synergies with SFRT through its focusing [Martínez-Rovira et al., 2015, Kokurewicz et al., 2019]. And (3),

given the logistical challenges with implementing VHEE therapy from a typical LINAC in a clinical setting, more modern and compact solutions such as laser wakefield accelerators have been proposed [Nakajima et al., 2015], and magnetic focusing lenses placed around the patient have been proposed as a solution to reduce the high entrance and exit doses [Kokurewicz et al., 2019]. However, the feasibility of implementing these solutions is still not certain, and additional physical collimation may be a necessity. To this end the impact of a conventional electron applicator used in conjunction with these beams was investigated.

The following section describes all the technical details of the simulations performed in this chapter.

4.2 Simulation details

All MC simulations in this work were performed in TOPAS [Perl et al., 2012, Faddegon et al., 2020] version 3.5. As previously stated, Geant4, and by extension TOPAS, has been extensively validated for the field of medical physics [Allison et al., 2016], and Geant4 is comparable to PENELOPE (a different MC code) for radiation shielding applications [Ibarmia et al., 2013]. In terms of its applicability to dose equivalent calculations, TOPAS has recently been used to calculate the ambient neutron dose equivalents in both conventional proton therapy [Yu and Chen, 2023] and pMBRT [Charyyev and Wang, 2020]. In terms of its applicability to VHEEs, TOPAS has been validated through comparisons to FLUKA, in which good agreement was found between the respective dose distributions and beam spread, thus making it a viable alternative to older MC codes in the study of VHEEs [Lagzda, 2019]. A schematic depiction of the simulation is shown in Fig. 4.1.

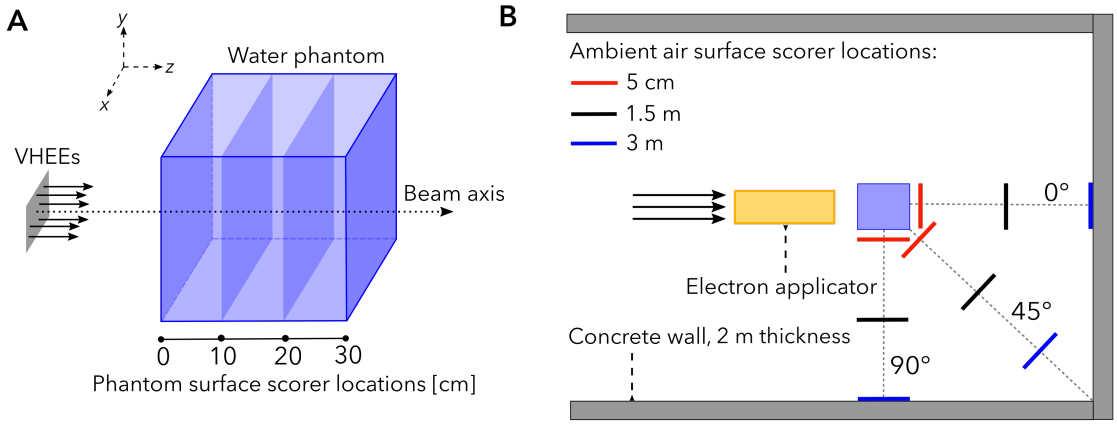

Figure 4.1: Schematic drawing of the TOPAS simulations. Panel **A** depicts the beam of electrons, directed towards the water phantom, within which surface scorers are placed at depths of 0, 10, 20, and 30 cm. Panel **B** depicts a global vision of the simulation, including the electron applicator, placed between the source and the water phantom, the locations of all the scoring surfaces in the ambient air, and the surrounding concrete walls.

Both the 2 GeV and 200 MeV VHEE beams were simulated in three configurations: collimated with a source to surface distance (SSD) of 100 cm or 5 cm, or uncollimated. Following the technical specifications outlined by Shahzad *et al.*, an electron applicator with an open sidewall diaphragm design, was recreated in TOPAS [Shahzad et al., 2017]. The choice of this kind of electron applicator was in line with clinical practice, as both Varian and Elekta make use of this open sidewall design, while Siemens uses the partially

opened variation of the design [van Battum et al., 2003]. The applicator used in this work was made entirely of aluminium (`G4_Al` from the Geant4 materials database) with a density of 2.699 g/cm^3. While all three manufacturers provide MLC technology in their accelerators, and despite the capability to achieve similar treatment plan quality through multileaf collimation as opposed to applicator collimation, the standard practice in clinics is still to use patient-specific cut-outs, made from a material known as Cerrobend, placed in the insert tray at the end of an applicator to further conform the dose to the target [Mueller et al., 2018]. Consequently, a Cerrobend block with a 2×2 cm^2 opening was included at the end of the applicator. It had thickness of 5 cm with a density of 9.4 g/cm^3, and a material composition of 50% bismuth, 26.7% lead, 13.3% tin, and 10% cadmium [Di Venanzio et al., 2015]. The visualisation of the TOPAS simulation is shown in Fig. 4.2.

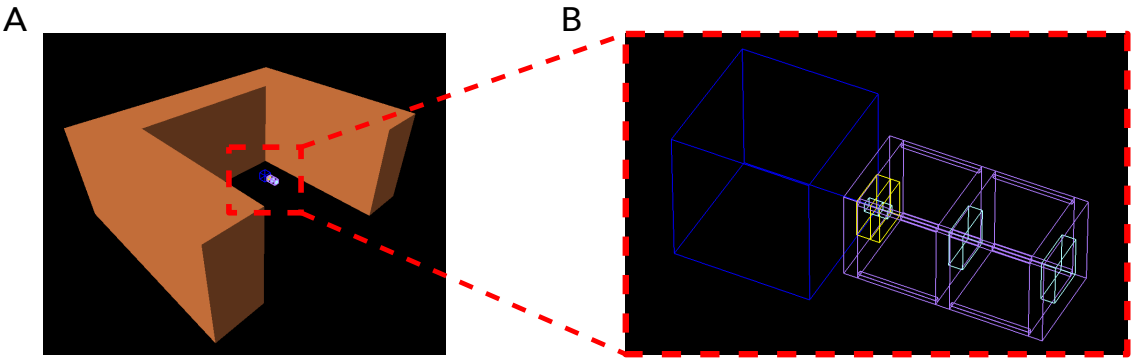

Figure 4.2: TOPAS generated graphical view of the simulation. Panel **A** depicts the water phantom and electron applicator in relation to the concrete walls, while panel **B** depicts a zoomed in view of both the applicator and the water phantom.

A 5 cm air gap was left between the end of the Cerrobend insert and the surface of the 30×30×30 cm^3 water phantom (`G4_WATER`) in order to emulate the distance to the patient's skin in clinical treatments. Quantification of the absorbed dose within the phantom was performed through a calculation of the PDD, lateral dose profiles, and the absorbed dose to a 2×2×2 cm^3 target. As shown in Fig. 4.1, surface scorers were placed at 0, 10, 20, and 30 cm in the water phantom in order to record the particle yields. Beyond the water phantom, surface scorers were also placed at angles of 0°, 45°, and 90° from the central beam axis, and at distances of 5 cm, 1.5 m, and 3 m, with the latter distance corresponding to the surface of a concrete wall with a thickness of 2 m. `G4_CONCRETE` from Geant4 material database with a density of 2.3 g/cm^3 was assigned to be the material of the wall, due to the fact that ordinary concrete of this density is one of the most common shielding materials in EBRT treatment rooms [Podgorsak, 2005].

4.2.1 Particle sources and physics processes

A total of 100 - 300 million primary particles were simulated in order to reach a satisfactory compromise between computation time and accuracy. Multiple computing nodes of the Joliot Curie-SKL supercomputer were used in order to reduce statistical uncertainties, and the results were combined as outlined in section 3.2. Both the 2 GeV and 200 MeV VHEE sources were simulated using a TOPAS `Beam` source with a Gaussian distribution. *Source 1* in Table 4.1 describes the source used in the majority of the simulations of this chapter. These beam characteristics were taken from the FLUKA input files of Kokurewicz *et al.* [Kokurewicz et al., 2019]. The smaller, *Source 2* and *Source 3* were simulated solely to evaluate the impact of the collimating Cerrobend block through the creation of the lateral

dose profiles shown in Figure 4.4.

Table 4.1: Source details for the 2 GeV and 200 MeV VHEE beams

Name	Distribution	x,y cutoff [cm]	FWHM [cm]	Divergence [°]
Source 1	Gaussian	20	15.9	5
Source 2	Gaussian	1	1	0.3
Source 3	Gaussian	2	1.7	0.7

The `QGSP_BERT_HP_EMZ` reference physics list was used for all simulations in this chapter. The `QGSP` and `BERT` models describe hadronic physics, while `EMZ` designates the electromagnetic physics options. These models are described in slightly more detail in section 3.1.1, however full descriptions can be found in the Geant4 physics manual [Geant4 Collaboration, 2021]. Both `QGSP_BERT` and `QGSP_BIC` (Binary Cascade) physics lists are suitable for radiation protection and medical applications, however `BERT` is more suited to higher energies, while the `BIC` option is preferable for hadron therapy applications at energies below 200 MeV due to its increased accuracy around the Bragg peak [Zacharatou Jarlskog and Paganetti, 2008, Arce et al., 2021]. Given the energies and type of particle (exclusively VHEEs) simulated in this work, the `QGSP_BERT` model was default model chosen. Geant4 simulates four types of neutron interactions, namely radiative capture, elastic and inelastic scattering, and fission, and including the `HP` option activates the *High Precision* neutron model for more precise simulation of neutrons below 20 MeV [Geant4 Collaboration, 2021]. A default particle tracking cut[34] of 0.05 mm was used for all simulations.

One of the challenges encountered while performing the work contained in this chapter was verifying the degree of validity of the results obtained, in the sense that at the time of writing, there were no other published works on using TOPAS to calculate neutron dose equivalents from VHEE beams. Indeed perhaps the choice of a MC code could result in systematic differences which include, but are not limited to, uncertainties in the inherent physics parameters - such as the interaction cross sections or models utilised, simulation geometries, and mass attenuation coefficients (which govern the particle transport) [Baumann et al., 2019]. Ultimately, one of the approaches that was used to evaluate these type B (systematic) uncertainties, was to re-perform the simulations with different physics options governing the photonuclear process (creation of neutrons). These comparisons are shown in Figures 4.8 and 4.11, where the `BERT` model was compared against `BIC` and `INCLXX` (Liège Intranuclear Cascade Model). In addition to the photonuclear processes, this latter model provides a more refined description of nucleon-nucleus spallation[35] between 50 MeV and 3 GeV [Mancusi et al., 2014].

[34] This represents the production threshold for secondary particles. Secondaries unable to travel at least this distance are not produced [Agostinelli et al., 2003].

[35] As noted in section 2.2.2, these interactions become relevant for neutrons with an energy > 100 MeV.

4.2.2 TOPAS scorers

Throughout this work, the three standard TOPAS scorers used were the `DoseToMedium` discretized volume scorer, the `SurfaceTrackCount` surface scorer, and the `AmbientDoseEquivalent` scorer. In order to create the PDD curves, doses were scored using the `DoseToMedium` scorer in voxels of $5\times5\times1$ mm^3 (x,y,z) along the central axis of the beam, with 300 total voxels in the z dimension. These total on-axis doses were then compared against two quantities: the Bremsstrahlung contribution originating solely from the Cerrobend insert, and the contribution of electrons (both primary and secondary) having undergone an interaction within the entirety of the applicator structure. The former was evaluated by applying the `OnlyIncludeIfParticleOrAncestorFromProcess` and `OnlyIncludeIfParticleOrAncestorFromVolume` filters, while the latter was evaluated through an application of the filters `OnlyIncludeParticlesNamed` and `OnlyIncludeIfParticleOrAncestorFromVolume`. Lateral dose profiles were similarly calculated using the `DoseToMedium` scorer with voxels of $0.5\times5\times5$ mm^3, with a total of 600 voxels in the x dimension. And finally, the last quantity calculated using the `DoseToMedium` scorer was that of the absorbed doses to a $2\times2\times2$ cm^3 target centred at a depth of 10 cm in the water phantom. Total absorbed doses in this target were compared to the contribution by primaries and secondaries by using the `OnlyIncludeParticlesOfGeneration` filter, as well as the contribution of individual particles by using the `OnlyIncludeParticlesNamed` filter.

Surface scorers of 30×30 cm^2 were placed at the locations depicted in panels A and B of Fig. 4.1. The surface scorers in the ambient air lay on the same y-plane as the water phantom. TOPAS's `SurfaceTrackCount` scorer was used to score the fluence of incident particles. This scorer was used to calculate the particle yields per cm^2 per primary electron at various locations in the simulation. These yields were filtered according to the both the name of the particle (`OnlyIncludeParticlesNamed`), as well as the volume of the simulation from which they originated (`OnlyIncludeIfParticleOrAncestorFromVolume`).

Calculation of the ambient neutron dose equivalent was done in TOPAS by filtering for neutrons, and making use of the `AmbientDoseEquivalent` scorer, placed in the locations depicted in panel B of Fig. 4.1. This scorer converts the neutron fluence to a dose equivalent by specifying a set of energy bins as well as a conversion coefficient associated to each bin. At the time of writing, the default conversion coefficients used in TOPAS were those outlined by M. Pelliccioni [Pelliccioni, 2000]. Therefore the first sets of simulations were launched using the conversion coefficients of M. Pelliccioni, with the `QGSP_BERT_HP_EMZ` physics list, as dose equivalents calculated with this physics list were shown to be in good agreement with the dose equivalents calculated in MCNP [MacFadden et al., 2018]. As stated in section 2.6, a more recent set of fluence to dose equivalent coefficients were published in ICRU report 95 [ICRU, 2020], just a few months before the work described in this chapter began. It was considered that these coefficients were one of the other sources of systematic uncertainties, and so consequently the older default conversion coefficients in TOPAS were manually replaced with those described in ICRU report 95 [ICRU, 2020] and all simulations were re-launched. A comparison between dose equivalents obtained using the different sets of coefficients is shown in Fig. 4.12.

The following sections describe the main results of the work performed in this chapter.

4.3 Absorbed doses within the water phantom

The behaviour in depth of 2 GeV and 200 MeV beams with and without an applicator is shown by the PDD curves in panel A of Fig. 4.3, which depicts the curves for an SSD of 100 cm. Statistical uncertainties on the absolute absorbed dose in each voxel along these PDD curves was maintained below 1% in all cases. It is evident that the use of an applicator drastically alters the nature of dose depositions in depth for both beam energies. Through its use, both the 2 GeV and 200 MeV beams experience high entrance doses which decrease with depth into the phantom. When an applicator is not used, the 2 GeV profile undergoes a steady increase of dose deposited with depth, whereas the curve for the 200 MeV electrons is nearly uniform in nature. This is consistent with previous works highlighting the dose deposition in depth for uncollimated VHEE beams [DesRosiers et al., 2000, Kokurewicz et al., 2019, Ronga et al., 2021].

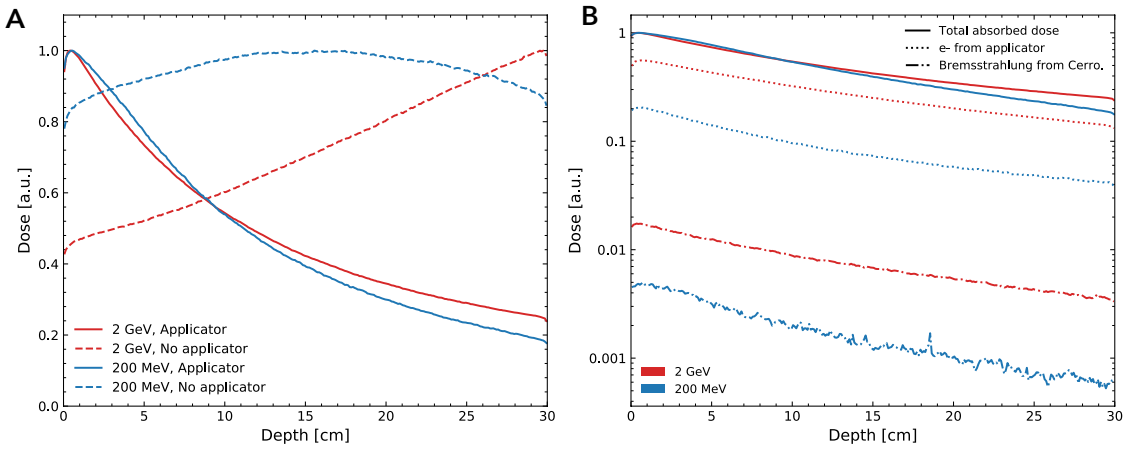

Figure 4.3: On-axis PDD curves. Panel **A** depicts the relative PDD curves with and without an applicator, at an SSD of 100 cm, for both 2 GeV and 200 MeV VHEE beams. Doses in each voxel were normalised to the maximum voxel dose of that configuration. Panel **B** depicts the relative contribution to the total on-axis absorbed dose when an applicator is used. It considers electrons or electrons with ancestors originating from the applicator structure, as well as specifically dose depositions resulting from a Bremsstrahlung interaction within the Cerrobend.

In clinical electron beams, interactions within the head of the accelerator and collimating material both contribute to the absorbed dose. In a similar vein, these relative contributions due to the presence of an applicator were evaluated in panel B of Fig. 4.3. In the entrance region, approximately 50% of all on-axis dose depositions are a result of electron interactions within the applicator structure for the 2 GeV beam, which decreases to approximately 20% at the end of the water phantom. This is compared to the Bremsstrahlung contribution from the Cerrobend block, which is orders of magnitude lower. Similar observations were made for the 200 MeV beam, however the interactions within the applicator only contribute to 20% in the entrance region and drop to approximately 4% at 30 cm. While Cerrobend blocks are known to have a higher Bremsstrahlung contribution than the partially open diaphragm applicators which don't use Cerrobend [Di Venanzio et al., 2015], Fig. 4.3 shows that for VHEE beams this contribution is nevertheless still negligible when compared to the total absorbed dose. In order to further investigate the collimating effect of the Cerrobend in particular, lateral dose profiles of Fig. 4.4 were created, where the statistical uncertainty within each voxel was maintained below 1%, and doses were normalised to the maximum.

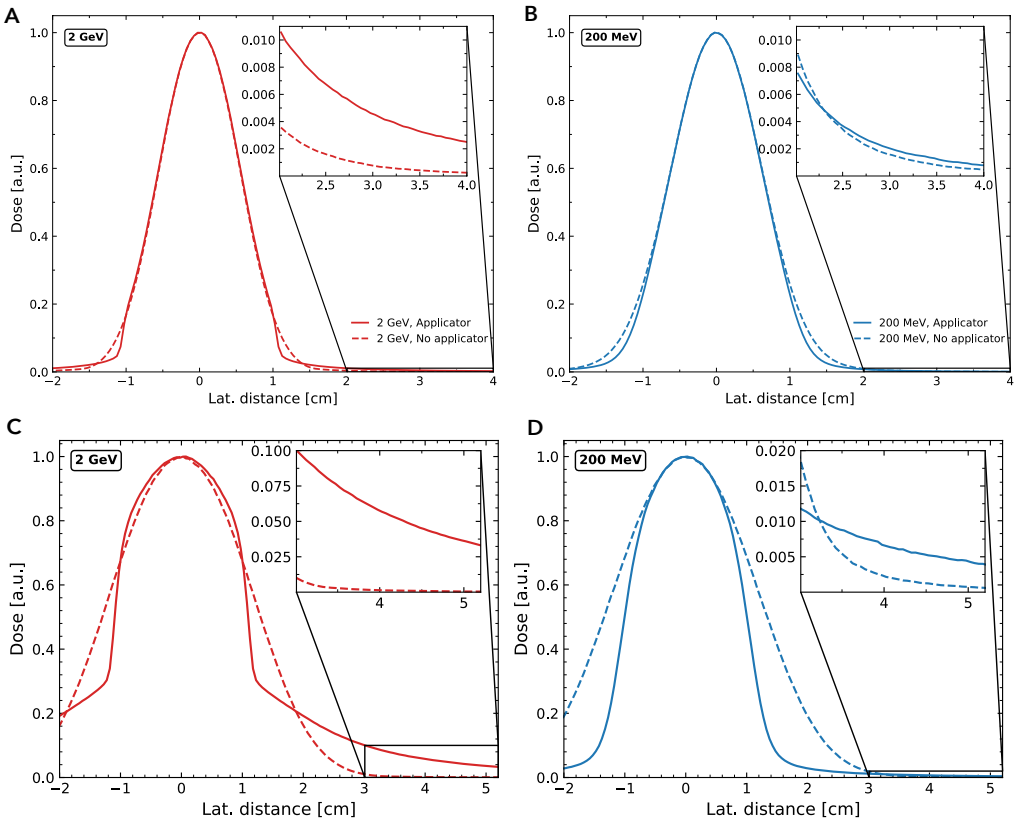

Figure 4.4: Lateral dose profiles at 10 cm in the water phantom. Panels **A** and **B** were obtained from Source 2 in Table 4.1 while panels **C** and **D** were obtained through the use of Source 3. Zoomed-in inserts show the behaviour in the tails of the profiles.

The use of Source 2 resulted in a radiation field covering approximately 3×3 cm^2 at the surface of the Cerrobend, while Source 3 resulted in a field of approximately 6×6 cm^2. Given that the Cerrobend block had an opening of 2×2 cm^2, Source 3 was representative of a greater area of the Cerrobend being in the beam path. As highlighted in Fig. 4.4, for all configurations there is a slight reduction in the distant beam penumbra ($>$ 2 cm lateral distance) when an applicator is used. However this trend is short-lived, and in all cases the zoomed-in inserts highlight the increased doses in the tails of the profile when an applicator is used, which is more severe for the 2 GeV beam than the 200 MeV beam. It should be noted however, that there is greater dosimetric importance to the slight reduction in relative dose in the distant penumbra region compared to the tails, as the tail doses correspond to less than 1% of the maximum dose. Nevertheless, this seems to not be the case the higher the energy of the beam, and the greater the area of Cerrobend interacted with - as highlighted in panel C of Fig. 4.4. In this configuration, scatterings of the 2 GeV beam within the Cerrobend appeared to lead to a slight increase in the dose deposited in the immediate vicinity of the central beam axis.

Absorbed doses in a 2×2×2 cm^3 target are depicted in Fig. 4.5, where the dose in the target was normalised to a 2 Gy total absorbed dose in order to make comparisons between each configuration. The term *neutron dose* in the figure refers to the dose deposited by neutrons or any secondary particle produced as a result of a neutron interaction. This was achieved in the simulation by applying the `OnlyIncludeIfParticleOrAncestorNamed` filter. Statistical uncertainties on the dose deposited by primary and secondary electrons,

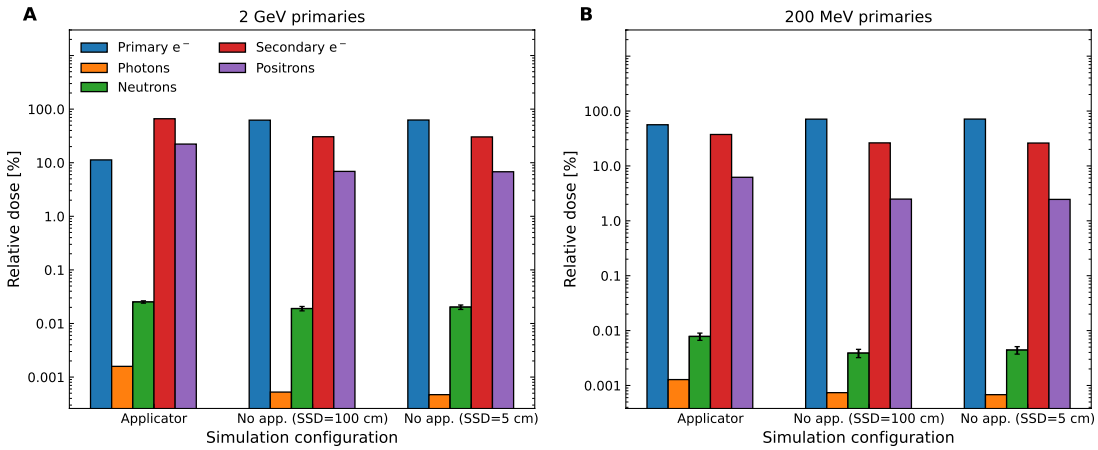

Figure 4.5: Absorbed dose contributions of secondaries to the target, as a percentage of the total target dose which was normalised to 2 Gy. Contributions of primary and secondary electrons, photons, neutrons and positrons were investigated for **A)** 2 GeV and **B)** 200 MeV primaries.

photons, and positrons were all below 1%, while the neutron dose was subjected to a statistical uncertainty of between 4 and 17% depending on the simulation configuration. For both the 2 GeV and 200 MeV beams, there was a greater proportion of dose deposited due to photons and secondary electrons when an applicator was used compared to its absence. This effect was more severe for the higher energy 2 GeV VHEEs. In both cases, due to the increased presence of photons there was a corresponding increase in the dose deposited by positrons due to pair production. The increased proportion of secondary electron dose deposition was attributed to an increased number of scatterings of the beam in the applicator structure, which corresponded with a decrease in the dose deposited due to primary electrons. It was found that both the 2 GeV and 200 MeV beam received ∼50% higher absorbed dose due to neutrons when an applicator was used relative to when an applicator was not used.

In summary, the presence of an applicator results in higher neutron doses in the target. It acts to considerably reduce the depth of the dose build-up region, whereby the trade-off for lower exit doses compared to uncollimated VHEE beams is higher entrance doses. Furthermore, the higher the beam energy, the lower the applicator's impact on beam penumbra reduction.

The following section details the simulation results for particle yields at various depths within the water phantom.

4.4 Particle yields within the water phantom

Figure 4.6 depicts the particle yields within the water phantom for each of the configurations of the 2 GeV and 200 MeV VHEE beams. Similarly to the relative dose contribution in the target, it was observed that at all depths there was a higher photon yield in the presence of an applicator compared to in its absence. This can be attributed to Bremsstrahlung interactions within the applicator structure. The higher photon yields in the 2 GeV beam are representative of the fact that the higher the beam energy, the more dominant the Bremsstrahlung interaction is over collisional energy losses, as seen in Fig. 2.8. The photon

yield difference between the presence/lack of an applicator is most severe in the entrance region, but normalises as the depth increases. Due to the generation of photoneutrons, the applicator injects neutrons into the entrance region of the phantom and the yield gradually decreases with increasing depth. This is in contrast to the configurations where no applicator was used in which, broadly speaking, there was an increase in the neutron yield in depth, leading to a situation whereby, similarly to the yield of photons, there is a normalisation of neutron yields between the applicator/no applicator configurations at the distal end of the phantom.

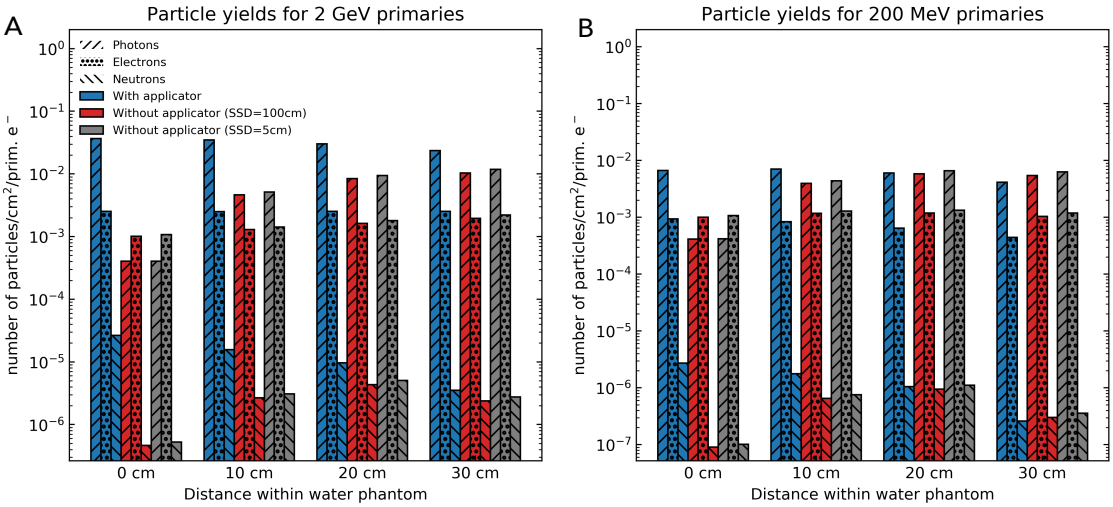

Figure 4.6: Particle yields in number of particles/cm^2/primary electron for 0, 10, 20, and 30 cm in the water phantom for both the 2 GeV (panel **A**) and 200 MeV (panel **B**) beams. Each configuration is represented by a colour, and each particle is represented by a different bar hatching.

The drop in particle yields at shallow depths after the removal of an applicator is better visualised in Fig. 4.7, in which the total fluence of particles at 0 cm was compared to the fluence where a filter was applied to exclude particles (or particles with ancestors) not originating from the applicator.

Figure 4.7 highlights the fact that essentially the totality of the neutron and photon yields at 0 cm are due to the presence of an applicator. Naturally this was not the case for electrons as the Cerrobend opening allowed electrons to reach the phantom without first interacting with the applicator. Consequently, there is a substantial gap observed between the electron fluences, with the largest difference occurring at the maximum energy, corresponding to primary electrons not having undergone any interaction upon reaching the water phantom surface. This difference being almost negligible at low energies highlights the fact that the majority of low energy electrons originate from the applicator. The sharp rise in the neutron fluence at approximately 30 MeV is particularly interesting as this is a visual representation of the increased neutron production due to the giant dipole resonance, as discussed in section 2.8.2. Maximum and minimum neutron yields for each configuration are shown in Table 4.2, with yields given in amount of neutrons/cm^2/primary electron.

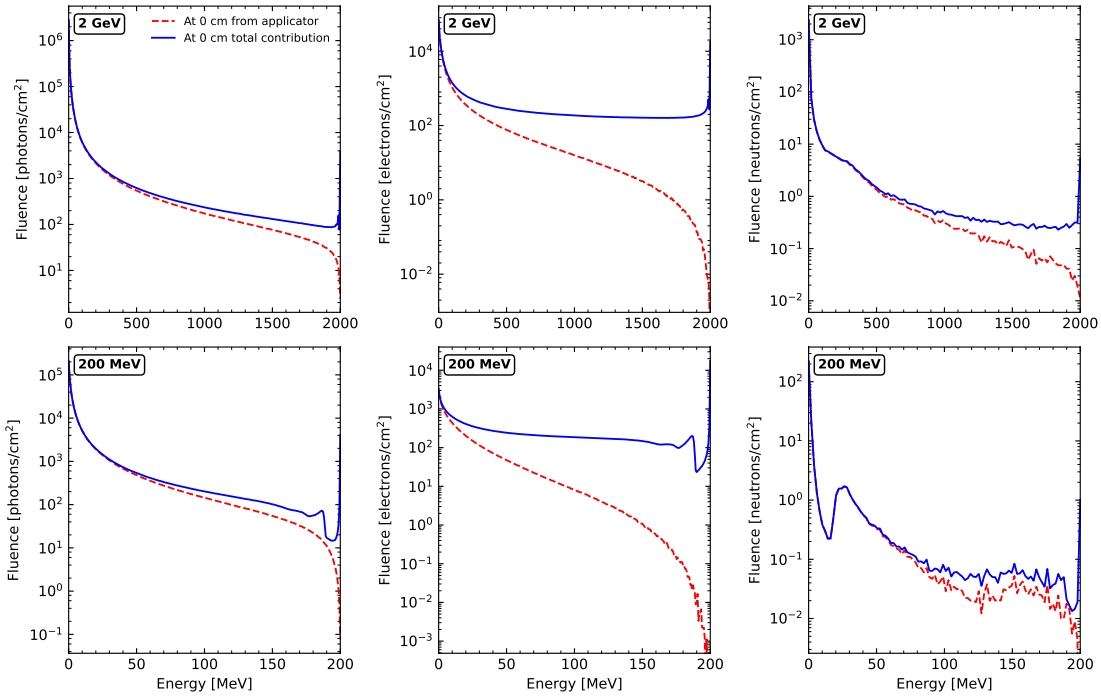

Figure 4.7: Photon, electron, and neutron fluences for the 2 GeV and 200 MeV VHEE beams at 0 cm in the water phantom, comparing the total contribution and the contribution from the applicator.

Table 4.2: Minimum and maximum neutron yields in the water phantom for each configuration of the 2 GeV and 200 MeV VHEE beams.

Beam energy	Configuration	Min yield [$\times 10^{-7}$]	Depth [cm]	Max yield [$\times 10^{-7}$]	Depth [cm]
2 GeV	With applicator (SSD = 100 cm)	35.09	30	264.40	0
	Without applicator (SSD = 100 cm)	4.62	0	43.16	20
	Without applicator (SSD = 5 cm)	5.26	0	50.68	20
200 MeV	With applicator (SSD = 100 cm)	2.61	30	27.33	0
	Without applicator (SSD = 100 cm)	0.91	0	9.45	20
	Without applicator (SSD = 5 cm)	1.01	0	11.13	20

Interestingly, as observed in Fig. 4.6, the neutron yield in the uncollimated VHEE beams increases in depth, reaches a maximum at 20 cm (yield values provided in Table 4.2), then decreases again at 30 cm. This was attributed to the fact that at shallower depths in the water phantom neutrons are arriving from both negative and positive z directions, whereas at 30 cm the only contribution is from the negative z direction.

As previously stated, systematic uncertainties on the yield of neutrons produced in the water phantom were evaluated by re-performing the simulations with different physics

lists. These evaluations are highlighted in the following subsection.

4.4.1 Systematic uncertainty evaluation

The difference in neutron yields for each configuration, arising due to the use of either the BERT, BIC, or INCLXX physics options are depicted in Fig. 4.8. The VHEE work of Lagzda *et al.* showed that while a 2% variation in dose distributions was observed between TOPAS and FLUKA, a 5 to 10% difference was observed between TOPAS and experimental measurements [Lagzda, 2019]. Consequently, using these values as a baseline, a conservative estimate of 20% combined statistical and systematic uncertainty arising from inter-code/physics options differences was assumed. This 20% difference is visualised by the errors bars in Fig. 4.8, which were added to the yield results of the simulation using the BERT option.

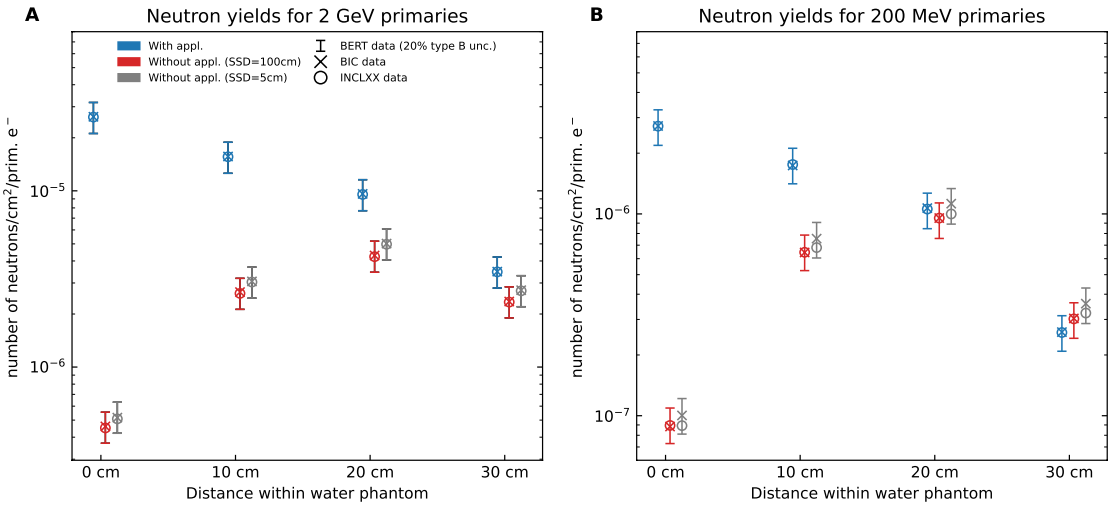

Figure 4.8: Neutron yields in number of neutrons/cm^2/primary electron for 0, 10, 20, and 30 cm in the water phantom for both the **A)** 2 GeV and **B)** 200 MeV beams. The 20% uncertainty applied to the simulation results using the BERT physics option are depicted by the error bars. Use of the BIC and INCLXX options are marked with a cross and circle respectively.

It was observed that for the 2 GeV beam, all data points for both BIC and INCLXX were within 5% of the BERT data. This was similarly the case for the 200 MeV beam BIC data points. However use of the INCLXX options with the 200 MeV VHEE beam resulted in neutron yields with a greater than 5% difference to the BERT data - with the largest being an approximate 12% decrease for the configuration without an applicator for a 5 cm SSD at 0 cm in the water phantom. Nevertheless all data points were comfortably within the 20% combined statistical and systematic uncertainty estimate applied to the BERT results - indicating that this conservative estimate should be sufficient in accounting for the variations in neutron production as a result of different physics options. As a final note, the previously mentioned normalising of the neutron yields when an applicator was used down to the level of the yields in the absence of an applicator is is clearly observable in Fig. 4.8.

In summary, changing the physics options has a minimal effect on neutron yields within the phantom, and a conservative estimate of 20% combined statistical and systematic is more that sufficient to account for these differences. The presence of a

physical collimating structure in the path of both the 200 MeV and 2 GeV VHEE beams acts to inject additional neutrons into the entrance region of the phantom. While the neutron yield of the beams with an applicator decreased in depth, the yield of the uncollimated beams - broadly speaking - increased in depth.

The following section details the simulation results for particle yields and ambient neutron dose equivalents in the surrounding air, between the water phantom and the concrete walls.

4.5 Neutron dose equivalent and yields in ambient air

As detailed in section 4.2, TOPAS surface scorers were placed at various distances and off-axis angles from the water phantom. These scorers were used to calculate the yields of each particle at each particular location. When used in conjunction with a filter, it was also possible to evaluate the contribution from the surrounding concrete wall. Fig. 4.9 depicts these yields in air for both the 2 GeV and 200 MeV VHEE beams at 0° and for all configurations.

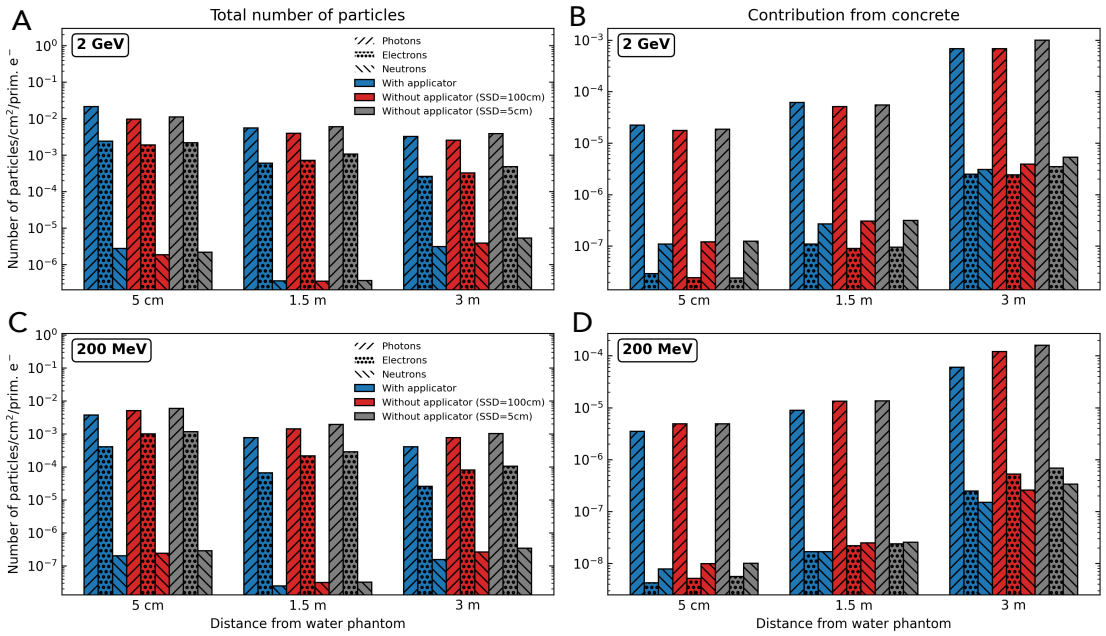

Figure 4.9: Particle yields in number of particles/cm^2/primary electron for all distances and configurations at 0°, and for both the 2 GeV (panels **A** and **B**) and 200 MeV (panels **C** and **D**) VHEE beams. Total yields from all sources are shown in panels **A** and **C**, while the yield contribution due to the concrete walls is given in panels **B** and **D**.

Looking first to the total yields of photons and electrons for both the 2 GeV and 200 MeV case, their behaviour with increasing distance from the water phantom is as expected. Their greatest presence is in the direct vicinity of the water phantom, at 5 cm, and there is a clear reduction in the yields which occurs between 5 cm and 3 m, regardless of the configuration or particle energy. This trend of decreasing particle yield with distance, however, is not replicated by the neutrons. Still looking at the total yields, for both the 2 GeV and 200 MeV VHEE beams there appears to be a reduction in the neutron yield from 5 cm to 1.5 m, followed by an increase in the yield from 1.5 m to 3

m. Ultimately, this increasing characteristic of the neutron yield was attributed to the presence of a concrete wall - as depicted in panels B and D of Fig. 4.9.

Now looking at the **yields of neutrons having undergone an interaction within the concrete, or being the descendants of a particle originating from the concrete**, the highest neutron yield for both the 2 GeV and 200 MeV VHEE beams was found at 3 m, in other words right beside the concrete wall. The closer to the phantom, the smaller the neutron yield as a result of the concrete wall. This highlights the observation that these VHEE beams, primarily through the generation of high energy photons, cause an increase in the neutron yields within the treatment room - particular in the vicinity of the concrete wall. Additionally, the composition of the radiation field is different for the yield coming from the concrete. While photons are still the dominant particle, the neutron and electron yields are similar at 3 m. All yields decrease as the distance from the concrete wall increases, and at 5 cm the neutron yield is significantly more than the electron yield. This was attributed to the greater range of neutrons generated in the concrete over electrons generated in the concrete.

The order of magnitude of the neutron yields generated for the 2 GeV VHEE beam right against the concrete wall was approximately 10^{-6} neutrons/cm^2/primary electron, while the 200 MeV neutron yields were approximately one order of magnitude lower. This additional generation of neutrons due to the concrete wall was one of the main concerns pinpointed at the outset of this chapter, and therefore a calculation of ambient neutron dose equivalents was warranted. These dose equivalents are depicted in Fig. 4.10. As previously noted, these dose equivalents were calculated by multiplying the neutron fluence by specific fluence to dose equivalent conversion coefficients [Pelliccioni, 2000], according to Equation 2.26. In order to compare the different simulation configurations which may have been simulated with a different number of primary histories, all dose equivalents were normalised to the dose delivered to the 2×2×2 cm^3 target in the water phantom.

Statistical uncertainties are depicted by the error bars in Fig. 4.10. In most cases, these error bars are not able to be visualised due to the low statistical uncertainty, however the largest uncertainties in all cases were obtained for the neutron dose equivalent originating from the concrete wall. The average statistical uncertainty on the total ambient neutron dose equivalent for the 2 GeV and 200 MeV beams was 1.36% and 4.81% respectively. The average statistical uncertainty on the ambient neutron dose equivalent due to the concrete wall for the 2 GeV and 200 MeV beams was 2.87% and 9.47% respectively.

Concerning first the total ambient neutron dose equivalents depicted by the solid lines in Fig. 4.10, the highest values are typically found right besides the concrete wall at a distance of 3 m and angle of 0° for most configurations. This is a consequence of the photons that were forward scattered in the water phantom. This conclusion can not be made for the 200 MeV VHEE beam with an applicator since the dose equivalents at 0° between the 5 cm and 3 m distance are not statistically significantly different. Besides this case, at 0° the second highest dose equivalent always occurs at 5 cm and the lowest is found at 1.5 m, highlighting the idea that if not for the concrete wall the dose equivalents would decrease with increasing distance from the water phantom. At 45° and 90° the highest total dose equivalent is always found at 5 cm, followed by the dose equivalent at 1.5 m and finally 3 m. The 2 GeV VHEE primaries experienced a maximum total ambient neutron dose equivalent of approximately 1.717 ± 0.619 mSv/Gy while the maximum value for the 200 MeV VHEE primaries was found to be 0.1942 ± 0.0701 mSv/Gy. In all cases, the total ambient neutron dose equivalents for 200 MeV beams were found to be one order of magnitude lower than the 2 GeV beams.

Sticking with the total ambient neutron dose equivalents, for both the 2 GeV

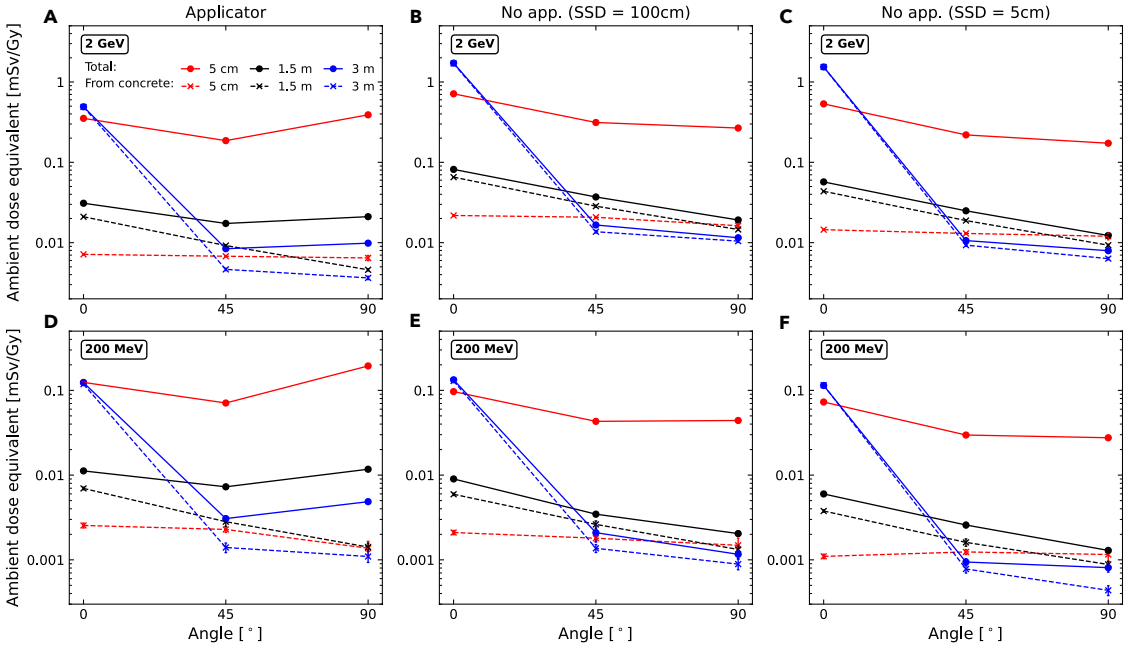

Figure 4.10: Ambient neutron dose equivalent per treatment gray at 5 cm, 1.5 m, and 3 m from the water phantom, for angles of 0°, 45°, and 90° from the central beam axis, and for all simulation configurations. Panels **A**, **B**, and **C** of the upper row correspond to the 2 GeV primaries, while panels **D**, **E**, and **F** of the bottom row correspond to the 200 MeV primaries. Each column represents a specific configuration. Solid lines with circular markers are the total dose equivalent values, while dashed lines with cross markers are dose equivalent values based on the fluence of neutrons coming from the concrete.

and 200 MeV beams, at all distances from the water phantom, and for all configurations, as the angle increases from 0° to 45° there is a decrease in the total ambient neutron dose equivalent. Interestingly, for the configurations without an applicator, Fig. 4.10 shows that the dose equivalent was either maintained at approximately the same level or decreased between 45° and 90°. This contrasts to the configuration with an applicator, in which the dose equivalent was either maintained at the same level or increased between 45° and 90°. It was therefore hypothesised that this effect occurs due to the broader scattering of neutrons by the electron applicator. Furthermore, for the applicator configurations, a more severe increase was observed between 45° and 90° for the 200 MeV beam as opposed to the 2 GeV beam which could be attributed to the neutrons generated by the more broadly scattered photons of the lower energy beam.

The dashed lines in Fig. 4.10 are representative of the ambient dose equivalents of neutrons originating from, or arising from interactions within, the concrete wall. **Considering first the configurations without an applicator**; for both the 2 GeV and 200 MeV beams a close agreement was observed between the total dose equivalent values at 1.5 m and 3 m, and the respective values of the dose equivalent contribution from concrete. This suggested that the majority of the dose equivalent at these distances was due to the concrete's contribution to the neutron fluence, with the smallest difference occurring at 3 m and 0°, where the totality of the dose equivalent is attributed to the concrete wall. At the 5 cm distance however, large differences appeared between the total dose equivalent and the dose equivalent from the concrete wall, highlighting the dominance of neutrons generated in the water phantom at this distance. If we **consider the configuration with an applicator**, this previously stated 5 cm difference holds true, however for the

dose equivalent values at 1.5 m and 3 m there is an increase in difference between the total values and the contribution from concrete between 45° and 90°. This observation provided further evidence in favour of the hypothesis that neutrons were more broadly scattered due to the presence of an applicator.

The following subsection investigates the systematic uncertainties associated with neutron yields and dose equivalent values as a result of changes in the physics list and conversion coefficients.

4.5.1 Systematic uncertainty evaluation

As stated in section 4.4.1 a conservative estimate of 20% systematic uncertainty was applied to particle yields obtained using the BERT physics option. This 20% uncertainty is visualised by the error bars in Fig. 4.11, which depicts the differences in the yield of neutrons at 0°, for different distances in ambient air.

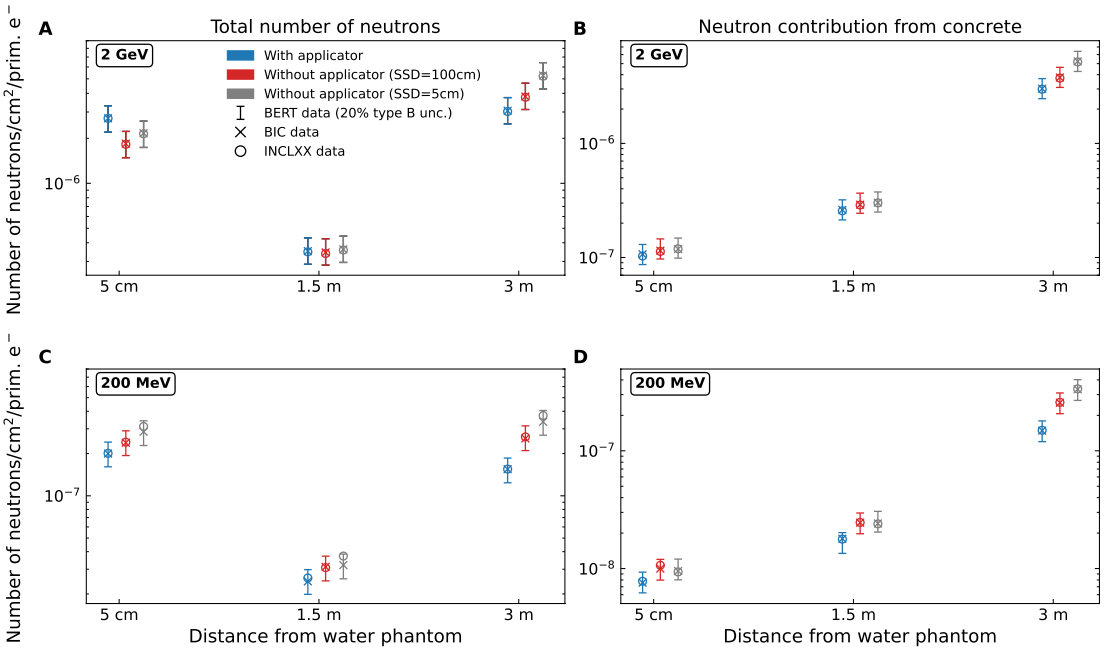

Figure 4.11: Comparison of the BERT, BIC, and INCLXX neutron yields at 5 cm, 1.5 m, and 3 m from the water phantom, for all configurations, and at angle of 0°. The 2 GeV beam is depicted in panels **A** and **B**, while the 200 MeV beam is depicted in panels **C** and **D**. The total neutron yields are shown in panels **A** and **C**, while the neutron yield contribution due to the concrete walls is shown in panels **B** and **D**.

Similarly to Fig. 4.8, which evaluated the change in neutron yields within the phantom resulting from different physics options, Fig. 4.11 highlights the fact that at all distances there was generally a good agreement between the BERT, BIC, and INCLXX results. For the 2 GeV beam, the total neutron yields using the BIC and INCLXX options were within 5% of the BERT results. This increased to 8% when considering the neutron yield contribution from concrete. All the BIC data points for the 200 MeV beam were also maintained below this 8% threshold, however use of INCLXX resulted in a greater variation, reaching a maximum of approximately 17% for the total neutron yield without an applicator for a 5 cm SSD at a distance of 1.5 m from the water phantom. Nevertheless, the conservative 20% systematic uncertainty estimate applied to the BERT results was sufficient to account for possible variations in physics options.

As stated in section 4.2.2, one of the other possible sources of systematic uncertainties are the fluence to dose equivalent conversion coefficients. Fig. 4.12 depicts the differences in the total ambient neutron dose equivalent arising when the default coefficients specified in TOPAS [Pelliccioni, 2000] were changed to the more recent coefficients of ICRU report 95 [ICRU, 2020]. Error bars in the figure are representative of a conservative 30% estimate of the systematic uncertainty arising due to changes in the conversion coefficients. This value was chosen as previous MC studies have been performed in which the variation induced by the use of older/newer conversion coefficients was found to be 15% [Zheng et al., 2008] and 30% [Schneider et al., 2002] for MCNP and FLUKA respectively.

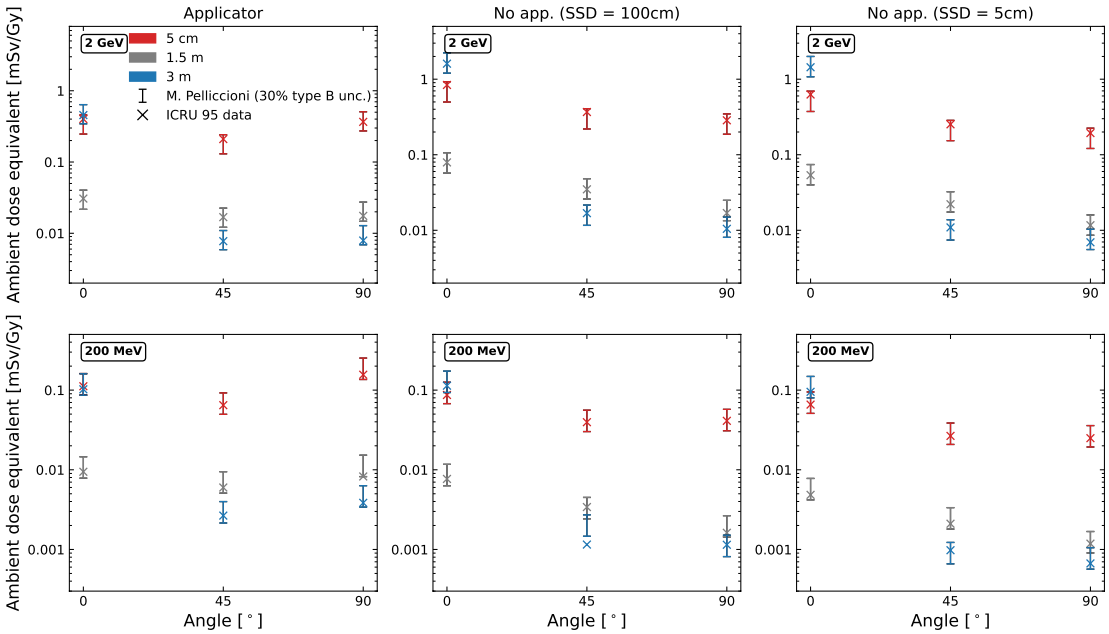

Figure 4.12: Total ambient neutron dose equivalent per treatment gray for the 2 GeV and 200 MeV beams, at 5 cm, 1.5 m, and 3 m from the water phantom, for angles of 0°, 45°, and 90° from the central beam axis, and for all simulation configurations. Error bars are indicative of the 30% type B uncertainty applied to the ambient neutron dose equivalent values obtained using the default TOPAS coefficients of M. Pelliccioni [Pelliccioni, 2000]. The cross markers are representative of the values obtained using the coefficients reported in ICRU report 95 [ICRU, 2020].

Barring one outlier for the 200 MeV beam (without an applicator for an SSD of 100 cm at 3 m from the water phantom at an angle of 45°) all variations in ambient neutron dose equivalent due to a change in the conversion coefficient were within the 30% estimate.

Table 4.3: Range of ambient neutron dose equivalent values for each configuration of the 2 GeV and 200 MeV VHEE beams. The last column of the table indicates the percentage change of the dose equivalent range reported, when the ICRU 95 conversion coefficients were used in place of the default TOPAS coefficients.

Beam energy	Simulation details	Dose equivalent [mSv/Gy]	Details	TOPAS to ICRU 95 [%]
2 GeV	With applicator (SSD = 100 cm)	0.0084 ± 0.0002 to 0.491 ± 0.002	At 300 cm. 45 ° to 0°	-7.8% to -19.8%
	Without applicator (SSD = 100 cm)	0.0115 ± 0.0004 to 1.717 ± 0.008	At 300 cm. 90° to 0°	-9.2% to -6.5%
	Without applicator (SSD = 5 cm)	0.0079 ± 0.0003 to 1.538 ± 0.005	At 300 cm. 90° to 0°	-12.7% to -6.4%
200 MeV	With applicator (SSD = 100 cm)	0.0031 ± 0.0002 to 0.1942 ± 0.0018	At 300 cm 45° to 5 cm 90°	-13.3% to -19.7%
	Without applicator (SSD = 100 cm)	0.0012 ± 0.0001 to 0.1333 ± 0.0019	At 300 cm. 90° to 0°	-1.4% to -14.7%
	Without applicator (SSD = 5 cm)	0.0008 ± 0.0001 to 0.1142 ± 0.0015	At 300 cm. 90° to 0°	-17.4% to -16.6%

Table 4.3 depicts the maximum and minimum dose equivalents obtained for each configuration, with the last column indicating the percentage change in these maximum and minimum values when the conversion coefficients were changed to the newer ICRU report 95 coefficients [ICRU, 2020]. Uncertainties on dose equivalents shown in the table are statistical uncertainties obtained from the original TOPAS simulation using the `BERT` physics options with the default TOPAS coefficients of M. Pelliccioni [Pelliccioni, 2000]. Consequently, Table 4.3 seems to indicate that the use of the newer ICRU 95 coefficients [ICRU, 2020] leads to a shift to a lower range of dose equivalent values for all configurations. This shift occurred due to a decreased minimum dose equivalent, and decreased maximum dose equivalent - thereby implying that the older coefficients used by TOPAS [Pelliccioni, 2000] were overestimating the ambient neutron dose equivalents.

In summary, the yield of neutrons initially decreased from 5 cm to 1.5 m away from the phantom, then increased between 1.5 m and 3 m. This increase was attributed to the concrete wall injecting additional neutrons into the treatment room. This injection primarily occurred on-axis, at 0°, due to the forward scattered photons. Consequently the highest ambient neutron dose equivalents occurred at 3 m and 0°, with the dose equivalents of the 2 GeV beam being approximately one order of magnitude higher than the 200 MeV beam.

Final discussions and conclusions able to drawn from the work performed in this chapter are provided in the following section.

4.6 Discussion and conclusions

This chapter of the thesis was dedicated to the work performed in view of assessing the potential additional radioprotection considerations within a treatment room delivering VHEE therapy. As previously outlined, VHEEs represent a promising new RT modality for the treatment of deep-seated tumors, due to the increased practical range compared to low energy electrons, and the narrowing of the beam penumbra at depth - both of

which becomes more severe with increasing beam energy [DesRosiers et al., 2000, Papiez et al., 2002]. Furthermore, VHEEs have been shown to be relatively insensitive to tissue heterogeneities [Papiez et al., 2002, Moskvin et al., 2010]. Despite these advantages, one of the concerns was the increased presence of photoneutrons due to the high energy beams. As noted in previous studies, this production of neutrons, while likely negligible within the phantom [DesRosiers et al., 2000, Subiel et al., 2014], is dependent on various other factors related to the type of treatment machine used [Ronga et al., 2021, Naseri and Mesbahi, 2010]. Consequently, the work of this chapter extended the scope of previous dose equivalent calculations and investigated the effect of surrounding concrete walls, as well as the impact of a physical collimating structure for better dose conformality.

Firstly, investigations were performed looking at the absorbed doses within the water phantom. This work was outlined in section 4.3. It was observed that the presence of an applicator reduces the depth of the dose build-up region, resulting in lower exit doses, but higher entrance doses for both the 2 GeV and 200 MeV beams. This is in contrast to the uncollimated beams in which the 200 MeV beam is approximately constant throughout, while the 2 GeV beam starts off at a low dose and gradually increases with depth into the phantom. In terms of the beam penumbra, the higher the beam energy, the lower the applicator's impact on beam penumbra reduction, and it is uncertain whether the slight gain in distant penumbra doses is sufficient to compensate for the additional neutrons produced by the physical structure.

Looking at the **neutron yields within the phantom**, the applicator acts to inject additional neutrons into the entrance region of the phantom, however evaluations of ambient neutron dose equivalents surrounding the water phantom appeared to indicate a more broader scattering due to the presence of an applicator. This led to the situation shown in Fig. 4.8, whereby the additional neutron yield within the phantom from the applicator normalised to a level comparable to when an applicator was not used (i.e. the broader scattering of neutrons meant that fewer were able to reach the scoring surfaces in the latter depths of the phantom). Similarly to the work of DesRosiers *et al.* and Subiel *et al.*, figures 4.6 and 4.8 seem to indicate an approximate quasi-isotropic neutron yield within the water phantom with a lower fluence in the first few centimetres [DesRosiers et al., 2000, Subiel et al., 2014].

The early works of DesRosiers *et al.* evaluated the theoretical production of neutrons by the giant dipole resonance, which was described as being 6×10^{-5} neutrons per electron per MeV. From this value they predicted approximately 0.03 and 0.04 neutrons/cm^2/primary electron for 150 MeV and 200 MeV VHEE beams respectively [DesRosiers et al., 2000]. This was contrasted with the more recent work of Subiel *et al.*, who used the FLUKA MC code and calculated yields within a water phantom of between 10^{-7} and 10^{-5} neutrons/cm^2/primary electron for a 165 MeV VHEE beam [Subiel et al., 2014]. As seen in Table 4.2, the neutron yields within the phantom were found to be on the order of between 10^{-8} and 10^{-5} neutrons/cm^2/primary electron, depending on the configuration of the simulation. Despite the orders of magnitude higher neutron yield found by Subiel *et al.*, similarly to DesRosiers *et al.*, the conclusion was that there would be a negligible contribution of neutrons to the dose equivalent within a water phantom [DesRosiers et al., 2000, Subiel et al., 2014]. Consequently similar conclusions were reached in the work presented in this chapter given the similar neutron yields found.

Concerning the ambient neutron dose equivalents within the treatment room, there was an additional injection of neutrons on-axis at 3 m due to the presence of a concrete wall. As shown in Fig. 4.9, despite these additional neutrons due to the concrete wall, their yield was on the order of approximately 10^{-7} to 10^{-6} neutrons/cm^2/primary

electron for the 2 GeV beam, with the yields for the 200 MeV beam being approximately one order of magnitude lower. In fact, these additional neutrons due to the presence of a concrete wall were similarly observed for proton beams [Schneider et al., 2002, Hälg and Schneider, 2020].

Within this chapter, systematic uncertainties arising from changes in both the physics list and fluence to dose equivalent conversion coefficients was performed, as shown in Figures 4.8, 4.11, and 4.12. In both cases, conservative estimates of 20% and 30% were found to adequately describe the possible variations in the MC calculated quantities. Ultimately, these systematic uncertainties were combined in quadrature with the statistical uncertainties on dose equivalents shown in Table 4.3 in order to have a more realistic range of values from which comparisons to conventional RT could be made. This combination in quadrature provides an adequate estimation of the combined standard uncertainty for MC simulations [Andreo et al., 2012]. Table 4.4 depicts these new combined uncertainties for each configuration in relation to a few studies on the ambient neutron dose equivalent values of proton beams.

Table 4.4: Range of ambient neutron dose equivalent values for this work with a combined uncertainty accounting for variations due to physics options and conversion coefficients. The results of this work were then compared to other studies involving protons [Schneider et al., 2002, Charyyev and Wang, 2020, Zheng et al., 2008].

Reference	Particle	Simulation details	Dose equivalent [mSv/Gy]	Details
This work	2 GeV, VHEE	With applicator (SSD = 100 cm)	0.0084 ± 0.0031 to 0.491 ± 0.177	At 300 cm. 45 ° to 0°
		Without applicator (SSD = 100 cm)	0.0115 ± 0.0042 to 1.717 ± 0.619	At 300 cm. 90° to 0°
		Without applicator (SSD = 5 cm)	0.0079 ± 0.0029 to 1.538 ± 0.555	At 300 cm. 90° to 0°
	200 MeV, VHEE	With applicator (SSD = 100 cm)	0.0031 ± 0.0011 to 0.1942 ± 0.0701	At 300 cm 45° to 5 cm 90°
		Without applicator (SSD = 100 cm)	0.0012 ± 0.0005 to 0.1333 ± 0.0481	At 300 cm. 90° to 0°
		Without applicator (SSD = 5 cm)	0.0008 ± 0.0003 to 0.1142 ± 0.0412	At 300 cm. 90° to 0°
Schneider *et al.*	177 MeV Protons	Spot scanned pencil	0.02 to 7	Dose equivalent from 100 cm to 5 cm (lateral distances from central beam axis)
Charyyev *et al.*	120 MeV Protons	Minibeam collimator	0.017 to 3.23	Dose equivalent from 0°, 105 cm from phantom to 135° and 11 cm from water phantom
		Uncollimated pencil	0.0013 to 0.242	Dose equivalent from 135°, 105 cm from phantom to 0° and 11 cm from water phantom
Zheng *et al.*	100 to 200 MeV Protons	Passively scattered	0.3 to 19	14.1 cm diameter scattered field, to 35.4 cm diameter scattered field

The dose equivalent values obtained by Zheng *et al.* [Zheng et al., 2008] and Charyyev *et al.* [Charyyev and Wang, 2020] were from MC simulations carried out on MCNP and TOPAS respectively. These MC calculations concluded, similarly to previous experimental

work, that ambient neutron dose equivalent values of a few mSv per treatment gray in proton therapy can be expected - depending on the size of the field, presence/absence of a physical collimator, and beam energy among other physical parameters [Schneider et al., 2002, Han et al., 2017, Howell and Burgett, 2014]. The range of dose equivalent values in proton therapy are extensively covered by the review paper of Hälg *et al.*, where the main conclusion reached was that the neutron dose in proton therapy was unlikely to have a considerable influence on the risk of secondary cancers [Hälg and Schneider, 2020]. Furthermore, Hälg *et al.* also concluded that the ambient neutron dose equivalent in active scanning treatments is lower compared to passively scattered protons, and in general, is also lower than the neutron dose equivalents in the vicinity of the patient for conventional RT treatments with photons, which lie in the range of approximately 0.1 to 20.4 mSv/Gy [Takam et al., 2011, Hälg and Schneider, 2020].

Given the conservative estimate for the range of dose equivalent values likely to be obtained in VHEE, shown in Table 4.4, the conclusion was made that a **clinical implementation of VHEEs would be quite similar to conventional proton therapy treatments**, given the ambient neutron dose equivalent values of a couple of mSv per treatment gray. Although there have been more published works showing the benefits of VHEEs in the 200 MeV energy range compared to 2 GeV beams, the work in the chapter has shown that from an ambient neutron dose equivalent point of view there should be no considerable radioprotection issues outside of the norm for even higher energy electron beams when compared to conventional treatments. Nevertheless, dedicated facilities with appropriately shielded bunkers would be necessary.

One of the limitations of this work is that the scoring surfaces used in the calculation of the neutron dose equivalent were placed at a limited amount of locations. This gives a general idea of the area monitoring considerations one would need to take into account, however a full picture would only be able to be gleamed by considerably expanding the locations investigated. Secondly, the induced activation caused by secondary neutrons was not explicitly considered, however previous studies have concluded that the induced radioactivity is negligible in terms of its contribution to the dose deposited within a water phantom [Kokurewicz et al., 2019, DesRosiers et al., 2000, Subiel et al., 2014]. Lastly, the impact of the thickness of the concrete wall was not evaluated. It has been previously shown that there is a higher neutron yield for higher energy photons (in the energy range well above the giant dipole resonance) when the thickness of the target is increased [IAEA, 1979] - which could be one of the contributing factors to the increased neutron yield observed for the 2 GeV VHEE beams in the vicinity of concrete wall.

In conclusion, the use of an applicator as a collimating structure for VHEEs results in additional neutrons in the first few centimetres of the water phantom, as well as a broader scattering of those neutrons in the ambient air surrounding the collimating structure. Despite this, given the relatively low ambient neutron dose equivalent, a clinical implementation of collimated or uncollimated VHEEs would likely not warrant any supplementary safeguards from a radioprotection point of view compared to conventional proton therapy. **The results of this work have been published in *Scientific Reports* [Masilela et al., 2021].**

Chapter 5

Theoretical RBE calculation for VHEEs

This chapter details investigations into the theoretical RBE for beams of VHEEs, which was performed in collaboration with R. Delorme, C. Etoh, F. Smekens, and Y. Prezado. This work was eventually published in *Scientific Reports* [Delorme et al., 2021], where I was listed as the second author and assigned the role of performing the appropriate GATE simulations. Given that VHEEs have already been discussed in the previous chapter, only a brief rationale is provided in section 5.1, followed by the simulation details (section 5.2), results of the macroscopic study (section 5.3), results of the microscopic study (sections 5.4 and 5.5), and the discussion and conclusions (section 5.6).

5.1 Rationale for the work

As described in the previous chapter, the main advantages of VHEE therapy are the increased practical range compared to clinical low energy electrons, narrowing of the beam penumbra with depth, and relative insensitivity to tissue heterogeneities [DesRosiers et al., 2000, Papiez et al., 2002, Lagzda et al., 2020]. However one of the major uncertainties with the use of these beams remains the lack of knowledge about their biological impact and RBE.

As noted in chapter 4, the high energy photons produced from these beams have been pinpointed as one of the potential areas of concern due to their high biological effectiveness. While DesRosiers *et al.* hypothesised that an RBE of 1.02 should be sufficient for dose prescription in VHEE therapy [DesRosiers et al., 2000], a direct evaluation of RBE from these VHEE beams had, at the time this work was performed, not yet been evaluated.

Consequently, there was a clear interest in better understanding the biological consequences of VHEEs in view of providing additional arguments in favour creating more facilities at which these biological consequences could be investigated experimentally. To this end, the work in this chapter was performed which made use of MC simulations in GATE to evaluate the potential biological effects from both a macroscopic, and microscopic point of view. In the macroscopic study, dose-averaged LETs were calculated, which have been shown to correlate well with biological effects [McMahon et al., 2018] and are in fact sufficiently good predictors of RBE for regions of narrow LET distributions [Grün et al., 2019]. In the microscopic study, a TEPC geometry was implemented into the GATE simulation to record lineal energy spectra, from which cell survival curves and theoretical RBE values were calculated using the modified MKM (described in section 2.5). This TEPC geometry operates similarly to an ionisation chamber, however instead of air, the sensitive volume is filled with a low pressure tissue-equivalent gas, thus allowing the detector to mimic the shape and composition of micrometer size biological structures [Chang and Kim, 2008].

Details of the GATE simulations performed in this chapter are provided in the following section.

5.2 Simulation details

All simulations were performed with GATE [Jan et al., 2011, Sarrut et al., 2014] version 8.2, with Fig. 5.1 depicting a schematic representation of the simulation geometry.

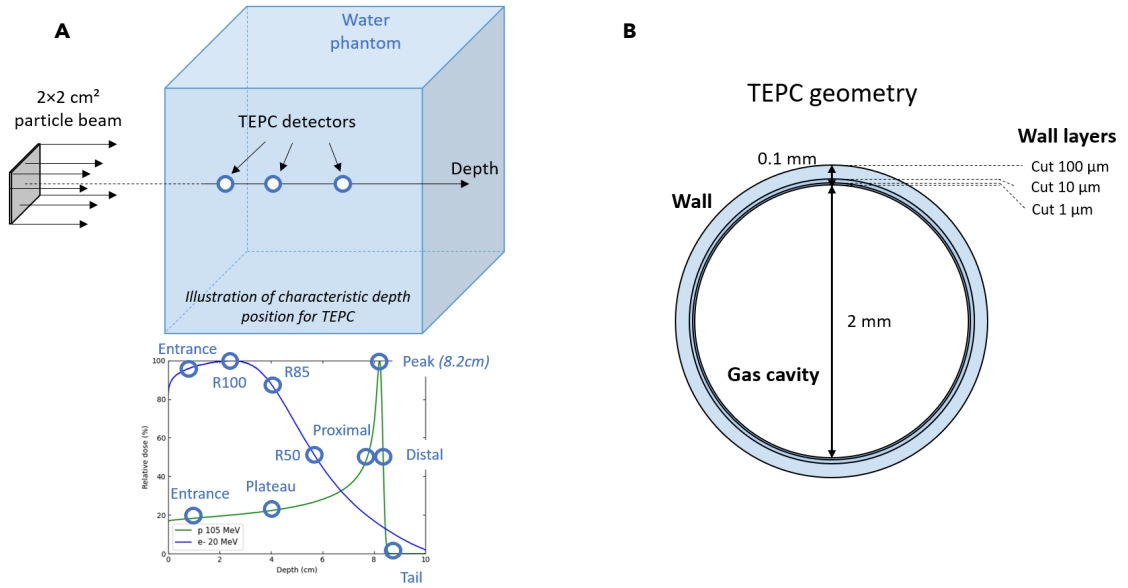

Figure 5.1: Panel **A** depicts the 2×2 cm^2 irradiation field, and 10×10×10 cm^3 water phantom with GATE TEPC actors positioned at various depths. Panel **B** depicts the geometry of the TEPC detector, along with the tracking cuts of various dimensions applied to each layer of the wall. Taken from [Delorme et al., 2021].

Panel A of Fig. 5.1 depicts the 2×2 cm^2 source of photons, electrons, protons, ^{12}C ions, and ^{20}Ne ions, irradiating a 10×10×10 cm^3 water phantom, with TEPC actors placed at various depths. For the proton and heavy ions beams, these TEPC actors were positioned in the entrance region (at 1 cm), in the plateau (at 4 cm), in the Bragg peak position (at 8.2 cm), in the distal dose fall-off region (corresponding to 50% of the peak dose), and in the fragmentation tail. For the electron and photon beams, TEPC actors were placed in the entrance region (at 1 cm depth), and at depths of R100, R85, and R50, corresponding to 100%, 85% and 50% of the maximum on-axis dose deposited respectively. Additional TEPCs were placed at 4 cm and 8.2 cm in order to be able to make comparisons with the proton and heavy ion beams. Panel B of Fig. 5.1 depicts the TEPC geometry implemented in the simulation. The simulation can effectively be thought of as two separate sets. In the first set of simulations (macroscopic), doses and dose-averaged LETs were calculated. In the second set of simulations (microscopic), lineal energies were recorded and used to calculate the dose-mean lineal energy. Both the macroscopic and microscopic sets of simulations will be further detailed in the following subsection.

5.2.1 GATE actors

In the macroscopic study, both the absorbed dose (in the form of PDD profiles) and the dose-averaged LET ($\bar{L}_d$) were calculated in order to have a more comprehensive physical description of the particle beams. The quantities were obtained by using the `Dose` and `LET` actors of GATE, and scoring was performed on a discretized on-axis volume of the water phantom, corresponding to voxel sizes of 1 mm × 1 mm × 100 μm (x,y,z). The

GATE particle tracking cut for the simulation of these macroscopic quantities was set to 0.1 mm, which was found to be the best compromise between precision and computational expense, and was in line with the recommendation made by Guan *et al.* for the calculation of dose-averaged LET [Guan et al., 2015].

Given the fact that the stochastic nature of energy depositions on the micrometer scale are not fully considered in the absorbed dose or LET, a microscopic study was performed in which a TEPC actor of GATE was used to calculate the lineal energy spectra. This microdosimetric quantity was detailed in section 2.2.4. The probability density $f(y)$ for each depth within the water phantom was obtained using the TEPC actor, and the dose-weighted lineal energy distributions ($yd(y)$), and dose-mean lineal energies ($\bar{y}_d$) were then calculated from these distributions. The evaluation of beam quality using these specific quantities is in line with previous microdosimetric work [Cortés-Giraldo and Carabe, 2015, Guan et al., 2015, Wilkens and Oelfke, 2003, Liamsuwan et al., 2014]. Calculation of these quantities from the $f(y)$ spectra was done through Equations 2.12 and 2.13, reproduced below for better readability:

$$d(y) = \frac{y}{\bar{y}_F} f(y) \tag{5.1}$$

$$\bar{y}_D = \int_0^\infty y d(y) dy = \frac{1}{\bar{y}_F} \int_0^\infty y^2 f(y) dy \tag{5.2}$$

The TEPC sensitive volume was filled with gaseous mixture of propane (C_3H_8), oxygen (O_2), and nitrogen (N_2), and set to a pressure of 277 mbar, calculated according to Equation 5.3, where subscript t refers to the tissue, and subscript g refers to the TEPC gas. The variable P_g is the pressure of the TEPC gas, ρ refers to the respective densities in g/cm^3, d refers to the respective diameters in mm, P_{atm} refers to the atmospheric pressure in bars, and T is the room temperature in degrees Celsius [Chang and Kim, 2008]. This allows the TEPC to emulate the interactions within a 1 μm sphere of tissue equivalent material.

$$\begin{aligned} P_g &= \frac{\rho_t}{\rho_g} \cdot \frac{d_t}{d_g} \cdot P_{atm} \cdot \frac{273 + T}{273} \\ &= \frac{1}{1.83 \times 10^{-3}} \cdot \frac{0.001}{2} \cdot 1.01325 \cdot \frac{273 + 0}{273} \\ &= 277 \text{ mbar} \end{aligned} \tag{5.3}$$

As can be see in panel B of Fig. 5.1, various particle tracking cuts were applied to the wall of the TEPC geometry. The total wall thickness was 0.1 mm and consisted of 3 concentric spherical water shells of radius 1.1, 1.01 and 1.001 mm. The particle tracking cut was then set to 100 μm, 10 μm and 1 μm respectively in each spherical water shell, and the tracking cut of 1 μm was also applied to the sensitive volume. These tracking cuts were assigned so as to increase the precision of particle transport within the GATE TEPC. This configuration of a TEPC detector implemented into GATE has been shown to reproduce the measured lineal energy spectra data of Kase *et al.* for a proton beam [OpenGATE Collaboration, 2023, Kase et al., 2013].

5.2.2 Physics processes and particle sources

Monoenergetic particles were uniformly generated on a square surface of 2×2 cm^2 and launched towards the water phantom with no angular divergence. The types of particle and their energy are shown in Table 5.1 where the energies of the protons and heavy ions

were chosen so as to have the Bragg peak occurring at approximately the same location (∼8.2 cm in this case). Additionally, beams of neon ions were added to this study due to the recent renewed interest in their use in combination with MBRT [Prezado et al., 2021].

Table 5.1: Type of particle and energy used in this work.

Particle	Energy [MeV or MeV/nucleon]
Photons	1.25
Protons	105
^{12}C ions	194.2
^{20}Ne ions	262
Electrons	5
	20
	100
	300

Between 10^9 and 10^{10} primary particles were simulated for each source in order to have a satisfactory compromise between simulation time and statistical uncertainty. To this end, the number of primaries simulated was chosen such that the statistical uncertainty in each on-axis voxel of the PDD or $\bar{L}_d$ profiles was lower than 2%. The energy of the beam of photons was set to 1.25 MeV, as this is the mean energy of two ^{60}Co rays. The `QGSP_BERT_HP_EMY` physics list was then used for all simulations.

5.2.3 Cell survival and theoretical RBE from the modified MKM

Using the microdosimetric spectra $f(y)$ obtained from the GATE TEPC actor, cell survival curves were calculated according to the modified MKM, described by Equations 2.24 and 2.25 in section 2.5 but repeated below for readability:

$$S = e^{\left(-\left(\alpha_0 + \frac{\beta}{\rho \pi r_d^2} y^*\right) D - \beta D^2\right)} \tag{5.4}$$

$$y^* = \frac{{y_0}^2 \int 1 - e^{-\left(\frac{y}{y_0}\right)^2} f(y) dy}{\int y f(y) dy} \tag{5.5}$$

Consequently, theoretical RBE values (RBE_{10}) were then calculated as the ratio of the dose required in the reference ^{60}Co beam to the beams of protons, electrons, and heavy ions, resulting in a 10% survival fraction.

The following section describes the results of the macroscopic study, namely the calculation of PDD profiles and the dose-averaged LET.

5.3 Macrodosimetric study: dose and dose-averaged LET

Figure 5.2 depicts the PDD curves obtained for each of the particle sources. Statistical uncertainties within each scoring voxel depositing at least 0.1% of the maximum dose was kept below 1%. These PDD curves are consistent with what is expected from literature. Electrons at the clinically relevant energies of 5 and 20 MeV exhibit a maximum dose deposition at relatively shallow depths, thus making them suitable for the treatment of superficial tumors. The beam of protons exhibits a characteristic Bragg peak at approximately 8.2 cm, and both carbon and neon ions have similar PDD profiles to that of the proton beam, however they exhibit a *sharper* pristine Bragg peak, as well as a fragmentation tail.

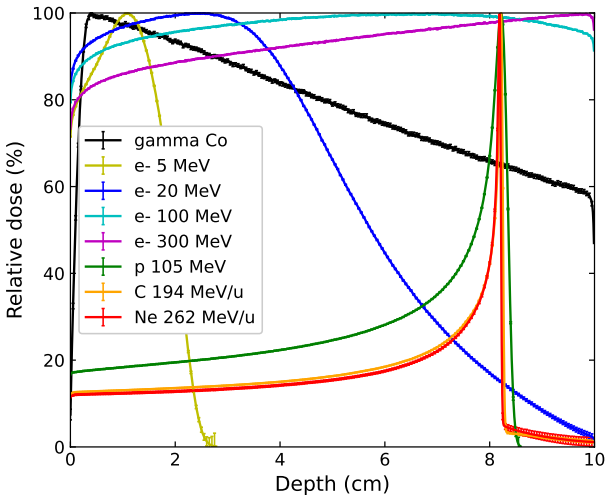

Figure 5.2: PDD profiles in the water phantom for the beams of photons, clinical electrons, 100 and 300 MeV electrons, protons, ^{12}C ions, and ^{20}Ne ions.

The VHEEs, as seen in sections 2.8 and 4.3, presents a flatter, almost homogeneous profile throughout the water phantom, in comparison to both the lower energy electrons or photon beams which vary significantly over their respective ranges. This is one of the dosimetric characteristics of VHEE therapy that is often put forward as an argument in favour of its use over photons for the treatment of deep-seated tumors, particularly if used in combination with intensity modulation techniques [Bazalova-Carter et al., 2015, Schüler et al., 2017].

The second macrodosimetric quantity evaluated was the dose-averaged LET, as shown in Fig. 5.3. Statistical uncertainties within each voxel were kept below 2%. Based on these $\bar{L}_d$ profiles it is evident that the heavier neon ion beam has a higher LET ($>$ 30 keV/μ m) than all the other beams at all depths in the water phantom. While protons, carbon ions, and neon ions all have a similar behaviour in depth, the carbon and neon ion beams exhibit very high LETs ($>$ 200 keV/μ m) in the vicinity of the Bragg peak. Nevertheless, the $\bar{L}_d$ for ^{20}Ne was found to be approximately 3 times higher than that of the ^{12}C beam, thus suggesting, similar to the work of González *et al.*, that neon ion beams may induce a greater biological effect than carbon beams, for very similar physical dosimetric behaviour [González and Prezado, 2018]. Both the carbon and neon beams exhibited a non-negligible $\bar{L}_d$ beyond the Bragg peak due to the fragmentation tail.

Compared to the heavy ion beams, the beam of protons have a much reduced LET,

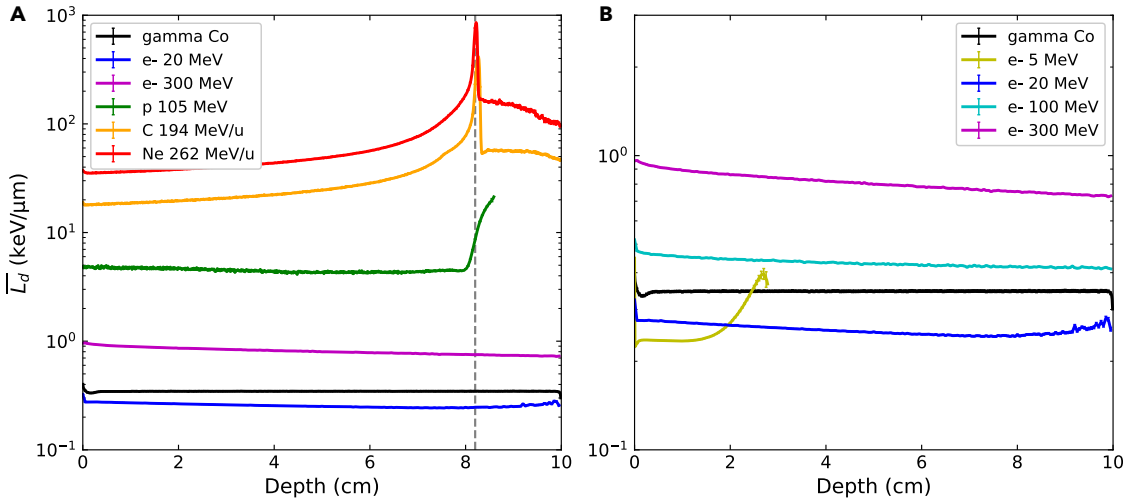

Figure 5.3: Dose-averaged LET in the water phantom for the beams of photons, clinical electrons, 100 and 300 MeV electrons, protons, ^{12}C ions, and ^{20}Ne ions. The Bragg peak location (∼8.2 cm) is depicted by the vertical dashed line in panel **A**. Panel **B** specifically shows the VHEE beams in comparison to clinical electrons/photons.

staying below 10 keV/μ up to the Bragg peak. The maximum $\bar{L}_d$ for the beam of protons is shifted to a depth greater than the point corresponding to the maximum of the dose deposited (Bragg peak). This observation is consistent with the literature on proton therapy [Lu and Flanz, 2020] in which the low energy protons at the end of their range cause this increase in the $\bar{L}_d$ beyond the Bragg peak. Interestingly, from this macroscopic point of view the VHEE beams of 100 and 300 MeV seemed to display a higher LET (of approximately unity) compared to conventional low energy electrons or the beam of photons. These low LET radiations have an LET that remains approximately constant over the entire depth as shown in panel B of Fig. 5.3, except for the 5 MeV electrons which exhibit an increase in their $\bar{L}_d$ due to their limited range. The $\bar{L}_d$ values at 4 cm and 8.2 cm in the water phantom are depicted in Table 5.2. At 4 cm, the ratio of the $\bar{L}_d$ values of the 300 MeV VHEE to that of the beams of neon ions, carbon ions, protons, 100 MeV electrons, 20 MeV electrons, and photons, is 0.02, 0.04, 0.2, 1.9, 3.2 and 2.4 respectively. The ratios at 8.2 cm were found to be 0.001, 0.003, 0.09, 1.8, 3.1 and 2.2.

In summary, work in this macroscopic study yielded PDD curves consistent with literature. Interestingly, evaluation of the dose-averaged LET highlighted a slightly higher $\bar{L}_d$ for the VHEE beams compared to electrons at clinical energies or beams of photons. This increased $\bar{L}_d$ suggests a potential slightly higher biological efficacy of these VHEE beams compared to clinical photons or electrons.

The following section details the simulation results in the microscopic study, in which lineal energy spectra were calculated.

5.4 Microdosimetric study: lineal energy spectra

As described in section 5.2, a GATE TEPC was used to score the lineal energy spectra $f(y)$, from which the dose-weighted lineal energy spectra $yd(y)$ could be calculated according to Equation 5.1. These spectra are shown in Fig. 5.4 for each of the sources at different

depths. Not only do these spectra take into account the stochasticity of energy deposition events which is missed in the dose-averaged LET, but the expectation is that two different types of radiation with identical dose-weighted lineal energy spectra should have the same RBE [Liamsuwan et al., 2014].

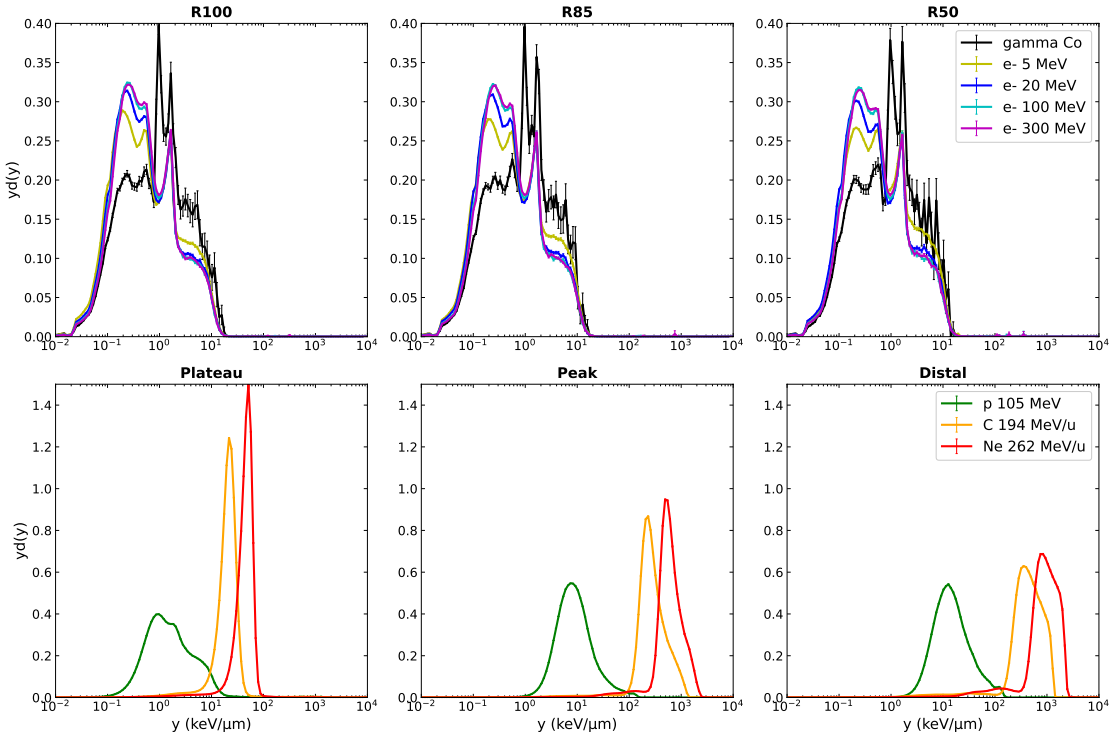

Figure 5.4: Dose-weighted lineal energy spectra $yd(y)$ at various distances for the photon and electron beams (panels of the upper row), and the proton and ion beams (panels of the lower row).

The y-axis of Fig. 5.4 can be interpreted as analogous to the dose, while larger lineal energies shown on the x-axis correspond with larger event sizes, i.e. more energy transmitted per event [Liamsuwan et al., 2014]. The photon and electron beams have very similar spectra, regardless of beam energy, covering approximately the same range of lineal energies between 0.01 and 10 keV/μm. Beyond approximately 1 keV/μm, there are large spikes in the photon spectra, indicating the highly stochastic nature of dose depositions by photons as their energy increases. Generally speaking, the electron beams have a higher frequency of low energy deposition events, while more energy is transmitted per photon interaction at higher energies. Based on these lineal energy spectra, no strong conclusions could be drawn about the behaviour of VHEE beams compared to electron beams of clinical energies.

A shift of the spectra to higher lineal energies, as was the case for the ion beams, implies an increase in the aggressiveness of the event, i.e. a greater frequency of lethal, high energy deposition events. As seen in Fig. 5.4, the higher the mass of the particle, the narrower the dose-weighted lineal energy spectra and the larger the shift to high lineal energy values. At depths closer to the Bragg peak, there is a broadening of the spectra and decrease in amplitude due to the slowing down of the particles. A comparison of all sources at 4 cm (plateau) and 8.2 cm (Bragg peak) is shown in Fig. 5.5.

At 4 cm, the narrowest spectra was obtained for the beam of ^{20}Ne ions, extending over one order of magnitude between approximately 10 and 100 keV/μm. This was increased to

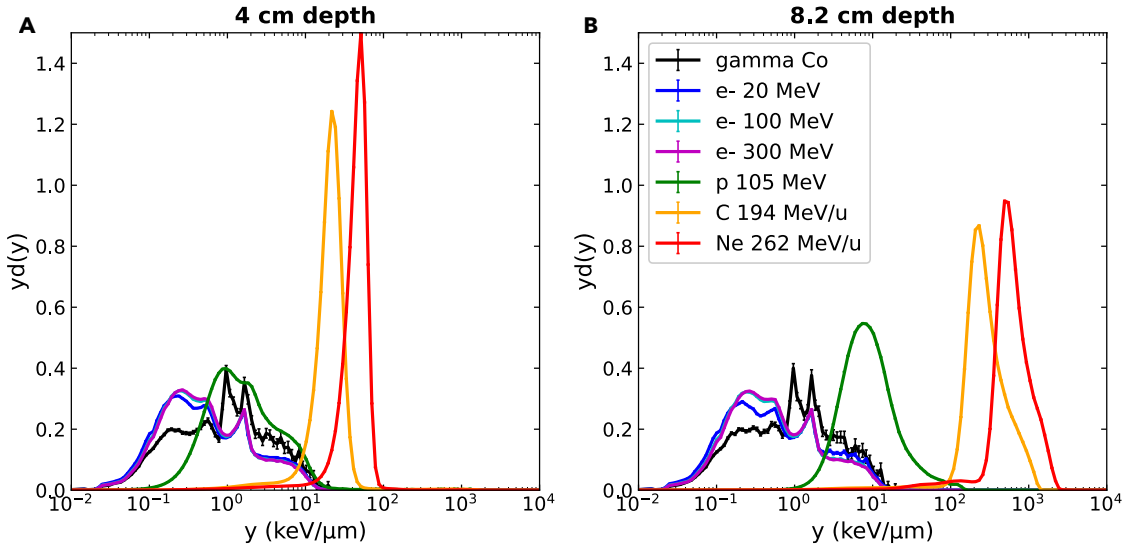

Figure 5.5: Comparison of dose-weighted lineal energy spectra $yd(y)$ for all beams at the same depths of 4 cm (panel **A**) and 8.2 cm (panel **B**) in the water, corresponding to the plateau and Bragg peak regions respectively.

between approximately 200 and 2000 keV/μm in the Bragg peak. Protons behave similarly to the beam of photons and electrons in the plateau region, however shift to higher lineal energies in the Bragg peak. Figure 5.5 clearly highlighted the difference in microscopic behaviour of low LET particles such as electrons, photons, and protons in the plateau region, to the high LET particles of carbon ions, neon ions, and protons in the Bragg peak. The dose-mean lineal energies were then calculated according to Equation 5.2 in order to act as the microdosimetric analogue to the dose-averaged LET. The resulting graphs are shown in Fig. 5.6

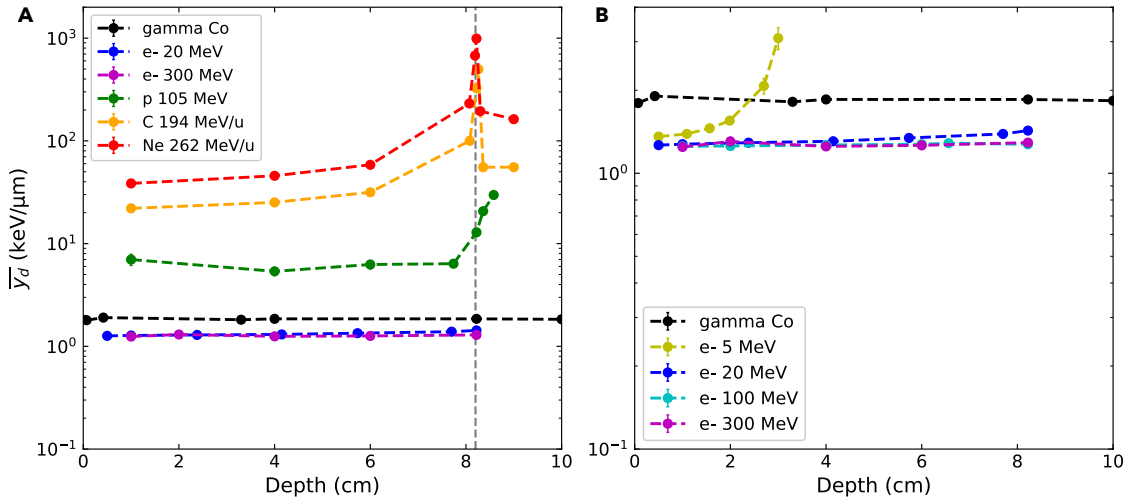

Figure 5.6: Dose-mean lineal energies $\bar{y}_d$ for each particle beam as a function of depth into the water phantom. The vertical dashed line in panel **A** represents the location of the Bragg peak, and panel **B** specifically compares the $\bar{y}_d$ of the electron beams to the beam of photons.

As was the case for the $\bar{L}_d$ profiles in Fig. 5.3, the ion and protons beams exhibit an increase in the $\bar{y}_d$ with depth, with the carbon and neon beams in particular observing high

$\bar{y}_d$ values at depths beyond the Bragg peak due to the fragmentation tail. A comparison of the low LET beams is shown in panel B of Fig. 5.6. In contrast to the $\bar{L}_d$ profiles for VHEEs shown in Fig. 5.3, the dose-mean lineal energy profiles of Fig. 5.6 do not seem to indicate a higher $\bar{y}_d$ of the VHEEs compared to the clinical low energy electrons. In fact these high energy electron beams have an even lower $\bar{y}_d$ than the beam of photons. A comparison of the different $\bar{L}_d$ and $\bar{y}_d$ values for each source at the depths of 4 cm and 8.2 cm is shown in Table 5.2.

Table 5.2: Calculated values of $\bar{L}_d$ and $\bar{y}_d$ for all simulated particles at the depths of 4 cm and 8.2 cm in the water phantom.

Particle	$\bar{L}_d$ **- 4 cm**	$\bar{y}_d$ **- 4 cm**	$\bar{L}_d$ **- 8.2 cm**	$\bar{y}_d$ **- 8.2 cm**
^{60}Co gammas	0.345 ± 0.003	1.85 ± 0.05	0.346 ± 0.003	1.85 ± 0.05
20 MeV e^-	0.255 ± 0.001	1.307 ± 0.006	0.244 ± 0.001	1.43 ± 0.01
100 MeV e^-	0.431 ± 0.001	1.265 ± 0.007	0.420 ± 0.001	1.273 ± 0.005
300 MeV e^-	0.817 ± 0.001	1.251 ± 0.006	0.757 ± 0.001	1.29 ± 0.02
Protons	4.384 ± 0.009	5.3 ± 0.6	8.695 ± 0.02	12.86 ± 0.08
^{12}C ions	22.26 ± 0.03	25.2 ± 0.2	231.9 ± 0.4	325.4 ± 0.4
^{20}Ne ions	43.8 ± 0.2	45.73 ± 0.08	762 ± 5	990.7 ± 0.7

The differences between $\bar{y}_d$ and $\bar{L}_d$ shown in Table 5.2 highlight the idea that different results can be obtained depending on if a situation is evaluated from either a macroscopic or microscopic point of view. At 4 cm, there appears to be a good agreement between $\bar{y}_d$ and $\bar{L}_d$ values for the proton and ion beams, as values of a similar order of magnitude were obtained. This similarity becomes less so in the Bragg peak. In comparison, the $\bar{y}_d$ and $\bar{L}_d$ for the photon and electron beams are significantly different from one another at both depths, with $\bar{y}_d$ values being approximately on order of magnitude higher.

In summary, the $yd(y)$ spectra highlight how, from a microdosimetric point of view, the photon and electron beams behave very similarly, regardless of differences in the electron energy. This was quantitatively assessed through a calculation of $\bar{y}_d$. Ultimately it was observed that the $\bar{y}_d$ for the VHEE beams was not substantially different from that of the lower energy clinical electrons, which directly contradicts the findings from the macroscopic study. There was a clear distinction between the microscopic behaviour of low LET photons/electrons and the high LET ions/protons in the Bragg peak, in that protons and ions were more aggressive, inducing more frequently lethal events.

The following section details the use of these microdosimetric spectra, through the modified MKM, to calculate the cell survival curves and theoretical RBE.

5.5 Cell survival curves and theoretical RBE

Using microdosimetric spectra obtained from the TEPC in GATE, the surviving fraction of cells was calculated using the modified MKM, shown in Equations 5.4 and 5.5. Cell

survival curves from the experimental measurements by Kase *et al.* were also included in Fig. 5.7 in order to validate the simulations performed.

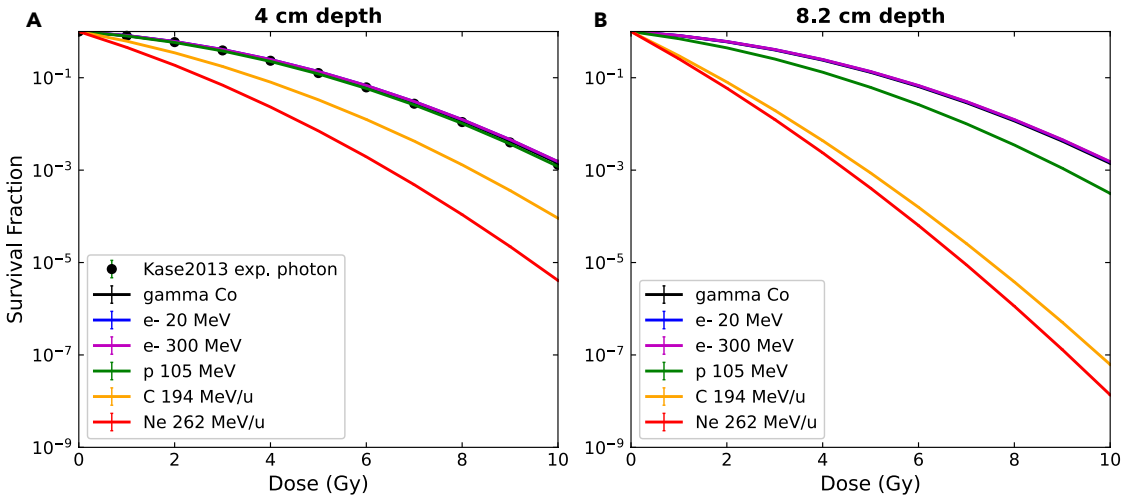

Figure 5.7: Theoretical cell survival curves calculated from the modified MKM for all particle sources. Panels **A** and **B** represent the survival fraction as a function of dose for the depths of 4 cm and 8.2 cm respectively. Experimental cell survival curves from Kase *et al.* are shown by the black circles in panel **A** [Kase et al., 2013].

Given the fact that the only physical descriptor of the particle beam in the calculation of cell survival from the modified MKM is the lineal energy spectra, it was expected that the cell survival of the VHEE beams would be indifferent from those of the photon/low energy electron beams. This similarity between the irradiation modalities is evident in Fig. 5.7 for both 4 cm and 8.2 cm. The benefit of the higher LET protons, carbon ions, and neon ions over low LET radiations is also evident in Fig. 5.7, which depicts a lower survival associated with the use of these beams over the use of photons or electrons. In the plateau region the calculated cell survival of the beam of protons was similar to that of the beams of photons or electrons - highlighting one of the benefits with their use, namely the greater sparing of normal tissue at shallow depths. The survival curves of ^{12}C in comparison to ^{20}Ne are more separated in the plateau region than they are in the peak, which was attributed to the increased overkill effect for neon ions in the Bragg peak [Mehnati et al., 2005]. Using the cell survival of the ^{60}Co photons as the reference, RBE_{10} values associated with a 10% survival fraction were calculated, as shown in Table 5.3.

Table 5.3: Relative biological effectiveness at 4 cm and 8.2 cm for the beams of 20 MeV electrons, 300 MeV electrons, protons, carbon ions, and neon ions.

Particle	**RBE_{10} - 4 cm**	**RBE_{10} - 8.2 cm**
20 MeV e^-	0.989 ± 0.001	0.991 ± 0.001
300 MeV e^-	0.988 ± 0.001	0.988 ± 0.001
Protons	1.023 ± 0.001	1.233 ± 0.001
^{12}C ions	1.446 ± 0.001	2.934 ± 0.003
^{20}Ne ions	2.045 ± 0.002	3.267 ± 0.004

RBE values of approximately unity were found for the 20 MeV electrons, 100 MeV electrons, and protons in the plateau region. This proton RBE increased to approximately 1.2 in the Bragg peak - which is consistent with some of the work of Paganetti *et al.* [Paganetti et al., 2002]. Concerning the carbon and neon ion beams, RBE values in the Bragg peak of approximately 3, obtained for the same human salivary gland cells have been reported by Furusawa *et al.* [Furusawa et al., 2000].

In summary, given the similar lineal energy spectra, the VHEE cell survival curves were similar to those of the low energy electrons and photon beams, thus highlighting once again, that from a microdosimetric point of view there is no expected increased biological effectiveness of these beams over clinical electrons or photons. Nevertheless, the proton and ion beams exhibit an increased biological effectiveness which is consistent with what is known from literature.

Based on the work performed in this chapter, final discussions and conclusions drawn are described in the following section.

5.6 Discussion and conclusions

The work detailed in this chapter of the thesis was performed in view of addressing one of the outstanding areas of knowledge with respect to VHEE therapy - namely their biological effectiveness. To this end, MC simulations were performed in GATE, and a two-pronged approach was used to assess their potential for inducing biological damage. In the macroscopic arm of the study, GATE was used to calculated the dose-averaged LET ($\bar{L}_d$) which, compared to track-averaged LET, better correlates to biological damage to tissues [Granville and Sawakuchi, 2015, McMahon et al., 2018]. In the microscopic arm, lineal energy spectra were recorded using GATE's TEPC geometry, and dose-mean lineal energies ($\bar{y}_d$) were calculated, which can be considered the microscopic analogue to LET [ICRU, 1983]. Ultimately, these lineal energy spectra were used as inputs to the modified MKM to generate cell survival curves, from which theoretical RBE values were calculated.

From a macrodosimetric point of view, the 100 and 300 MeV VHEE beams evaluated in this work displayed a potential improved biological efficacy over clinical photon and electron beams. This judgement was reached on the basis that the $\bar{L}_d$ calculated for

the 300 MeV beam VHEE was a factor of 3.2, 2.4, and 1.9 greater than the beam of 20 MeV electrons, photons, and 100 MeV electrons respectively at 4 cm, and these ratios remained approximately the same at 8.2 cm (3.1, 2.2, and 1.8). These comparisons between the $\bar{L}_d$ of each beam was shown in Fig. 5.3. Previous studies have highlighted that $\bar{L}_d$ is a sufficiently good predictor of RBE for regions of narrow LET distributions [Grün et al., 2019]. Given that this was indeed the case for the VHEE beams, these macrodosimetric results suggested that the radiobiological effectiveness of VHEEs should be situated somewhere between clinical electrons/photons and protons/ion beams.

In contrast, **from a microdosimetric point of view** these VHEE beams do not display any increased biological effectiveness compared to clinical electrons/photons. This judgement was made due to the fact that neither their dose-weighted lineal energy spectra ($yd(y)$), shown in Fig. 5.5, nor their $\bar{y}_d$ profiles in depth, shown in Fig. 5.6, displayed any substantial differences to the low energy electrons or photons. Consequently, inserting these lineal energy spectra into the modified MKM yielded cell survival curves for the VHEE beams that were indistinguishable to those of the clinical electrons/photons beams, therefore resulting in a theoretical RBE of ∼1 for both the 100 MeV and 300 MeV VHEE beam. While the research paper resulting from this work was being prepared, Small *et al.* published the only other study evaluating VHEE RBE, however they used an experimental approach. Instead of cell survival, plasmid DNA damage was used as the biological endpoint for the RBE calculation, and they found an RBE of approximately unity for the irradiation of dry plasmids, and an RBE between 1.1 and 1.2 for wet plasmids [Small et al., 2021]. Both the results of Small *et al.* and the work carried out in this chapter give confidence to the clinical implementation of VHEE therapy due to the fact that the biological damage caused by these beams is likely similar to those caused by conventional beams of photons.

One of the limitations of this study is that the $\bar{L}_d$ and $\bar{y}_d$ may not be directly comparable as the macroscopic $\bar{L}_d$ was scored in voxels of 100 μm while the microscopic $\bar{y}_d$ was calculated in spherical volumes of 1 μm diameter equivalent tissue. Previous authors have noted that both $\bar{L}_d$ and $\bar{y}_d$ may be influenced, not only by changes in the simulation parameters, but also by changes in the size of the given volume [Liamsuwan et al., 2014, Cortés-Giraldo and Carabe, 2015, Guan et al., 2015]. Nevertheless, the importance of this work lies in the fact that a first step was taken to evaluate the VHEE RBE, and in this case through the lens of LET, lineal energies, and the modified MKM. Looking to the future, there is a clear interest in performing complementary studies, perhaps using different approaches in evaluating the RBE of these beams.

In conclusion, the MC work performed in this chapter is representative of an important first step taken towards a full evaluation of the biological effectiveness of VHEE beams. Through both a macro- and microscopic study, evidence in favour of the clinical translation of these beams was put forth, which was based on the fact that these beams potentially display either negligibly different or slightly higher biological effectiveness when compared to electrons and photons at clinically relevant energies. Given these results, the conclusion is that the **increased probability of photoneutrons from nuclear reactions - which would lead to an increase in the RBE - is likely negligible**, as was observed in other studies [DesRosiers et al., 2000, Subiel et al., 2014, Masilela et al., 2021]. Given that there is currently no standard procedure for experimental or numerical microdosimetry studies of these beams of VHEEs, both biological experiments and complementary MC studies are required in order to draw more concrete conclusions about the biological effectiveness of these beams. **The results of this work were published in *Scientific Reports* [Delorme et al., 2021].**

Chapter 6

ROS production between MB peaks and valleys

This chapter of the thesis contains the work performed looking at the production of ROS in MBRT between peaks and valleys and has been recently published in *Medical Physics* [Masilela and Prezado, 2023]. It is split into three main parts. Firstly, an overview, and rationale for performing the work is provided in section 6.1, followed by details of the TOPAS and TOPAS-nBio simulations in section 6.2. Validation of the in-house chemical scorer is provided in section 6.3 along with a characterisation of each source in section 6.4. Primary yield results are provided in section 6.5, along with an estimation of possible sources of systematic uncertainty in section 6.6, before ending off with some discussions and conclusions in section 6.7.

6.1 Rationale for the work

The use of MBRT has been shown to offer advantages in terms of both normal tissue sparing [Deman et al., 2012, Prezado et al., 2017a, Prezado et al., 2018], and tumor control [Prezado et al., 2019, Lamirault et al., 2020a, Bertho et al., 2021, Sotiropoulos et al., 2021]. Furthermore, its seeming flexibility with regards to the types of particles/energies able to be used in conjunction with this technique - from photons at synchrotrons/small animal irradiators [Dilmanian et al., 2006, Prezado et al., 2017a] to protons and helium ions [Prezado and Fois, 2013, Schneider et al., 2019] to heavier ion species such as carbon, oxygen, and neon [González et al., 2017, Martínez-Rovira et al., 2017a, Prezado et al., 2021] - make it an exciting prospect in view of advancing RT treatment efficacy. Although the exact biological mechanisms underpinning the efficacy of spatially fractionated treatments are still not fully understood, a few candidates have been put forth such as cell migration, vascular and non-targeted effects, and immunomodulatory responses [Griffin et al., 2020, Prezado, 2022].

Free radicals and ROS are particularly interesting in this context as they are not only important to conventionally thought of concepts such as the level of DNA damage, but are also implicated in some of the aforementioned underlying biological mechanisms. Specifically speaking, the three species investigated were the aqueous electron (e^-_{aq}), the hydroxyl radical ($^\bullet OH$), and the hydrogen peroxide molecule (H_2O_2). The aqueous electron has an impact on target oxygenation, which is one of the indicators of the expected level of radiosensitivity of a biological system [Boscolo et al., 2020]. It reacts rapidly with oxygen, producing superoxide ($O_2^{\bullet -}$), which itself inevitably forms H_2O_2 [Azzam et al., 2012]. The $^\bullet OH$ radical is an important species as it is primarily responsible for the indirect portion of DNA damage [von Sonntag, 2006], which itself accounts for approximately 70% of all DNA damage induced by low LET irradiations [Roots and Okada, 1975]. Furthermore, this free radical is the primary mediator of the oxygen enhancement effect [Hirayama et al., 2013]. Hydrogen peroxide is an important cell signalling molecule [Forman et al., 2014, Gough and Cotter, 2011, Hancock et al., 2001] and may contribute to the bystander effect [Azzam et al., 2002]. As highlighted in section 2.9.6, these ROS are also implicated in some of the

underlying radiobiological mechanisms thought to describe SFRT efficacy.

Moreover, the role of ROS in MBRT still remains a poorly studied area of research. It was therefore important to undertake an investigation in which some first insights into the production and distribution of these radical and molecular species between the peaks and valleys of MBRT could be gleamed. The main question we wanted to reply to was whether there would be any inherent differences in the early radiochemistry in the peaks and valleys as a result of spatially fractionating the radiation, and whether this would have any radiobiological implications. Consequently, this chapter of the thesis details the work performed to this end, which was carried out through the lens of MC simulations in TOPAS-nBio. The primary yields of $^{\bullet}OH$, e^{-}_{aq}, and H_2O_2 in the MB peaks at various depths were calculated and compared against the associated yields in the MB valleys, and a BB configuration.

Technical details of the TOPAS and TOPAS-nBio simulations performed in this chapter are provided in the following section.

6.2 Simulation details

All MC simulations were performed using TOPAS [Perl et al., 2012, Faddegon et al., 2020] version 3.6.1, and TOPAS-nBio [Schuemann et al., 2018a] version 1.0. A $5{\times}5{\times}10$ cm^3 water phantom was created in TOPAS, and the material was assigned to be `G4_WATER`. This water phantom was then irradiated with beams of photons, protons, helium ions, and carbon ions, in both BB and MB configurations. G-values were scored in peak and valley regions at depths 10, 30, 50, 70, and 76.5 mm which corresponds to the approximate depth of the Bragg peak for all of the beams considered. Primary yields were then recorded from the scored G-values, and a comparison of these yields between the different irradiation modalities was performed.

One of the challenges with these types of simulations is that there is a severe difference in scales involved when switching from the macroscopic simulation of particle tracks in a ∼cm size water phantom, to chemical yields in a $\sim\mu$m size volume of water. The commonly used approach in such multi-scale simulations to reconcile the physical/biological consequences of realistic macroscopic-scale sources on microscopic-scale targets with sufficient precision, involves splitting the simulation into a series of distinct steps. In the first step, a macroscopic simulation is performed to *capture* the radiation field of a specific location, then this field is *replayed* in the second step simulation which is representative of the fully microscopic, cell-scale simulation [Schuemann et al., 2018b]. There is precedent in both Geant4-DNA [Dos Santos et al., 2020] and TOPAS-nBio [Ramos-Méndez et al., 2018] for the implementation of this technique, and its implementation in the context of this thesis is shown in Fig. 6.1.

Panel A of Fig. 6.1 depicts the macroscopic first step of the simulation, where the hatched markings indicate that CH physics was applied throughout the water phantom. The physics list employed will be detailed in a relevant subsection below. In addition to the production of ROS between MB peak and valley regions, one of the interests was to evaluate the impact of increasing particle LET on said production. Consequently, the water phantom was irradiated with particles of photons [Prezado et al., 2015], protons [Peucelle et al., 2015b, Guardiola et al., 2017], ^{4}He ions [Schneider et al., 2021], and ^{12}C ions [González et al., 2017] in both a BB and MB configuration. The physical characteristics of the MBs (beamlet width and ctc distance) were taken from these aforementioned references, and the conventional BBs were generated with a width equal to two times the MB ctc

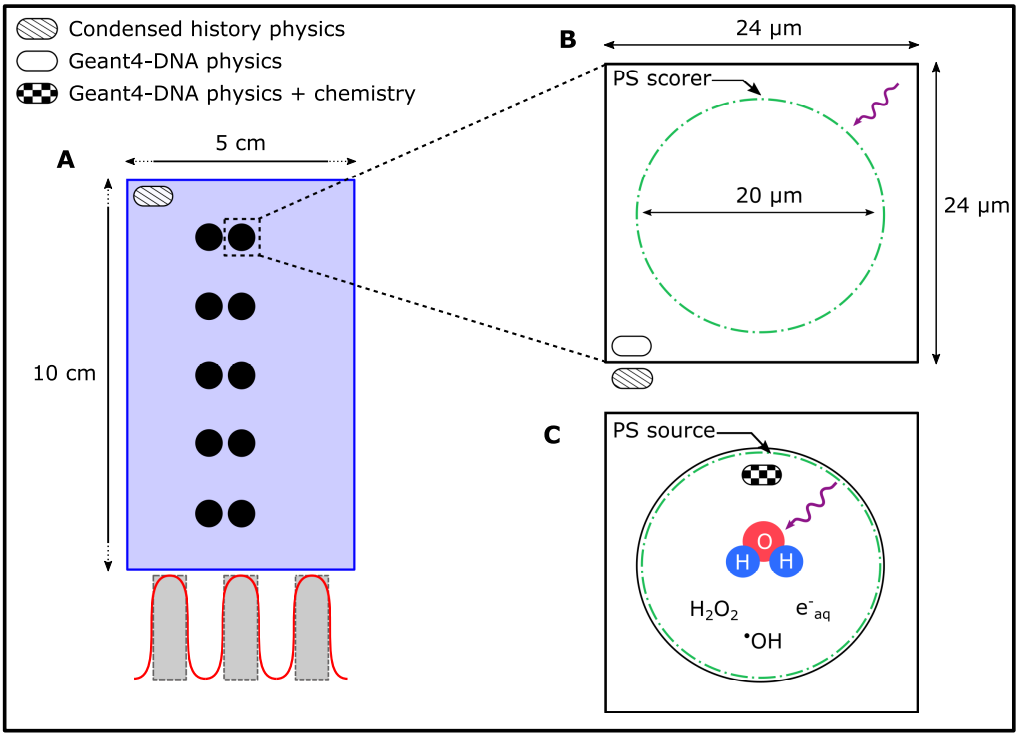

Figure 6.1: Schematic drawing of the TOPAS simulations. Panel **A** depicts the macroscopic water phantom, being irradiated by particle beams, where the black circles are representative of the 20 μm diameter spherical water *cells*, located in the peak and valley regions, and at the depths of 10, 30, 50, 70, and 76.5 mm. Panel **B** depicts a zoomed in view of one the spheres of water, showing the change from CH to TS physics, where the dashed green line represents the surface on which particle information was saved. Panel **C** shows the fully microscopic scale simulation within which chemistry processes were activated and G-values were scored.

distance plus the MB width[36]. In order to increase the statistics of particles reaching the targets and reduce the computational requirements, a physical collimator was not simulated, but instead rectangular sources were used, and in the case of MBs, an array composed of three MB beamlets was simulated.

As shown in panel B of Fig. 6.1, a TOPAS phase space (PS) scorer was used to save all the particles crossing over into a 20 μm diameter spherical volume of water, representative of cellular targets. One of the interesting capabilities of TOPAS is the possibility to assign different physics processes to different regions of your simulation geometry. This assigning of different physics processes was used to change from CH physics, to TS physics in a 24 μm^3 cube of water surrounding the spherical volume of interest. This was done in order to have a more detailed radiation field entering the cells, thereby resulting in a reduction in the eventual systematic and statistical uncertainties of our results.

The second step (fully microscopic) part of the simulation is shown in panel C of Fig. 6.1, where TOPAS-nBio was exclusively used, and where the aforementioned PS was used as the particle source. In addition to TS physics, chemical processes were also activated in this step of the simulation, and a G-value scorer was attached to this entire volume to record the yield of $^{\bullet}OH$, e^-_{aq}, and H_2O_2 as a function of time.

[36] This BB width was chosen in order for the lateral extent of the irradiation field at the entrance of the water phantom to be approximately equivalent to the MB case.

6.2.1 Physical and chemical processes

As highlighted in section 3.1, the physical and chemical processes are specified by supplying a list of modules to TOPAS. In this work, the CH physics list used in the macroscopic first step simulation was: `g4h-phy_QGSP_BIC_HP`, `g4em-livermore`, `g4decay`, `g4ion-binarycascade`, `g4h-elastic_HP`, and `g4stopping`, which is similar to the recommended physics lists for medical physics applications [Baumann et al., 2020]. The hadronic physics interactions were specified by `g4h-phy_QGSP_BIC_HP`, which handles the inelastic interactions of protons and neutrons. Given the presence of hadron beams in this work, the `BIC` option was chosen over `BERT` due to its enhanced accuracy around the Bragg peak [Zacharatou Jarlskog and Paganetti, 2008], and the `HP` option activates the high precision neutron tracking. As opposed to the recommended `g4em-standard_opt3` or `g4em-standard_opt4` for photons and protons respectively [Baumann et al., 2020], the `g4em-livermore` was instead used as it is the best performing CH model for nanoscale electron transport when compared to TS models. It handles photon processes down to 250 eV and electron ionisation and Bremsstrahlung down to 10 eV [Kyriakou et al., 2019]. The remaining processes of `g4decay`, `g4ion-binarycascade`, `g4h-elastic_HP`, and `g4stopping` handle decay physics, inelastic interactions for ions, elastic hadronic physics, and stopping power physics [Geant4 Collaboration, 2021]. The default particle tracking cut of 0.05 mm was used for all CH simulations.

Geant4-DNA *option 2* physics processes (`g4em-dna_opt2`) were used in the second step, TS part of the simulation. Although newer options such as the so-called *option 4* and *option 6* have shown to result in more accurate simulation of electron interactions in liquid water, `g4em-dna_opt2` is still widely used as it covers the widest energy range (7.4 eV - 1 MeV) [Incerti et al., 2018]. One of the consequences of saving the radiation field resulting from CH physics and using the saved PS file as a source for TS simulations is a discrepancy that appears between the types of particles able to transported. As previously mentioned, TOPAS-nBio can simulate the transport of electrons, photons, protons, hydrogen atoms, alpha particles, and the ion species of ^{4}He through to ^{16}O, ^{28}Si, and ^{56}Fe [Schuemann et al., 2018a, Incerti et al., 2018]. However given the greater wealth of interaction cross sections available for CH simulations, the PS sources may contain positrons, neutrons, deuterons, tritons, as well as other elemental isotopes of helium, up to and including carbon. These particles are *unrecognised* in the TOPAS-nBio second step simulation and in the case where these particles are launched from a PS source, they are simply transported through the volume without undergoing any interaction. This strict limit on the type of particles able to be simulated in TOPAS-nBio is one of the main reasons why radioactive decay processes (`g4radioactivedecay`) were not included in the first step CH simulation.

The chemical processes activated in the second step simulation come from one of the default options in TOPAS-nBio, namely `TsEmDNAChemistry`. It was the module of choice in recent TOPAS-nBio publications, and its use was validated through the comparison of calculated G-values to experimental data [Ramos-Méndez et al., 2018, Zhu et al., 2020]. The physicochemical processes, and chemical reactions of the module were initially provided in Table 3.1, but are repeated in Table 6.1 below for ease of readability. Henceforth, any reference to a chemical reaction will use the shorthand R with a *number*. For example, R6 refers to the chemical reaction $^{\bullet}OH + {}^{\bullet}OH \longrightarrow H_2O_2$. Although the use of `TsEmDNAChemistry` was shown to provide a good approximation of chemical yields when compared to experimental data, there are various assumptions that had to be made, both inherent in the SBS diffusion and reaction model of TOPAS-nBio, and on the user-end. The assumptions inherent in the model were described in section 3.1.

Table 6.1: Non-homogeneous chemical stage reactions used in TOPAS-nBio. Taken from Table 3 in Ramos-Meńdez *et al.* [Ramos-Méndez et al., 2018].

Chemical stage reactions	
(1) $e^-_{aq} + e^-_{aq} \longrightarrow H_2 + 2\,OH^-$	(2) $e^-_{aq} + {}^\bullet OH \longrightarrow OH^-$
(3) $e^-_{aq} + H^\bullet \longrightarrow H_2 + OH^-$	(4) $e^-_{aq} + H_3O^+ \longrightarrow H^\bullet$
(5) $e^-_{aq} + H_2O_2 \longrightarrow OH^- + {}^\bullet OH$	(6) ${}^\bullet OH + {}^\bullet OH \longrightarrow H_2O_2$
(7) ${}^\bullet OH + H^\bullet \longrightarrow H_2O$	(8) $H^\bullet + H^\bullet \longrightarrow H_2$
(9) $H_3O^+ + OH^- \longrightarrow H_2O$	

As an end-user, one also needs to take into account the intracellular radical scavenging which affects the evolution of the chemical stage [Kreipl et al., 2009b]. Given that a scavenging capacity was not incorporated into TOPAS-nBio v1.0, the accepted approach is to limit the duration of the chemical stage [Kyriakou et al., 2022], with the convention being to use 1 ns as the cut-off [Schuemann et al., 2018a, Zhu et al., 2020].

6.2.2 Particle sources

As previously stated, sources of photons [Prezado et al., 2015], protons [Peucelle et al., 2015b, Guardiola et al., 2017], ^{4}He ions [Schneider et al., 2021], and ^{12}C ions [González et al., 2017] were used in both a BB and MB configuration. The characteristics of these sources are shown in Table 6.2.

Table 6.2: Details of the sources used in this work.

Source characteristics				
Particle	**ctc distance**	**MB size**	**BB size**	**Beam energy**
Photons	1200 μm	600 μm×5 mm	3000 μm×5 mm	69 keV effective
Protons	3200 μm	400 μm×5 mm	6800 μm×5 mm	100 MeV
^{4}He ions	3500 μm	600 μm×5 mm	7600 μm×5 mm	99.3 MeV/u
^{12}C ions	3500 μm	600 μm×5 mm	7600 μm×5 mm	185.8 MeV/u
Total number of primaries				
Particle	**BB simulations**	**MB simulations**		
Photons	4.8×10^{12} - 2.4×10^{13}	2.4×10^{12} - 4.8×10^{13}		
Protons	4.5×10^{8} - 1.35×10^{9}	4.5×10^{8} - 3.6×10^{10}		
^{4}He ions	5.4×10^{7} - 4.95×10^{8}	1.8×10^{7} - 1.62×10^{10}		
^{12}C ions	1.8×10^{8}	1.8×10^{7} - 1.08×10^{10}		

Each source was simulated as monodirectional and monoenergetic, with the exception of the photon source in which the beam was simulated as a spectrum of energies, characterisitic of the SARRP [Xstrahl, 2023, Wong et al., 2008]. Any further references to this photon

energy spectrum in the text will be done so by referring to the effective energy of said spectrum, as indicated in Table 6.2. The total number of histories were varied in order to have a satisfactory compromise between statistical uncertainty and computational expense.

6.2.3 TOPAS scorers used

Throughout this work, the three standard TOPAS/TOPAS-nBio scorers used were the `DoseToMedium` discretized volume scorer, the `PhaseSpace` scorer, and the `gvalue` scorer. The discretized volume scorer was used to create the lateral dose profiles and PDD curves. In the case of the PDD curves, a $5\times5\times100$ mm^3 (x,y,z) scoring volume was placed along the central axis of the water phantom, and the z dimension was discretized into 1000 voxels. The same scorer was used for the creation of lateral dose profiles. A $2\times2\times x$ mm^3 scoring volume was placed at various depths in the water phantom, where the x dimension length was modified depending on the lateral extent of the source and then discretized into 1000 voxels.

The PS scorer, as previously stated, was assigned to the surface of the 20 μm diameter spheres of water shown in Fig. 6.1. This scorer outputs an ASCII file containing information about all particles crossing the specified surface. The information includes, but is not limited to, the type of particle, its position in space, and its energy. The `OnlyIncludeParticlesGoing = ''In''` filter was applied to only record those particles entering into the cell. Scoring of the chemical yield in TOPAS-nBio was accomplished through the use of the `gvalue` scorer, which was assigned to each spherical target. This scorer records the evolution of the yield of each species from 1 ps up to 1 ns in 100 logarithmic bins and outputs an ASCII file, similar to that of the PS scorer.

While TOPAS-nBio v1.0 provides the user a way to access the yield and spatio-temporal information of the chemical species created, there is no dedicated scorer to track the frequency of specific chemical reactions in the non-homogeneous chemical stage. This feature was deemed necessary to explain the differences in the calculated primary yields, and thus a custom *chemical scorer* was created.

The development of this scorer, along with its validation is presented in the following section.

6.3 Validation of the chemical scorer

In contrast to the well-packaged volume or surface scorers of TOPAS, specific information about the exact frequency of chemical reactions was, at the time, not yet packaged into a user-friendly scorer. Fortunately however, this chemical information was stored in TOPAS-nBio and could be accessed using the `ReportOriginOfMoleculesToAsciiFile` string parameter. By specifying this string parameters in the TOPAS-nBio simulation, a *.chem* ASCII file would be output containing raw data detailing the species' event and track IDs, name, and track IDs of both parents. Correspondingly, a python script was created which took these *.chem* files as an input, and matched the reported parent track IDs of a species with the corresponding parent names, which could then be used to determine which of the 9 chemical reactions listed in Table 6.1 occurred. The workflow diagram outlining how this scorer was used in the context of this work is shown in Fig. 6.2 for the case of a second step TOPAS-nBio simulation of a PS source in the peak at a depth of 10 mm.

There are two main drawbacks with the use of this scorer. Firstly, it does not account for the occurrence of reactions R7 and R9. This is because the product of these reactions,

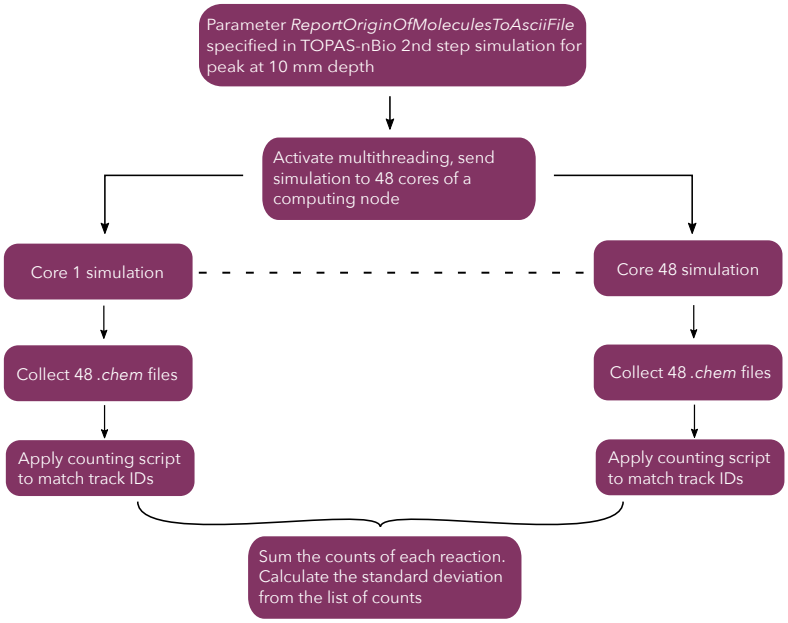

Figure 6.2: Workflow depicting the specification of the `ReportOriginOfMoleculesToAsciiFile` string parameter in a TOPAS-nBio simulation, to the eventual calculation of the standard deviation (statistical uncertainty).

H_2O, is not involved in any other chemical process and is not able to be irradiated given the nature of how water radiolysis in TOPAS-nBio is handled. Secondly, there is no statistical uncertainty information available in the *.chem* outputs. This was overcome as follows: For each microscopic second step simulation, all 48 available cores of the computing node were used to calculate the diffusion and reaction of chemical species. I remind you that this is possible since TOPAS-nBio simulates the three stages of water radiolysis history by history, independent of subsequent histories [Ramos-Méndez et al., 2018]. This resulted in 48 *.chem* files for each simulation, to which the script was applied which counted chemical reactions. Consequently these 48 outputs were combined, the counts of each reaction were summed, and the standard deviation of the list of counts (48 in total) was calculated and used as the statistical uncertainty associated to that specific reaction.

There were other users on the TOPAS-nBio forum which required similar functionality (being able to count chemical reactions) in their simulations. It was later realised that the only other known way to achieve this count is by setting the TOPAS parameter `ChemistryVerbosity` to be equal to 2. In contrast to the python script described above in which track IDs needed to be matched, this parameter explicitly outputs all the chemical reactions per history in plain text format. While more *humanly* readable, this second option is more disk space intensive. Ultimately the users *A. Baikalov* and *L. Derksen* on the TOPAS-nBio forum provided a new python script to read in the outputs of this verbosity parameter. A comparison of my own python script using the `ReportOriginOfMoleculesToAsciiFile` parameter to that of the python script using `ChemistryVerbosity` is shown in Fig. 6.3.

The chemical reactions counted in Fig. 6.3 are from the TOPAS-nBio example *particleTuple.txt*. The chemical stage was allowed to run up to 1 ns, a 1 μm diameter sphere of water was irradiated with an isotropic source of 50 mono-energetic 10 keV electrons, and both chemical scoring methods were implemented. As is evident, both methods yielded equivalent results. This independent, third party validation of the python

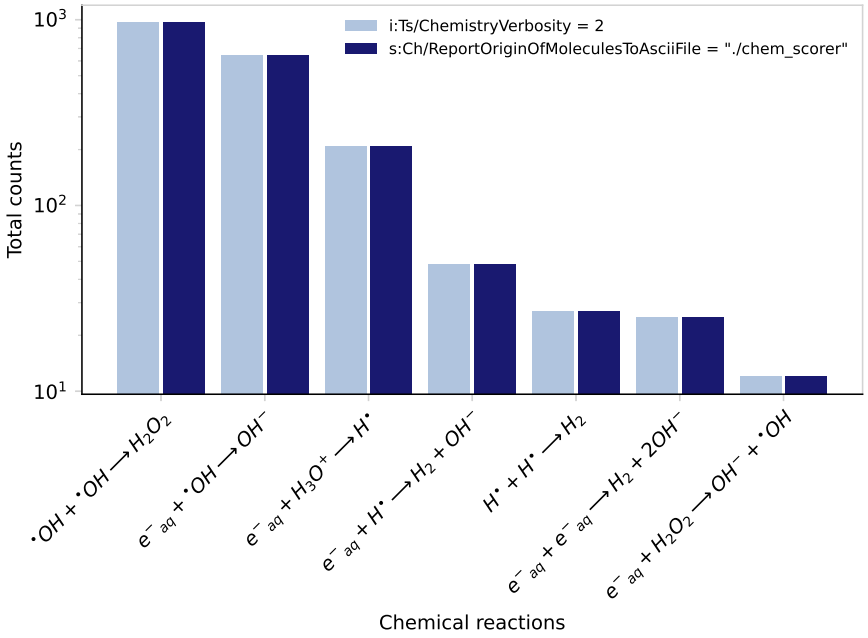

Figure 6.3: Comparison of the chemical scoring methods `ChemistryVerbosity` (light blue), and `ReportOriginOfMoleculesToAsciiFile` (dark blue).

script applied to the *.chem* outputs of the `ReportOriginOfMoleculesToAsciiFile` gave confidence to its use in this thesis. Additionally, the use of this chemical scorer to analyse the frequency of chemical reactions was limited to evaluations on the production and consumption of $^{\bullet}OH$ and H_2O_2 due to their involvement in a limited number of reactions, thereby easing the interpretation of results. H_2O_2 is involved in two reactions, R5 and R6, where it is consumed and produced respectively, whereas $^{\bullet}OH$ is involved in R2, R5, R6, and R7, where it is consumed in all of the reactions barring R5.

In order to characterize the beams and provide a more comprehensive physical description such that later discussions about chemical yields may be related to associated dose distributions, the PDD curves and lateral dose profiles contained in the following section were created.

6.4 Characterising the beams

By taking advantage of the multithreaded capability of TOPAS, 10 computing nodes were used in view of achieving a satisfactory statistical uncertainty within each voxel. Simulations sent to each node were comprised of between 10^6 and 10^8 primaries depending on the particle source, resulting in a total number of histories between 10^7 and 10^9. The resulting dose and uncertainty quantities contained within the output *.csv* files were combined according to the methodology outlined in section 3.2. PDD curves of the BB irradiations are displayed in Fig. 6.4.

The initial energy of the primary charged particles was chosen such that the Bragg peak would occur in approximately the same location. As shown in Fig. 6.4, this occurs at approximately 76.5 mm. For the beam of photons, the statistical uncertainty in all voxels was maintained below 1%. Concerning the charged particle beams, given the steep fall off

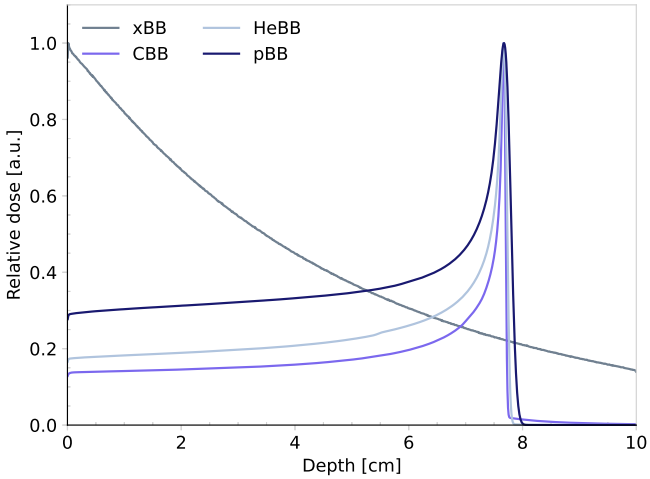

Figure 6.4: PDD profiles for the beams of photons, protons, ^{4}He, and ^{12}C. Doses were normalised to the maximum voxel dose along the entire depth.

after the Bragg peak resulting in trailing voxels with high variations in energy deposition events, the uncertainty was only evaluated in voxels with at least 1% of the maximum dose. In adherence to this criteria, the maximum statistical uncertainty in each voxel for the charged particle beams was also maintained below 1%. The depths at which primary yields were calculated (10, 30, 50, 70, and 76.5 mm) were chosen such that the yields could be associated with a *relatively* low LET, characteristic of the plateau region, or high LETs present near the Bragg peak region. Correspondingly, lateral dose profiles were also calculated for these depths, which are depicted in Figures 6.5, 6.6, 6.7, and 6.8 for the beams of photons, protons, helium ions, and carbon ions respectively in both BB and MB configurations. Additionally, tables of PVDR values for the respective MB modalities were calculated and are depicted in each figure.

As can be seen, the degree of heterogeneity in depth is dependent on the particle simulated. For xBB and xMBRT, as is expected from literature, the PVDR remains approximately constant in depth, highlighting that there is very little difference in the composition of the radiation field between peaks and valleys regardless of depth. Contrastingly, the degree of heterogeneity decreased in all other cases, corresponding to a reduction in the PVDR. Among the charged particles simulated, protons are the most susceptible to lateral scattering and were thus the most homogenised in depth, whereas the beams of carbons retained their heterogeneity at all depths. It should be noted that these PVDR values are inflated compared to what can be expected of experimental PVDR values. This is due to the fact that no mechanical collimation was simulated which would otherwise contribute scattered particles to the valley dose. Similarly to the PDD curves, statistical uncertainties were evaluated in all voxels with at least 1% of the maximum dose, and the maximum voxel uncertainties for the BB and MB cases are referenced in each figure.

With the particle beams now characterised, the following section describes the calculation of primary yields resulting from the simulation of each of these beams.

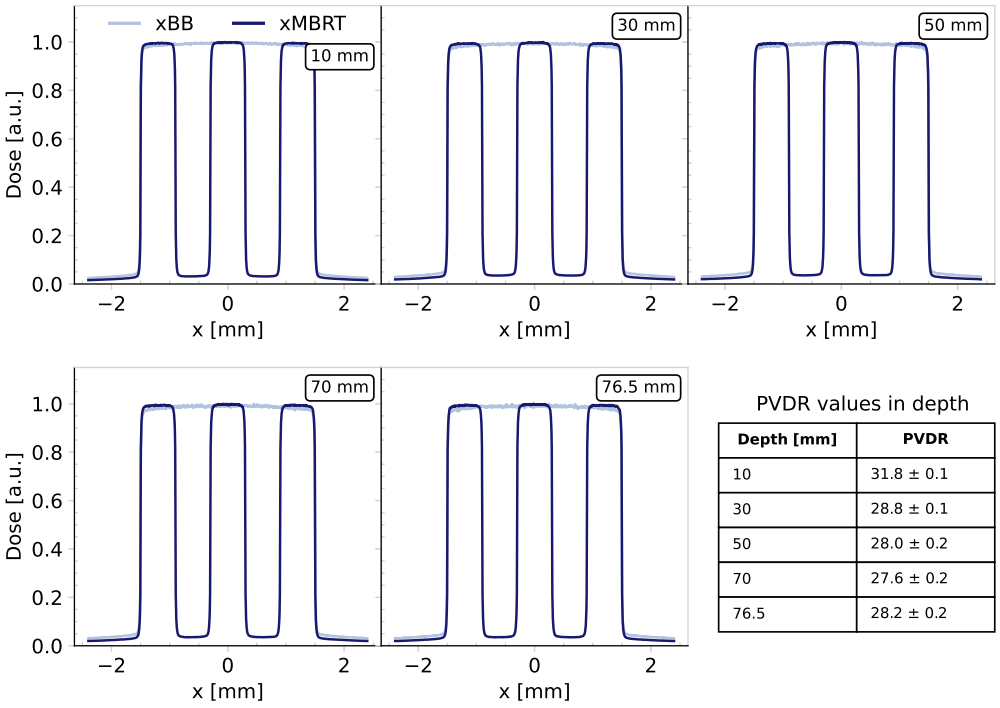

PVDR values in depth

Depth [mm]	PVDR
10	31.8 ± 0.1
30	28.8 ± 0.1
50	28.0 ± 0.2
70	27.6 ± 0.2
76.5	28.2 ± 0.2

Figure 6.5: Lateral dose profiles for x-ray broad beam (xBB) and x-ray minibeam radiation therapy (xMBRT), with statistical uncertainties maintained below 1.8% and 1% respectively.

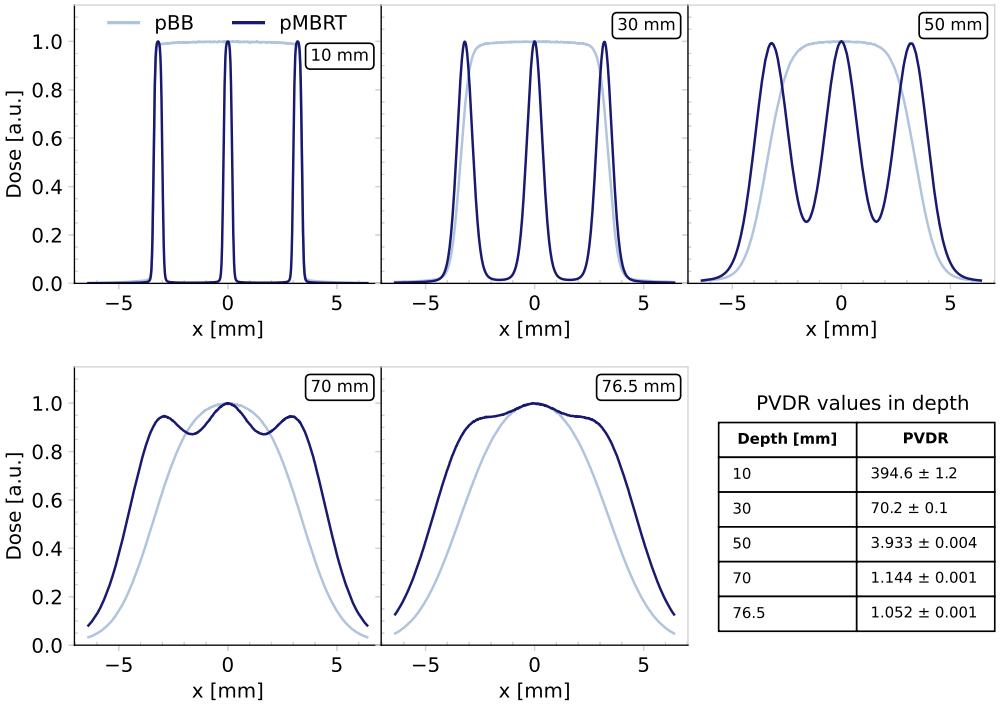

PVDR values in depth

Depth [mm]	PVDR
10	394.6 ± 1.2
30	70.2 ± 0.1
50	3.933 ± 0.004
70	1.144 ± 0.001
76.5	1.052 ± 0.001

Figure 6.6: Lateral dose profiles for proton broad beam (pBB) and pMBRT, with statistical uncertainties maintained below 0.4% and 0.3% respectively.

6.5 Calculation of primary yields

As previously highlighted, the simulation was split into 2 steps due to the multi-scalar nature of the problem. In the first step using CH physics, the main goal was to obtain *rich*

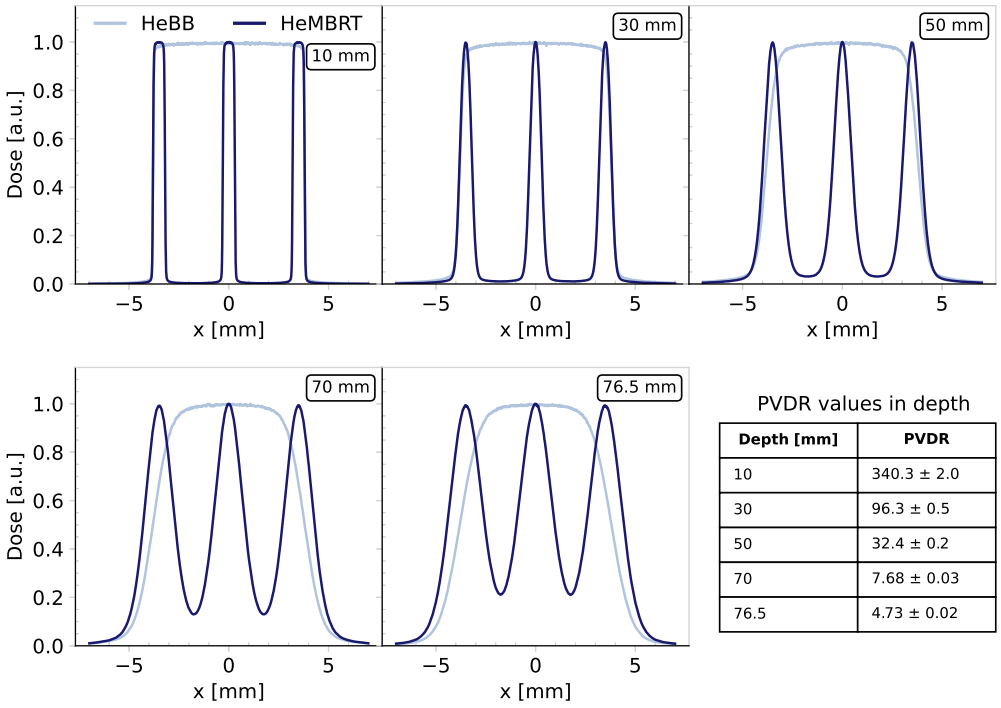

Depth [mm]	PVDR
10	340.3 ± 2.0
30	96.3 ± 0.5
50	32.4 ± 0.2
70	7.68 ± 0.03
76.5	4.73 ± 0.02

Figure 6.7: Lateral dose profiles for helium broad beam (HeBB) and helium minibeam radiation therapy (HeMBRT), with statistical uncertainties maintained below 2.9% and 1.4% respectively.

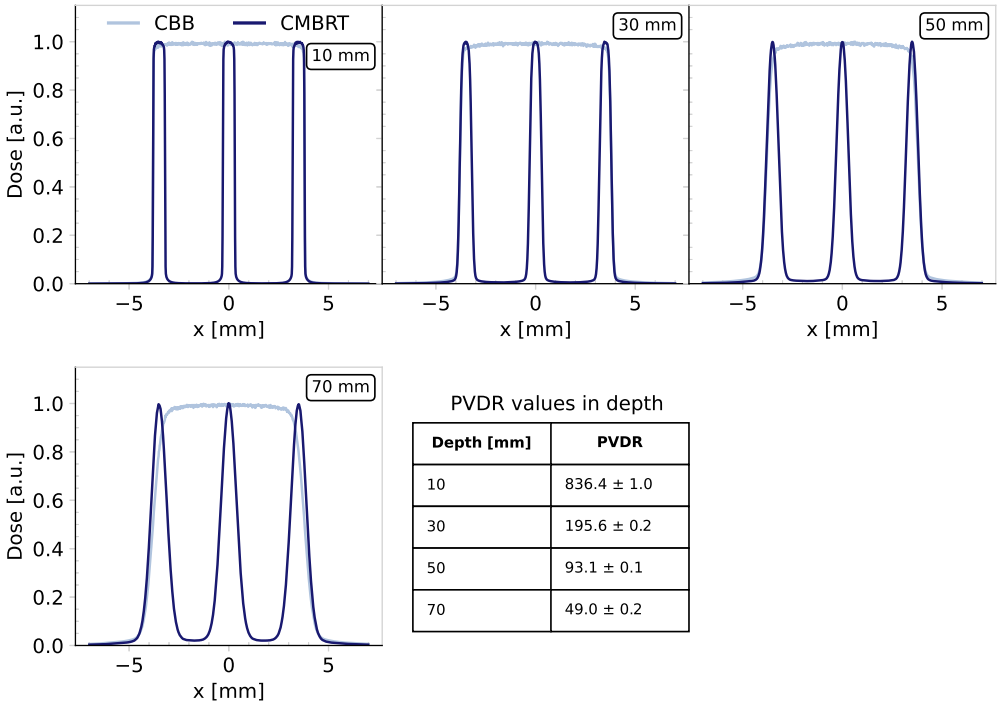

Depth [mm]	PVDR
10	836.4 ± 1.0
30	195.6 ± 0.2
50	93.1 ± 0.1
70	49.0 ± 0.2

Figure 6.8: Lateral dose profiles for carbon broad beam (CBB) and carbon minibeam radiation therapy (CMBRT), with statistical uncertainties maintained below 0.3% and 0.7% respectively.

phase spaces that accurately describe the composition of the radiation field in the peaks and valleys at the depths evaluated. The inherent contradiction in obtaining these rich PS

files however, is that the second step TS simulation, which uses these recorded PSs as a source, becomes significantly more computationally expensive[37]. So on the one hand, one wants rich sources in order to be scientifically accurate while limiting the statistical and systematic uncertainties, but on the other hand one needs to be mindful of whether or not those sources are able to be practically simulated given the available computing resources.

Performing an accurate trade off becomes increasingly challenging and complex when TS simulations need to be performed near the Bragg peak, where there is a high ionisation density resulting in abundantly generated water radiolysis products. In fact, previous simulation work on radiolysis species generated near Bragg peaks have highlighted how challenging these simulations are on CPU based architectures [Baba et al., 2021]. One of the approaches used in the afore-cited work of Baba *et al.* is to split the TS simulations into multiple parallel jobs then combine the outputs. This approach was therefore used in this work. Furthermore, the primary yields calculated for the ^{12}C beams were limited to depths of 70 mm. In addition to the exponentially more species created directly in the Bragg peak, there are known issues in TOPAS-nBio surrounding TS simulations at very high LET[38]. All of these considerations meant that these simulations are particularly challenging both from the points of view of optimising the available computing resources, and post-processing the large amount of split/unsplit simulations. The methodology eventually employed can be summarised by the set of workflow diagrams depicted in the remainder of this section. The process followed for the recording of particles in the first step CH simulation, and the subsequent post-processing in order to get these PS files ready to be used as sources in the second step TS simulation is shown in Fig. 6.9.

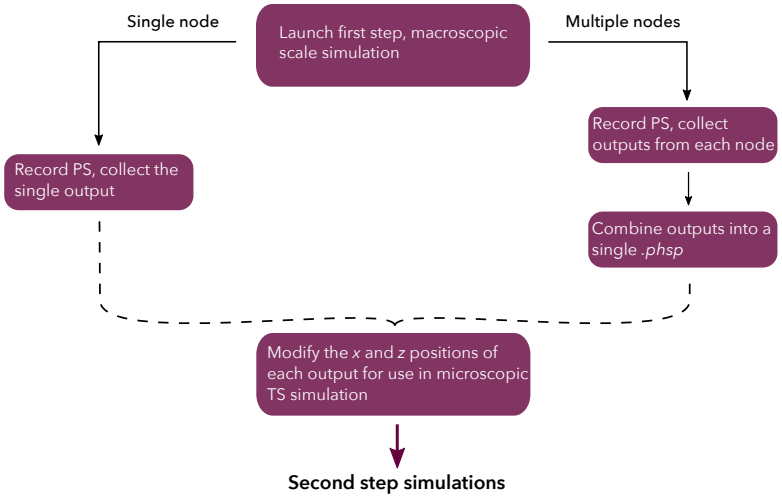

Figure 6.9: Workflow diagram depicting the launching of a first step simulation, and subsequent combination and modification of *.phsp* outputs according to a python script for use in the second step simulations.

For each source (photons, protons, helium, carbon) and each configuration (BB and MB), individual macroscopic first step simulations were launched for each lateral location (peak and valley) and each depth (10, 30, 50, 70, and 76.5 mm). These simulations were

[37] The complexity of the water radiolysis simulations in TOPAS is $O(N_M^2 \cdot N_t)$, where N_M^2 is the number of molecules squared and N_t is the number of time steps [Karamitros et al., 2014].

[38] Occasionally, *Out of Memory (OOM)* errors occur at high LETs, thus causing the simulation to fail. In addition to my own personal experience, this issue has been discussed by the PI of the TOPAS-nBio collaboration (Dr. Jan Schuemann) on the TOPAS-nBio user forum.

launched individually as opposed to having a single simulation with a single source of a certain number of histories and multiple PS scorers. This was done due to the fact that - particularly in the entrance region - there is a severe lack of particles being recorded in the MB valleys. Consequently individual simulations were launched such that the number of primary histories launched could be increased for scorers located in these valleys. In the case that simulations were launched on multiple computing nodes in order to have more detailed phase space files, a python script was created to combine the individual *.phsp* files into a single output to be then used in the second step TS simulation. A second python script was created to modify the x and z positions of scored particles in the PS file. TOPAS records positions relative to the *world* volume, and since the second step simulation did not comprise the entire water phantom but simply 20 μm spheres centred in the world, positions needed to be changed in order for the PS source to be accurately positioned around the 20 μm G-value scoring volume of the second step simulation. For recorded particles located in the peak, only a z translation was performed, whereas for recorded particles in the MB valleys, both an x and z translation was performed. The process followed for the use of these sources in the second step simulation is summarised by the workflow diagram in Fig 6.10.

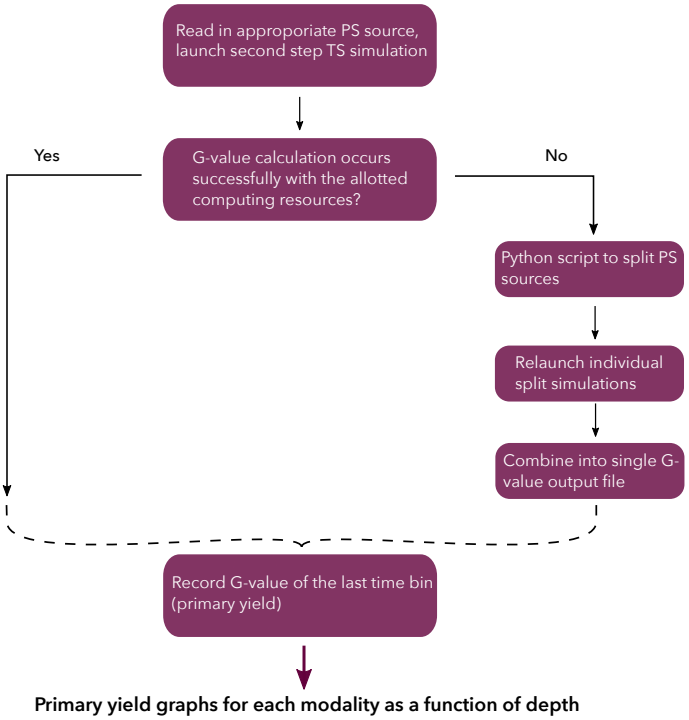

Figure 6.10: Workflow diagram depicting the launching of a second step simulation, and the subsequent splitting, relaunching, and recombination of G-value outputs if the allotted computing resources are not sufficient to simulate the entire PS source.

From the PS files obtained in the first step simulation, a second step simulation was launched for each 20 μm volume. If the available computing resources of the cluster were able to simulate the chemistry of an entire PS source then the primary yield resulting from that simulation was simply taken from the last time bin of the output G-value *.phsp* file. If the computing resources were not sufficient to simulate the entire source, then a python script was applied which was used to split the PS file in view of running individual split simulations in accordance with the methodology used by Baba *et al.* [Baba et al., 2021]. It was important to ensure that the first entry of each of these split files was an

original history, as a secondary particle listed as the first entry of a PS source would cause TOPAS to crash. The G-value outputs of the split simulations were then combined with another python script in order to produce a single *.phsp* file. This file contained the combined results of the split simulations where the G-value in each time bin was calculated as the arithmetic mean, and statistical uncertainties in each time bin were combined in quadrature.

6.5.1 Protons

Figure 6.11 depicts the primary yields as a function of depth for the pBB and pMBRT modalities. The maximum statistical uncertainty occurred in the MB valley at 10 mm. This was to be expected since, given the fact that ideal sources were generated flush at the surface of the water phantom, there was very little scattering in this region. Nevertheless, the statistical uncertainty at this location was still very low (0.38%) and all other statistical uncertainties were maintained below this value. Due to the increased rate of radical-radical reactions associated with increasing particle LET, there is an expected increase in the production of molecular products in depth [Wasselin-Trupin et al., 2002]. Correspondingly, the trends observed in Fig. 6.11 are expected, namely a decrease in the primary yields of $^{\bullet}OH$ and e^{-}_{aq}, and an increase in the primary yield of H_2O_2. Interestingly, it was observed that there were no statistically significant differences between the primary yields in the BB modality compared to the MB peaks and valleys beyond the first few centimetres in the water phantom. In the MB peaks, the $^{\bullet}OH$ primary yield decreased by approximately 5% from 4.01 species/100 eV at 10 mm to 3.81 species/100 eV at 76.5 mm. This corresponded with an increase of approximately 17% in the H_2O_2 primary yield from 0.444 species/100 eV at 10 mm to 0.518 species/100 eV at 76.5 mm. Similarly to $^{\bullet}OH$, the e^{-}_{aq} primary yield decreased by approximately 4% from 3.70 species/100 eV at 10 mm to 3.57 species/100 eV at 76.5 mm.

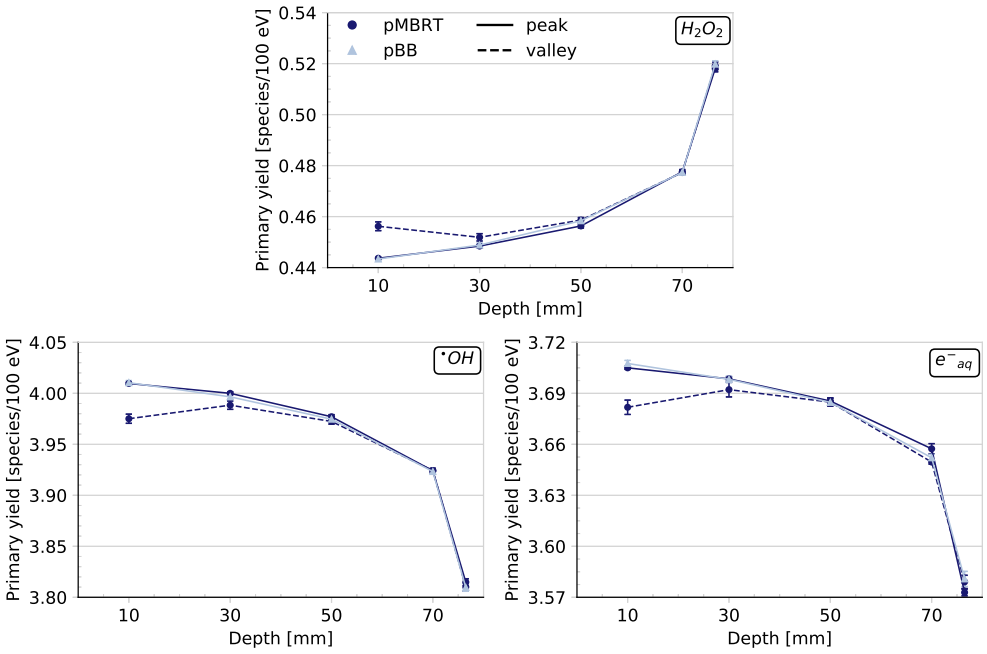

Figure 6.11: pMBRT and pBB primary yields in the peak (solid line) and valley (dashed line) for the species: $^{\bullet}OH$, H_2O_2, and e^{-}_{aq}, depicted as a function of depth in the water phantom.

The difference between the peak and valley primary yields in the entrance region were attributed to differences in the composition of the PS sources used. Figure 6.11 shows an approximate increase in the yield of H_2O_2 by 3% from the peaks to the valleys, and a decrease in the $^{\bullet}OH$ and e^-_{aq} yields by approximately 1%. The compositional differences between peak and valley PS sources in the entrance region are due to the fact that the valleys at this shallow depth are composed primarily of scattered and secondary particles which have a lower energy, and thus a higher LET [Schneider et al., 2019, Lansonneur et al., 2020]. Upon analysis of the PS sources used at this depth, it was found that the maximum proton energy in the peak was 1.5 MeV compared to the 0.12 MeV in the valleys - thus aligning with this notion of increased particle LET in the valleys. Figure 6.12 depicts the compositional differences in these PS sources, where the two most prevalent particles (protons and secondary electrons) were compared.

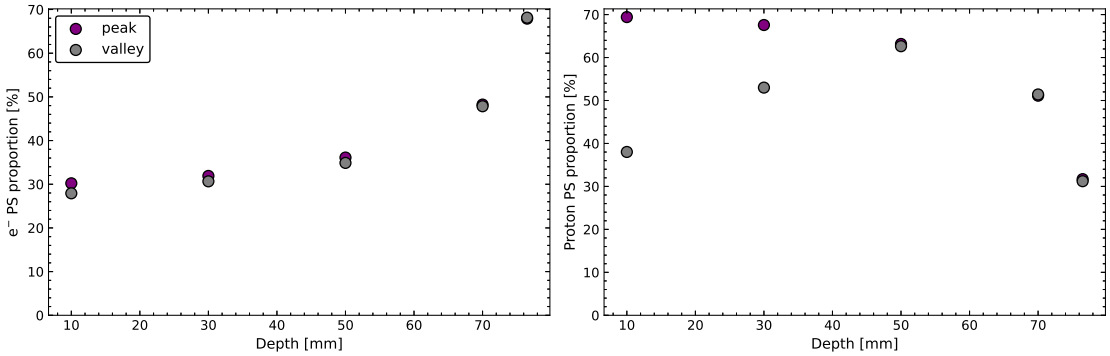

Figure 6.12: Proportion of secondary electrons (left) and protons (right) in the PS sources used in the pMBRT modality at each location within the water phantom.

While there were largely no differences in the presence of secondary electrons in the peaks and valleys at all depths, the most striking difference observed was the percentage composition of protons in the peaks (69%) compared to the valleys (38%) at the 10 mm depth. The percentage of protons in the peaks decreased from 69% at 10 mm to 32% in the Bragg peak due to lateral scattering away from the central beam axis, thus contributing to the increasing proportion of protons in the valleys (up to 62% at 50 mm). In both peaks and valleys the decreased range of protons in depth leads to a reduction in their presence in the PS sources. In the case of the MB peaks, this reduction is complementary to the reduction caused by lateral scattering, whereas for the MB valleys, this reduction eventually overcomes the increase caused by laterally scattered protons from the peak - causing the decrease observed in the valleys beyond 50 mm. It should also be noted that a large proportion (13%) of the valley PS source at 10 mm is composed of neutrons - which at the time of writing have no physical process in Geant4-DNA [Incerti et al., 2018] and are therefore simply transported through the volume without undergoing any interactions. These compositional difference between peaks and valleys is consistent with previously published work on pMBRT [Peucelle, 2016].

The expectation was that the increase in particle LET in the valleys at 10 mm was responsible for the decrease in primary yields of radical species, which would correspond with an increase in the primary yield of H_2O_2. At this time however, it is uncertain if this increase in the primary yield would be in spite of, or complementary to the decreased proportion of protons in the valleys at this shallow depth. Nevertheless, to verify whether an increased proportion of radical-radical reactions led to the increase in H_2O_2 yields in the entrance region, the chemical scorer was used to count chemical reactions, resulting in

Fig. 6.13 and Table 6.3.

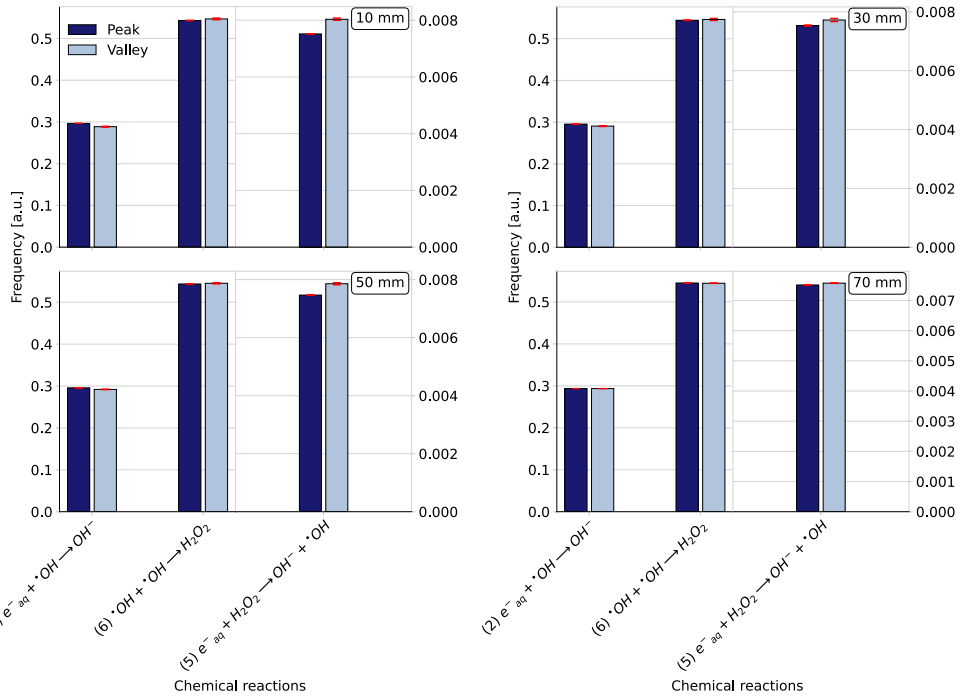

Figure 6.13: Normalised frequencies for the chemical reactions R2, R5, and R6, in pMBRT peak and valley regions at 10 mm, 30 mm, 50 mm, and 70 mm.

The frequency of each reaction was normalised according to the total amount of chemical reactions counted for that specific location within the water phantom. Note that the error bars are displayed in red, and the normalised frequency of R5 is displayed on the second y-axis, on the right hand side of each graph of Fig. 6.13. Upon first glance, the only major difference at 10 mm occurs for reaction R5 between peaks and valleys, which, if taken in isolation, implies a reduced yield of H_2O_2 in the valleys over the peaks due to its consumption. However the frequency of occurrence of this reaction is several orders of magnitude smaller than the other reactions, R2 and R6.

While difficult to discern visually, the reduced frequency of R2 in the valleys at 10 mm compared to the peaks suggests less $^\bullet$OH being consumed, and the increased frequency of R6 suggests more H_2O_2 being produced. Therefore with respect to the production of H_2O_2, the reactions R2 and R6 seem to act in a complementary manner. It is hypothesised that the increased $^\bullet$OH recombination from the increased LET in the valleys is responsible for the reduced presence of R2, however the opposite effect may also play a role, i.e. the reduced frequency of R2 means there is an excess of $^\bullet$OH which can then undergo reaction R6. While complementary, at this point in time the exact mechanisms of said complementarity are not fully understood. What can be said however, is that analysis of the frequency of chemical reactions shows that R6 dominates and seems to dictate the presence/lack of $^\bullet$OH and H_2O_2 in the water phantom, leading to the trend observed in Fig. 6.11, namely an increase in the primary yield of H_2O_2 in the valleys. In order to be able to discern the quantitative differences between reactions in the peaks and valleys for the other depths, Table 6.3 is provided which depicts the frequencies of Fig. 6.13 as percentages.

Table 6.3: Proportion of chemical reactions R2, R5, and R6 in pMBRT, expressed as a percentage of the total occurring chemical reactions at the corresponding depth and lateral location. Blue highlighting indicates a lower expected yield of H_2O_2 in the valleys compared to the peaks for that specific reaction, while values highlighted in grey indicate the contrary; a higher expected yield of H_2O_2 in the valleys compared to the peaks.

Reaction	Lateral location	10 mm	30 mm	50 mm	70 mm
R2	Peak	29.66	29.53	29.57	29.36[a]
	Valley	28.86	29.05	29.19	29.35
R5	Peak	0.752	0.753	0.747	0.751
	Valley	0.803	0.772	0.786	0.757
R6	Peak	54.31	54.41[a]	54.36[a]	54.51[a]
	Valley	54.69	54.60	54.53	54.45
H_2O_2 net yield: production - consumption (R6 - R5)					
	Peak	53.56	53.66	53.61	53.76
	Valley	53.89	53.83	53.74	53.69
Peak - Valley		-0.33	-0.17	-0.13	0.07

[a] indicates that there is no statistically significant difference between the peak and valley values for this reaction at this location.

The values highlighted in blue indicate a lower expected yield of H_2O_2 in the valleys compared to the peaks for that specific reaction at the corresponding location, whereas values highlighted in grey indicate the contrary; a higher expected yield of H_2O_2. For visual clarity, statistical uncertainty values were not displayed, however all uncertainties were maintained below the maximum of 0.73%, which corresponds with the statistical uncertainty of R5 in the valleys at 30 mm. As previously stated, the contradictory behaviour of R5 (i.e. a greater proportion of H_2O_2 consuming reactions in the valleys) is dominated by the behaviour of R6 (i.e. a greater proportion of H_2O_2 producing reactions in the valleys). The subscript *a* indicates that there were no statistically significant differences in the proportions of R6 between peaks and valleys beyond 10 mm, supporting the observations of Fig. 6.11. Subtracting the proportion of reaction R5 from R6 provides a measure of the *net* H_2O_2 producing effect, and, as seen in Table 6.3, this net effect is greater in the valley at 10 mm compared to the peak. The penultimate row highlights that the greatest difference occurs at 10 mm and progressively gets smaller as the depth increases, with the negative values indicating less H_2O_2 being produced in the peak. However as previously stated, differences in the proportions of H_2O_2 between peaks and valleys beyond 10 mm are not statistically significant.

In summary, due to the increasing particle LET, the primary yield of H_2O_2 increases in depth, and the primary yields of $^{\bullet}OH$ and e^-_{aq} decrease in depth. There were no significant differences beyond 10 mm for the yields of the peaks/valleys compared to the BB modality. Lastly, there was a decreased yield of $^{\bullet}OH$ and e^-_{aq}, and an increased H_2O_2 primary yield in the valleys at 10 mm, due to an increased proportion of R6.

6.5.2 Helium ions

Primary yields of $^{\bullet}OH$, e^{-}_{aq}, and H_2O_2 as a function of depth for the beam of helium ions is depicted in Fig. 6.14. All statistical uncertainties were maintained below 0.73%, which corresponds with the statistical uncertainty of the yield of H_2O_2, on-axis, for the BB irradiation modality, and at the Bragg peak depth of 76.5 mm. Similarly to the primary yield graph obtained for protons (Fig. 6.11) beyond the depth of 10 mm there are not any substantial differences between the primary yields of the peaks/valleys compared to the BB case. A second similarity is the increasing trend in H_2O_2 and decreasing trends in $^{\bullet}OH$ and e^{-}_{aq} with depth. Nevertheless, given that helium ions have a higher LET in both peaks and valleys compared to the corresponding regions in a proton beam [Schneider et al., 2019], there is a greater proportion of radical-radical reactions associated with the use of ^{4}He ions than there is for protons, leading to an increase in the production of molecular products. Consequently, for the BB modality and the MB peak and valley regions, it was observed that there was a lower primary yield of $^{\bullet}OH$ and e^{-}_{aq}, and a higher yield of H_2O_2 compared to the beam of protons at all depths. A third, and final similarity is the divergence in the primary yields between the MB peak and valley regions at 10 mm.

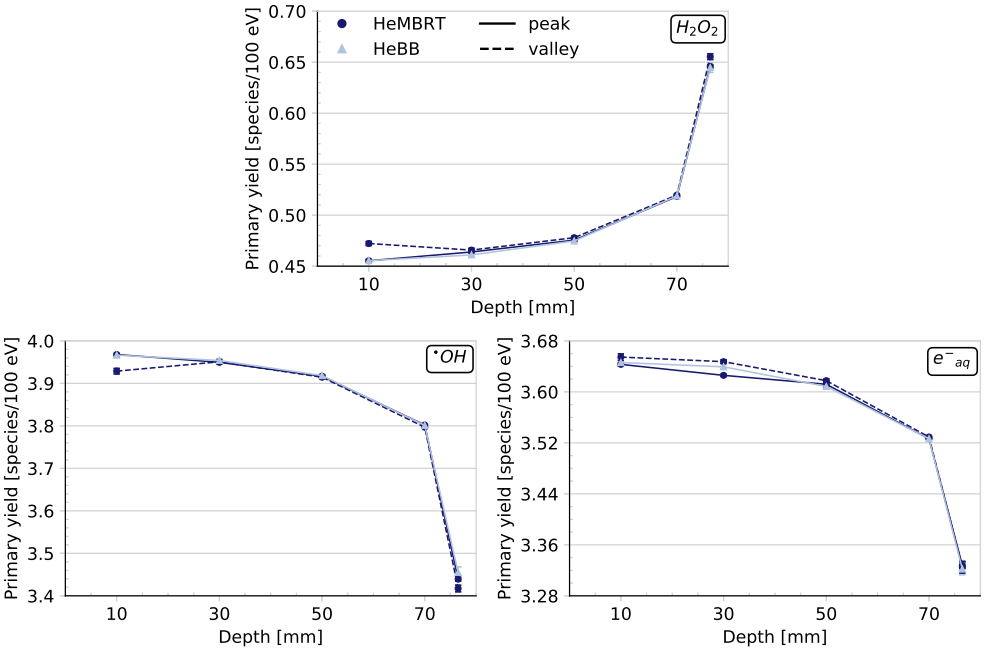

Figure 6.14: HeMBRT and HeBB primary yields in the peak (solid line) and valley (dashed line) for the species: $^{\bullet}OH$, H_2O_2, and e^{-}_{aq}, depicted as a function of depth in the water phantom.

Fig. 6.14 depicts a decrease of about 13%, from 3.97 species/100 eV at 10 mm to 3.44 species/100 eV at 76.5 mm for the $^{\bullet}OH$ species in the MB peaks. The H_2O_2 primary yield changed from 0.455 species/100 eV at 10 mm to 0.646 species/100 eV at 76.5 mm, for an increase of approximately 30%. And finally the e^{-}_{aq} primary yield decreased by approximately 9% from 3.64 species/100 eV at 10 mm to 3.33 species/100 eV at the Bragg peak depth of 76.5 mm. The increase/decrease of the primary yields of each species with depth for the ^{4}He ion beams represents, on average, a factor of two augmentation over the increase/decrease observed for the primary yields for protons, which is linked with the aforementioned greater LET (higher ionisation density) of the beam of helium ions over protons. In the entrance region (10 mm), the primary yield of $^{\bullet}OH$ decreased

by approximately 1% from the MB peak to the valley, and a corresponding increase of approximately 4% was observed in the H_2O_2 primary yields. The similarities between the beam of helium ions and the beam of protons extends beyond the primary yield graphs, and is even the case when comparing the composition of the PS sources, as shown in Fig. 6.15.

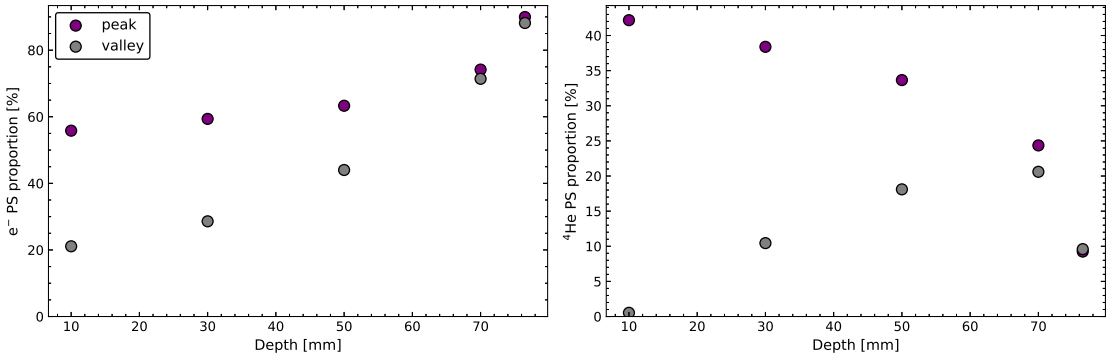

Figure 6.15: Proportion of secondary electrons (left) and ^{4}He ions (right) in the PS sources used in the HeMBRT modality at each location within the water phantom.

As shown in Fig. 6.15, there was a similar trend in depth in the primary and scattered ^{4}He ions as was observed for protons. However, the trend is more severe due to the decreased lateral scattering of ^{4}He, and steeper increase in LET with increasing depth [Mairani et al., 2022]. At 10 mm, the minimum energy of ^{4}He ions in the MB peak was 83.6 MeV/u compared to the 6.8 MeV/u which was present in the MB valley - thus indicating the presence of higher LET particles in the valleys which is consistent with a previously performed MC work [Schneider et al., 2019]. This implicates a greater recombination of $^{\bullet}$OH through R6, which could explain the increase in the primary yield of H_2O_2 observed at this depth. One fact that should be noted is that in contrast to the case of protons, where the valley PS files at 10 mm had a 13% neutron composition, the neutrons in the PS file at this location for the beam of helium ions was in fact representative of the majority. While an approximately similar proportion of protons and electrons was found (∼20%), neutrons comprised approximately 28.9% of the PS file. This proportion of the PS file was effectively ignored as Geant4-DNA does not have physical processes for dealing with neutrons [Incerti et al., 2018]. At this point in time it can not yet be concluded with certainty if this large proportion of neutrons would have an impact on the primary yields or not.

In view of verifying if the similarities between primary yields for the beams of protons and helium ions could be linked with similar trends in frequencies of chemical reactions, the chemical scorer was used to provide the data for Fig. 6.16 and Table 6.4, shown below.

At the depth of 10 mm, similarly to the beam of protons, the increased frequency of R5 between peaks and valleys suggests a reduced yield of H_2O_2 in the valleys over the peaks due to its consumption. This is in contrast to the increased frequency in the valleys seen for R6 which implies a greater production of H_2O_2 in the valleys which, given its prevalence, is thought to be primarily responsible for the increase in the primary yield of H_2O_2 observed in the entrance region of Fig. 6.14. All statistical uncertainties were kept below 0.86% which corresponds with the statistical uncertainty of R5 in the valleys at a depth of 10 mm.

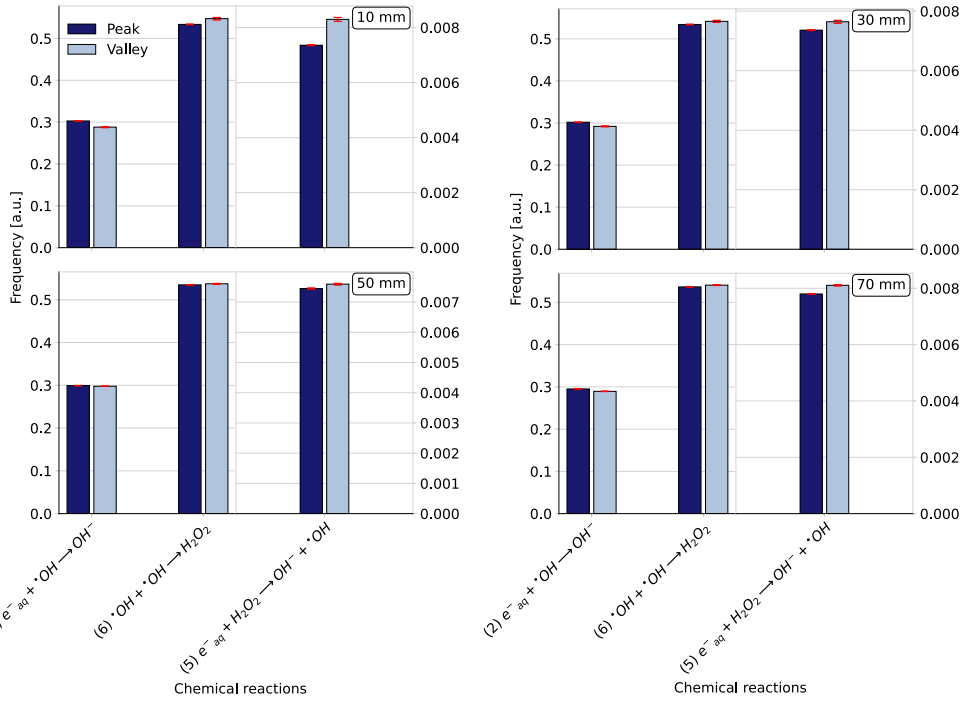

Figure 6.16: Normalised frequencies for the chemical reactions R2, R5, and R6, in HeMBRT peak and valley regions at 10 mm, 30 mm, 50 mm, and 70 mm.

Table 6.4: Proportion of chemical reactions R2, R5, and R6 in HeMBRT, expressed as a percentage of the total occurring chemical reactions at the corresponding depth and lateral location. Blue highlighting indicates a lower expected yield of H_2O_2 in the valleys compared to the peaks for that specific reaction, while values highlighted in grey indicate the contrary; a higher expected yield of H_2O_2 in the valleys compared to the peaks.

Reaction	**Lateral location**	**10 mm**	**30 mm**	**50 mm**	**70 mm**
R2	Peak	30.29	30.19	29.93	29.51
	Valley	28.81	29.20	29.78	28.94
R5	Peak	0.736	0.736	0.745	0.780
	Valley	0.830	0.764	0.759	0.811
R6	Peak	53.36	53.42	53.48	53.68
	Valley	54.73	54.16	53.72	54.08
H_2O_2 net yield: production - consumption (R6 - R5)					
	Peak	52.62	52.68	52.74	52.90
	Valley	53.90	53.40	52.96	53.27
Peak - Valley		-1.28	-0.72	-0.22	-0.37

In contrast to the beam of protons, Table 6.4 highlights that in all cases the differences in the proportion of a specific reaction in the peak compared to that same reaction in the valley are statistically significant from one another (due to the lack of a subscript a). While

the results for reaction R5 at all depths implies a lower proportion of H_2O_2 in the valleys, its presence is in fact dominated by R6 which suggests a greater production of H_2O_2. When evaluating the net effect of H_2O_2 production/consumption, it was found that there was a 1.28% increased proportion of H_2O_2 producing reactions in the valleys compared to the peaks, which was greatest at 10 mm but steadily declined in depth. Nevertheless, the negative values of Table 6.4 highlight that this slightly increased production of H_2O_2 in the valleys appears to continue all the way to the Bragg peak (see Fig. 6.26).

In summary, the behaviour of primary yields for the beam of helium ions is very similar to that of the beam of protons. The primary yield of H_2O_2 increases in depth, and the primary yields of $^{\bullet}OH$ and e^-_{aq} decrease in depth. Beyond 10 mm, the primary yield of the BB modality is similar to that of the MB peaks and valleys. Lastly, there was a decreased yield of $^{\bullet}OH$ and e^-_{aq}, and an increased H_2O_2 primary yield in the valleys at 10 mm, due to an increased proportion of R6.

6.5.3 Photons

The primary yields as a function of depth for the beam of photons is depicted in Fig. 6.17. In contrast to the beam of protons or ^{4}He ions, there were statistically significant differences at all depths in the primary yields of all species when comparing the MB peak/BB modality yields, to the primary yields of the MB valleys. The difference across all depths between the peaks and valleys appeared to be approximately constant, and an average difference of 0.93% and 2.46% was found for $^{\bullet}OH$ and H_2O_2 respectively. The MB peak $^{\bullet}OH$ primary yield ranged from approximately 3.74 species/100 eV at 10 mm to 3.77 species/100 eV at 76.5 mm, while the MB valley yield ranged from approximately 3.71 species/100 eV to 3.73 species/100 eV over the same distance. The MB peak H_2O_2 primary yield decreased from about 0.514 species/100 eV to 0.506 species/100 eV between 10 mm and 76.55 mm and over the same distance, the MB valley yield decreased from 0.526 species/100 eV to 0.521 species/100 eV.

All statistical uncertainties were maintained below 0.1% at all depths. Nevertheless, the seemingly erratic trend in depth (particularly for e^-_{aq}) seems to suggest some systematic uncertainties in the simulation. Indeed, compared to the charged particle beams, obtaining statistically relevant results in microscopic targets for a macroscopic source of photons is particularly challenging. This is primarily due to the low interaction probability of a beam of photons over microscopic distances. Ultimately, two explanations were found to explain the seeming erratic trends in Fig. 6.17. Firstly, it should be noted that the scale of Fig. 6.17 is significantly smaller than the scale of Figures 6.11 and 6.14. In these latter figures, the primary yield changes substantially from the entrance region to the Bragg peak due to the increasing LET of the particle. This is not the case for the beam of photons, where if the same scale was used, the primary yield would appear approximately constant (as can be seen in Fig. 6.26). Compared to the proton and helium yields, the scale of the primary yields for photons is approximately a factor of 5 and 10 smaller respectively. The second reason has to do with composition of the PS sources. As can be seen in Table 6.2, the number of photon primaries simulated were several orders of magnitude greater than any of the other modalities evaluated in this work, however the computing time required to calculate the G-values corresponding to the resulting PS source was not representative of this substantial gap. This is due to the fact that, as can be seen in Fig. 6.18, the PS sources were composed of approximately 99% photons and 1% secondary electrons regardless of depth. According to the NIST database, the mean free path for the 69 keV

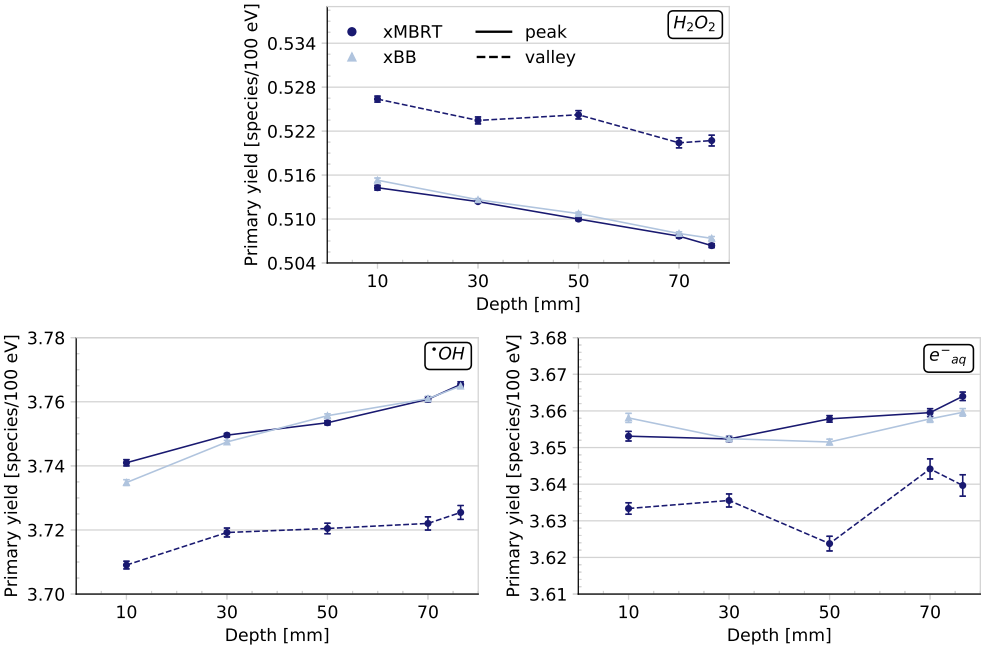

Figure 6.17: xMBRT and xBB primary yields in the peak (solid line) and valley (dashed line) for the species: $^{\bullet}$OH, H_2O_2, and e^-_{aq}, depicted as a function of depth in the water phantom.

effective energy photons used in this work is approximately 0.2 cm [Berger et al., 2010a]. It is therefore evident that photons of a similar energy within the PS sources are unlikely to interact within the 20 μm diameter spherical target volume - leading to a situation whereby the statistical and systematic integrity of the primary yields hinges solely on the distribution of secondary electrons.

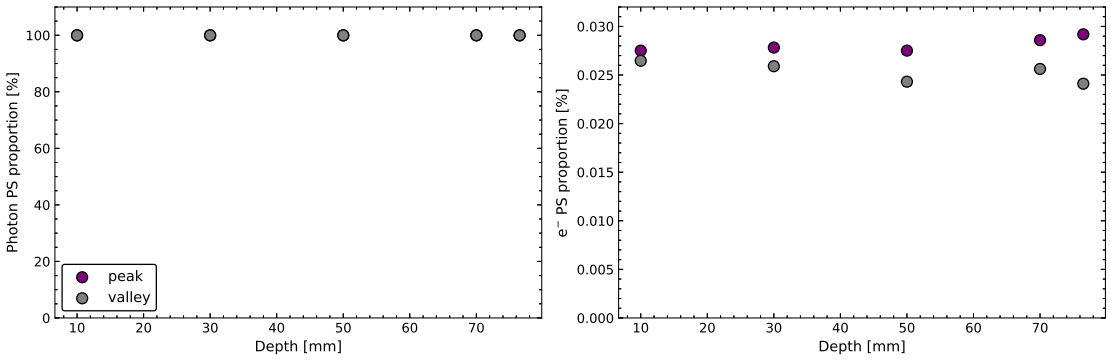

Figure 6.18: Proportion of photons (left) and secondary electrons (right) in the PS sources used in the xMBRT modality at each location within the water phantom.

Fig. 6.19 depicts the energy spectra of these secondary electrons, normalised to the total counts. It seems to indicate that the PS sources of the valleys are composed of electrons with both a lower maximum energy than in the peaks, as well as there being a higher proportion of low energy electrons compared to the peaks. It was postulated that given the low interaction probability of photons within this 20 μm volume, these differences in electron energy spectra had an impact on the initial species generated during the physicochemical stage and resulting chemical reactions of the non-homogeneous chemical

stage, and were in fact primarily responsible for the primary yield trends of Fig. 6.17.

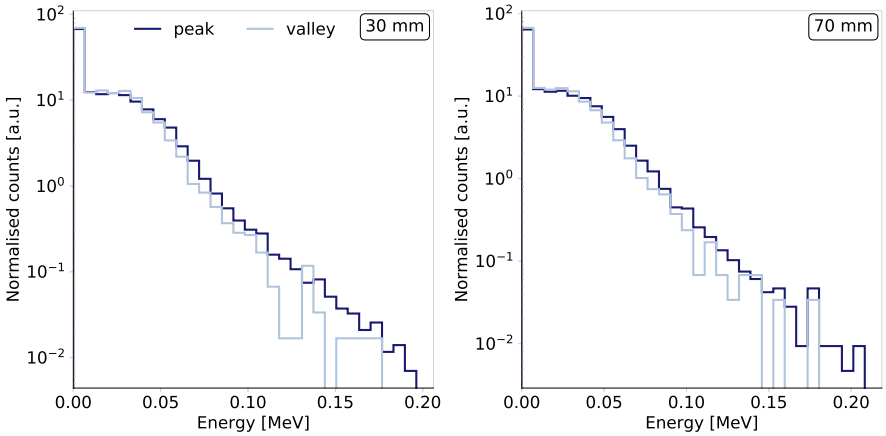

Figure 6.19: Secondary electron energies in the peak (dark blue) and valley (light blue) PS sources at 30 mm (left) and 70 mm (right) for the xMBRT modality.

As was the case with the beam of protons and helium ions, the chemical scorer was used to evaluate the frequencies of reactions R2, R5, and R6 where, as previously stated, the frequency of each reaction was normalised according to the total amount of chemical reactions counted for that specific location within the water phantom. These frequencies were graphed in Fig. 6.20, however given the difficulty at visually interpreting differences between peaks and valleys Table 6.5 was also provided.

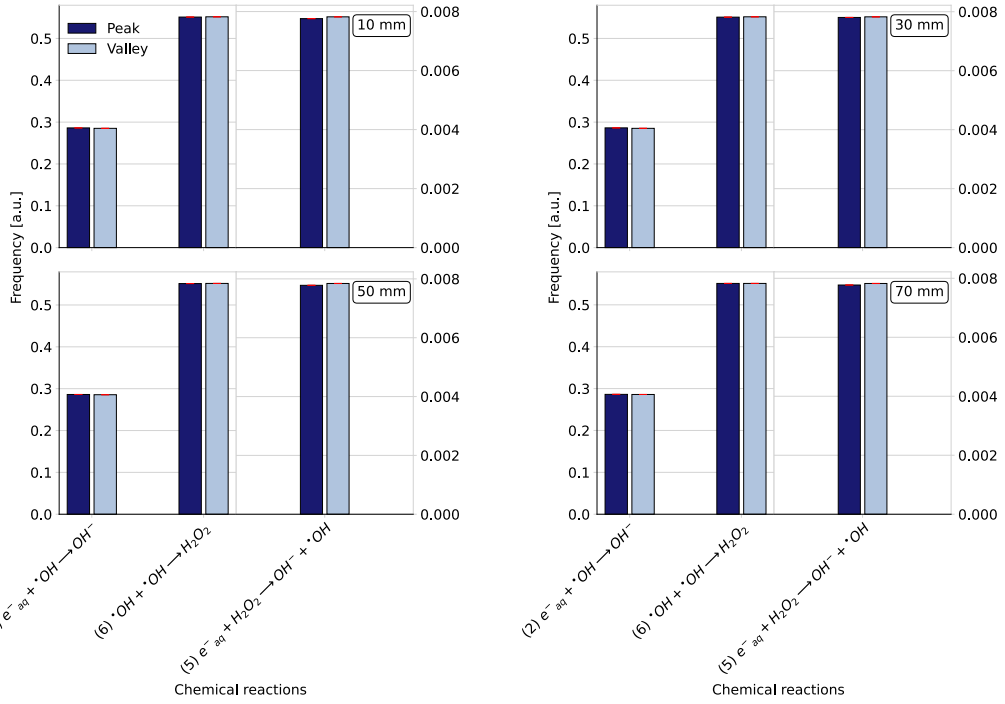

Figure 6.20: Normalised frequencies for the chemical reactions R2, R5, and R6, in xMBRT peak and valley regions at 10 mm, 30 mm, 50 mm, and 70 mm.

All statistical uncertainties were maintained below 0.03%, which corresponds with the statistical uncertainty of R5 in the valley at 70 mm. Both Fig. 6.20 and Table 6.5 indicate

that there was a higher proportion of H_2O_2 consuming reactions (thereby suggesting a lower expected yield of H_2O_2) in the valleys compared to the peaks, which contradicts what was observed in Fig. 6.17. However, as was the case for the proton and helium beams, this reaction occurred at a much lower frequency and it was in fact reaction R6 which was the principle determinant of the primary yields. At all depths, Table 6.5 indicates that there was a greater proportion of R6 in the valleys compared to the peaks, giving first indications that there is a greater production of H_2O_2 in the valleys. Subtracting the proportion of R5 from R6 provides an indication of the net H_2O_2 producing effect at that location, and as seen in Table 6.5, the net effect of the chemical reactions leads to a production of H_2O_2 in the valleys that is greater than in the peaks. This seems to be in line with what was observed in Fig. 6.17, namely an increased yield of molecular products, and a decreased yield of radical products in the valleys compared to the peaks. Subtracting the net H_2O_2 producing proportion of the valleys from those of the peaks yields negative values for 10, 30, and 50 mm, which is representative of the gap between peaks and valleys observed in Fig. 6.17. The one result of Table 6.5 that seems to go against the results of Fig. 6.17 is that of the 70 mm case. The table indicates that at 70 mm there is a lower H_2O_2 producing effect in the valleys compared to the peaks. However, these results need to be taken with a grain of salt due to the fact that, as indicated by the subscript *a*, the proportions of reaction R6 in the peak and valley at this depth are not statistically significantly different.

Table 6.5: Proportion of chemical reactions R2, R5, and R6 in xMBRT, expressed as a percentage of the total occurring chemical reactions at the corresponding depth and lateral location. Values highlighted in blue indicate a lower expected yield of H_2O_2 in the valleys compared to the peaks for that specific reaction, while values highlighted in grey indicate the contrary; a higher expected yield of H_2O_2 in the valleys compared to the peaks.

Reaction	**Lateral location**	**10 mm**	**30 mm**	**50 mm**	**70 mm**
R2	Peak	28.616	28.626	28.614	28.621
	Valley	28.514	28.515	28.559	28.595
R5	Peak	0.776	0.781	0.778	0.777
	Valley	0.782	0.783	0.784	0.783
R6	Peak	55.114	55.095	55.115	55.108[a]
	Valley	55.176	55.175	55.150	55.109
H_2O_2 net yield: production - consumption (R6 - R5)					
	Peak	54.338	54.314	54.337	54.331
	Valley	54.394	54.392	54.366	54.326
Peak - Valley		-0.056	-0.078	-0.029	0.005

[a] indicates that there is no statistically significant difference between the peak and valley values for this reaction at this location.

It is hypothesised that reaction R2 is complementary to the behaviour of reaction R6, in that the lower the consumption of $^{\bullet}OH$ through R2 in the valleys, the higher the recombination probability through R6. While the behaviour of R2 (increased presence of $^{\bullet}OH$ in the valleys) itself seems to contradict the reduced primary yield of $^{\bullet}OH$ observed in

Fig. 6.17, it is believed that the large proportion of R6 overcomes this contradiction and reduces the presence of •OH through its consumption.

In summary, the increased recombination of •OH at all depths in the valleys through R6, led to the increased primary yield of H_2O_2 in the valleys observed in Fig. 6.17. The difference between the peaks and valleys appears approximately constant in depth. The behaviour of R6 in the valleys compared to the peaks is complemented by R2, and appears to overcome the behaviour of R5, which itself is not consistent with what is depicted in the primary yield graphs.

6.5.4 Carbon ions

As previously stated, the exceptionally high number of chemical species produced in the Bragg peak of high LET particles makes water radiolysis simulations towards the end of the particle range extremely challenging [Baba et al., 2021]. Despite splitting the simulations, various technical challenges were encountered when attempting to simulate water radiolysis of the ^{12}C beams at the Bragg peak depth of 76.5 mm (see footnote 38). Consequently, all the results for the carbon beams were limited to a depth of 70 mm. The primary yields for these beams are shown in Fig. 6.21. The decrease in depth of the primary yields of •OH and e^-_{aq}, and the corresponding increase in the primary yield of H_2O_2 follows a similar trend to the other charged particle beams. Given the increased LET of ^{12}C ions over protons and ^4He ions, there is a greater proportion of radical-radical interactions, leading to a sharper decrease in the primary yields of both •OH and e^-_{aq} in depth, and a sharper increase in H_2O_2 primary yields in depth (see Fig. 6.26).

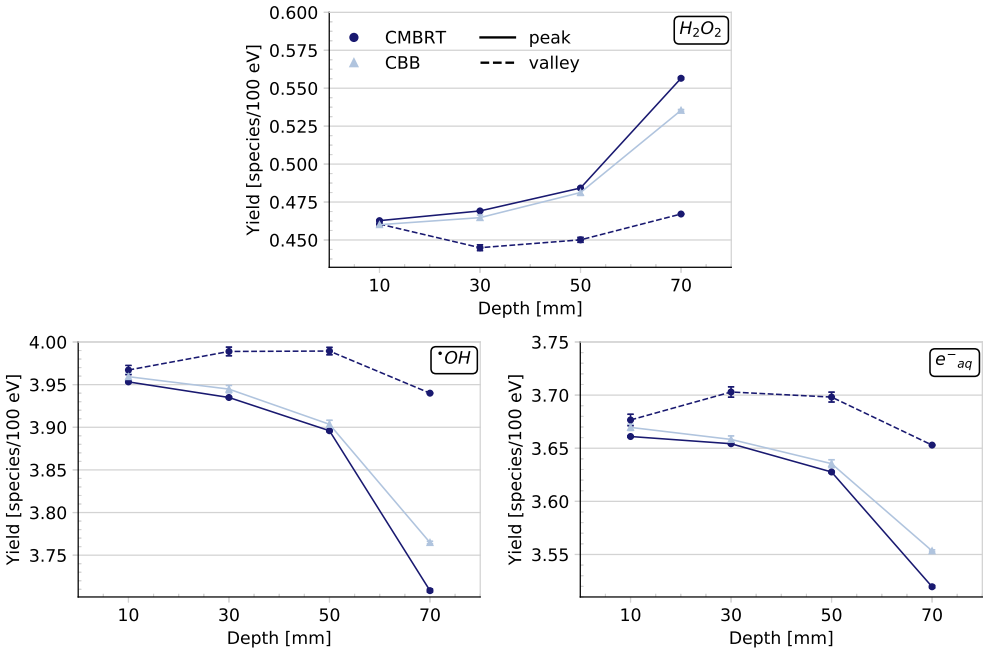

Figure 6.21: CMBRT and CBB primary yields in the peak (solid line) and valley (dashed line) for the species: •OH, H_2O_2, and e^-_{aq}, depicted as a function of depth in the water phantom.

It was observed that these yields behaved similarly in the entrance region to the beams of protons or ^4He ions, in the sense that there was an increase in the primary yield of •OH and e^-_{aq} between 10 mm and 30 mm, and a corresponding decrease in the primary yield of

H_2O_2 between the same depths. However, what differentiates carbon from these other two beams is that the primary yields in the valleys of each chemical species are significantly different from those in the BB modality/MB peak at all depths. All statistical uncertainties were maintained below the maximum of 0.15%, which was found for the e^-_{aq} primary yield at 10 mm in the MB valley. Figure 6.21 depicts a decrease in the primary yields of $^{\bullet}OH$ and e^-_{aq} in the MB peak of approximately 6% and 4% respectively, from 3.95 species/100 eV at 10 mm to 3.71 species/100 eV at 70 mm for the $^{\bullet}OH$ species, and from 3.66 species/100 eV at 10 mm to 3.52 species/100 eV for the e^-_{aq}. The primary yield of H_2O_2 in the MB peaks increased by 17% from 0.463 species/100 eV at 10 mm to 0.557 species/100 eV at 70 mm. The percentage increase of the primary yield in the valleys compared to the peaks was approximately 0.5% at 10 mm and 6% at 70 mm for the $^{\bullet}OH$ species. No statistically significant difference in the primary yield of H_2O_2 in the MB valley at 10 mm compared to the peak was observed, however at 70 mm the percentage decrease was found to be approximately 16%. At 10 mm the percentage increase of the e^-_{aq} primary yield in the valleys compared to the peaks was 0.5% which increased to 4% at 70 mm. Compared to the other irradiation modalities investigated, the beams of ^{12}C ions appear to be the only ones in which there is a statistically significant difference between the primary yields in the MB peaks compared to those on-axis in the BB case.

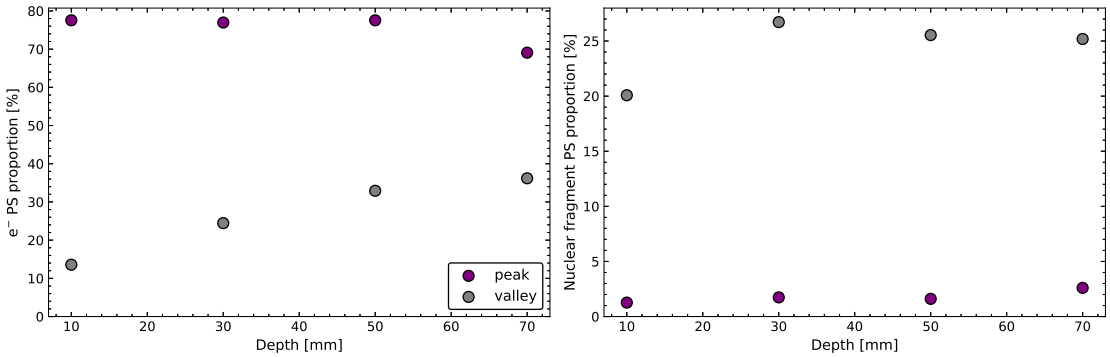

Figure 6.22: Proportion of secondary electrons (left) and nuclear fragments (right) in the PS sources used in the CMBRT modality at each location within the water phantom.

Due to the high LET of the particles on-axis in the MB peak, a sharp increase/decrease of the primary yields was observed in these regions. Contrastingly, Fig. 6.21 depicts a quasi-plateau up to 50 mm for the primary yields in the MB valleys, beyond which the primary yields begin to follow the same increasing/decreasing trend as is observed in the peak region. One of the initial hypotheses to explain the different primary yields in the peak and valley regions, is the presence of nuclear fragments in the valleys. In contrast to the beams of protons and helium ions, the ^{12}C beam induces a more *exotic* radiation field in the valleys as a result of the nuclear reactions of ^{12}C within the water phantom. Previous MC studies have shown that for carbon beams with the same ctc used in this thesis (3500 μm), the main contributor to the dose in the MB peaks is delta rays up until the Bragg peak region, at which point the nuclear fragments begin to take over. However in the MB valleys at all depths, nuclear fragments are the main contributors to the dose [González et al., 2017]. These findings were corroborated by Fig. 6.22, which depicts the proportion of secondary electrons and nuclear fragments in the PS sources used.

As can be seen in Fig. 6.22, there are significantly more nuclear fragments in the valleys compared to the peaks at all depths. The initial hypothesis was that the increased presence of nuclear fragments in the MB valleys would lead to an increase in the proportion

of ionisations in the MB valleys, since the only physical process available for ions is the *G4DNAIonisation* process [Incerti et al., 2018]. Consequently, the expectation was that there would be an increase in the dissociative decay process of the physicochemical stage (see Table 3.1) resulting in an excess production of $H_3O^+ + {}^{\bullet}OH$, which could have an impact on the subsequent chemistry of the non-homogeneous chemical stage. While an in depth analysis of the proportions of physicochemical processes was not possible in TOPAS-nBio v1.0, the chemical scorer was used to calculate the frequencies of chemical reactions in the chemical stage, from which assumptions were made about the proportions of physicochemical processes, which were then used to either corroborate or reject this initial hypothesis. The frequencies of chemical reactions are depicted in Fig. 6.23 and Table 6.6.

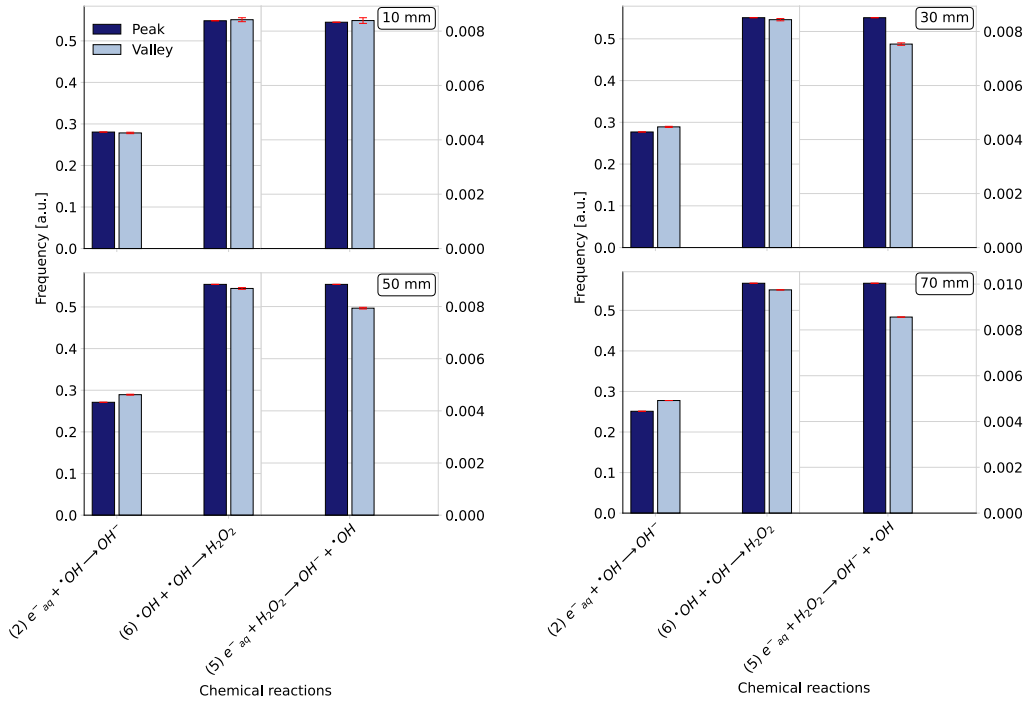

Figure 6.23: Normalised frequencies for the chemical reactions R2, R5, and R6, in CMBRT peak and valley regions at 10 mm, 30 mm, 50 mm, and 70 mm.

All statistical uncertainties were maintained below the maximum of 1.2%, which was found for R5 in the MB valley at 10 mm. It is evident from Fig. 6.23 that at the depths of 30, 50, and 70 mm, there is a reduced proportion of R5 (i.e. a lower consumption of H_2O_2) in the valleys compared to the peaks, with the exact values provided in Table 6.6. While this finding seems to contradict what is observed in Fig. 6.21 which depicts a lower primary yield of H_2O_2 at all depths beyond 10 mm, the occurrence of R5 is substantially lower than R6, which ends up dominating the behaviour of ${}^{\bullet}OH$ and H_2O_2 - as was the case for the beams of protons, photons, and helium ions. Fig. 6.23 also shows a decreased proportion of R6 in the valleys compared to the peaks, which is consistent with the primary yield graphs of Fig. 6.21. This lower recombination of ${}^{\bullet}OH$ through R6 is evident in Table 6.6 for the depths of 30, 50, and 70 mm, however an increased proportion of this reaction was found for the depth of 10 mm. Nevertheless, as is seen in Fig. 6.21 and as is represented by the subscript a in the table, yield values between the peak and valley at this depth are not statistically significantly different. The net behaviour of H_2O_2, found by subtracting the R5 proportion from the R6 proportion, is consistent with the observations of Fig. 6.21.

At the depths of 30 mm and beyond, there was an increased proportion of R2 in the valleys compared to the peaks, implicating an increased consumption of $^{\bullet}OH$. This is hypothesised to be complementary to the behaviour of R6 in the valleys. Fewer R6 reactions means there is more $^{\bullet}OH$ species able to react with e^{-}_{aq} in R2, and more R2 reactions means there is less available $^{\bullet}OH$ species which would otherwise recombine to form H_2O_2 through R6. The difference between the net H_2O_2 producing effect in the valleys compared to the peaks is shown in the penultimate row of Table 6.6 with values of 0.37%, 0.89%, and 1.49%, for 30, 50, and 70 mm. The increasing trend in these values, which are indicative of the difference of H_2O_2 yields between the peaks and valleys, are consistent with the increasing gap between the peak and valley yields observed in Fig. 6.21.

Table 6.6: Proportion of chemical reactions R2, R5, and R6 in CMBRT, expressed as a percentage of the total occurring chemical reactions at the corresponding depth and lateral location. Values highlighted in blue indicate a lower expected yield of H_2O_2 in the valleys compared to the peaks for that specific reaction, while values highlighted in grey indicate the contrary; a higher expected yield of H_2O_2 in the valleys compared to the peaks.

Reaction	**Lateral location**	**10 mm**	**30 mm**	**50 mm**	**70 mm**
R2	Peak	28.05	27.69	27.10	25.12
	Valley	27.84	28.91	28.94	27.77
R5	Peak	0.83[a]	0.85	0.88	1.00
	Valley	0.84	0.75	0.79	0.86
R6	Peak	54.84[a]	55.06	55.42	56.69
	Valley	55.10	54.59	54.44	55.06
H_2O_2 net yield: production - consumption (R6 - R5)					
	Peak	54.01	54.21	54.54	55.69
	Valley	54.26	53.84	53.65	54.20
Peak - Valley		-0.25	0.37	0.89	1.49

[a] indicates that there is no statistically significant difference between the peak and valley values for this reaction at this location.

Given the increased presence of nuclear fragments in the valleys, it initially seemed counter-intuitive that there would be a higher primary yield of $^{\bullet}OH$ in the valleys, combined with a lower proportion of $^{\bullet}OH$ recombining through R6 to yield H_2O_2. These doubts were based on that fact that high LET particles are known to induce more radical-radical reactions, thereby reducing the yield of radical species and increasing the yield of molecular products. While it is indeed true that a greater proportion of nuclear fragments would cause a greater production of $^{\bullet}OH$ through dissociative decays from an ionised state (see Table 3.1), it should be remembered that the composition of these PS sources is only descriptive of the particles entering into the 20 μm volume, and not representative of the distribution of ionisations and excitations occurring within the actual volume. Consequently, it is reasonable to assume that while there are indeed a high number of dissociative decays from an ionised state, there would also be a substantial creation of other secondary particles such as protons and electrons within the actual

volume, which themselves are able to cause both excitations and ionisations due to the presence of appropriate Geant4-DNA physics processes. These excited water molecules would, in thermalising, produce $^{\bullet}OH$ and e^{-}_{aq} among other species. Ultimately, the excess creation of these radical species, leading to a large proportion of these species not being consumed in a chemical reaction before the simulation was ended, would explain the increased radical species yield observed in Fig. 6.21. Furthermore, an excess of these species would also be consistent with the observation in Fig. 6.23 and Table 6.6 that there is an increased proportion of R2 in the valleys compared to the peaks. This is the second most common reaction after R6, and the most occurring reaction involving e^{-}_{aq} - one of the major chemical species produced from excited water molecules in the physicochemical stage.

In summary, at depths beyond 10 mm, there was a reduced primary yield of H_2O_2 and an increased primary yield of the radical species $^{\bullet}OH$ and e^{-}_{aq} in the MB valleys compared to the peaks - which appears to become more severe in depth. This difference was attributed to the presence of nuclear fragments in the valleys. The behaviour of the most dominant reaction, R6, suggested a lower $^{\bullet}OH$ recombination to produce H_2O_2, which was indeed observed in Fig. 6.21, and the excess radical species created from excited water molecules led to an increase in R2 which had a complementary effect on R6.

The possible sources of systematic uncertainty in the simulations are evaluated in the following section.

6.6 Possible sources of systematic uncertainty

Given its novelty, there were no other published resources with which to compare the ROS primary yields obtained in the MB peaks and valleys of this work. Even less so due to the fact that multiple different particles were studied. It was therefore of interest to perform a brief evaluation of the possible sources of type B (systematic) uncertainty. To this end, two possible sources were investigated:

- The splitting methodology employed.
- Influence of the number of scored particles in each PS source.

6.6.1 Validation of the splitting methodology

As previously stated, the recommendation when dealing with computationally demanding TS simulations of particles near the Bragg peak is to split the simulation into multiple smaller and independent simulations [Baba et al., 2021]. This splitting makes logical sense in TOPAS-nBio due to the fact that water radiolysis is simulated on a history-by-history basis, with each original history being independent from one another [Ramos-Méndez et al., 2018].

In order to verify this logical belief, a test simulation was performed in which the G-value for the pMBRT modality was calculated in the peak at a depth of 70 mm. This location was chosen due to the fact that simulations near the Bragg peak depths are primarily those that need to be split. Protons were chosen over carbon ions due to fact that, from a computational point of view, entire simulations *sans splitting* are significantly easier to perform for protons as opposed to carbon ions due to their lower LET. A full macroscopic simulation of 9×10^{8} original histories was launched, leading to a PS file with 9632 scored particles. Two independent microscopic second step simulations were launched

using this PS file - one in which the entire file was used as the source, and a second in which the file was first split 50 times, before G-value simulations were launched with each of these 50 individual PS files as the particle source. A comparison between the two methodologies is shown in Fig. 6.24.

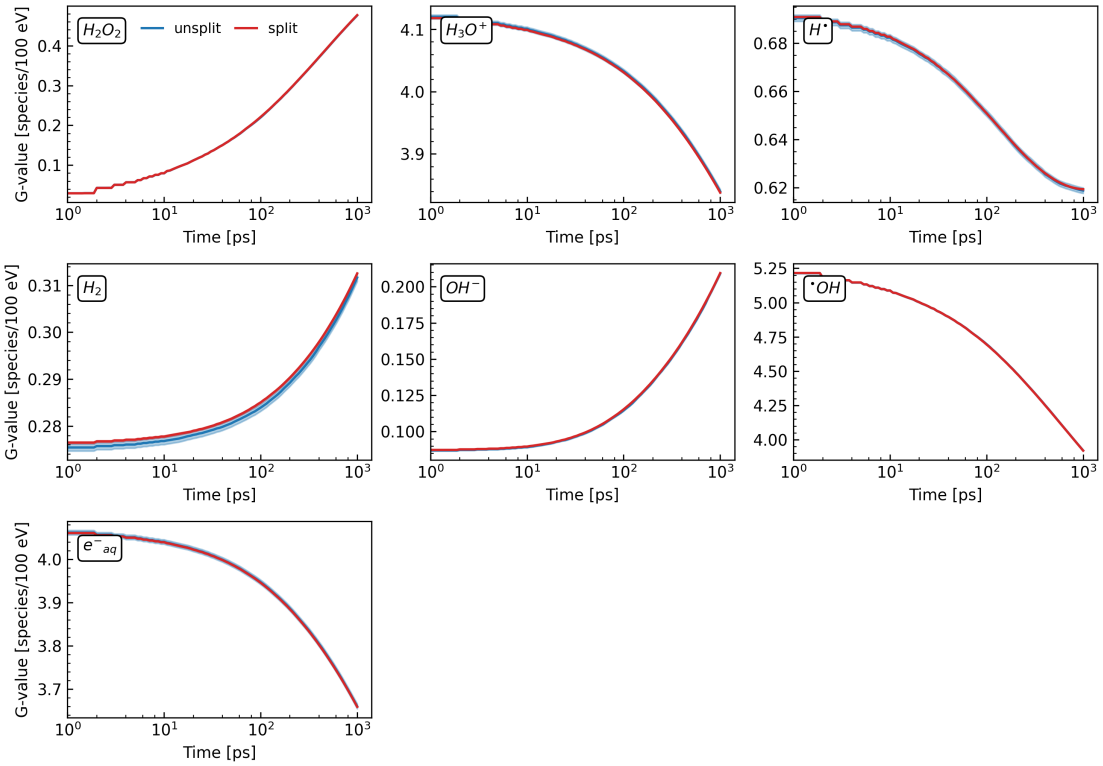

Figure 6.24: Comparison of G-values for all chemical species for the pMBRT modality in the peak at 70 mm. Unsplit simulations are depicted in blue, and split simulations are shown in red.

The shaded area around each line represents the statistical uncertainty, and as can be seen, both the G-values and the statistical uncertainties of the split vs. unsplit simulations are approximately equivalent. The primary yields were collected from the last binned values of these G-values and are shown in Table 6.7 along with the associated statistical uncertainties.

Table 6.7: Primary yield differences between the split and unsplit simulations.

Species	Unsplit yield [species/100 eV]	Split yield [species/100 eV]	Difference after split [%]
H_2O_2	0.4763 ± 0.0012	0.4769 ± 0.0002	0.126
H_3O^+	3.8400 ± 0.0032	3.8378 ± 0.0004	-0.057
$H^\bullet$	0.6187 ± 0.0012	0.6193 ± 0.0002	0.097
H_2	0.3116 ± 0.0008	0.3125 ± 0.0002	0.288
OH^-	0.2090 ± 0.0007	0.2094 ± 0.0002	0.191
$^\bullet OH$	3.9210 ± 0.0039	3.9198 ± 0.0005	-0.031
e^-_{aq}	3.6601 ± 0.0056	3.6588 ± 0.0008	-0.036

It should be noted that statistical uncertainties of the split simulations are smaller than those of the unsplit simulation. This is due to the combination in quadrature of statistical uncertainties which was performed. As can be seen in Table 6.7, there are negligible differences between the primary yields of the two methodologies, with the largest being a 0.288% increase in the primary yield of the split simulation over the unsplit simulation. These minor differences thus gave confidence to the application of the splitting methodology to radiolysis simulations performed in this thesis.

6.6.2 Influence of the number of scored particles

One of the challenges with radiolysis simulations of the carbon beam in particular was linked with the contradiction of wanting to obtain rich PS sources, that well describe the radiation field, but then ultimately needing to use a lower number of histories in order for the simulations to be carried out successfully given the available computational resources. While macroscopic simulations of millions of particles can be completed in a matter of minutes (of course depending on the simulation set-up), TS simulations of these high LET beams can only be performed with PS files containing a few thousand scored particles at most. However, use of these PS sources with a few thousand scored particles is extremely complicated, not only from a computational point of view, but also due to the post-processing considerations i.e. how to handle *OOM* errors (see footnote 38). And so in an effort to ease the burden of using large PS sources, smaller PS sources were always favoured in the radiolysis simulations performed in this work. Consequently, it was important to evaluate to what degree the size of these phase space files could be reduced without negatively impacting the primary yields.

To this end, test simulations were performed calculating the G-value in the peak at 70 mm for the CMBRT modality. In the case of the smaller PS source, a total of 4.5×10^6 original histories were simulated in the macroscopic first step simulation, resulting in 316 scored particles in the PS file. For the larger PS source, the total number of original histories was increased four-fold, to 1.8×10^7, resulting in 1356 scored particles to be simulated in the PS source. While both sets of simulations were split 50 times, for the simulations involving the 1356 scored particles, a special *Quality of Service* needed to be associated with the job submission scripts on the computing cluster. This quality of service was specified by the `-Q` option which was explicitly supplied with the parameter `long`, thus allowing the simulation to continue for up to 3 days without being cancelled[39]. G-values for both sets of simulations are shown in Fig. 6.25.

It is visually verifiable that despite the smaller number of scored particles, there are no negligible differences in the G-values. Primary yields associated with each species are shown below in Table 6.8.

[39] https://www-hpc.cea.fr/tgcc-public/en/html/toc/fulldoc/Job_submission.html

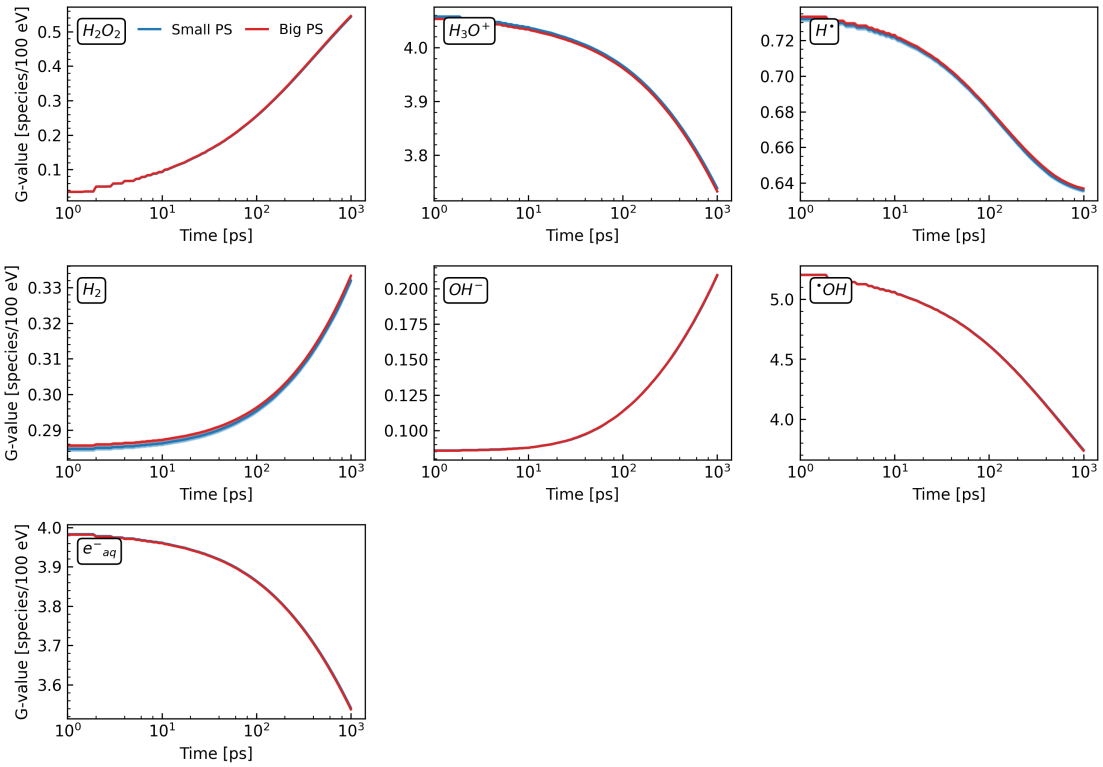

Figure 6.25: Comparison of G-values for all chemical species for the CMBRT modality in the peak at 70 mm. Simulations with the small PS source (316 scored particles) are depicted in blue, while the larger PS source of 1356 particles is shown in red.

Table 6.8: Primary yield differences between the use of a small PS source (316 scored particles), compared to a big PS source (1356 scored particles).

Species	Small PS yield [species/100 eV]	Big PS yield [species/100 eV]	Difference big to small [%]
H_2O_2	0.5431 ± 0.0014	0.5456 ± 0.0008	0.458
H_3O^+	3.7386 ± 0.0023	3.7328 ± 0.0012	-0.155
$H^\bullet$	0.6359 ± 0.0009	0.6370 ± 0.0005	0.173
H_2	0.3320 ± 0.0007	0.3333 ± 0.0003	0.390
OH^-	0.2091 ± 0.0005	0.2097 ± 0.0002	0.286
$^\bullet OH$	3.7439 ± 0.0036	3.7362 ± 0.0019	-0.206
e^-_{aq}	3.5412 ± 0.0024	3.5375 ± 0.0012	-0.105

As expected, in all cases where the big PS source was used, smaller statistical uncertainties were obtained. However, given that the largest difference between the yields was 0.458%, it was concluded that the gain in precision with the use of the larger PS source was not worth the required computational and post-processing resources. Consequently, the approach used in this thesis was to perform a retrospective analysis of the statistical uncertainties of the primary yields, and subsequently conclude that the systematic uncertainty associated with said primary yields was low as long as the statistical uncertainty was maintained below 1%. As noted when describing the results of

each modality in section 6.5, the maximum statistical uncertainty for the primary yields for protons, helium ions, photons, and carbon ions was found to be 0.38%, 0.73%, 0.10%, and 0.15% respectively. This therefore gave confidence to the belief that the number of scored particles in each PS source was sufficiently high enough to avoid incurring systematic uncertainties.

Synthesising all these primary yield results, final discussions concerning the implications on the underlying mechanisms of MBRT efficacy are described in the following section.

6.7 Discussion and conclusions

This chapter detailed investigations into the relative production of ROS between peak and valley regions of MBRT. As previously outlined, these investigations were warranted due to the fact that, firstly, MBRT represents an exciting new RT modality with advantages in terms of normal tissue sparing [Deman et al., 2012, Prezado et al., 2017a, Prezado et al., 2018] and tumor control [Prezado et al., 2019, Bertho et al., 2021, Lamirault et al., 2020a, Sotiropoulos et al., 2021], however the candidates thought to be responsible for the underlying radiobiological mechanisms are still not fully understood. Secondly, the production of ROS from water radiolysis are potentially involved in some of these aforementioned mechanisms, but there were, at the time of writing, no systematic studies investigating the potential differences in their production between MB peak and valley regions. This work therefore represents a first microdosimetric MC study, characterising the expected early time point differences in the distribution of ROS produced from MBs of different particles.

Looking first to the primary yields for protons and ^{4}He ions of Figures 6.11 and 6.14, very similar results were observed. Both graphs depicted an increasing trend in the yield of H_2O_2 in depth, and a decreasing yield of $^{\bullet}OH$ and e^-_{aq}, which are in line with what was expected from literature [Wasselin-Trupin et al., 2002]. Given the higher LET of the helium ion beam, these trends in depth are more extreme than that of the proton beam, as is shown in Fig. 6.26. Through a counting of the chemical reactions with the chemical scorer, entrance region differences in the MB valleys were attributed to an increased rate of recombination reactions through R6, and as evidenced by an evaluation of the difference between the net H_2O_2 producing effect of the valleys compared to the peaks (shown in the penultimate row of Tables 6.3 and 6.4 for protons and helium ions respectively), protons exhibit a slightly higher primary yield of H_2O_2 up 50 mm, while helium ions exhibited the difference at all depths. It should be noted however, that given the statistical uncertainties between the peak and valley yields, particularly for the beam of protons, it is not certain that this slightly higher primary yield of H_2O_2 in the valleys is a reasonable expectation. However, a difference between peaks and valley observed up to 50 mm for protons and at all depths for helium ions would be in line with the lateral dose profiles of Figures 6.6 and 6.7 which show that protons exhibit a greater homogenisation in depth compared to helium.

Figures 6.11 and 6.14 also depict ROS yields in the MB peaks which are not statistically significantly different from the BB condition at all depths. In other words, for an equivalent energy deposited there is no difference in the primary yields produced in the MB peaks compared to in a conventional BB. If we consider for a moment a more macroscopic scale, in which a pMBRT/HeMBRT irradiation is performed delivering the same average dose as a BB irradiation. The results of this work suggest that it would be reasonable to assume that the total ROS at any point in time would be equivalent between the MBRT modality

and the BB modality (due to the high ROS production of the peaks being compensated by the low ROS production of the valleys). Nevertheless, there may be differences in the spatial distribution of ROS, depending on the level, if any, of ROS diffusion from the peaks to the valleys.

One of the implications of the •OH primary yields in the peaks being largely equivalent to the •OH yields of the valleys (beyond the entrance region), is that we can conclude that for protons and helium ions, the level of indirect DNA damage across the irradiated volume is directly related to the PVDR. Similar conclusions were reached about the direct DNA damage by a previous member of our team [Dos Santos et al., 2020]. This extrapolation of microsecond yields of •OH to an irradiation dose delivered over seconds/minutes is coherent due to the fact that •OH is rapidly scavenged and does not diffuse long distances. In order to simulate this biological scavenging, the chemical stage was limited to 1 ns, which is in line with the seminal work by Roots and Okada [Roots and Okada, 1975] who calculated an average •OH lifetime of approximately 4 ns. This rapid scavenging implies a lack of background reactions beyond the spur that would otherwise need to be taken into account when performing such an extrapolation.

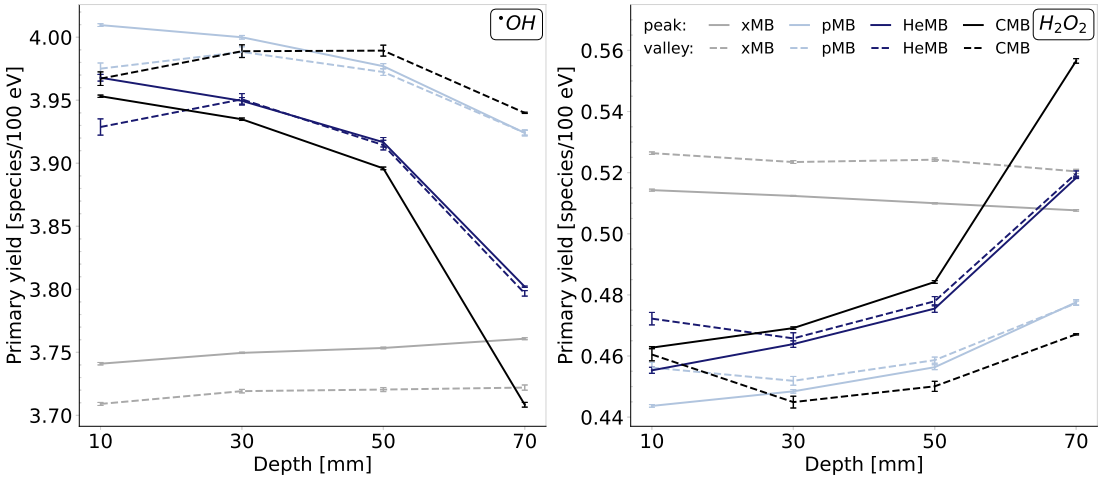

Figure 6.26: Primary yield comparisons between xMBRT, pMBRT, HeMBRT, and CMBRT in the peaks (solid lines) and valleys (dashed lines), up to a depth of 70 mm in the water phantom. Each modality is represented by a colour. The left panel depicts •OH yields, while the right panel represents the yields of H_2O_2.

The xMBRT modality represents a divergence from the pMBRT and HeMBRT modalities in the sense that at all depths there was a difference in the primary yields of •OH, H_2O_2, and e^-_{aq} between peak and valley regions. For xMBRT, the reduced primary yield of •OH could imply a lower amount of indirect DNA damage in the valleys of xMBRT than what is suggested by the PVDR. However at this point in time, it is still unclear if these differences in the primary yields of the peaks compared to the valleys can be decoupled from the experimental uncertainty to realistically observe the biological consequences of this difference. From a macroscopic point of view, conclusions similar to those described for the pMBRT/HeMBRT modality can be drawn given that the ROS primary yields in the MB peaks are largely equivalent to the calculated yields in the corresponding BB.

Now looking at the CMBRT modality: at all depths in the water phantom there is a higher primary yield of •OH and e^-_{aq}, and a lower primary yield of H_2O_2 in the valleys compared to the peaks. Interestingly, the ROS primary yields observed in the CMBRT valleys is most comparable to the pMBRT yields, as depicted in Fig. 6.26. In fact, among

the charged particle beams, beyond 10 mm the primary yield of H_2O_2 in the CMBRT valleys was the lowest, while simultaneously being the highest in the peaks. This is a consequence not only of the highly heterogeneous nature of the dose profile at all depths, but also the high LET of the beam. Performing the same extrapolation to the more macroscopic absorbed dose, these results imply an increased level of indirect DNA damage in the CMBRT valleys than what would be suggested by the PVDR. This difference in the primary yield between between peaks and valleys was attributed to the unique radiation field in the MB valleys, which was composed of a large proportion of nuclear fragments, which in turn induced a different set of pre-chemical processes and chemical reactions than was observed in the peaks.

As stated when discussing the results for the beam of carbon ions, results of the chemical scorer suggested a lower proportion of $^{\bullet}OH$ recombination reactions through R6 to form H_2O_2, which was further complemented by the increased consumption of $^{\bullet}OH$ with e^-_{aq} through R2. These results do not exist in isolation, and there is in fact a theoretical basis for this seemingly contradictory decrease of H_2O_2 primary yields in the MB valleys which are filled with high LET nuclear fragments. Wasselin-Trupin *et al.* observed that a decrease in the H_2O_2 primary yields begins in the very high LET regions of Carbon, Nitrogen, and Neon ions beams [Wasselin-Trupin et al., 2002]. They hypothesised that this decrease occurs due to the increased reactions of H_2O_2 with $^{\bullet}OH$ through $^{\bullet}OH + H_2O_2 \longrightarrow H_2O + HO_2^{\bullet}$, and the increased reactions of H_2O_2 with e^-_{aq} through $e^-_{aq} + H_2O_2 \longrightarrow OH^- + {}^{\bullet}OH$, therefore leading to a situation whereby there is a smaller concentration of H_2O_2 escaping the high radical concentration chemical track. Consequently, the conclusion draw from the work performed in this thesis is that a similar effect is occurring in the MB valleys. While the first reaction is not included in the default chemical reactions of TOPAS-nBio v1.0, the second reaction is R5 in this work. While the behaviour of R5 in the MB valleys shown in Fig. 6.23 is not in line with the hypothesis of Wasselin-Trupin *et al.*, the increased proportion of R2 seems to adhere to the assumptions inherent in the hypothesis, namely an excess of radical species.

At this point in time, it is still difficult to form concrete conclusions about the biological implications of these results, particularly for the yields of H_2O_2, however biological experiments evaluating the level of ROS production between MBs and BBs has recently been started within our team. The level of expected indirect DNA damage can be, and was reasonably inferred from the $^{\bullet}OH$ yields, and while the proportion of indirect DNA damage in the peaks compared to the valleys is expected to be the same as the PVDR for the pMBRT and HeMBRT modalities, the results of the xMBRT modality suggests a higher proportion, while the results of the CMBRT modality suggests the opposite. It has been shown that the anti-tumor immune response triggered by ICD is weakened for elevated levels of H_2O_2 [Lennicke et al., 2015, Deng et al., 2020]. Consequently, it could be inferred that the valley regions of the MBRT modalities in which a dose heterogeneity is maintained at all depths would be the most beneficial to the triggering of an immune response due to the low expected primary yields of H_2O_2. This effect could be even more prevalent for the beam of carbon ions due to the fact that it resulted in the lowest primary yields of H_2O_2. Nevertheless, these conclusions are contingent on two very important aspects, namely the lifetime and diffusion distance of H_2O_2, which would implicate either a heterogeneous or homogeneous distribution of this species. The main limitations of this work are as follows:

- Due to the limited cross-sections available in Geant4-DNA [Incerti et al., 2018], and given that the SBS method assumes an isotropic volume [Karamitros et al., 2014], all simulations were performed in pure liquid water. The complex heterogeneities present in the microenvironment of the cell may affect water radiolysis [Le Caër,

2011].

- Systematic uncertainties arising from the difference in choice of chemical reactions between different simulation codes was unavoidable. For example, the reaction $^{\bullet}OH + H_2O_2 \longrightarrow H_2O + HO_2^{\bullet}$ was not included in TOPAS-nBio v1.0 however it is partly responsible for a reduction in the primary yield of H_2O_2, particularly at high LETs. A combined statistical and systematic uncertainty of approximately 6% has been previously reported [Ramos-Méndez et al., 2018].

- Discrepancies between experimental and simulation yields of H_2O_2 have been previously attributed to the fact that multiple ionisations of the same water molecule have no physical process in Geant4-DNA [Baba et al., 2021].

Looking to the future, novel accelerators such as LhARA could provide flexible and tunable beam parameters to further investigate exactly how certain radiobiological responses are modulated by changes in the physical characteristics of the irradiation [Aymar et al., 2020]. In the free radical work described in this chapter of the thesis, ideal sources (assumed to be magnetically focused) were used, and particles of protons, helium ions, and carbon ions were investigated in anticipation of this novel accelerator. A first set of MC simulations have already been performed showing this accelerator's capability to produce beams of exceptionally small emittances, making it suitable for the generation of magnetically focused MBs [Schneider, 2020]. Furthermore, MC simulations have also shown an anticipated instantaneous dose rate up to, and beyond the FLASH regime [Aymar et al., 2020]. Consequently, given the flexibility in the time, energy, and spatial structure aspects of the beam [Aymar et al., 2020], one of the potential future avenues of research could be looking at combination FLASH + SFRT MC simulations of the IR induced chemical species. This time-structure avenue of research could be faciliated by the newly released TOPAS-nBio v2.0. This new version of the software implements the IRT method of diffusion/reaction [Ramos-Méndez et al., 2020b] and a first study has been released demonstrating the calculation of the chemical yields from pulsed beams [Ramos-Méndez et al., 2020a]. This time-structure aspect to the beams is not considered in the simulations performed in this thesis, but is particularly interesting from a radiobiological point of view given the potential radiochemical implications [Ramos-Méndez et al., 2020a].

Furthermore, TOPAS-nBio v2.0 facilitates the inclusion of Fenton chemistry [Ramos-Méndez et al., 2020a] and more complex structures such as nanoparticles and organelle geometries [Henry et al., 2017]. One of the important aspects of the Fenton reaction, given by $H_2O_2 + Fe^{2+} \longrightarrow {}^{\bullet}OH + OH^{-} + Fe^{3+}$, is its modification of the yields of H_2O_2. The potential high levels of H_2O_2 in the MB peaks may catalyse this reaction, thereby producing cytotoxic $^{\bullet}OH$ at distant sites due to the longer diffusion distance of H_2O_2. The catalysis of this reaction is a strategy that has already been investigated in conjunction with the use of nanoparticles [Ranji-Burachaloo et al., 2018]. A recent study using TOPAS-nBio v2.0 has demonstrated the implementation of a cell model containing organelles, and investigated the dose enhancement in these organelles due to radioactive gold nanoparticles [Hahn and Zutta Villate, 2021]. There may be as of yet unexplored synergies with the combination of MBRT and nanoparticles as previous studies have shown an enhanced abscopal effect with combining BB irradiations with manganese dioxide nanoparticles [Meng et al., 2018] and hafnium oxide nanoparticles [Zhang et al., 2020]. Finally, the inclusion of more complex biological geometries such as mitochondria could prompt studies looking at the role that MBRT plays in the destabilization of these mitochondria, which are major sources of ROS for the cell [Widel et al., 2012].

In conclusion, the work of this chapter hypothesises a ROS primary yield in the MB peaks which is approximately equivalent to a BB irradiation of the same particle. The primary yields of $^{\bullet}OH$ suggests that the proportion of indirect DNA damage in the peaks compared to the valleys is similar to the PVDR in the case of pMBRT and HeMBRT, slightly higher in the valleys of xMBRT, and lower in the valleys of the CMBRT modality. Lower absolute yields of H_2O_2 in the CMBRT valleys owing to the low doses deposited in these regions could indicate a more suitable environment for the triggering of anti-tumor immune responses, however more experimental work needs to be performed to confirm these observations. **The results of this work have been published in *Medical Physics* [Masilela and Prezado, 2023].**

Chapter 7

Diffusion of H_2O_2 in MBRT

This chapter of the thesis contains the work performed looking at the long time scale diffusion of H_2O_2 in MBRT. Firstly, the rationale for performing the work is provided in section 7.1, followed by simulation details in section 7.2, and results and discussions in sections 7.3, 7.4, and 7.5.

7.1 Rationale for the work

The work of the previous chapter hypothesised that the distribution of signalling molecules such as H_2O_2 could be potentially important in the mechanisms underlying MBRT efficacy. This hypothesis was informed by other studies which found that anti-tumor immune responses triggered by ICD are weakened for elevated levels of H_2O_2 [Lennicke et al., 2015, Deng et al., 2020]. Consequently, it is hypothesised that a heterogeneous distribution of this species would provide a more suitable environment for the triggering of immune responses in the MB valleys, given the low expected yields of H_2O_2 in these regions. However the work of the previous chapter was not able to form concrete conclusions in this direction, given that the calculated primary yields were relevant to the end of the non-homogeneous chemical stage at 1 μs, whereas the timescales relevant to most biological processes are orders of magnitude larger.

Therefore, an attempt was made in this chapter to gain some preliminary insights into the distribution of H_2O_2 at more biologically relevant timescales. This was done through lens of TOPAS-nBio, where water radiolysis simulations were performed up to 1 μs, at which point the simulation was shut down, the distribution of H_2O_2 was recorded, and each molecule was then freely diffused analytically up to longer timescales without undergoing any further chemical reactions. This diffusion was performed up to a point where homogenisation was achieved. Given the computational complexity of simulating the high LET carbon beams (which yielded the most interesting results in terms of its implication on potential immune responses), the much simpler proton MBs were considered in this work, and the lateral diffusion at a depth of 10 mm in a water phantom was evaluated. Nevertheless, conclusions drawn on the degree of diffusion are not expected to be influenced by the type of particle - therefore the observations made in this chapter would also be applicable to carbon MBs.

The following section details specifics of the TOPAS and TOPAS-nBio simulations used to generate the initial distribution of H_2O_2 in a water phantom.

7.2 Simulation details

Given the computational difficulties with performing water radiolysis simulations over ~mm distances, only a single monoenergetic proton MB beamlet was simulated with an energy of 100 MeV. A total of 10^5 protons were uniformly generated on a 400 μm×6 mm rectangle, placed on the surface of a water phantom. A similar strategy as employed in chapter 6 was used, whereby the simulation was split into two distinct steps. In the first step, CH physics

was used from the same physics list, namely: `g4h-phy_QGSP_BIC_HP`, `g4em-livermore`, `g4decay`, `g4ion-binarycascade`, `g4h-elastic_HP`, and `g4stopping`. Each module was described in more depth in section 6.2.1.

A PS surface was then placed at a depth of 10 mm in a water phantom of `G4_WATER`, and discretized into 100 voxels. This discretized surface is shown in panel A of Fig. 7.1. Any particles crossing this surface were then scored by TOPAS. As previously noted, the act of splitting simulations which were performed with CH physics may yield recorded particles in the PS which are not able to be handled by Geant4-DNA. Consequently, in this work the `OnlyIncludeParticlesNamed` was added to only score those particles able to be handled by Geant4-DNA [Schuemann et al., 2018a, Incerti et al., 2018].

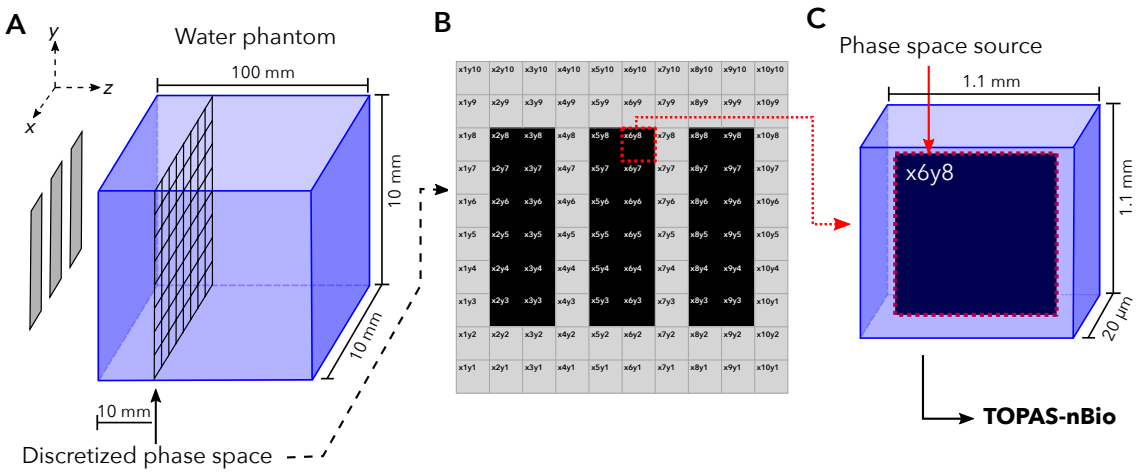

Figure 7.1: Schematic drawing depicting the workflow of TOPAS and TOPAS-nBio simulations used in this work. Panel **A** depicts the first step CH simulation, with a discretized surface to record the relevant particles. Panel **B** depicts the discretized surface, with black squares corresponding to irradiated areas. Panel **C** depicts the second step TS simulation in which chemical processes were activated, and which was performed for each square of the discretized surface.

Note that since only a single MB was simulated, after the CH simulation it is only the discretized squares of the central MB shown in panel B of Fig. 7.1 which contain particle track information. The recorded PS for each of these squares was then used as the particle source for a second simulation in which TOPAS-nBio SBS chemistry processes were activated. This second simulation is shown in panel C of Fig. 7.1 where the PS source was placed inside of a 1.1 mm x 1.1 mm x 20 μm box of `G4_WATER`. These dimensions were specifically chosen so as to allow the diffusion and reaction of chemical species up to 1 μs without any species reaching the border of the volume, which would have ultimately led to some species being removed from the simulation. The same TS physics options of `g4em-dna_opt2` as was used in chapter 6 was used in this work. However at the time of writing, the original list of 9 chemical reactions outlined in Table 6.1 had been updated with 13 additional chemical reactions in order to better correlate with experimental ROS yields [Ramos-Méndez et al., 2021]. Consequently the simulation in this chapter made use of this updated chemistry list, specified as `TsEmDNAChemistryExtended` in TOPAS-nBio, and shown in Table 7.1.

The `Tuple` scorer was used which enabled the recording of positional information of the chemical track. Given the computation difficulties of performing radiolysis simulations up to 1 μs in volumes of this size, a further split was performed at this point. Each PS source used in the TS simulations of panel C in Fig. 7.1 was split in order for there to be less than 500 scored particles within each of the splits. This value of 500 was chosen so

as to facilitate the completion of each simulation within the 24 hour time limit imposed on the HPC VEGA supercomputer[40]. I remind you that this splitting is possible due to TOPAS-nBio performing water radiolysis simulations history by history, independent of subsequent histories [Ramos-Méndez et al., 2018], and its use was validated in section 6.6.1. These simulations were then sent to the VEGA cluster, where water radiolysis was simulated up to 1 μs, corresponding to the end of non-homogeneous chemical stage. The resulting output files were then recombined in order to have the positions of all H_2O_2 species in the central beamlet shown in panel B of Fig. 7.1.

Table 7.1: Chemical reactions and rate constants used in the `TsEmDNAChemistryExtended`. Taken from [Derksen et al., 2023].

No.	Reaction			$k(10^{10}$/M/s)[b]
1[a]	$e^-_{aq} + e^-_{aq}$	$\longrightarrow$	$2OH^- + H_2$	0.647
2[a]	$e^-_{aq} + {}^{\bullet}OH$	$\longrightarrow$	OH^-	2.953
3[a]	$e^-_{aq} + H^{\bullet}$	$\longrightarrow$	$OH^- + H_2$	2.652
4[a]	$e^-_{aq} + H_3O$	$\longrightarrow$	$H^{\bullet}$	2.109
5	$e^-_{aq} + H_2O_2$	$\longrightarrow$	$OH^- + {}^{\bullet}OH$	1.405
6[a]	${}^{\bullet}OH + {}^{\bullet}OH$	$\longrightarrow$	H_2O_2	0.475
7[a]	${}^{\bullet}OH + H^{\bullet}$	$\longrightarrow$	No product	1.438
8[a]	$H^{\bullet} + H^{\bullet}$	$\longrightarrow$	H_2	0.503
9[a]	$H_3O + OH^-$	$\longrightarrow$	No product	11.031
10[a]	$H_2 + {}^{\bullet}OH$	$\longrightarrow$	$H^{\bullet}$	0.0045
11	${}^{\bullet}OH + H_2O_2$	$\longrightarrow$	HO_2	0.0023
12	${}^{\bullet}OH + HO_2$	$\longrightarrow$	O_2	1.0
13	${}^{\bullet}OH + O^-_2$	$\longrightarrow$	$O_2 + OH^-$	0.9
14	${}^{\bullet}OH + HO_{-2}$	$\longrightarrow$	$HO_2 + OH^-$	0.9
15	$e^-_{aq} + HO_2$	$\longrightarrow$	HO_{-2}	2.0
16	$e^-_{aq} + O_2$	$\longrightarrow$	O^-_2	1.9
17	$e^-_{aq} + O2^-$	$\longrightarrow$	$OH^- + HO_{-2}$	1.3
18	$H^{\bullet} + H_2O_2$	$\longrightarrow$	${}^{\bullet}OH$	0.01
19	$H^{\bullet} + HO_2$	$\longrightarrow$	H_2O_2	2.0
20	$H^{\bullet} + O_2$	$\longrightarrow$	HO_2	2.0
21[a]	$H^{\bullet} + OH^-$	$\longrightarrow$	e^-_{aq}	0.002
22	$H^{\bullet} + O^-_2$	$\longrightarrow$	HO_{-2}	2.0
23	$H_3O + O^-_2$	$\longrightarrow$	HO_2	3.0
24	$H_3O + HO_{-2}$	$\longrightarrow$	H_2O_2	2.0
25	$HO_2 + HO_2$	$\longrightarrow$	$H_2O_2 + O_2$	0.000076
26	$HO_2 + O^-_2$	$\longrightarrow$	$O2 + HO_{-2}$	0.0085

Notes.

[a] These reactions can occur directly after the pre-chemical stage.

[b] $M = 1$ mol dm^{-3}.

The following section briefly describes how an initial distribution of H_2O_2 was then obtained.

[40] https://doc.vega.izum.si/

7.3 Initial distribution of H_2O_2

In order to have an initial distribution of H_2O_2 at 1 μs corresponding to a MB array (as opposed to just a single MB beamlet), from which diffusion between the peaks of each MB beamlet could be evaluated, a perfectly symmetrical irradiation was assumed. As a result of this assumption, the distribution of H_2O_2 obtained from the simulations described in section 7.2 were mirrored in both positive and negative x-directions with a ctc of 3.2 mm [Peucelle et al., 2015b, Guardiola et al., 2017], thus resulting in a distribution of H_2O_2 representative of an array of 3 MBs.

In order to obtain an H_2O_2 concentration per treatment gray, the dose resulting from a three MB array of 10^5 particles per beamlet was scored in a $5\times5\times5$ mm^3 cubic target centred in the water phantom. In contrast to the water radiolysis simulations where only a single MB beamlet was explicitly simulated due to the computational expense (before applying the symmetrical conditions described in the paragraph above), simulations of the absorbed dose could be performed considering the entire array. A total dose of approximately 0.0007 Gy was obtained. The spatial distribution of H_2O_2 with a concentration of μM per Gy is thus shown in Fig. 7.2.

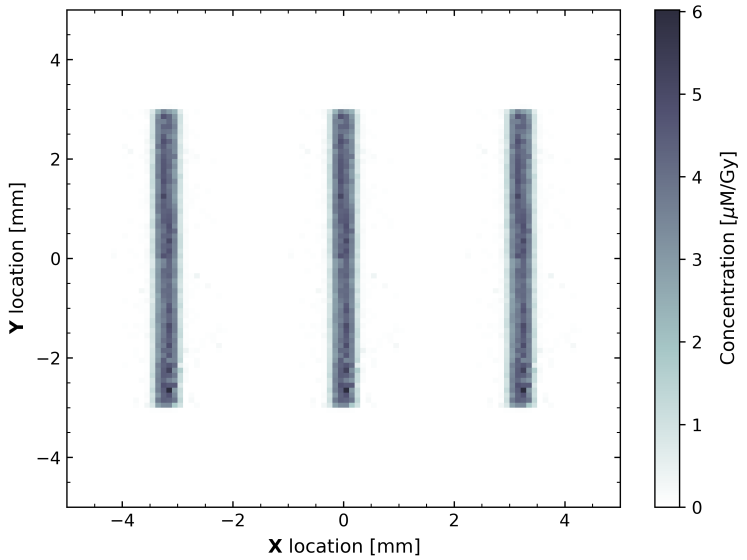

Figure 7.2: Concentration of H_2O_2 at 1 μs and at a depth of 10 mm in a water phantom, obtained purely through MC simulation in TOPAS-nBio.

Figure 7.2 depicts the concentration of H_2O_2 right at the end of the chemical stage at 1 μs. As can be seen, not enough time has elapsed and the MBs pattern is still quite well characterised by the concentration of H_2O_2.

The following section describes the methodology used to freely diffuse the chemical species to longer timescales, as well as the results thereof.

7.4 Diffusion according to the 1-D Smoluchowski

At the time of writing there was no efficient way to perform long-time scale simulations in TOPAS-nBio. These simulations would need to consider the biological scavenging of the

cell, and a completely different set of chemical reactions corresponding to homogeneous chemistry. While the IRT method implemented into TOPAS-nBio can perform this biological scavenging, one loses spatiotemporal information relating to the chemical track [Ramos-Méndez et al., 2020b, Ramos-Méndez et al., 2020a], therefore it is more suited to the calculation of yields.

Consequently the approach used in this chapter was to assume a complete *free* diffusion of the species beyond 1 μs. This is a rough approximation, owing to the fact that no interactions with biological components of the cell are considered, there are no background/scavenging reactions, and there are no chemical reactions taking place beyond 1 μs. Nevertheless, it gives us an idea of the most extreme case of uninhibited H_2O_2 diffusion. As outlined in chapter 3.1, TOPAS-nBio uses the one-dimensional form of the Smoluchowski equation in order to perform the diffusion and reaction of chemical species. These equations are repeated below in Equation 7.1 for ease of readability, where $\hat{\xi}_{x,y,z}$ is a randomly sampled number from a Gaussian distribution with a mean of 0 and standard deviation of 1, D is the diffusion coefficient, τ is the time step, and x_0, y_0, and z_0 are the initial positions of the species [Karamitros et al., 2014].

$$\begin{aligned} \hat{x}(\tau) &= x_0 + \sqrt{2D \cdot \tau} \cdot \hat{\xi}_x \\ \hat{y}(\tau) &= y_0 + \sqrt{2D \cdot \tau} \cdot \hat{\xi}_y \\ \hat{z}(\tau) &= z_0 + \sqrt{2D \cdot \tau} \cdot \hat{\xi}_z \end{aligned} \tag{7.1}$$

Ultimately, these equations were applied in a post-processing script, where the τ was adjusted to various time points beyond 1 μs. The diffusion coefficient of H_2O_2 was set to $2.3{\times}10^{-9}$ m^2/s [Ramos-Méndez et al., 2018]. In order to verify that the script was working correctly, radial distances calculated using the 3D Smoluchowski formulation shown in Equation 3.1 were compared to radial distances calculated using 1D diffusion shown in Equation 7.1.

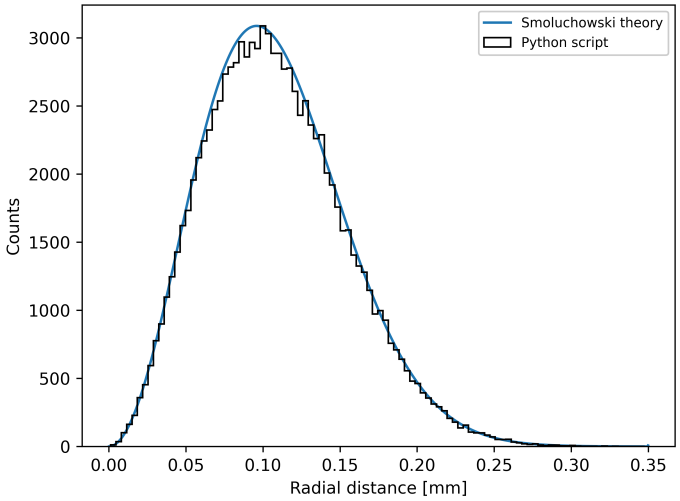

Figure 7.3: Comparison of 3D Smoluchowski diffusion (Equation 3.1) to the 1D diffusion implemented in the python script (Equation 7.1).

The results of Fig. 7.3 were obtained from the diffusion up to 1 second of 10^6 H_2O_2 species, all originally located at the same position. This gave confidence to the use of the python script to appropriately diffuse H_2O_2 beyond 1 μs. This diffusion was carried out for

times of 1, 60, 200 and 600 seconds after the conclusion of the non-homogeneous chemical stage, and can be visualised in Figures 7.4, 7.5, 7.6, and 7.7.

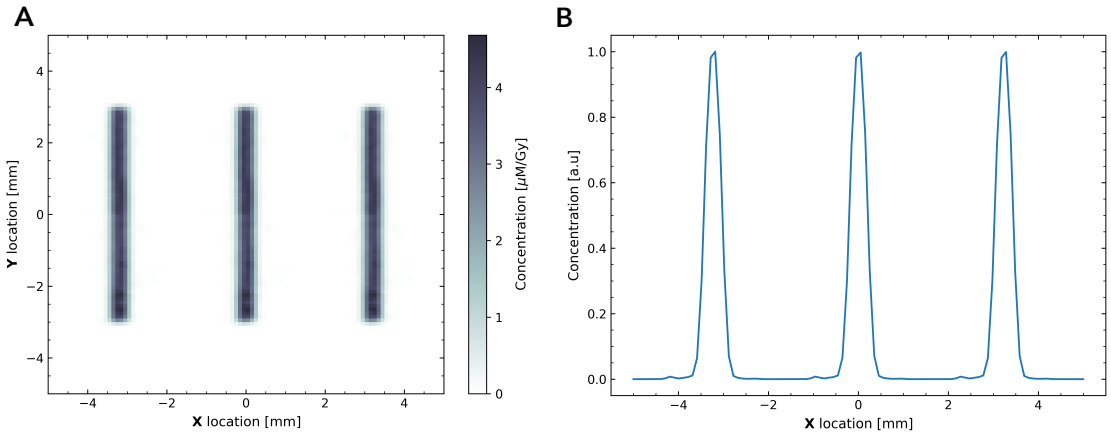

Figure 7.4: Diffusion of H_2O_2 from 1 μs (Fig. 7.2) up to 1 s. Panel **A** depicts the concentration heatmap, while panel **B** depicts the lateral concentration profile at y=0.

Visually speaking, we don't observe much differences between the concentration of H_2O_2 at 1 μs (Fig. 7.2) and the concentration at 1 s (Fig. 7.4). The characteristic pattern of peaks and valleys still remains. Indeed, if we look at Fig. 7.3, it can be seen that at 1 s the majority of the species will be diffused approximately 0.1 mm from their initial locations. This 0.1 mm displacement, while not sufficient to blur the pattern of peaks and valleys, resulted in a drop of approximately 25% in the maximum concentration of H_2O_2 located in the centre of each MB. As will be discussed below, this time-point of 1 s is already a similar order of magnitude to some of the values for the lifetime of H_2O_2 described in literature.

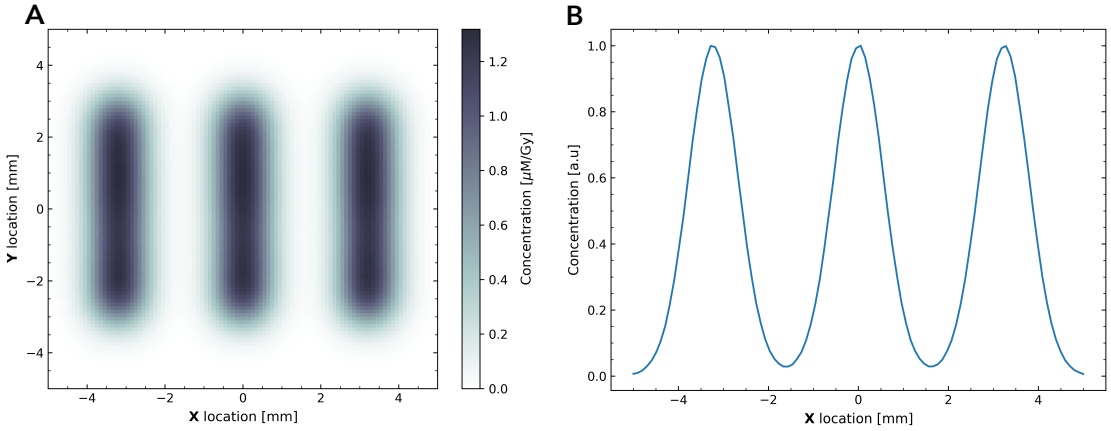

Figure 7.5: Diffusion of H_2O_2 from 1 μs (Fig. 7.2) up to 60 s. Panel **A** depicts the concentration heatmap, while panel **B** depicts the lateral concentration profile at y=0.

A progressive loss of the characteristic peak and valley pattern can be observed when increasing the diffusion times, and an approximately homogeneous distribution of H_2O_2 begins to appear at 600 s. If one considers the 95 - 107% homogeneous tumor coverage in conventional RT set out by the ICRU [ICRU, 1999], Fig. 7.7 indicates that at 10 minutes post irradiation there would be a homogeneous coverage of a tumor of approximately 6 mm in width. However, as will be discussed in the following section, it is

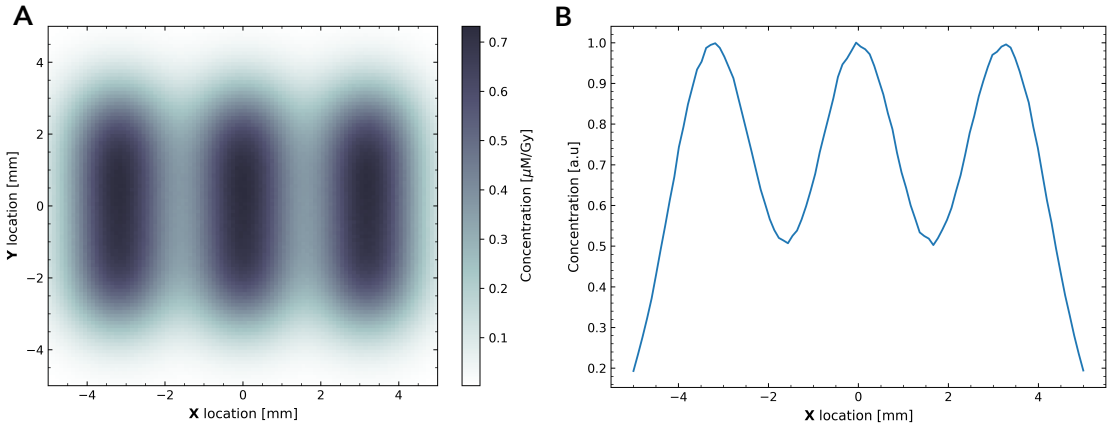

Figure 7.6: Diffusion of H_2O_2 from 1 μs (Fig. 7.2) up to 200 s. Panel **A** depicts the concentration heatmap, while panel **B** depicts the lateral concentration profile at y=0.

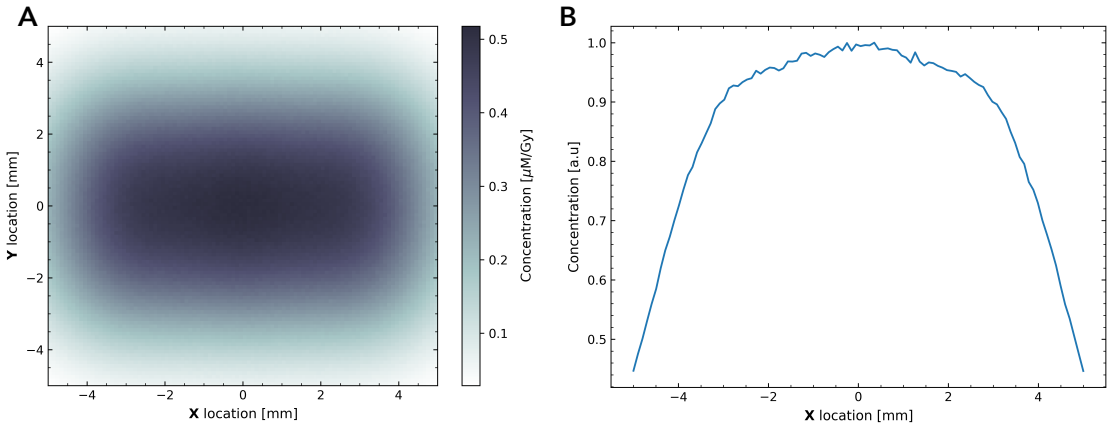

Figure 7.7: Diffusion of H_2O_2 from 1 μs (Fig. 7.2) up to 600 s. Panel **A** depicts the concentration heatmap, while panel **B** depicts the lateral concentration profile at y=0.

uncertain whether lifetimes of H_2O_2 on this scale in a biological environment are reasonable.

Discussions on the results of this work in relation to the lifetime of H_2O_2 known from literature is contained within the following section.

7.5 Discussion and conclusions

This chapter reports on the work performed evaluating the long time-scale implications on the distribution of H_2O_2 in the context of MBRT. As discussed in section 2.9.6, ROS may have an important role to play in the underlying mechanisms of MBRT efficacy, and H_2O_2 in particular is interesting in terms of its role in cell signalling [Forman et al., 2014, Azzam et al., 2002]. Correspondingly, while the previous chapter provided insights into ROS primary yields at the end of the non-homogeneous chemical stage of water radiolysis, there was an interest in expanding that work to more biologically relevant timescales in order to potentially gain some preliminary insights. Nevertheless, as previously noted - the work contained in this chapter is a rough approximation owing to the fact that no scavenging or homogeneous chemical reactions were considered.

In terms of what we know from literature, it was historically considered that H_2O_2

is able to freely diffuse within a cellular environment, due to its similar physicochemical characteristics to that of water [Bienert et al., 2007]. However Gough and Cotter *et al.* warned against blindly accepting the 'freely diffusible' theory of H_2O_2 [Gough and Cotter, 2011] owing to the fact that there were an increasing number of studies being released which pointed to the diffusion of H_2O_2 across membranes actually being mediated by certain aquaporin proteins present in those membranes [Miller et al., 2010, Bienert et al., 2007, Sorrentino et al., 2022]. The leading hypothesis is that it is through these aquaporins that H_2O_2 is truly allowed to exert its signalling effects intercellularly [Gough and Cotter, 2011, Miller et al., 2022].

However, the lifetime and diffusion distance of H_2O_2 appears to be strongly dependent on the local environment. In the work of Ledo *et al.*, the H_2O_2 lifetime and diffusion in the brain striatum of living mice was determined to be 2.2 s, allowing it to diffuse approximately 180 μm in extracellular space [Ledo et al., 2022]. Winterbourn *et al.* performed a chemical kinetic study which pinpointed peroxiredoxin or GPX as the main scavengers of H_2O_2, and for a homogeneous environment without any membrane barriers this scavenging would limit diffusion to between 50% and 10% of a cellular diameter, leading to a diffusion range in the tens of μm [Winterbourn, 2013]. Similar conclusions were reached by Lim *et al.*, who in their chemical kinetic model predicted a lifetime on the order of ∼ms and diffusion distance of a few microns in the cytosol before being scavenged [Lim et al., 2015]. The work of Sousa *et al.* highlighted that while in most cases H_2O_2 lifetime would be limited to below 40 ms, thus being transported less than 50 μm, there may be some situations whereby blood flow within the vasculature could transport H_2O_2 over mm-scales [Sousa et al., 2022].

These seemingly contradictory results highlight the importance of providing complementary studies from different angles of approach in order to better understand the underlying mechanisms. In the context of MBRT, previous work has been performed using a combination of MC simulations and a convolution-based analytical model [Dal Bello et al., 2020], as well as a purely analytical free diffusion model [Zhang et al., 2023] to investigate the long-time scale behaviour of H_2O_2. The authors hypothesised that H_2O_2 concentration could be used as a surrogate for the dose and may be homogeneously distributed during beam-on time. While the results presented in this chapter point to the homogeneous coverage of a tumor of a few mm in diameter occurring on the order of ∼minutes (Fig. 7.7), this would require H_2O_2 diffusion which is uninhibited by chemical reactions or other biological components, which I argue is not a reasonable assumption to make. In comparison to the *in vivo* results of Ledo *et al.* who observed a lifetime of 2.2 seconds [Ledo et al., 2022], Fig. 7.4 highlights that even with completely free diffusion from the Smoluchowski theory, at these timescales one would still expect a highly heterogeneous distribution of H_2O_2, similar to the dose distribution which produced it. The question of whether a homogenisation of H_2O_2 would even be desirable is still uncertain. While from one point of view it could be viewed as beneficial to tumor control in a heterogeneously irradiated tumor by inducing more cell in the valleys which are exposed to low doses, the other viewpoint - as hypothesised in the previous chapter - is that low H_2O_2 yields in the valleys (i.e. limited diffusion) would be more beneficial for the induction of anti-tumor immune responses. Consequently, further investigations are required. To this end, more advanced MC studies taking into account other biological structures and homogeneous chemistry are essential and could in fact be possible in the near future, as will be discussed in chapter 8.

In conclusion, free diffusion of H_2O_2 without any homogeneous chemical reactions or biological scavenging would lead to a homogeneous coverage of a tumor of a few mm in

width over the course of a few minutes. There is scant evidence for diffusion over these distances [Sousa et al., 2022], and if the more realistic scenario of diffusion ≤ 2.2 seconds is considered then the distribution of H_2O_2 remains highly heterogeneous. Preliminary experiments in our team comparing ROS production between BBs and MBs highlighted the idea that the production of these ROS are dose distribution dependent. In other words, heterogeneous doses would produce heterogeneously distributed ROS, and this chapter showed how diffusion would need take place over ∼minutes in order to achieve homogeneous tumor coverage.

Chapter 8

Final discussion and conclusions

At the outset of this thesis I highlighted the idea that better cancer treatments are needed to handle the expected increase in the global cancer burden. To this end, the novel RT techniques of VHEE therapy, FLASH, and MBRT could be well situated, and through their development, may provide avenues for the exploration, and eventual clinical implementation of radically different RT treatment regimes. The fundamental objective at the heart of these new techniques lies in the desire to obtain a widening of the therapeutic window, either through better tumor control, enhanced normal tissue sparing, or a combination therein. Achieving this widening has been particularly difficult with conventional RT for tumors such as high grade malignant gliomas, which still have a poor prognosis owing to the fact that dose escalation strategies are not an effective avenue of recourse due to the excessive normal tissue damage which would inevitably result from the high curative doses needed [Bleeker et al., 2012, Mattiuzzi and Lippi, 2019].

In this context, it is evident that in order to advance our understanding of novel RT techniques, it is important to have a clear understanding of how the physical characteristics of these beams modulate the biological response. The new frontier clearly involves the performance of more radiobiologically oriented evaluations, explicitly linking the physics and the biology, in view of gaining better insights on the radiobiological mechanisms underpinning these novel techniques. As will be discussed, the continued development of simulation codes such as TOPAS [Perl et al., 2012, Faddegon et al., 2020] and TOPAS-nBio [Schuemann et al., 2018a] dramatically lowers the barrier of entry associated with the use of powerful MC codes to perform such radiobiological investigations.

Illuminating the dark landscapes of this vast *terra incognita* of how the physical parameters of the irradiation modify the biological response, may offer enormous opportunities for the creation of optimal patient treatments [Prezado, 2022], however this is no easy task. The scope of our investigations need to be scaled back due to the limited tunability of the machines providing these beams which, more often than not, are installations of facilities/platforms at which radiobiology is not the highest priority [Pommarel et al., 2017, Aymar et al., 2020]. It is therefore in our best interest that we invest in dedicated platforms, focused on the investigations of the radiobiological implications of IR, which thus highlights the importance of the LhARA collaboration. As was introduced at the start of the thesis, it is within the framework of this international collaboration between the CNRS in France and the CCAP in the United Kingdom, that this thesis took place. While the main focus of the student hosted in the UK was on FLASH RT, my main focus was MBRT with the goal of shedding light on some of the important beam parameters that may need to be taken into account during the design of LhARA. Therefore, in view of advancing our understanding of these novel RT techniques, with the belief that their clinical implementation would make a meaningful difference to the treatment of cancer, this thesis leveraged MC simulations to answer two main questions:

1: What is the biological effectiveness of VHEEs, and should there be additional radioprotection concerns within a treatment room?

2: Is there a distinct pattern of ROS production between MB peaks and valleys that goes beyond simply being a function of the dose, and what are the most relevant LhARA beam parameters in view of modulating the production of these ROS?

To answer the first question, I performed MC simulations in both TOPAS and GATE, as outlined in chapters 4 and 5 respectively. While LhARA itself is not being designed to cater to the production of VHEEs, laser-based accelerator technologies are well suited to their production [Labate et al., 2020, Svendsen et al., 2021], and this RT modality was an auxiliary interest of the NARA team. Consequently, the work carried out in this thesis represents a realisation of previously planned studies.

One of the logistical challenges with generating VHEEs in a clinical context, is the large space requirement from traditional LINAC machines [Ronga et al., 2021]. However, recent advances in compact high-gradient RF-based accelerators, such as those of the PHASER [Maxim et al., 2019] and CLEAR [Gamba et al., 2018] projects give confidence to the notion that clinically compatible VHEE sources may likely become a reality in the near future. Both the PHASER and CLEAR installations make use of magnetic focusing technologies to overcome one of the main limitations of VHEEs, namely the high entrance and exit doses [DesRosiers et al., 2000]. Interestingly Kokurewicz *et al.*, in their work on CLEAR, demonstrated the feasibility of using magnetic focusing to concentrate the dose into small volumetric elements [Kokurewicz et al., 2019, Kokurewicz et al., 2021], suggesting potential as of yet unexplored synergies of combination VHEE+MBRT treatments. In the work performed in chapter 4 it was shown that the use of a conventional electron applicator had a negligible impact on beam penumbra. Furthermore, while lower exit doses were achieved, it came at the cost of high entrance doses, leading to a PDD profile similar to that of megavoltage photons, and a broader scattering of the beam in the first few centimetres of phantom. Consequently, it was concluded that likely these applicators are not suited to be used in conjunction with VHEEs.

Both the PHASER and CLEAR facilities boast FLASH-compatible dose-rates, which opens up the possibility of investigations looking into combined FLASH+VHEEs irradiations. This is particularly interesting as the majority of FLASH studies (barring the few on photon [Montay-Gruel et al., 2019] and proton [Diffenderfer et al., 2020] beams) have been performed with low energy electrons [Favaudon et al., 2014], therefore limiting their application to the treatment of superficial tumors. Consequently, a combined FLASH+VHEE irradiation is appealing due to the potential to benefit from the FLASH effect while treating deep-seated tumors.

One of the major uncertainties with the use of VHEE beams was their biological efficacy, particularly owing to the generation of photoneutrons through the giant dipole resonance [IAEA, 1979]. The early work of DesRosiers *et al.* observed only a 0.2% increase in the dose due to neutrons, and through the application of a quality factor of 10, hypothesised that an RBE of 1.02 would be appropriate [DesRosiers et al., 2000]. Nevertheless, at the time this thesis was started there had been no direct evaluation of the RBE of these VHEE beams. Today, there are two studies which have attempted to evaluate the potentially increased RBE. One of which is the work performed in chapter 5, and the other was performed by Small *et al.* at CLEAR [Small et al., 2021]. Small *et al.* calculated the RBE resulting from the irradiation of dry and wet DNA plasmids and found a value of approximately unity for the dry plasmids, and a value between 1.1 and 1.2 for the wet plasmids [Small et al., 2021]. Instead of plasmid DNA damage, cell survival was used as the biological endpoint, and a theoretical RBE of 1 was calculated in

chapter 5. However, a calculation of the dose-averaged LET in the same chapter indicated a higher LET for VHEEs compared to clinical photon/electron beams. Ultimately, both the results of Small *et al.* and the results of chapter 5 point to the conclusion that the RBE of VHEE beams is similar to clinical photons/electrons or potentially slightly higher, lying somewhere between these conventional beams and proton beams.

Despite the improvement of compact RF-based accelerators, laser-plasma wakefield accelerator technologies [Nakajima et al., 2015, Labate et al., 2020, Svendsen et al., 2021, Kokurewicz et al., 2019] represent an even further reduction in machine size, and could prove to be an even more cost-effective and efficient alternative for the clinical realisation of VHEE therapy. Nevertheless, the unique pulse-structure of VHEE beams from both compact RF or laser-based sources engenders some dosimetric challenges, such as the shot-to-shot fluctuations, or the very short pulse lengths of ns to fs compared to the conventional μs pulses. While passive dosimetry techniques using radiochromic films have been shown to be suitable for use in conjunction with VHEEs [Subiel et al., 2014, Cavallone et al., 2021], solutions still need to be developed for real-time dosimetry [McManus et al., 2020, Subiel et al., 2017, Schüller et al., 2020].

Regardless of whether the beam of VHEEs is generated from compact RF or laser-based sources, the work of chapter 4 highlights the need for a dedicated bunker to limit the radiation exposure of workers and the public. Through TOPAS simulations, the ambient neutron dose equivalent at various points within a treatment room was evaluated. Ultimately, dose equivalent values of a similar order of magnitude to proton therapy treatments were found, highlighting the fact that this novel RT technique cannot simply be implemented at any clinical facility. Similar radioprotection considerations as performed for conventional EBRT with protons are required.

In response to the first question, an RBE of unity or potentially slightly higher can be expected. Similar radiation shielding and bunker design protocols to that of conventional proton therapy treatments should be used.

To answer the second question, I performed MC simulations in TOPAS and TOPAS-nBio, as outlined in chapters 6 and 7. Compared to VHEEs, which represents a RT modality which is still in its infancy, MBRT is a more established technique and its clinical translation is not hindered by the same logistical challenges as VHEE therapy. In fact, the generation of MBs in clinical proton therapy centres has already been successfully implemented through the use of mechanical collimators [Schneider, 2022]. Nevertheless, in the absence of mechanical collimation, the quadrupole magnets contained inside the PBS nozzles at these facilities are likely not capable of focusing the beams down to the submillimetric sizes characteristic of MBRT [Schneider, 2022]. In this context, the LhARA facility is particularly interesting for advancing the field of MBRT as previous studies have highlighted its capability to generate magnetically focused proton and ion MBs [Aymar et al., 2020, Schneider, 2020], which - compared to mechanical collimation - yields better PVDRs which is more beneficial to the sparing of normal tissue.

Despite the significant normal tissue sparing, and equivalent or superior tumor control when compared to conventional RT, the exact radiobiological mechanisms underpinning the efficacy of the technique are not fully understood. Various hypotheses have been put forward such as differential vascular effects, cell migration, cell signaling effects (bystander/abscopal), or immunomodulatory effects [Prezado, 2022], all with varying degrees of experimental evidence for their involvement, as discussed in section 2.9.5. Despite ROS being implicated in essentially all of these effects (see section 2.9.6), in depth evaluations on their role in

MBRT are severely lacking. Even in the most recently published textbook about SFRT, ROS were only briefly mentioned a single time in the context of MRT, where high dose rates similar to those employed in FLASH were used [Zhang and Mayr, 2023, Djonov et al., 2023]. Consequently the work performed on ROS in this thesis was an important addition to our knowledge of MBRT. At the time of writing, this work was one of the first in which the role of radiochemistry and ROS production in MBRT was evaluated, and could therefore serve as a base from which future experiments could be designed. While two other papers were published over the course of my PhD [Dal Bello et al., 2020, Zhang et al., 2023], these studies focused more on the possible diffusion of H_2O_2 to homogeneously cover the tumor as opposed to the relative production of these species between MB peaks and valleys.

One of the precursors to the work carried out in this thesis was the publication of Dos Santos *et al.*, a previous member of the team, who published the first micro- and nanodosimetric study of the level of direct DNA damage induced by MBRT [Dos Santos et al., 2020]. They observed that amongst photons, electron, and proton MBRT modalities, pMBRT likely offered the best normal tissue sparing capabilities due to the lower number of DNA damage events in the peak up to a depth of 70 mm compared to the other two modalities. This was accompanied by a higher number of complex DNA breaks in the Bragg peak at 75 mm. Furthermore, while the number of complex DNA breaks in the pMBRT valleys was negligible below 50 mm, it rose to a level equivalent to that of the peak at 75 mm [Dos Santos et al., 2020], thus mimicking the homogenisation of the dose at Bragg peak depths as has been shown to be possible for spatially fractioned protons [Prezado and Fois, 2013, De Marzi et al., 2019, Martínez-Rovira et al., 2015]. In other words, the work of Dos Santos *et al.* highlighted the idea that the level of direct DNA damage was directly related to the dose deposited (or PVDR), and given the low doses in the valleys, it is not expected that the DNA damage in those regions would contribute to killing the tumor, thereby implying the involvement of other mechanisms which have been previously observed.

Interestingly, analysis of the ROS primary yields of the proton and helium ion beams, as discussed in section 6.5, leads to the same conclusions as drawn by Dos Santos *et al.* The primary yields of $^{\bullet}OH$, e^-_{aq}, and H_2O_2 in the MB modality (in both peak and valley regions) was not significantly different to the calculated yields in the BB modality. This was the case for both proton and helium ion beams, at all depths beyond 10 mm. In other words, these results imply that for these types of beams the inherent property of being *spatially fractionated* is completely unrelated to the resulting primary yields. Similarly to the level of direct DNA damage, the proportion of indirect DNA damage induced by $^{\bullet}OH$ in the peaks compared to the valleys is expected to be approximately equivalent to the PVDR. Interestingly, the primary yields calculated for the photon and carbon ion beams did not display this same equivalence to the PVDR. While the primary yields in the MB peak of the photon beam were more or less equivalent to the BB yields, a constant difference of approximately 2.5% (for H_2O_2) between MB peak and valley primary yields was observed. Given these small differences it is not certain that this would lead to any biological consequences. However, the even more striking result came from the carbon ion beams, where for the first time a divergence between the primary yields in the MB peak compared to the BB modality was observed at 70 mm. Furthermore, there was a significant difference of approximately 16% between the H_2O_2 yields in the MB peaks compared to the valleys at this depth. The conclusion reached was that from a radiochemical point of view, the higher LET carbon beams presented the greatest divergence from the *norm*.

In the context of LhARA the results of the work performed in this thesis which are

most relevant are the proton, helium ion, and carbon ion primary yields calculated. From the point of view of ROS primary yields for protons or light ions such as helium, the work of this thesis makes the recommendation that modifications to the geometrical parameters of the LhARA MBs (beam width, ctc) would likely not be the best strategy in view of observing underlying radiobiological responses as a result of radiochemical changes. This recommendation is made on the basis that for these beams the primary yields of ROS are directly dependent on the well known effects of deposited dose. However, there may be an interest in modifying these parameters for the carbon beams, given not only the significant differences between the ROS yields in the peak and valley, but also differences between the MB peak and BB ROS yields in the vicinity of the Bragg peak. In other words, the quality of *spatial fractionation*, seems to have a more meaningful impact on the peak-to-valley ROS ratio of high LET beams due to the composition of the radiation field in these regions. What the work of this thesis has shown is that, unlike the high dose rates of FLASH, there is less evidence for radiochemical changes induced by spatial fractionation as being the core mechanism underlying MBRT efficacy. Nevertheless, the LhARA beams are being designed to have high beam currents of 10^9 particles per shot, resulting in average dose rates $\geq$120 Gy/s for protons and $\geq$700 Gy/s for carbon ions [Aymar et al., 2020]. The delivery of beams at these high dose rates therefore opens up the possibility of investigations looking at combined FLASH+MBRT treatments [Wright et al., 2021, Schneider et al., 2022]. Consequently, the tuning of MBRT beam parameters at FLASH dose rates could be the more interesting avenue of research in terms of observing radiochemical changes as a result of intertrack effects [Kreipl et al., 2009a, Ramos-Méndez et al., 2020a].

One of the key questions that still remains for MBRT at conventional dose rates is how we reconcile the fact that tumor control is still ensured with heterogeneous doses within the tumor, where a significant proportion of the cells do not receive a tumoricidal dose [Prezado et al., 2018, Prezado et al., 2019, Bertho et al., 2021, Sotiropoulos et al., 2021]. The implication of these results is that there is indeed some other mechanism involved, such as immunomodulation. In fact, in the recent work of Bertho and Iturri *et al.*, it was shown that MBRT provoked a faster and more efficient infiltration of T-cells into the tumor compared to a conventional BB irradiation and was also responsible for the induction of long term anti-tumor immunity [Bertho et al., 2022a]. Could this therefore be a potential avenue where ROS plays a role?

In relation to the work performed in this thesis, both the helium and carbon ion MBs exhibited highly heterogeneous dose distributions at the Bragg peak depth. In the case of helium, the similar H_2O_2 primary yields in the peak and valley regions suggest that at the end of the non-homogeneous chemical stage of water radiolysis, one could expect a heterogeneous distribution of H_2O_2 - which is an important signalling molecule [Forman et al., 2014, Gough and Cotter, 2011, Hancock et al., 2001]. The degree of heterogeneity would be even more severe for the carbon beam, not only due to the higher PVDR, but also due to the fact that H_2O_2 primary yields were even lower in the MB valleys compared to the MB peaks. It has been shown that the anti-tumor immune response is increased for lower levels of extracellular H_2O_2 [Lennicke et al., 2015, Deng et al., 2020]. Consequently the results of this thesis provokes the hypothesis that perhaps the low levels of H_2O_2 in the valleys of HeMBRT and CMBRT could play a role in triggering an immune response. Particularly for carbon, an even greater differential between peak and valley H_2O_2 yields was induced due to the presence of nuclear fragments in the valley, which could imply an even more efficient immune activation. First experiments in our team showed that tumor control could be achieved in tumor bearing mice receiving only 1

Gy in the CMBRT valleys, compared to the 5 Gy needed in xMBRT. In the context of LhARA, perhaps it is through the lens of this valley H_2O_2 yield that beam parameter modulation strategies should be designed. In my opinion, these types of evaluations could be interesting avenues of research to be included in the LhARA radiobiology program.

In response to the second question, there are no radiochemical changes between MB peak and valley ROS yields as a result of the inherent spatial fractionation of these beams. In general, the ratio of peak-to-valley ROS yields would be approximately equivalent to the PVDR, with the only exception being the CMBRT modality. While modulating the beam width/ctc to change the valley H_2O_2 yields could be an interesting avenue of research, importance should also be given to the radiochemical changes induced by pulse length and dose-rate, as has already been demonstrated in the context of FLASH.

In line with the above-mentioned ideas about dose-rate effects and ROS diffusion, advancements in the various MC codes will prove essential in further studies evaluating the underlying radiobiological mechanisms of these novel RT techniques. At the time the work on ROS production was performed, there was no way to include beam time structure aspects into the simulation, which is a critical characteristic of the LhARA beams. However recently, the simulation of dose-rate effects, and pulsed beam time structures became possible in TOPAS-nBio with the inclusion of the IRT approximation [Ramos-Méndez et al., 2020b, Ramos-Méndez et al., 2020a]. Furthermore, while this thesis was being performed, TOPAS-nBio was limited to the simulation of the diffusion and reaction of chemical species up to the end of the non-homogeneous chemical stage of water radiolysis. A recently released publication by the TOPAS developers detailed the implementation of the Gillespie algorithm, which enabled the simulation of longer time scale homogeneous chemistry [D-Kondo et al., 2023]. These advancements in the development of TOPAS and TOPAS-nBio represent exciting new tools to be potentially applied to future MC simulations of MBs. There is now an opportunity to investigate effects such as the potential differential impact on generated ROS of passively scattered as opposed to scanned MBs, or the impact of different MB pulse structures on the generation of ROS - which will be most relevant to LhARA.

In conclusion, the work performed in this thesis has led to the advancement of our understanding of novel RT techniques through two axes, namely: (1) the biological effectiveness and radioprotection concerns of VHEEs, and (2) the primary yields of ROS in MB peaks and valleys, which are potentially involved in some of the underlying radiobiological mechanisms. Up to this point, the paradigm shift in RT has been characterised by irradiations at previously unthought of energies (VHEEs), at ultra high dose rates (FLASH), with unique spatial distributions (MBRT), in view of provoking novel mechanisms beyond the dogmas of conventional RT. The advancements in MC codes, in tandem with dedicated platforms for radiobiological studies (LhARA) present promising avenues for the continued investigation of these novel techniques with the ultimate goal of achieving optimal treatments schemes. Beyond this thesis, I hope to use the expertise gained over the past few years to drive further advancements in the field of RT, and play a role, however small it might be, in the development of techniques to reduce the global cancer burden.

Chapter 9

List of scientific productions

Publications in peer-reviewed journals

Masilela, T. A. M., Prezado, Y. Monte Carlo study of the free radical yields in minibeam radiation therapy. *Medical Physics*, **50(8):5115-5134** (2023).

Masilela, T. A. M., Delorme, R. Prezado, Y. Dosimetry and radioprotection evaluations of very high energy electron beams. *Scientific Reports*, **11(1):20184** (2021).

Delorme, R., **Masilela, T. A. M.**, Etoh, C. *et al.* First theoretical determination of relative biological effectiveness of very high energy electrons. *Scientific Reports*, **11(1):11242** (2021).

Presentations at international conferences

Oral presentations

Masilela, T. A. M., **Prezado, Y.**[41] Spatiotemporal evolution of ROS yields in minibeam radiation therapy: a TOPAS-nBio Monte Carlo study. *17th ICRR*, August 2023, Montréal, Canada.

Masilela, T. A. M., Prezado, Y. Impact of spatially fractionated minibeams on the production of reactive oxygen species: a Monte Carlo study using TOPAS-nBio. *1st international workshop on PMBT*, March 2023, Paris, France.

Masilela, T. A. M., Prezado, Y. A Monte Carlo study of the free radical production in minibeam radiation therapy. *60th annual PTCOG*, **IJPT**, June 2022, Miami, USA.

Masilela, T. A. M., Delorme, R. Prezado, Y. Dosimetry and radioprotection evaluations of very high energy electron beams. *iNanoTheRad*, November 2021, Paris-Saclay, France.

Poster presentations

Masilela, T. A. M., Prezado, Y. Monte Carlo calculation of the production of reactive oxygen species in minibeam radiation therapy. *2nd FRPT*, November 2022, Online.

[41] Presented in my place due to visa issues which prevented international travel.

Masilela, T. A. M., Prezado, Y. A Monte Carlo study of the free radical production in minibeam radiation therapy. *4th ECMP*, **EJMP**, August 2022, Online.

Delorme, R., **Masilela, T. A. M.**, Etoh, C. *et al.* First theoretical determination of relative biological effectiveness of very high energy electron beams. *1st FRPT*, **EJMP**, December 2021, Online.

Chapter 10

Résumé du travail de thèse en français

Ce chapitre contient un résumé de la thèse en français, en commençant par le contexte dans lequel cette thèse a été réalisée dans la section 10.1. Je décrirai ensuite les deux principaux travaux de cette thèse dans les sections 10.2 et 10.3, qui décrivent respectivement les recherches sur la thérapie VHEE et MBRT. Enfin, la section 10.4 présente les discussions et les conclusions finales.

10.1 Contexte de la thèse

Le terme *cancer* est utilisé pour définir un groupe de maladies, toutes caractérisées par la croissance anormale de cellules mutées. Avec environ 19.3 millions de nouveaux cas de cancer et 10 millions de décès par cancer rien qu'en 2020, cette maladie est l'une des principales causes de décès dans le monde. Les projections actuelles estiment que d'ici 2040, le nombre de cas mondiaux devrait avoir augmenté de 47% [Sung et al., 2021b]. Outre cette augmentation du nombre de cas de cancer, les tumeurs radiorésistantes telles que les gliomes malins de haut grade ont toujours un mauvais pronostic car les stratégies d'escalade des doses ne sont pas efficaces. L'obtention des doses curatives élevées nécessaires pour contrôler la tumeur entraînerait inévitablement des dommages excessifs aux tissus normaux [Bleeker et al., 2012, Mattiuzzi and Lippi, 2019]. Par conséquent, il y a un réel intérêt à développer de nouvelles stratégies RT pour mieux gérer le fardeau mondial du cancer dans les années à venir.

Dans cette optique, l'objectif philosophique de cette thèse était ***d'investiguer l'impact des nouvelles techniques de radiothérapie*** *en vue de mieux gérer le fardeau mondial du cancer.*

Le développement technologique rapide des ordinateurs et des simulations informatiques a joué un rôle essentiel dans l'étude des effets des rayonnements sur le corps humain, et c'est grâce à ces simulations informatiques que l'objectif philosophique de la thèse a été atteint. Plus précisément, l'utilisation des simulations MC (du nom du casino de Monaco) a augmenté de façon exponentielle depuis les années 1970 et constitue désormais l'outil informatique de référence pour le calcul des doses absorbées à partir de RT. Des logiciels tels que TOPAS [Perl et al., 2012, Faddegon et al., 2020] et TOPAS-nBio [Schuemann et al., 2018a] nous permettent d'étudier non seulement les interactions physiques de IR, mais aussi d'avoir un aperçu des conséquences chimiques et biologiques précoces. Par conséquent, ces deux logiciels ont été les principaux outils utilisés dans cette thèse pour faire progresser notre compréhension de la thérapie VHEE et de MBRT.

En commençant par la thérapie VHEE, cette technique se caractérise par l'utilisation d'électrons de 150 - 250 MeV qui présentent divers avantages dosimétriques par rapport aux électrons de 4 - 25 MeV généralement utilisés dans les cliniques [DesRosiers et al., 2000]. L'un de ces avantages est que, par rapport aux électrons de faible énergie, ils

ont une portée plus grande et une pénombre de faisceau plus étroite en profondeur, deux caractéristiques qui s'aggravent avec l'augmentation de l'énergie du faisceau. Par conséquent, ils conviennent mieux au traitement des tumeurs profondes [DesRosiers et al., 2000, Papiez et al., 2002]. En outre, par rapport aux photons ou protons conventionnels, les VHEEs se sont révélés relativement insensibles aux hétérogénéités tissulaires [Papiez et al., 2002, Moskvin et al., 2010]. Néanmoins, l'une des préoccupations a été la production de neutrons à partir de ces faisceaux de haute énergie, qui peut se produire par les réactions (γ, xn), (γ, p), et (γ, pn), où (γ, xn) est la plus dominante [DesRosiers et al., 2000, Subiel et al., 2014]. Ces neutrons sont un sujet de préoccupation car ils sont très nocifs sur le plan biologique et pourraient présenter un risque de cancers secondaires [IAEA, 1979]. Compte tenu de ces connaissances, le premier objectif technique de la thèse est née.

Objectif 1: étudier les considérations de radioprotection dans une salle de traitement délivrant une thérapie VHEE par un calcul de ***l'équivalent de dose de neutrons dans l'air ambiant****, et effectuer un calcul théorique de* ***l'efficacité biologique relative (EBR)*** *de ces VHEEs.*

La deuxième partie de cette thèse a porté sur MBRT, qui est un type de fractionnement spatial. Comme indiqué dans la Fig. 10.1, par rapport à MBRT GRID utilise des faisceaux plus grands, tandis que MRT utilise des faisceaux plus petits.

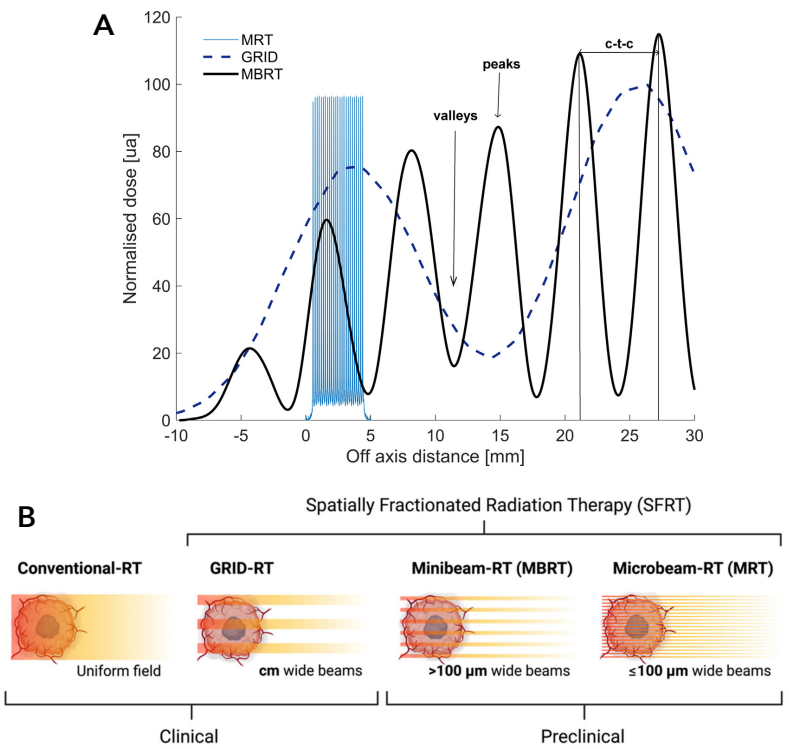

Figure 10.1: Profils de dose latéraux pour GRID, MRT et MBRT, montrant certains des paramètres importants (panneau **A**), ainsi qu'une illustration (panneau **B**), indiquant les différentes distributions spatiales du rayonnement pour chacune des techniques. Tiré de [De Marzi et al., 2019] et [Fernandez-Palomo et al., 2022] respectivement.

Il a été démontré que l'utilisation de MBRT présente des avantages en termes d'épargne des tissus normaux [Deman et al., 2012, Prezado et al., 2017a, Prezado et al., 2018] et

de contrôle des tumeurs [Prezado et al., 2019, Lamirault et al., 2020a, Bertho et al., 2021, Sotiropoulos et al., 2021], mais les mécanismes biologiques exacts qui sous-tendent l'efficacité des traitements fractionnés dans l'espace ne sont pas encore entièrement compris. Les principaux candidats sont la migration cellulaire, les effets vasculaires et non ciblés, et les réponses immunomodulatrices [Griffin et al., 2020, Prezado, 2022].

Il est intéressant de noter que les espèces réactives de l'oxygène (ROS) générées par la radiolyse de l'eau sont impliquées non seulement dans les mécanismes plus traditionnels de l'action des rayonnements, mais aussi dans certains de ces mécanismes sous-jacents. Le radical hydroxyle $^{\bullet}OH$ est une espèce importante car il est principalement responsable de la partie indirecte des dommages à l'ADN [von Sonntag, 2006]. Le peroxyde d'hydrogène (H_2O_2) est une importante molécule de signalisation cellulaire [Forman et al., 2014, Gough and Cotter, 2011, Hancock et al., 2001] et peut contribuer à l'effet *bystander* [Azzam et al., 2002]. Des données récentes montrent que les vésicules extracellulaires (EVs) ont un rôle à jouer dans l'effet *bystander* [Doyle and Wang, 2019], et que les EVs irradiées ont un effet radiosensibilisant sur les cellules cancéreuses voisines en augmentant le niveau de ROS intracellulaire. [Nakaoka et al., 2021]. En outre, il a également été démontré que la diminution des niveaux de ROS extracellulaire augmentait l'infiltration des lymphocytes T, qui jouent un rôle essentiel dans le système immunitaire [Deng et al., 2020].

Malgré toutes ces preuves liant ROS à certains des mécanismes sous-jacents potentiels de l'efficacité de MBRT, ces ROS sont à peine abordés dans le dernier manuel publié sur les radiothérapies spatialement fractionnées [Zhang and Mayr, 2023]. Il y avait donc un réel intérêt à étudier la production de ces ROS en relation avec MBRT, et c'est ainsi qu'est né le deuxième objectif technique de cette thèse.

Objectif technique 2 : Calculer la ***production (rendements primaires) de ROS entre les pics et la vallée de MBRT*** *par rapport à RT conventionnel, et étudier la* ***diffusion possible de ces ROS*** *à des échelles de temps plus longues.*

Les sections suivantes examinent certains des principaux résultats de la thèse, qui ont été obtenus dans le but de répondre à ces deux objectifs techniques.

10.2 Électrons de très haute énergie: principaux résultats

Afin d'étudier l'équivalent de dose de neutrons dans l'air ambiant des VHEEs, des simulations MC ont été réalisées dans TOPAS [Perl et al., 2012, Faddegon et al., 2020] version 3.5 et une géométrie de simulation présentée dans la Fig. 4.1 a été créée. Les rendements en neutrons à différentes distances dans le fantôme d'eau ont d'abord été calculés. Comme le montre le tableau 4.2, les rendements en neutrons à l'intérieur du fantôme étaient de l'ordre de 10^{-8} à 10^{-5} neutrons/cm^2/électron primaire, en fonction de la configuration de la simulation ou de l'énergie du faisceau (2 GeV ou 200 MeV). Les rendements les plus élevés ont été obtenus lors de l'utilisation d'un applicateur d'électrons qui injectait les neutrons dans la zone d'entrée du fantôme. Les premiers travaux de DesRosiers *et al.* ont trouvé des rendements en neutrons de 0.03 et 0.04 neutrons/cm^2/électron primaire pour des faisceaux VHEE de 150 MeV et 200 MeV respectivement [DesRosiers et al., 2000], tandis que les travaux ultérieurs de Subiel *et al.* ont calculé des rendements dans un fantôme d'eau compris entre 10^{-7} et 10^{-5} neutrons/cm^2/électron primaire pour un faisceau VHEE de 165 MeV [Subiel et al., 2014]. Dans les deux cas, les auteurs ont conclu que la contribution des neutrons à l'équivalent de dose dans un fantôme d'eau serait négligeable [DesRosiers et al., 2000, Subiel et al., 2014]. Par conséquent, étant donné que les rendements d'un

ordre de grandeur similaire ont été obtenus dans cette thèse, des conclusions similaires ont été tirées.

Ensuite, pour calculer l'équivalent de dose de neutrons dans l'air ambiant, la fluence neutronique a été multipliée par un ensemble de coefficients de conversion de la fluence en équivalent de dose selon l'équation 2.26. Alors que TOPAS utilise les coefficients par défaut de M. Pelliccioni [Pelliccioni, 2000], des coefficients plus récents ont été publiés dans le rapport 95 de l'ICRU [ICRU, 2020]. Par conséquent, la figure 10.2 représente l'équivalent de dose de neutrons dans l'air ambiant à différents endroits de la salle de traitement et compare les deux séries de coefficients.

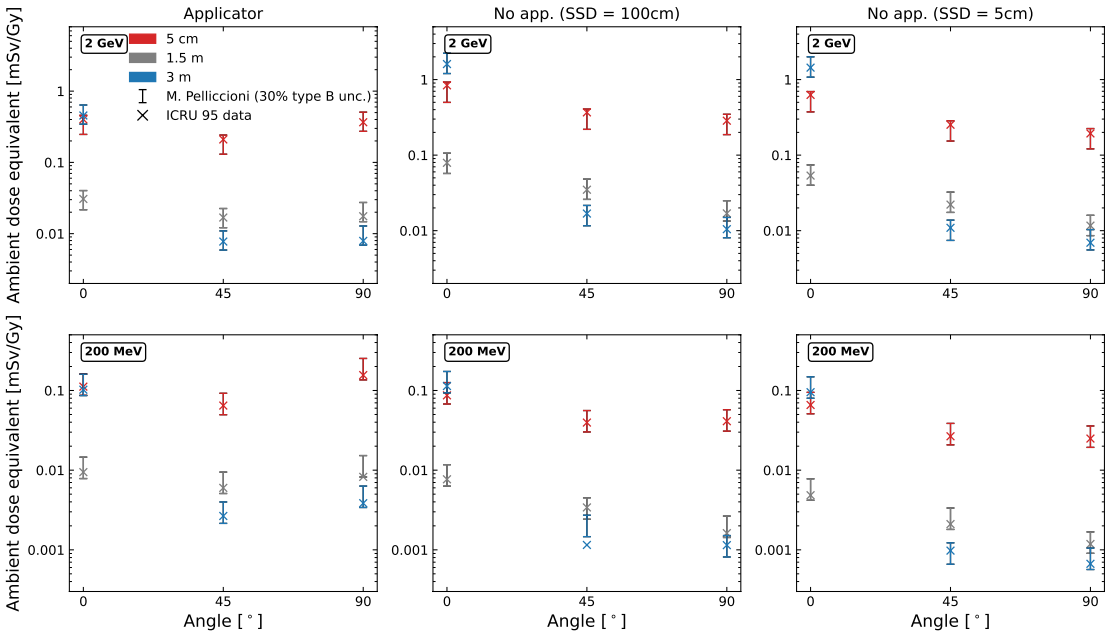

Figure 10.2: L'équivalent de dose de neutrons dans l'air ambiant total par gray de traitement pour les faisceaux de 2 GeV et de 200 MeV, à 5 cm, 1.5 m et 3 m du fantôme d'eau, pour des angles de 0°, 45° et 90° par rapport à l'axe central du faisceau, et pour toutes les configurations de simulation.

Comme le montre la figure 10.2, l'équivalent de dose le plus élevé a généralement été obtenu à 0° et à 3 m, directement à proximité du mur en béton, soulignant l'idée que le mur en béton augmente l'équivalent de dose de neutrons dans la salle de traitement. L'équivalent de dose maximal obtenu pour le faisceau de 200 MeV était de 0.19 mSv/Gy, tandis que le maximum obtenu pour le faisceau de 2 GeV était de 1.7 mSv/Gy. Le tableau 4.4 compare ces valeurs aux traitements conventionnels de protonthérapie, et l'on constate que des valeurs d'un ordre de grandeur similaire sont obtenues. Nous pouvons donc conclure que **des protocoles de protection contre les rayonnements et de conception des bunkers similaires à ceux des traitements de protonthérapie conventionnels devraient être utilisés**.

Si nous considérons ensuite le calcul de EBR de VHEEs, il a été effectué à l'aide de GATE [Jan et al., 2011, Sarrut et al., 2014] version 8.2, avec la Fig. 5.1 décrivant une représentation schématique de la géométrie de la simulation. Les faisceaux RT conventionnelles ont été comparées aux faisceaux VHEE. Un détecteur TEPC a été placé à différentes profondeurs dans l'axe et a été utilisé pour enregistrer les spectres d'énergie

lineal ($f(y)$) de chacun des faisceaux. Ces spectres ont ensuite été utilisés comme entrées dans le MKM modifié, comme indiqué dans les équations 10.1 et 10.2.

$$S = e^{\left(-\left(\alpha_0 + \frac{\beta}{\rho \pi r_d^2} y^*\right) D - \beta D^2\right)} \tag{10.1}$$

$$y^* = \frac{{y_0}^2 \int 1 - e^{-\left(\frac{y}{y_0}\right)^2} f(y) dy}{\int y f(y) dy} \tag{10.2}$$

Ce MKM modifié est un modèle biophysique qui permet de calculer la survie cellulaire en utilisant les données biologiques d'un rayonnement de référence et les données physiques (dans ce cas, les spectres d'énergie *lineal*) d'un rayonnement de test [Kase et al., 2013, Mairani et al., 2017]. La figure 10.3 représente la survie cellulaire d'un faisceau VHEE de 300 MeV par rapport aux faisceaux conventionnels.

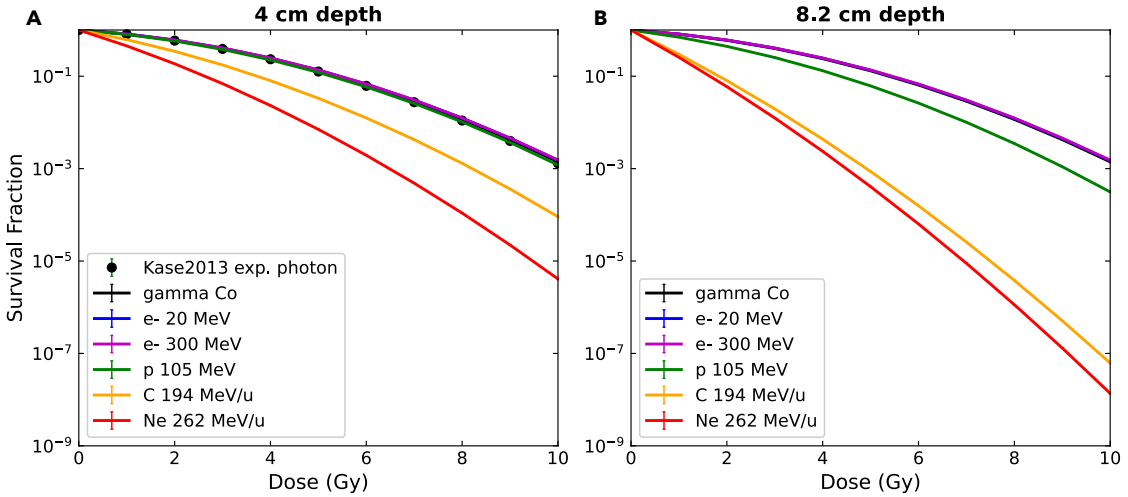

Figure 10.3: Courbes théoriques de survie cellulaire calculées à partir du modèle MKM modifié pour toutes les sources de particules. Les panneaux **A** et **B** représentent la fraction de survie en fonction de la dose pour les profondeurs de 4 cm et 8.2 cm respectivement. Les courbes expérimentales de survie cellulaire de Kase *et al.* sont représentées par les cercles noirs dans le panneau **A** [Kase et al., 2013].

Par rapport aux photons conventionnels et aux électrons de faible énergie, il est évident qu'il n'y a pas de différence significative dans la survie cellulaire attendue associée à l'utilisation des VHEEs. L'EBR a ensuite été calculé pour une fraction de survie de 10%, et un EBR d'environ 0.99 a été obtenu pour les électrons de 20 MeV et les électrons de 300 MeV, quelle que soit la profondeur considérée. Nous pouvons donc conclure que l'augmentation de la probabilité à cause de photoneutrons provenant de réactions nucléaires - qui entraînerait une augmentation de l'EBR - est probablement négligeable et que, par conséquent, **l'efficacité biologique des VHEEs devrait être similaire à celle des traitements RT conventionnels** avec de photons et des électrons de faible énergie.

10.3 Radiothérapie par mini-faisceau: principaux résultats

Afin de calculer le ROS produit à partir du MBRT, des simulations MC ont été réalisées à l'aide de TOPAS [Perl et al., 2012, Faddegon et al., 2020] version 3.6.1, et TOPAS-nBio

[Schuemann et al., 2018a] version 1.0. Comme le montre la figure 10.4, un fantôme d'eau a été irradié par des faisceaux de photons, de protons, d'ions hélium et d'ions carbone. Le *rendement primaire* représente la *G-value* à la fin de l'étape chimique de la radiolyse de l'eau et est mesuré en quantité d'espèces par eV d'énergie déposée. Ces rendements primaires ont été calculés pour les pics et les vallées et à différentes profondeurs dans le fantôme d'eau.

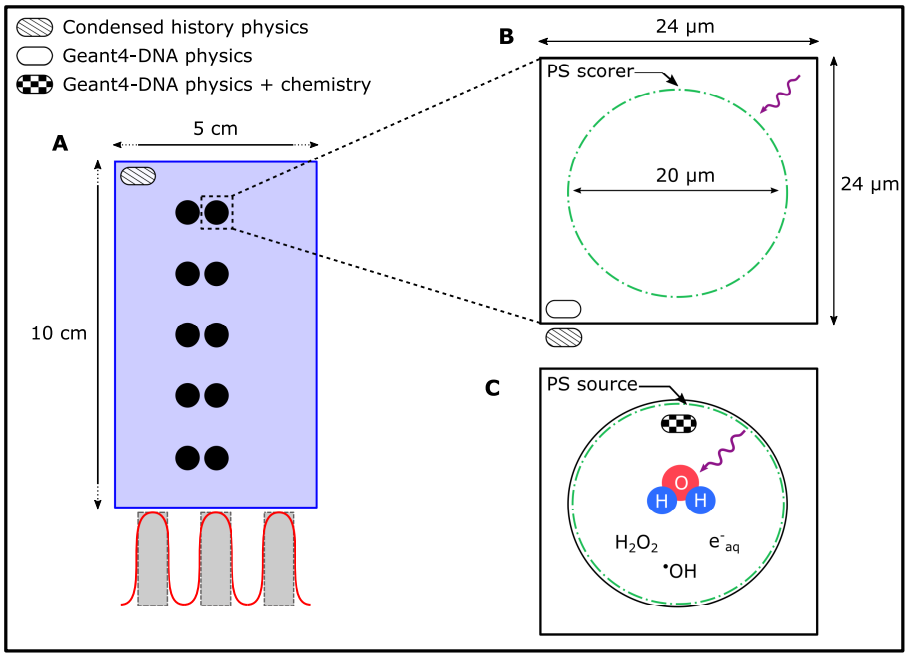

Figure 10.4: Schéma des simulations TOPAS. Le panneau **A** représente le fantôme d'eau macroscopique, irradié par des faisceaux de particules, oú les cercles noirs sont représentatifs des *cellules* sphériques d'eau de 20 μm de diamètre, situées dans les régions de pic et de vallée, et aux profondeurs de 10, 30, 50, 70, et 76.5 mm. Le panneau **B** représente une vue agrandie de l'une des sphères d'eau, montrant le passage à une physique plus détaillée. Le panneau **C** montre la simulation à l'échelle microscopique dans laquelle les processus chimiques ont été activés et les *G-values* ont été notées.

Dans ce résumé français, seuls les rendements primaires pour le faisceau d'ions carbone seront discutés car ils représentent le résultat le plus intéressant obtenu dans cette thèse. Ces rendements sont présentés dans la Fig. 10.5. étant donné l'augmentation du transfert d'énergie linéaire (TEL) pour le faisceau de carbone, il y a une plus grande proportion d'interactions radicales-radicales. Par conséquent, on observe une augmentation du rendement primaire des produits moléculaires tels que H_2O_2 en profondeur et une réduction correspondante des produits radicaux tels que $^{\bullet}OH$ et e^-_{aq}. Il est toutefois intéressant de noter qu'il semble y avoir une différence dans les rendements primaires dans les vallées par rapport aux pics, et que cette différence s'accentue en profondeur. A une profondeur de 10 mm, la différence de rendement primaire dans les vallées par rapport aux pics n'était pas statistiquement différente pour H_2O_2, et était d'environ 0.5% pour $^{\bullet}OH$ et e^-_{aq}. Cependant, à une profondeur de 70 mm, la différence de rendement primaire dans les vallées par rapport aux pics était de 4, 6 et 16% pour e^-_{aq}, $^{\bullet}OH$ et H_2O_2 respectivement.

La différence entre les rendements primaires des pics et des vallées a été attribuée aux fragments nucléaires présents dans les vallées, qui déclenchent un ensemble différent de réactions chimiques. Comme le montrent la figure 6.23 et le tableau 6.6, la proportion de réactions de recombinaison de $^{\bullet}OH$ pour former H_2O_2 était plus faible dans les vallées,

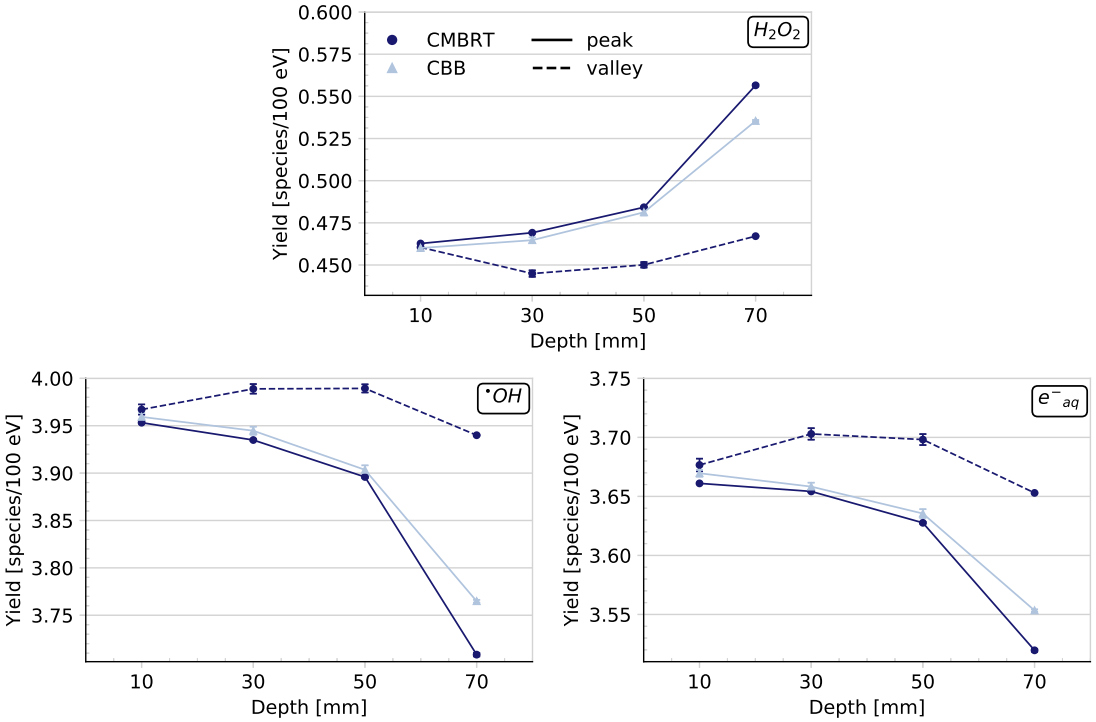

Figure 10.5: Rendements primaires de CMBRT et CBB dans le pic (ligne continue) et la vallée (ligne pointillée) pour les espèces: $^{\bullet}$OH, H_2O_2 et e^-_{aq}, en fonction de la profondeur dans le fantôme d'eau.

complétée par une proportion accrue de $^{\bullet}$OH réagissant avec e^-_{aq}. Compte tenu des fragments nucléaires présents dans les vallées, ces régions présentent une moyenne très élevée de TEL, et il a été rapporté dans la littérature qu'une réduction de H_2O_2 commence lorsque le TEL devient extrêmement élevé, comme à proximité du pic de Bragg [Wasselin-Trupin et al., 2002].

étant donné qu'il a été démontré que les réponses immunitaires antitumorales sont affaiblies pour des niveaux élevés de H_2O_2 [Lennicke et al., 2015, Deng et al., 2020], j'ai émis l'hypothèse que l'utilisation de mini-faisceaux de carbone pourrait être plus adaptée à l'activation du système immunitaire en raison des rendements primaires de H_2O_2 plus faibles que prévu dans les vallées par rapport aux pics. Nous pouvons donc conclure que s'il n'y a **aucune modification radiochimique entre les pics et les vallées des mini-faisceaux en raison du fractionnement spatial inhérent** de ces faisceaux, les **minibeams au carbone font exception et sont peut-être plus aptes à déclencher des réponses immunitaires antitumorales**.

Enfin, la diffusion de H_2O_2 a été évaluée en simulant une radiolyse de l'eau jusqu'à 1 μs, puis en laissant l'espèce se diffuser librement jusqu'à 10 minutes. L'intérêt d'examiner la diffusion de H_2O_2 est que les études précédentes ont émis l'hypothèse d'une couverture homogène potentielle de la tumeur par H_2O_2 malgré la distribution hétérogène de la dose de MBRT. [Dal Bello et al., 2020]. La figure 10.6 représente la concentration de H_2O_2 dans une tranche d'un fantôme d'eau à 60 s.

Dans les travaux récents de Ledo *in vivo*, la durée de vie de H_2O_2 dans le cerveau du striatum de souris vivantes a été déterminée comme étant de 2.2 s. Pour des temps

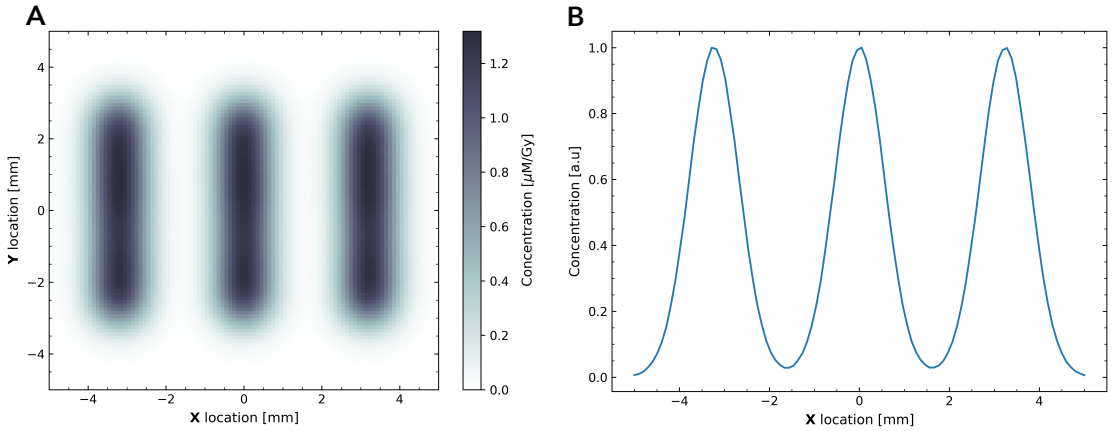

Figure 10.6: Diffusion de H_2O_2 à partir de 1 μs (Fig. 7.2) jusqu'à 60 s. Le panneau **A** représente la carte thermique de la concentration, tandis que le panneau **B** représente le profil latéral de la concentration à y=0.

de diffusion de cette ampleur, les résultats de cette thèse indiquent que la distribution de H_2O_2 reste assez hétérogène, comme le montre la Fig. 10.6. La conclusion est donc que **des doses hétérogènes produiraient des ROS distribués de manière hétérogène, avec une diffusion limitée entre les pics et les vallées**.

10.4 Discussion finale et conclusions

J'ai souligné au début de ce résumé en français que l'un des défis les plus pressants auxquels le domaine de la RT est actuellement confronté est celui des tumeurs radiorésistantes telles que les gliomes malins [Bleeker et al., 2012]. Les progrès des nouvelles techniques de RT au cours des dernières années ont montré que ces techniques peuvent élargir la fenêtre thérapeutique, conduisant ainsi à une amélioration de l'efficacité du traitement pour ces types de tumeurs. Cependant, il est évident que pour faire avancer le domaine, nous devons mieux comprendre comment les caractéristiques physiques de ces nouvelles techniques modulent la réponse biologique. à cette fin, la frontière de RT implique la réalisation d'évaluations plus orientées vers la radiobiologie, reliant explicitement la physique et la biologie. C'est exactement ce que vise cette thèse en faisant progresser notre compréhension de la thérapie VHEE et de la MBRT grâce à des simulations MC.

En ce qui concerne les VHEE, les installations existantes telles que CLEAR au CERN [Gamba et al., 2018] ou le projet PHASER [Maxim et al., 2019] indiquent clairement que les sources VHEE cliniquement compatibles pourraient devenir une réalité dans un avenir proche. CLEAR et PHASER utilisent tous deux des technologies d'accélérateur compactes qui permettent de relever les défis logistiques liés à l'encombrement des LINAC médicaux traditionnels. Dans le cadre de cette thèse, d'autres éléments ont été fournis en faveur de la traduction clinique de cette technique. Premièrement, on s'attend à ce que le niveau de protection contre les rayonnements dans une salle de traitement soit similaire à celui de la protonthérapie conventionnelle. Cette conclusion a été obtenue grâce aux travaux sur les equivalents de dose de neutrons dans l'air ambiant. Deuxièmement, un calcul théorique de l'EBR a montré que la thérapie VHEE ne serait probablement pas plus efficace sur le plan biologique que les traitements conventionnels, ce qui nous permet de profiter des avantages dosimétriques sans nous préoccuper des effets indésirables potentiels des neutrons générés, qui sont eux-mêmes très nocifs sur le plan biologique.

Par rapport à la thérapie VHEE, MBRT représente une technique plus mature qui est beaucoup plus proche de l'adoption clinique. Les contributions relatives des différents mécanismes sous-jacents proposés à l'efficacité des mini-faisceaux restent inconnues, et alors que les recherches sur les conséquences physiques et biologiques sont relativement bien documentées, l'aspect chimique a été cruellement sous-estimé, malgré ses liens évidents avec la physique et la biologie résultante d'une irradiation. Les travaux de cette thèse ont montré que pour les mêmes doses moyennes délivrées, les ROS produits par les mini-faisceaux de photons, de protons et d'ions hélium ne différeraient probablement pas des faisceaux homogènes des mêmes particules. En d'autres termes, si l'objectif est d'observer les changements radiochimiques résultant des modifications des caractéristiques physiques du faisceau, le degré de fractionnement spatial du faisceau n'est pas le meilleur paramètre à étudier. Ce n'est toutefois pas le cas pour le faisceau de carbone en raison de son TEL plus élevé, ce qui se traduit par un rendement primaire H_2O_2 plus faible dans les vallées et est donc potentiellement mieux adapté à l'activation immunitaire.

Grâce à ces recherches, je pense que le travail de cette thèse a non seulement fait progresser notre compréhension de la thérapie VHEE et de la MBRT, mais qu'il a également ouvert la voie à de futures recherches dans le but d'améliorer le traitement du cancer.

Appendix A

Full scale primary yields for all modalities

As noted throughout section 6.5, the difference between the primary yields in the MB peaks and valleys compared to the BB modality, as well as increases/decreases in the primary yields as a function of depth, are largely on the order of magnitude of singular percentages. The graphs displayed in section 6.5 may exaggerate these differences (particularly for the pMBRT, HeMBRT, and xMBRT modalities), and thus the graphs contained in this appendix are full scale graphs with a y-axis starting from zero.

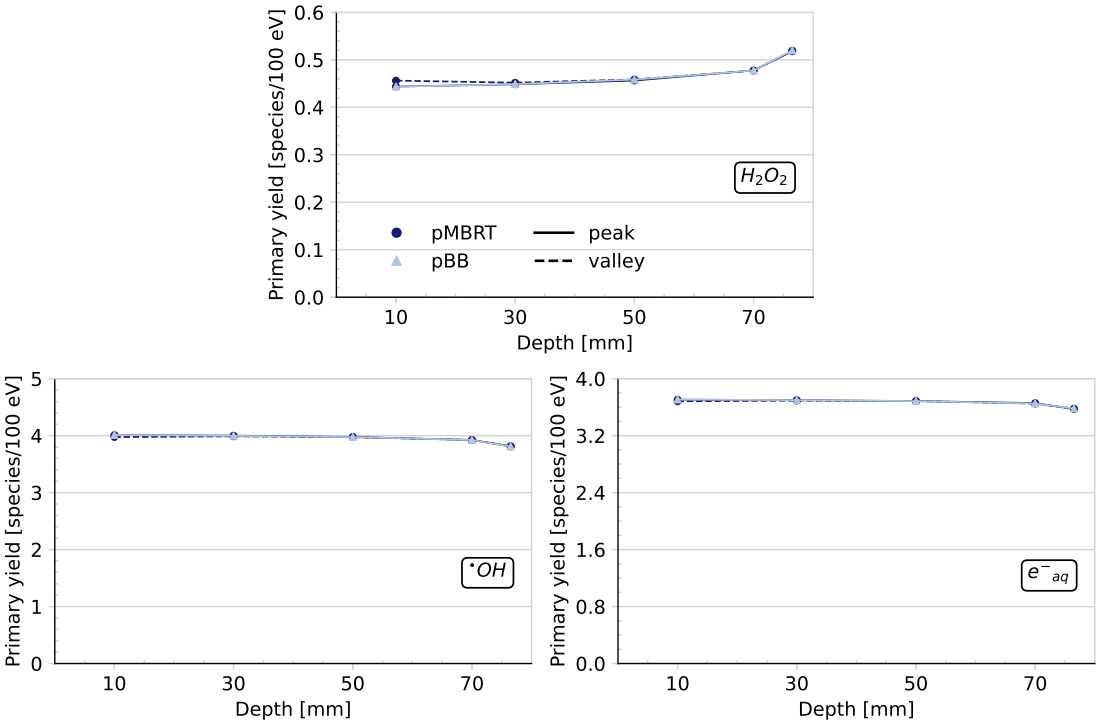

Figure A.1: pMBRT and pBB primary yields in the peak (solid line) and valley (dashed line) for the species: $^{\bullet}$OH, H_2O_2, and e^-_{aq}, depicted as a function of depth in the water phantom. Full scale graph.

As is evident in Figures A.1, A.2, and A.3 for the pMBRT, HeMBRT, and xMBRT modalities respectively, the differences between MB peak and valley primary yields compared to BB yields are largely inconsequential. However, as noted in the main part of the thesis, the most interesting result is that of the CMBRT modality, shown in Fig. A.4. Even in this full scale image, clear differences in the primary yields of $^{\bullet}$OH, H_2O_2, and e^-_{aq} between the MB peaks and valleys is observable and becomes more severe in depth. Furthermore, the CMBRT modality is the only modality evaluated in which there appears to be a difference between the H_2O_2 primary yields in the MB peak compared to the BB case in the vicinity

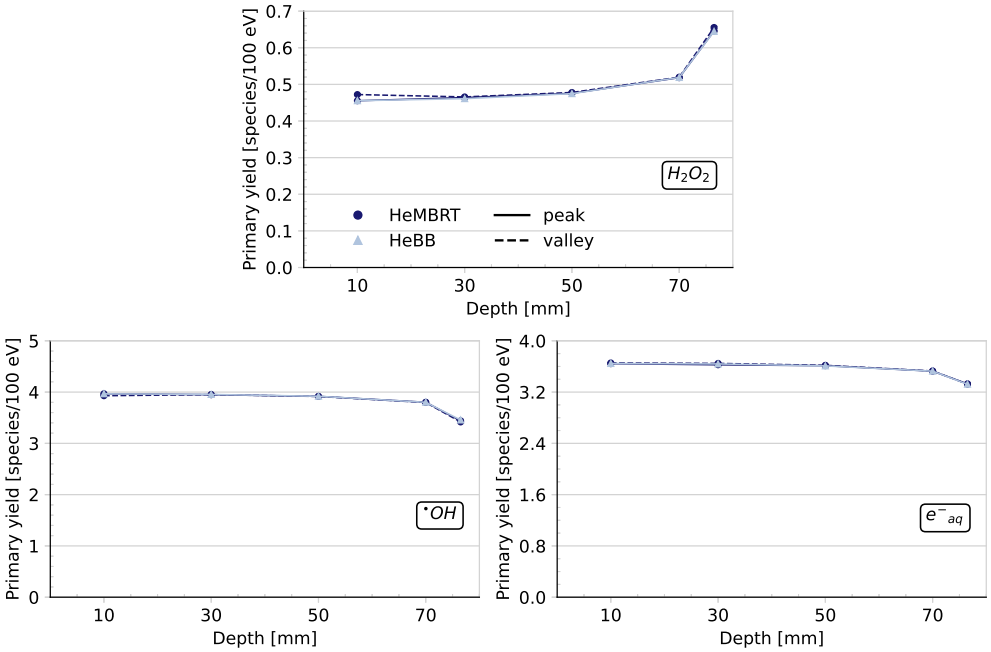

Figure A.2: HeMBRT and HeBB primary yields in the peak (solid line) and valley (dashed line) for the species: $^{\bullet}$OH, H_2O_2, and e^-_{aq}, depicted as a function of depth in the water phantom. Full scale graph.

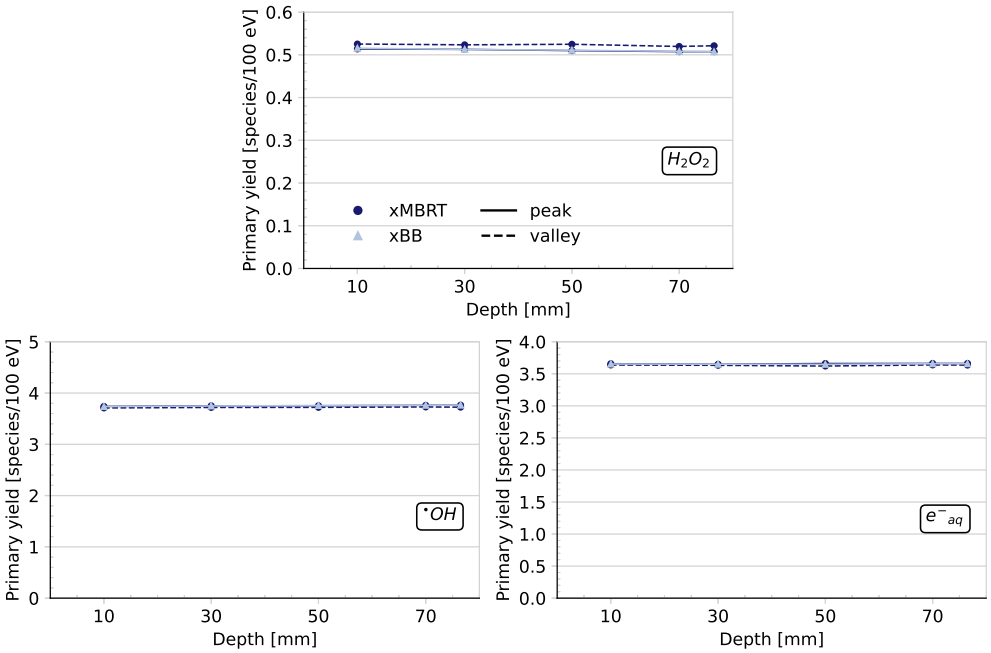

Figure A.3: xMBRT and xBB primary yields in the peak (solid line) and valley (dashed line) for the species: $^{\bullet}$OH, H_2O_2, and e^-_{aq}, depicted as a function of depth in the water phantom. Full scale graph.

of the Bragg peak.

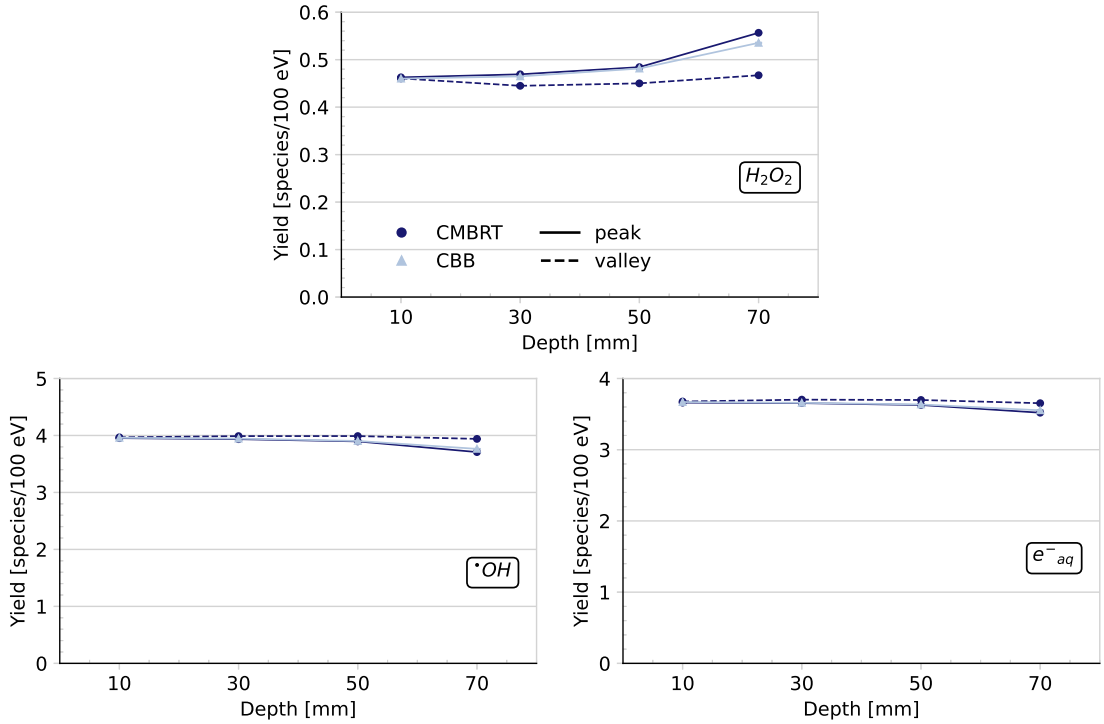

Figure A.4: CMBRT and CBB primary yields in the peak (solid line) and valley (dashed line) for the species: $^{\bullet}$OH, H_2O_2, and e^-_{aq}, depicted as a function of depth in the water phantom. Full scale graph.

List of Figures

Page

List of Tables

Bibliography

[Agostinelli et al., 2003] Agostinelli, S., Allison, J., Amako, K., et al. (2003). Geant4—a simulation toolkit. *Nuclear Instruments and Methods in Physics Research Section A: Accelerators, Spectrometers, Detectors and Associated Equipment*, **506(3):250–303**

[Alberts et al., 2019a] Alberts, B., Hopkin, K., Johnson, A., et al. (2019). Chapter 13 - How Cells Obtain Energy from Food. In *Essential Cell Biology (Fifth Edition)*. W. W. Norton & Company, **427–453**

[Alberts et al., 2019b] Alberts, B., Hopkin, K., Johnson, A., et al. (2019). Chapter 18 - The Cell-Division Cycle. In *Essential Cell Biology (Fifth Edition)*. W. W. Norton & Company, **609–649**

[Alexandre et al., 2007] Alexandre, J., Hu, Y., Lu, W., et al. (2007). Novel action of paclitaxel against cancer cells: bystander effect mediated by reactive oxygen species. *Cancer Res*, **67(8):3512–3517**

[Ali et al., 2020] Ali, M. Y., Oliva, C. R., Noman, A. S. M., et al. (2020). Radioresistance in Glioblastoma and the Development of Radiosensitizers. *Cancers (Basel)*, **12(9):2511**

[Allen, 1948] Allen, A. O. (1948). Radiation Chemistry of Aqueous Solutions. *The Journal of Physical and Colloid Chemistry*, **52(3):479–490**

[Allison et al., 2006] Allison, J., Amako, K., Apostolakis, J., et al. (2006). Geant4 developments and applications. *IEEE Transactions on Nuclear Science*, **53(1):270–278**

[Allison et al., 2016] Allison, J., Amako, K., Apostolakis, J., et al. (2016). Recent developments in Geant4. *Nuclear Instruments and Methods in Physics Research Section A*, **835:186–225**

[Alpen, 1997a] Alpen, E. L. (1997). Chapter 4 - Interaction of Radiation with Matter. In *Radiation Biophysics (Second Edition)*. Academic Press, **50–77**

[Alpen, 1997b] Alpen, E. L. (1997). Chapter 6 - Radiation Chemistry. In *Radiation Biophysics (Second Edition)*. Academic Press, **104–131**

[Alper and Bryant, 1974] Alper, T. and Bryant, P. E. (1974). Reduction in oxygen enhancement ratio with increase in LET: tests of two hypotheses. *Int J Radiat Biol Relat Stud Phys Chem Med*, **26(3):203–218**

[Amendola et al., 2019] Amendola, B. E., Perez, N. C., Wu, X., et al. (2019). Safety and Efficacy of Lattice Radiotherapy in Voluminous Non-small Cell Lung Cancer. *Cureus*, **11(3):e4263**

[Amendola et al., 2023] Amendola, B. E., Perez, N. C., Xu, B., et al. (2023). Lattice Radiotherapy SFRT: definitive radiation therapy in bulky primary tumors. In Zhang, H. and Mayr, N. A., editors of: *Spatially Fractionated, Microbeam and FLASH Radiation Therapy*. IOP Publishing, **7–1 to 7–17**

[Ando and Kase, 2009] Ando, K. and Kase, Y. (2009). Biological characteristics of carbon-ion therapy. *Int J Radiat Biol*, **85(9):715–728**

[Andreo, 2018] Andreo, P. (2018). Monte Carlo simulations in radiotherapy dosimetry. *Radiat Oncol*, **13(1):121**

[Andreo et al., 2012] Andreo, P., Burns, D. T., and Salvat, F. (2012). On the uncertainties of photon mass energy-absorption coefficients and their ratios for radiation dosimetry. *Phys Med Biol*, **57(8):2117–2136**

[Andrews and Bray, 2004] Andrews, S. S. and Bray, D. (2004). Stochastic simulation of chemical reactions with spatial resolution and single molecule detail. *Physical Biology*, **1(3):137**

[Arce et al., 2021] Arce, P., Bolst, D., Bordage, M.-C., et al. (2021). Report on G4-Med, a Geant4 benchmarking system for medical physics applications developed by the Geant4 Medical Simulation Benchmarking Group. *Med Phys*, **48(1):19–56**

[Assié et al., 2005] Assié, K., Gardin, I., Véra, P., and Buvat, I. (2005). Validation of the Monte Carlo simulator GATE for indium-111 imaging. *Phys Med Biol*, **50(13):3113–3125**

[Asur et al., 2015] Asur, R., Butterworth, K. T., Penagaricano, J. A., et al. (2015). High dose bystander effects in spatially fractionated radiation therapy. *Cancer Lett*, **356(1):52–57**

[Asur et al., 2012] Asur, R. S., Sharma, S., Chang, C.-W., et al. (2012). Spatially Fractionated Radiation Induces Cytotoxicity and Changes in Gene Expression in Bystander and Radiation Adjacent Murine Carcinoma Cells. *Radiation Research*, **177(6):751 – 765**

[Autsavapromporn et al., 2022] Autsavapromporn, N., Kobayashi, A., Liu, C., et al. (2022). Hypoxia and Proton microbeam: Role of Gap Junction Intercellular Communication in Inducing Bystander Responses on Human Lung Cancer Cells and Normal Cells. *Radiat Res*, **197(2):122–130**

[Autsavapromporn et al., 2013] Autsavapromporn, N., Suzuki, M., Funayama, T., et al. (2013). Gap junction communication and the propagation of bystander effects induced by microbeam irradiation in human fibroblast cultures: the impact of radiation quality. *Radiat Res*, **180(4):367–375**

[Averbeck and Rodriguez-Lafrasse, 2021] Averbeck, D. and Rodriguez-Lafrasse, C. (2021). Role of Mitochondria in Radiation Responses: Epigenetic, Metabolic, and Signaling Impacts. *Int J Mol Sci*, **22(20):11047**

[Aymar et al., 2020] Aymar, G., Becker, T., Boogert, S., et al. (2020). LhARA: The Laser-hybrid Accelerator for Radiobiological Applications. *Frontiers in Physics*, **8:567738**

[Azzam et al., 2001] Azzam, E. I., de Toledo, S. M., and Little, J. B. (2001). Direct evidence for the participation of gap junction-mediated intercellular communication in the transmission of damage signals from alpha -particle irradiated to nonirradiated cells. *Proc Natl Acad Sci U S A*, **98(2):473–478**

[Azzam et al., 2002] Azzam, E. I., De Toledo, S. M., Spitz, D. R., and Little, J. B. (2002). Oxidative metabolism modulates signal transduction and micronucleus formation in bystander cells from alpha-particle-irradiated normal human fibroblast cultures. *Cancer Res*, **62(19):5436–5442**

[Azzam et al., 2012] Azzam, E. I., Jay-Gerin, J.-P., and Pain, D. (2012). Ionizing radiation-induced metabolic oxidative stress and prolonged cell injury. *Cancer Lett*, **327(1-2):48–60**

[Baba et al., 2021] Baba, K., Kusumoto, T., Okada, S., et al. (2021). Quantitative estimation of track segment yields of water radiolysis species under heavy ions around Bragg peak energies using Geant4-DNA. *Scientific Reports*, **11(1):1524**

[Badziak, 2018] Badziak, J. (2018). Laser-driven ion acceleration: methods, challenges and prospects. *Journal of Physics: Conference Series*, **959(1):012001**

[Badziak et al., 2011] Badziak, J., Mishra, G., Gupta, N. K., and Holkundkar, A. R. (2011). Generation of ultraintense proton beams by multi-ps circularly polarized laser pulses for fast ignition-related applications. *Physics of Plasmas*, **18(5):053108**

[Baikalov et al., 2022] Baikalov, A., Abolfath, R., Mohan, R., et al. (2022). Modeling interspur interactions as a potential mechanism of the FLASH effect. *arXiv*, **2207:12287**

[Baker, 2012] Baker, C. (2012). Chapter 2 - Radiation interactions with amtter. In Symonds, P., Deehan, C., Mills, J. A., and Meredith, C., editors of: *Walter & Miller's Textbook of Radiotherapy: Radiation Physics, Therapy and Oncology (Seventh Edition)*. Elsevier, **15–32**

[Baldacchino et al., 2019] Baldacchino, G., Brun, E., Denden, I., et al. (2019). Importance of radiolytic reactions during high-LET irradiation modalities: LET effect, role of O_2 and radiosensitization by nanoparticles. *Cancer Nanotechnology*, **10(1):3**

[Baldacchino and Katsumura, 2010] Baldacchino, G. and Katsumura, Y. (2010). Chapter 8 - Chemical Processes in Heavy Ion Tracks. In Wishart, J. F. and Rao, B. S. M., editors of: *Recent Trends in Radiation Chemistry*. World Scientific, **231–253**

[Ballarini et al., 2000] Ballarini, F., Biaggi, M., Merzagora, M., et al. (2000). Stochastic aspects and uncertainties in the prechemical and chemical stages of electron tracks in liquid water: a quantitative analysis based on Monte Carlo simulations. *Radiat Environ Biophys*, **39(3):179–188**

[Balosso et al., 2022] Balosso, J., Febvey-Combes, O., Iung, A., et al. (2022). A randomized controlled phase III study comparing hadrontherapy with carbon ions versus conventional radiotherapy - including photon and proton therapy - for the treatment of radioresistant tumors: the ETOILE trial. *BMC Cancer*, **22(1):575**

[Banaee et al., 2021] Banaee, N., Goodarzi, K., and Nedaie, H. A. (2021). Neutron contamination in radiotherapy processes: a review study. *Journal of Radiation Research*, **62(6):947–954**

[Barkova and Kholin, 1971] Barkova, A. M. and Kholin, V. V. (1971). Theoretical calculation of the spatial distribution of a Co 60 gamma radiation dose field under a grid. *Med Radiol (Mosk)*, **16(11):64–70**

[Baró et al., 1995] Baró, J., Sempau, J., Fernández-Varea, J., and Salvat, F. (1995). PENELOPE: An algorithm for Monte Carlo simulation of the penetration and energy loss of electrons and positrons in matter. *Nuclear Instruments and Methods in Physics Research Section B: Beam Interactions with Materials and Atoms*, **100(1):31–46**

[Bartzsch et al., 2020] Bartzsch, S., Corde, S., Crosbie, J. C., et al. (2020). Technical advances in x-ray microbeam radiation therapy. *Physics in Medicine & Biology*, **65(2):02TR01**

[Baskar et al., 2012] Baskar, R., Lee, K. A., Yeo, R., and Yeoh, K.-W. (2012). Cancer and radiation therapy: current advances and future directions. *Int J Med Sci*, **9(3):193–199**

[Baumann et al., 2019] Baumann, K.-S., Horst, F., Zink, K., and Gomà, C. (2019). Comparison of penh, fluka, and Geant4/topas for absorbed dose calculations in air cavities representing ionization chambers in high-energy photon and proton beams. *Medical Physics*, **46(10):4639–4653**

[Baumann et al., 2020] Baumann, K.-S., Kaupa, S., Bach, C., et al. (2020). Monte Carlo calculation of beam quality correction factors in proton beams using TOPAS/GEANT4. *Phys Med Biol*, **65(5):055015**

[Baumann and Grégoire, 2018] Baumann, M. and Grégoire, V. (2018). Modified fractionation. In Joiner, M. C. and van der Kogel, A. J., editors of: *Basic Clinical Radiobiology (Fifth Edition)*. CRC Press, **135–148**

[Bazalova-Carter et al., 2015] Bazalova-Carter, M., Qu, B., Palma, B., et al. (2015). Treatment planning for radiotherapy with very high-energy electron beams and comparison of VHEE and VMAT plans. *Med Phys*, **42(5):2615–2625**

[Bazyar et al., 2017] Bazyar, S., Inscoe, C. R., O'Brian, E. T., et al. (2017). Minibeam radiotherapy with small animal irradiators; in vitro and in vivo feasibility studies. *Phys Med Biol*, **62(23):8924–8942**

[Bazyar et al., 2021] Bazyar, S., O'Brien, E. T. r., Benefield, T., et al. (2021). Immune-Mediated Effects of Microplanar Radiotherapy with a Small Animal Irradiator. *Cancers (Basel)*, **14(1):155**

[Bentzen, 2018] Bentzen, S. M. (2018). Dose-response relationships in radiotherapy. In Joiner, M. C. and van der Kogel, A. J., editors of: *Basic Clinical Radiobiology (Fifth Edition)*. CRC Press, **56–67**

[Berger et al., 2017] Berger, M. J., Coursey, J. S., Zucker, M. A., and Chang, J. (2017). ESTAR, PSTAR, and ASTAR: Computer Programs for Calculating Stopping-Power and Range Tables for Electrons, Protons, and Helium Ions (version 1.2.3). *National Institute of Standards and Technology (NIST)*, **NISTIR 4999**. Accessed June 3, 2023

[Berger et al., 2010a] Berger, M. J., Hubbell, J. H., Seltzer, S. M., et al. (2010). NIST Standard Reference Database 8 (XGAM). *NSBIR*, **87-3597**

[Berger et al., 2010b] Berger, M. J., Hubbell, J. H., Seltzer, S. M., et al. (2010). XCOM: Photon Cross Sections Database (version 1.5). *National Institute of Standards and Technology (NIST)*, **NBSIR 87–3597**. Accessed June 3, 2023

[Bernal et al., 2015] Bernal, M., Bordage, M., Brown, J., et al. (2015). Track structure modeling in liquid water: A review of the Geant4-DNA very low energy extension of the Geant4 Monte Carlo simulation toolkit. *Physica Medica*, **31(8):861–874**

[Bertho et al., 2022a] Bertho, A., Iturri, L., Brisebard, E., et al. (2022). Evaluation of the Role of the Immune System Response After Minibeam Radiation Therapy. *Int J Radiat Oncol Biol Phys*, **115(2):426–439**

[Bertho et al., 2022b] Bertho, A., Iturri, L., and Prezado, Y. (2022). Radiation-induced immune response in novel radiotherapy approaches FLASH and spatially fractionated radiotherapies. *Int Rev Cell Mol Biol*, **376:37–68**

[Bertho et al., 2021] Bertho, A., Ortiz, R., Juchaux, M., et al. (2021). First Evaluation of Temporal and Spatial Fractionation in Proton Minibeam Radiation Therapy of Glioma-Bearing Rats. *Cancers*, **13(19):4865**

[Bethe, 1930] Bethe, H. (1930). Zur Theorie des Durchgangs schneller Korpuskularstrahlen durch Materie. *Annalen der Physik*, **397(3):325–400**

[Biau et al., 2019] Biau, J., Chautard, E., Verrelle, P., and Dutreix, M. (2019). Altering DNA Repair to Improve Radiation Therapy: Specific and Multiple Pathway Targeting. *Front Oncol*, **9:1009**

[Bielski et al., 1985] Bielski, B. H. J., Cabelli, D. E., Arudi, R. L., and Ross, A. B. (1985). Reactivity of HO_2/O_2^- Radicals in Aqueous Solution. *Journal of Physical and Chemical Reference Data*, **14(4):1041–1100**

[Bienert et al., 2007] Bienert, G. P., Møller, A. L., Kristiansen, K. A., et al. (2007). Specific Aquaporins Facilitate the Diffusion of Hydrogen Peroxide across Membranes. *Journal of Biological Chemistry*, **282(2):1183–1192**

[Billena and Khan, 2019] Billena, C. and Khan, A. J. (2019). A Current Review of Spatial Fractionation: Back to the Future? *Int J Radiat Oncol Biol Phys*, **104(1):177–187**

[Blanco Suarez et al., 2015] Blanco Suarez, J. M., Amendola, B. E., Perez, N., et al. (2015). The Use of Lattice Radiation Therapy (LRT) in the Treatment of Bulky Tumors: A Case Report of a Large Metastatic Mixed Mullerian Ovarian Tumor. **7(11):e389**

[Bleddyn and G, 2007] Bleddyn, J. and G, D. R. (2007). Chapter 5 - Repopulation effects. In Bleddyn, J. and G, D. R., editors of: *Radiobiological Modelling in Radiation Oncology*. The British Institute of Radiology, **79–95**

[Bleeker et al., 2012] Bleeker, F. E., Molenaar, R. J., and Leenstra, S. (2012). Recent advances in the molecular understanding of glioblastoma. *J Neurooncol*, **108(1):11–27**

[Bloch, 1933] Bloch, F. (1933). Zur Bremsung rasch bewegter Teilchen beim Durchgang durch Materie. *Annalen der Physik*, **408(3):285–320**

[Bloomer and Hellman, 1975] Bloomer, W. D. and Hellman, S. (1975). Normal tissue responses to radiation therapy. *N Engl J Med*, **293(2):80–83**

[Blyth and Sykes, 2011] Blyth, B. J. and Sykes, P. J. (2011). Radiation-induced bystander effects: what are they, and how relevant are they to human radiation exposures? *Radiat Res*, **176(2):139–157**

[Bodega et al., 2019] Bodega, G., Alique, M., Puebla, L., et al. (2019). Microvesicles: ROS scavengers and ROS producers. *J Extracell Vesicles*, **8(1):1626654**

[Bodgi et al., 2016] Bodgi, L., Canet, A., Pujo-Menjouet, L., et al. (2016). Mathematical models of radiation action on living cells: From the target theory to the modern approaches. A historical and critical review. *J Theor Biol*, **394:93–101**

[Bolst et al., 2017] Bolst, D., Cirrone, G. A., Cuttone, G., et al. (2017). Validation of Geant4 fragmentation for Heavy Ion Therapy. *Nuclear Instruments and Methods in Physics Research Section A: Accelerators, Spectrometers, Detectors and Associated Equipment*, **869:68–75**

[Borras et al., 2015] Borras, J. M., Lievens, Y., Dunscombe, P., et al. (2015). The optimal utilization proportion of external beam radiotherapy in European countries: An ESTRO-HERO analysis. *Radiother Oncol*, **116(1):38–44**

[Boscolo et al., 2020] Boscolo, D., Krämer, M., Fuss, M. C., et al. (2020). Impact of Target Oxygenation on the Chemical Track Evolution of Ion and Electron Radiation. *Int J Mol Sci*, **21(2):424**

[Bouchet et al., 2016] Bouchet, A., Bräuer-Krisch, E., Prezado, Y., et al. (2016). Better Efficacy of Synchrotron Spatially Microfractionated Radiation Therapy Than Uniform Radiation Therapy on Glioma. *International Journal of Radiation Oncology, Biology, Physics*, **95(5):1485–1494**

[Bouchet et al., 2013a] Bouchet, A., Lemasson, B., Christen, T., et al. (2013). Synchrotron microbeam radiation therapy induces hypoxia in intracerebral gliosarcoma but not in the normal brain. *Radiother Oncol*, **108(1):143–148**

[Bouchet et al., 2010] Bouchet, A., Lemasson, B., Le Duc, G., et al. (2010). Preferential effect of synchrotron microbeam radiation therapy on intracerebral 9L gliosarcoma vascular networks. *Int J Radiat Oncol Biol Phys*, **78(5):1503–1512**

[Bouchet et al., 2013b] Bouchet, A., Sakakini, N., El Atifi, M., et al. (2013). Early gene expression analysis in 9L orthotopic tumor-bearing rats identifies immune modulation in molecular response to synchrotron microbeam radiation therapy. *PLoS One*, **8(12):e81874**

[Bouchet et al., 2015] Bouchet, A., Serduc, R., Laissue, J. A., and Djonov, V. (2015). Effects of microbeam radiation therapy on normal and tumoral blood vessels. *Phys Med*, **31(6):634–641**

[Boustani et al., 2019] Boustani, J., Grapin, M., Laurent, P.-A., et al. (2019). The 6th R of Radiobiology: Reactivation of Anti-Tumor Immune Response. *Cancers*, **11(6):860**

[Bräuer-Krisch et al., 2010] Bräuer-Krisch, E., Serduc, R., Siegbahn, E. A., et al. (2010). Effects of pulsed, spatially fractionated, microscopic synchrotron X-ray beams on normal and tumoral brain tissue. *Mutat Res*, **704(1-3):160–166**

[Bräuer-Krisch et al., 2013] Bräuer-Krisch, E., Némoz, C., Brochard, T., et al. (2013). The preclinical set-up at the ID17 biomedical beamline to achieve high local dose deposition using interlaced microbeams. *Journal of Physics: Conference Series*, **425:022001**

[Brönnimann et al., 2016] Brönnimann, D., Bouchet, A., Schneider, C., et al. (2016). Synchrotron microbeam irradiation induces neutrophil infiltration, thrombocyte attachment and selective vascular damage in vivo. *Sci Rep*, **6:33601**

[Buckey et al., 2010] Buckey, C., Stathakis, S., Cashon, K., et al. (2010). Evaluation of a commercially-available block for spatially fractionated radiation therapy. *J Appl Clin Med Phys*, **11(3):3163**

[Burton, 1947] Burton, M. (1947). Radiation Chemistry. *The Journal of Physical and Colloid Chemistry*, **51(2):611–625**

[Butterworth et al., 2023] Butterworth, K. T., Prezado, Y., and Prise, K. M. (2023). Introduction to the principles of spatially fractionated radiotherapy. In Zhang, H. and Mayr, N. A., editors of: *Spatially Fractionated, Microbeam and FLASH Radiation Therapy*. IOP Publishing, **1–1 to 1–17**

[Buxton, 2004] Buxton, G. V. (2004). Chapter 12 - The Radiation Chemistry of Liquid Water: Principles and Applications. In Mozumder, A. and Hatano, Y., editors of: *Charged Particle and Photon interactions with Matter: Chemical, Physiocochemical, and Biological Consequences with Applications (First Edition)*. CRC Press, **335–368**

[Carlos-Reyes et al., 2021] Carlos-Reyes, A., Muñiz-Lino, M. A., Romero-Garcia, S., et al. (2021). Biological Adaptations of Tumor Cells to Radiation Therapy. *Front Oncol*, **11:718636**

[Cavallone et al., 2021] Cavallone, M., Rovige, L., Huijts, J., et al. (2021). Dosimetric characterisation and application to radiation biology of a kHz laser-driven electron beam. *Applied Physics B*, **127(4):57**

[Chang and Kim, 2008] Chang, S.-Y. and Kim, B.-H. (2008). Understanding of the Microdosimetric Quantities Obtained by a TEPC. *Journal of Nuclear Science and Technology*, **45(sup5):213 – 216**

[Chargari et al., 2019] Chargari, C., Deutsch, E., Blanchard, P., et al. (2019). Brachytherapy: An overview for clinicians. *CA: A Cancer Journal for Clinicians*, **69(5):386–401**

[Charyyev et al., 2020] Charyyev, S., Artz, M., Szalkowski, G., et al. (2020). Optimization of hexagonal-pattern minibeams for spatially fractionated radiotherapy using proton beam scanning. *Medical Physics*, **47(8):3485–3495**

[Charyyev and Wang, 2020] Charyyev, S. and Wang, C.-K. C. (2020). Assessment of ambient neutron dose equivalent in spatially fractionated radiotherapy with protons using physical collimators. *Radiation Protection Dosimetry*, **189(2):190–197**

[Chen et al., 2011] Chen, S., Zhao, Y., Han, W., et al. (2011). Rescue effects in radiobiology: unirradiated bystander cells assist irradiated cells through intercellular signal feedback. *Mutat Res*, **706(1-2):59–64**

[Chen et al., 2016] Chen, X., Song, M., Zhang, B., and Zhang, Y. (2016). Reactive Oxygen Species Regulate T Cell Immune Response in the Tumor Microenvironment. *Oxidative Medicine and Cellular Longevity*, **2016:1580967**

[Cherry et al., 2012a] Cherry, S. R., Sorenson, J. A., and Phelps, M. E. (2012). Chapter 1 - What Is Nuclear Medicine? In *Physics in Nuclear Medicine (Fourth Edition)*. W.B. Saunders, Philadelphia, **1–6**

[Cherry et al., 2012b] Cherry, S. R., Sorenson, J. A., and Phelps, M. E. (2012). Chapter 6 - Interaction of Radiation with Matter. In *Physics in Nuclear Medicine (Fourth Edition)*. W.B. Saunders, Philadelphia, **63–85**

[Choi et al., 2019] Choi, J. I., Daniels, J., Cohen, D., et al. (2019). Clinical Outcomes of Spatially Fractionated GRID Radiotherapy in the Treatment of Bulky Tumors of the Head and Neck. *Cureus*, **11(5):e4637**

[Cirrone et al., 2013] Cirrone, G. A. P., Margarone, D., Maggiore, M., et al. (2013). ELIMED: a new hadron therapy concept based on laser driven ion beams. In Esarey, E., Schroeder, C. B., Leemans, W. P., et al., editors of: *Laser Acceleration of Electrons, Protons, and Ions II; and Medical Applications of Laser-Generated Beams of Particles II; and Harnessing Relativistic Plasma Waves III*. SPIE, **87791I**

[Clark et al., 2000] Clark, E., Krushelnick, K., Davies, J., et al. (2000). Measurements of energetic proton transport through magnetized plasma from intense laser interactions with solids. *Phys Rev Lett*, **84(4):670–673**

[Cobut et al., 1998] Cobut, V., Frongillo, Y., Patau, J. P., et al. (1998). Monte Carlo simulation of fast electron and proton tracks in liquid water – I. physical and physicochemical aspects. *Radiation Physics and Chemistry*, **51(3):229–243**

[Cortés-Giraldo and Carabe, 2015] Cortés-Giraldo, M. A. and Carabe, A. (2015). A critical study of different Monte Carlo scoring methods of dose average linear-energy-transfer maps calculated in voxelized geometries irradiated with clinical proton beams. *Phys Med Biol*, **60(7):2645–2669**

[Coutard, 1934] Coutard, H. (1934). Principles of x-ray therapy of malignant diseases. *The Lancet*, **224(5784):1–8**. Originally published as Volume 2, Issue 5784

[Craddock and Symon, 2008] Craddock, M. K. and Symon, K. R. (2008). Cyclotrons and Fixed-Field Alternating-Gradient Accelerators. In Chao, A. W. and Chou, W., editors of: *Reviews of Accelerator Science and Technology*. World Scientific, **65–97**

[Curtis, 1967] Curtis, H. J. (1967). The use of deuteron microbeam for simulating the biological effects of heavy cosmic-ray particles. *Radiat Res Suppl*, **7:250–257**

[D-Kondo et al., 2023] D-Kondo, J. N., Garcia-Garcia, O. R., LaVerne, J. A., et al. (2023). An integrated Monte Carlo track-structure simulation framework for modeling inter and intra-track effects on homogenous chemistry. *Phys Med Biol*, **68(12):125008**

[Daguenet et al., 2020] Daguenet, E., Louati, S., Wozny, A.-S., et al. (2020). Radiation-induced bystander and abscopal effects: important lessons from preclinical models. *British Journal of Cancer*, **123(3):339–348**

[Dal Bello et al., 2020] Dal Bello, R., Becher, T., Fuss, M. C., et al. (2020). Proposal of a Chemical Mechanism for Mini-Beam and Micro-Beam Efficacy. *Front Phys*, **8:564836**

[Dale and von Schantz, 2008] Dale, W. J. and von Schantz, M. (2008). Chapter 2 - Basic Molecular Biology. In *From Genes to Genomes: Concepts and Applications of DNA Technology (Second Edition)*. John Wiley & Sons, Ltd, **7–24**

[De Marzi et al., 2019] De Marzi, L., Nauraye, C., Lansonneur, P., et al. (2019). Spatial fractionation of the dose in proton therapy: Proton minibeam radiation therapy. *Cancer Radiother*, **23(6-7):677–681**

[De Marzi et al., 2018a] De Marzi, L., Patriarca, A., Nauraye, C., et al. (2018). Implementation of planar proton minibeam radiation therapy using a pencil beam scanning system: A proof of concept study. *Med Phys*, **45(11):5305–5316**

[De Marzi et al., 2018b] De Marzi, L., Patriarca, A., Nauraye, C., et al. (2018). Implementation of planar proton minibeam radiation therapy using a pencil beam scanning system: A proof of concept study. *Medical Physics*, **45(11):5305–5316**

[Debrot et al., 2018] Debrot, E., Tran, L., Chartier, L., et al. (2018). SOI microdosimetry and modified MKM for evaluation of relative biological effectiveness for a passive proton therapy radiation field. *Phys Med Biol*, **63(23):235007**

[Delgado and Guddati, 2021] Delgado, A. and Guddati, A. K. (2021). Clinical endpoints in oncology - a primer. *Am J Cancer Res*, **11(4):1121–1131**

[Delorme et al., 2021] Delorme, R., Masilela, T. A. M., Etoh, C., et al. (2021). First theoretical determination of relative biological effectiveness of very high energy electrons. *Scientific Reports*, **11(1):11242**

[Deman et al., 2012] Deman, P., Vautrin, M., Edouard, M., et al. (2012). Monochromatic minibeams radiotherapy: from healthy tissue-sparing effect studies toward first experimental glioma bearing rats therapy. *Int J Radiat Oncol Biol Phys*, **82(4):e693–700**

[Demaria et al., 2004] Demaria, S., Ng, B., Devitt, M. L., et al. (2004). Ionizing radiation inhibition of distant untreated tumors (abscopal effect) is immune mediated. *Int J Radiat Oncol Biol Phys*, **58(3):862–870**

[Deng et al., 2020] Deng, H., Yang, W., Zhou, Z., et al. (2020). Targeted scavenging of extracellular ROS relieves suppressive immunogenic cell death. *Nature Communications*, **11(1):4951**

[Derksen et al., 2023] Derksen, L., Flatten, V., Engenhart-Cabillic, R., et al. (2023). A method to implement inter-track interactions in Monte Carlo simulations with TOPAS-nBio and their influence on simulated radical yields following water radiolysis. *Phys Med Biol*, **68(13):135017**

[Desai et al., 2014] Desai, S., Kobayashi, A., Konishi, T., et al. (2014). Damaging and protective bystander cross-talk between human lung cancer and normal cells after proton microbeam irradiation. *Mutat Res*, **763-764:39–44**

[Desouky et al., 2015] Desouky, O., Ding, N., and Zhou, G. (2015). Targeted and non-targeted effects of ionizing radiation. *Journal of Radiation Research and Applied Sciences*, **8(2):247–254**

[DesRosiers et al., 2000] DesRosiers, C., Moskvin, V., Bielajew, A. F., and Papiez, L. (2000). 150-250 MeV electron beams in radiation therapy. *Physics in Medicine and Biology*, **45(7):1781–1805**

[Di Venanzio et al., 2015] Di Venanzio, C., Marinelli, M., Tonnetti, A., et al. (2015). Comparison between small radiation therapy electron beams collimated by Cerrobend and tubular applicators. *J Appl Clin Med Phys*, **16(1):5186**

[Diffenderfer et al., 2020] Diffenderfer, E. S., Verginadis, I. I., Kim, M. M., et al. (2020). Design, Implementation, and in Vivo Validation of a Novel Proton FLASH Radiation Therapy System. *Int J Radiat Oncol Biol Phys*, **106(2):440–448**

[Dilmanian et al., 2002] Dilmanian, F. A., Button, T. M., Le Duc, G., et al. (2002). Response of rat intracranial 9L gliosarcoma to microbeam radiation therapy. *Neuro Oncol*, **4(1):26–38**

[Dilmanian et al., 2015] Dilmanian, F. A., Eley, J. G., and Krishnan, S. (2015). Minibeam Therapy With Protons and Light Ions: Physical Feasibility and Potential to Reduce Radiation Side Effects and to Facilitate Hypofractionation. *International Journal of Radiation Oncology, Biology, Physics*, **92(2):469–474**

[Dilmanian et al., 2005] Dilmanian, F. A., Qu, Y., Liu, S., et al. (2005). X-ray microbeams: Tumor therapy and central nervous system research. *Nucl Instrum Methods Phys Res A*, **548(1-2):30–37**

[Dilmanian et al., 2012] Dilmanian, F. A., Rusek, A., Fois, G. R., et al. (2012). Interleaved carbon minibeams: an experimental radiosurgery method with clinical potential. *Int J Radiat Oncol Biol Phys*, **84(2):514–519**

[Dilmanian et al., 2006] Dilmanian, F. A., Zhong, Z., Bacarian, T., et al. (2006). Interlaced x-ray microplanar beams: a radiosurgery approach with clinical potential. *Proc Natl Acad Sci U S A*, **103(25):9709–9714**

[Dingfelder et al., 2008] Dingfelder, M., Ritchie, R. H., Turner, J. E., et al. (2008). Comparisons of calculations with PARTRAC and NOREC: transport of electrons in liquid water. *Radiat Res*, **169(5):584–594**

[Djonov et al., 2023] Djonov, V., Fernandez-Palomo, C., and Pellicioli, P. (2023). Microbeam SFRT with photons. In Zhang, H. and Mayr, N. A., editors of: *Spatially Fractionated, Microbeam and FLASH Radiation Therapy*. IOP Publishing, **20–1 to 20–24**

[Dörr and van der Kogel, 2018] Dörr, W. and van der Kogel, A. J. (2018). The volume effect in radiotherapy. In Joiner, M. C. and van der Kogel, A. J., editors of: *Basic Clinical Radiobiology (Fifth Edition)*. CRC Press, **191–206**

[Dos Santos et al., 2020] Dos Santos, M., Delorme, R., Salmon, R., and Prezado, Y. (2020). Minibeam radiation therapy: A micro- and nano-dosimetry Monte Carlo study. *Med Phys*, **47(3):1379–1390**

[Doyle and Wang, 2019] Doyle, L. M. and Wang, M. Z. (2019). Overview of Extracellular Vesicles, Their Origin, Composition, Purpose, and Methods for Exosome Isolation and Analysis. *Cells*, **8(7):727**

[Du et al., 2020] Du, Y., Du, S., Liu, L., et al. (2020). Radiation-Induced Bystander Effect can be Transmitted Through Exosomes Using miRNAs as Effector Molecules. *Radiat Res*, **194(1):89–100**

[Duncan et al., 2020] Duncan, M., Donzelli, M., Pellicioli, P., et al. (2020). First experimental measurement of the effect of cardio-synchronous brain motion on the dose distribution during microbeam radiation therapy. *Medical Physics*, **47(1):213–222**

[Dunn, 2012] Dunn, M. (2012). Chapter 4 - Radiation protection. In Symonds, P., Deehan, C., Mills, J. A., and Meredith, C., editors of: *Walter & Miller's Textbook of Radiotherapy: Radiation Physics, Therapy and Oncology (Seventh Edition)*. Elsevier, **59–76**

[Durante et al., 2021] Durante, M., Debus, J., and Loeffler, J. S. (2021). Physics and biomedical challenges of cancer therapy with accelerated heavy ions. *Nat Rev Phys*, **3(12):777–790**

[Edwards et al., 2015] Edwards, J. M., Shah, P. H., Huhn, J. L., et al. (2015). Definitive GRID and Fractionated Radiation in Bulky Head and Neck Cancer Associated With Low Rates of Distant Metastasis. *International Journal of Radiation Oncology, Biology, Physics*, **93(3):E334**

[El-Deiry, 2016] El-Deiry, W. S. (2016). p21(WAF1) Mediates Cell-Cycle Inhibition, Relevant to Cancer Suppression and Therapy. *Cancer Res*, **76(18):5189–5191**

[Elbakrawy et al., 2020] Elbakrawy, E., Kaur Bains, S., Bright, S., et al. (2020). Radiation-Induced Senescence Bystander Effect: The Role of Exosomes. *Biology (Basel)*, **9(8):191**

[Eley et al., 2021] Eley, J. G., Haga, C. W., Keller, A., et al. (2021). Heavy Ion Minibeam Therapy: Side Effects in Normal Brain. *Cancers (Basel)*, **13(24):6207**

[Elith et al., 2011] Elith, C., Dempsey, S. E., Findlay, N., and Warren-Forward, H. M. (2011). An Introduction to the Intensity-modulated Radiation Therapy (IMRT) Techniques, Tomotherapy, and VMAT. *J Med Imaging Radiat Sci*, **42(1):37–43**

[Endo, 2016] Endo, A. (2016). on behalf of ICRU Report Committee 26 on Operational Radiation Protection Quantities for External Radiation. Operational quantities and new approach by ICRU. *Ann ICRP*, **45(1 Suppl):178–187**

[Faddegon et al., 2020] Faddegon, B., Ramos-Méndez, J., Schuemann, J., et al. (2020). The TOPAS tool for particle simulation, a Monte Carlo simulation tool for physics, biology and clinical research. *Physica Medica*, **72:114–121**

[Favaudon et al., 2014] Favaudon, V., Caplier, L., Monceau, V., et al. (2014). Ultrahigh dose-rate FLASH irradiation increases the differential response between normal and tumor tissue in mice. *Sci Transl Med*, **6(245):245ra93**

[Fernandez-Palomo et al., 2022] Fernandez-Palomo, C., Chang, S., and Prezado, Y. (2022). Should Peak Dose Be Used to Prescribe Spatially Fractionated Radiation Therapy?– A Review of Preclinical Studies. *Cancers*, **14(15):3625**

[Fernandez-Palomo et al., 2013] Fernandez-Palomo, C., Schültke, E., Smith, R., et al. (2013). Bystander effects in tumor-free and tumor-bearing rat brains following irradiation by synchrotron X-rays. *Int J Radiat Biol*, **89(6):445–453**

[Fernandez-Palomo et al., 2020] Fernandez-Palomo, C., Trappetti, V., Potez, M., et al. (2020). Complete Remission of Mouse Melanoma after Temporally Fractionated Microbeam Radiotherapy. *Cancers (Basel)*, **12(9):2656**

[Ferrari et al., 2005] Ferrari, A., Sala, P. R., Fassò, A., and Ranft, J. (2005). FLUKA : A multi-particle transport code (program version 2005). *CERN*, **2005-10**

[Forman et al., 2014] Forman, H. J., Ursini, F., and Maiorino, M. (2014). An overview of mechanisms of redox signaling. *Journal of Molecular and Cellular Cardiology*, **73:2–9**

[Franken et al., 2006] Franken, N. A. P., Rodermond, H. M., Stap, J., et al. (2006). Clonogenic assay of cells in vitro. *Nat Protoc*, **1(5):2315–2319**

[Fricke et al., 1938] Fricke, H., Hart, E. J., and Smith, H. P. (1938). Chemical Reactions of Organic Compounds with X-Ray Activated Water. *The Journal of Chemical Physics*, **6(5):229–240**

[Friedland et al., 2011] Friedland, W., Dingfelder, M., Kundrát, P., and Jacob, P. (2011). Track structures, DNA targets and radiation effects in the biophysical Monte Carlo simulation code PARTRAC. *Mutation Research/Fundamental and Molecular Mechanisms of Mutagenesis*, **711(1):28–40**

[Frongillo et al., 1998] Frongillo, Y., Goulet, T., Fraser, M. J., et al. (1998). Monte Carlo simulation of fast electron and proton tracks in liquid water – II. nonhomogeneous chemistry. *Radiation Physics and Chemistry*, **51(3):245–254**

[Furusawa et al., 2000] Furusawa, Y., Fukutsu, K., Aoki, M., et al. (2000). Inactivation of aerobic and hypoxic cells from three different cell lines by accelerated (3)He-, (12)C- and (20)Ne-ion beams. *Radiat Res*, **154(5):485–496**

[Gamba et al., 2018] Gamba, D., Corsini, R., Curt, S., et al. (2018). The CLEAR user facility at CERN. *Nuclear Instruments and Methods in Physics Research Section A: Accelerators, Spectrometers, Detectors and Associated Equipment*, **909:480–483**

[Gao et al., 2018] Gao, M., Mohiuddin, M. M., Hartsell, W. F., and Pankuch, M. (2018). Spatially fractionated (GRID) radiation therapy using proton pencil beam scanning (PBS): Feasibility study and clinical implementation. *Med Phys*, **45(4):1645–1653**

[Geant4 Collaboration, 2021] Geant4 Collaboration (2021). Geant4 Physics Reference Manual Release 10.7. **Geant4 Collaboration**. Accessed March 21, 2021

[Geant4 Collaboration, 2023] Geant4 Collaboration (2023). Book For Application Developers Release 10.3. **Geant4 Collaboration**. Accessed August 14, 2023

[Geant4-DNA Collaboration, 2023] Geant4-DNA Collaboration (2023). Physics processes & models. **Geant4-DNA Collaboration**. Accessed August 15, 2023

[Gerber and Chan, 2008] Gerber, D. E. and Chan, T. A. (2008). Recent advances in radiation therapy. *Am Fam Physician*, **78(11):1254–1262**

[Gholami et al., 2017] Gholami, S., Nedaie, H. A., Longo, F., et al. (2017). Grid Block Design Based on Monte Carlo Simulated Dosimetry, the Linear Quadratic and Hug-Kellerer Radiobiological Models. *J Med Phys*, **42(4):213–221**

[Girst et al., 2016] Girst, S., Greubel, C., Reindl, J., et al. (2016). Proton Minibeam Radiation Therapy Reduces Side Effects in an In Vivo Mouse Ear Model. *Int J Radiat Oncol Biol Phys*, **95(1):234–241**

[González et al., 2017] González, W., Peucelle, C., and Prezado, Y. (2017). Theoretical dosimetric evaluation of carbon and oxygen minibeam radiation therapy. *Med Phys*, **44(5):1921–1929**

[González and Prezado, 2018] González, W. and Prezado, Y. (2018). Spatial fractionation of the dose in heavy ions therapy: An optimization study. *Med Phys*, **45(6):2620–2627**

[Gough and Cotter, 2011] Gough, D. R. and Cotter, T. G. (2011). Hydrogen peroxide: a Jekyll and Hyde signalling molecule. *Cell Death & Disease*, **2(10):e213–e213**

[Grams et al., 2023] Grams, M. P., Deufel, C. L., Kavanaugh, J. A., et al. (2023). Clinical aspects of spatially fractionated radiation therapy treatments. *Phys Med*, **111:102616**

[Grams et al., 2021] Grams, M. P., Owen, D., Park, S. S., et al. (2021). VMAT Grid Therapy: A Widely Applicable Planning Approach. *Practical Radiation Oncology*, **11(3):e339–e347**

[Granville and Sawakuchi, 2015] Granville, D. A. and Sawakuchi, G. O. (2015). Comparison of linear energy transfer scoring techniques in Monte Carlo simulations of proton beams. *Phys Med Biol*, **60(14):N283–91**

[Grass et al., 2016] Grass, G. D., Krishna, N., and Kim, S. (2016). The immune mechanisms of abscopal effect in radiation therapy. *Curr Probl Cancer*, **40(1):10–24**

[Green, 2023] Green, E. (2023). Genome. *National Human Genome Research Institute*. **genetics-glossary/Genome**. Accessed June 17, 2023

[Grevillot et al., 2010] Grevillot, L., Frisson, T., Zahra, N., et al. (2010). Optimization of GEANT4 settings for Proton Pencil Beam Scanning simulations using GATE. *Nuclear Instruments and Methods in Physics Research Section B: Beam Interactions with Materials and Atoms*, **268(20):3295–3305**

[Griffin et al., 2012] Griffin, R. J., Koonce, N. A., Dings, R. P. M., et al. (2012). Microbeam radiation therapy alters vascular architecture and tumor oxygenation and is enhanced by a galectin-1 targeted anti-angiogenic peptide. *Radiat Res*, **177(6):804–812**

[Griffin et al., 2020] Griffin, R. J., Prise, K. M., McMahon, S. J., et al. (2020). History and current perspectives on the biological effects of high-dose spatial fractionation and high dose-rate approaches: GRID, Microbeam & FLASH radiotherapy. *Br J Radiol*, **93(1113):20200217**

[Grotzer et al., 2015] Grotzer, M., Schültke, E., Bräuer-Krisch, E., and Laissue, J. (2015). Microbeam radiation therapy: Clinical perspectives. *Physica Medica*, **31(6):564–567**. Radiation Therapy with Synchrotron Radiation: Achievements and Challenges

[Grover et al., 2017] Grover, S., Longo, J., Einck, J., et al. (2017). The Unique Issues With Brachytherapy in Low- and Middle-Income Countries. *Semin Radiat Oncol*, **27(2):136–142**

[Grün et al., 2019] Grün, R., Friedrich, T., Traneus, E., and Scholz, M. (2019). Is the dose-averaged LET a reliable predictor for the relative biological effectiveness? *Med Phys*, **46(2):1064–1074**

[Guan et al., 2015] Guan, F., Peeler, C., Bronk, L., et al. (2015). Analysis of the track- and dose-averaged LET and LET spectra in proton therapy using the geant4 Monte Carlo code. *Med Phys*, **42(11):6234–6247**

[Guardiola et al., 2020] Guardiola, C., De Marzi, L., and Prezado, Y. (2020). Verification of a Monte Carlo dose calculation engine in proton minibeam radiotherapy in a passive scattering beamline for preclinical trials. *Br J Radiol*, **93(1107):20190578**

[Guardiola et al., 2017] Guardiola, C., Peucelle, C., and Prezado, Y. (2017). Optimization of the mechanical collimation for minibeam generation in proton minibeam radiation therapy. *Med Phys*, **44(4):1470–1478**

[Guardiola et al., 2018] Guardiola, C., Prezado, Y., Roulin, C., and Bergs, J. W. J. (2018). Effect of X-ray minibeam radiation therapy on clonogenic survival of glioma cells. *Clin Transl Radiat Oncol*, **13:7–13**

[Gudkov et al., 2015] Gudkov, S. V., Shilyagina, N. Y., Vodeneev, V. A., and Zvyagin, A. V. (2015). Targeted Radionuclide Therapy of Human Tumors. *Int J Mol Sci*, **17(1):33**

[Gulliford and El Naqqa, 2022] Gulliford, S. and El Naqqa, I. (2022). Modelling of Radiotherapy Response (TCP/NTCP). In El Naqqa, I. and Murphy, M. J., editors of: *Machine and Deep Learning in Oncology, Medical Physics and Radiology (Second Edition)*. Springer, **399–438**

[Gupta et al., 2012] Gupta, S. C., Hevia, D., Patchva, S., et al. (2012). Upsides and downsides of reactive oxygen species for cancer: the roles of reactive oxygen species in tumorigenesis, prevention, and therapy. *Antioxid Redox Signal*, **16(11):1295–1322**

[Ha et al., 2006] Ha, J. K., Zhang, G., Naqvi, S. A., et al. (2006). Feasibility of delivering grid therapy using a multileaf collimator. *Med Phys*, **33(1):76–82**

[Hahn and Zutta Villate, 2021] Hahn, M. B. and Zutta Villate, J. M. (2021). Combined cell and nanoparticle models for TOPAS to study radiation dose enhancement in cell organelles. *Scientific Reports*, **11(1):6721**

[Hälg and Schneider, 2020] Hälg, R. A. and Schneider, U. (2020). Neutron dose and its measurement in proton therapy-current State of Knowledge. *Br J Radiol*, **93(1107):20190412**

[Hall and Giaccia, 2012a] Hall, E. J. and Giaccia, A. J. (2012). Chapter 1 - Physics and Chemistry of Radiation Absorption. In *Radiobiology for the Radiologist*. Lippincott Williams & Wilkins, **3–11**

[Hall and Giaccia, 2012b] Hall, E. J. and Giaccia, A. J. (2012). Chapter 2 - Molecular Mechanisms of DNA and Chromosome Damage and Repair. In *Radiobiology for the Radiologist*. Lippincott Williams & Wilkins, **12–34**

[Hall and Giaccia, 2012c] Hall, E. J. and Giaccia, A. J. (2012). Chapter 6 - Oxygen Effect and Reoxygenation. In *Radiobiology for the Radiologist*. Lippincott Williams & Wilkins, **86–103**

[Hall and Giaccia, 2012d] Hall, E. J. and Giaccia, A. J. (2012). Chapter 7 - Linear Energy Transfer and Relative Biologic Effectiveness. In *Radiobiology for the Radiologist*. Lippincott Williams & Wilkins, **104–113**

[Han et al., 2017] Han, S.-E., Cho, G., and Lee, S. B. (2017). An Assessment of the Secondary Neutron Dose in the Passive Scattering Proton Beam Facility of the National Cancer Center. *Nuclear Engineering and Technology*, **49(4):801–809**

[Hancock et al., 2001] Hancock, J. T., Desikan, R., and Neill, S. J. (2001). Role of reactive oxygen species in cell signalling pathways. *Biochem Soc Trans*, **29(2):345–350**

[Harrison, 2010] Harrison, R. L. (2010). Introduction To Monte Carlo Simulation. *AIP Conf Proc*, **1204(1):17–21**

[Hawkins, 1994] Hawkins, R. B. (1994). A statistical theory of cell killing by radiation of varying linear energy transfer. *Radiat Res*, **140(3):366–374**

[Hawkins, 1996] Hawkins, R. B. (1996). A microdosimetric-kinetic model of cell death from exposure to ionizing radiation of any LET, with experimental and clinical applications. *Int J Radiat Biol*, **69(6):739–755**

[Henry et al., 2017] Henry, T., Ureba, A., Valdman, A., and Siegbahn, A. (2017). Proton Grid Therapy: A Proof-of-Concept Study. *Technology in Cancer Research & Treatment*, **16(6):749–757**

[Herbert, 2019] Herbert, J. M. (2019). Structure of the aqueous electron. *Phys. Chem. Chem. Phys.*, **21:20538–20565**

[Hill, 2018] Hill, M. A. (2018). Track to the future: historical perspective on the importance of radiation track structure and DNA as a radiobiological target. *Int J Radiat Biol*, **94(8):759–768**

[Hiramoto et al., 2007] Hiramoto, K., Umezawa, M., Saito, K., et al. (2007). The synchrotron and its related technology for ion beam therapy. *Nuclear Instruments and Methods in Physics Research Section B: Beam Interactions with Materials and Atoms*, **261(1):786–790**. The Application of Accelerators in Research and Industry

[Hirayama, 2014] Hirayama, R. (2014). Mechanism of oxygen effect for photon and heavy-ion beams. *Japanese journal of medical physics*, **34(2):65–69**

[Hirayama et al., 2013] Hirayama, R., Ito, A., Noguchi, M., et al. (2013). OH Radicals from the Indirect Actions of X-Rays Induce Cell Lethality and Mediate the Majority of the Oxygen Enhancement Effect. *Radiation Research*, **180(5):514–523**

[Hirayama et al., 2009] Hirayama, R., Ito, A., Tomita, M., et al. (2009). Contributions of direct and indirect actions in cell killing by high-LET radiations. *Radiat Res*, **171(2):212–218**

[Hopewell and Trott, 2000] Hopewell, J. W. and Trott, K. R. (2000). Volume effects in radiobiology as applied to radiotherapy. *Radiother Oncol*, **56(3):283–288**

[Howell and Burgett, 2014] Howell, R. M. and Burgett, E. A. (2014). Secondary neutron spectrum from 250-MeV passively scattered proton therapy: measurement with an extended-range Bonner sphere system. *Med Phys*, **41(9):092104**

[Huang et al., 2018] Huang, S., Kang, M., Souris, K., et al. (2018). Validation and clinical implementation of an accurate Monte Carlo code for pencil beam scanning proton therapy. *J Appl Clin Med Phys*, **19(5):558–572**

[Huhn et al., 2006] Huhn, J. L., Regine, W. F., Valentino, J. P., et al. (2006). Spatially fractionated GRID radiation treatment of advanced neck disease associated with head and neck cancer. *Technol Cancer Res Treat*, **5(6):607–612**

[IAEA, 1979] IAEA (1979). 2.5 Neutrons. In *Radiological Safety Aspects of the Operation of Electron Linear Accelerators, Technical Reports Series No. 188*. IAEA, **61–96**

[Ibarmia et al., 2013] Ibarmia, S., Eck, J., Ivanchenko, V., et al. (2013). Experimental Dose Enhancement in Multi-Layer Shielding Structures Exposed to High-Energy Electron Environments. *IEEE Transactions on Nuclear Science*, **60(4):2486–2493**

[ICRP, 1996] ICRP (1996). 4. Conversion Coefficients. In *ICRP Publication 74 Conversion Coefficients for use in Radiological Protection against External Radiation*. Ann. ICRP, **26:3–4**

[ICRP, 2003] ICRP (2003). 4. Weighting Factors for Radiation Quality. In *ICRP Publication 92 Relative Biological Effectiveness (RBE), Quality Factor (Q), and Radiation Weighting Factor (W_R)*. Ann. ICRP, **33:4**

[ICRU, 1983] ICRU (1983). 2. Microdosimetric Quantities and Distributions. In *ICRU Report 36: Microdosimetry*. Journal of the ICRU, **4–6**

[ICRU, 1985] ICRU (1985). 3. Specification of the Dose Equivalents for Environmental and Individual Monitoring. In *ICRU Report 39, Determination of Dose Equivalents Resulting from External Radiation Sources*. Journal of the ICRU, **3–5**

[ICRU, 1988] ICRU (1988). 2. Consideration of Quantities for the Practical Determination of Dose Equivalent. In *ICRU Report 43, Determination of Dose Equivalents from External Radiation Sources–Part II*. Journal of the ICRU, **3–5**

[ICRU, 1998] ICRU (1998). 4. Conversion Coefficients. In *ICRU Report 57, Conversion Coefficients for use in Radiological Protection against External Radiation*. Journal of the ICRU, **22–56**

[ICRU, 1999] ICRU (1999). 3. Absorbed Doses. In *ICRU Report 62, Prescribing, Recording and Reporting Photon Beam Therapy (Supplement to ICRU 50)*. Journal of the ICRU, **21–25**

[ICRU, 2007] ICRU (2007). 3. Beam Delivery and Properties. In *ICRU Report 78, Prescribing, Recording, and Reporting Proton-Beam Therapy*. Journal of the ICRU, **29–48**

[ICRU, 2011a] ICRU (2011). 4. Interaction Coefficients and Related Quantities. In *ICRU Report 85a (Revised), Fundamental Quantities and Units for Ionizing Radiation*. Journal of the ICRU, **17–21**

[ICRU, 2011b] ICRU (2011). 5. Dosimetry. In *ICRU Report 85a (Revised), Fundamental Quantities and Units for Ionizing Radiation*. Journal of the ICRU, **22–28**

[ICRU, 2013] ICRU (2013). 7. Radiobiolgical Considerations. In *ICRU Report 89, Prescribing, Recording, and Reporting Brachytherapy for Cancer of the Cervix*. Journal of the ICRU, **89–104**

[ICRU, 2020] ICRU (2020). 4. Conversion Coefficients. In *ICRU Report 95, Operational Quantities for External Radiation Exposure*. Journal of the ICRU, **30–37**

[Incerti et al., 2010] Incerti, S., Baldacchino, G., Bernal, M., et al. (2010). The Geant4-DNA project. *International Journal of Modeling, Simulation, and Scientific Computing*, **01(02):157–178**

[Incerti et al., 2018] Incerti, S., Kyriakou, I., Bernal, M. A., et al. (2018). Geant4-DNA example applications for track structure simulations in liquid water: A report from the Geant4-DNA Project. *Medical Physics*, **45(8):e722–e739**

[Inokuti, 1991] Inokuti, M. (1991). Subexcitation electrons: An appraisal of our understanding. *International Journal of Radiation Applications and Instrumentation. Part A. Applied Radiation and Isotopes*, **42(10):979–983**

[Iori et al., 2023] Iori, F., Cappelli, A., D'Angelo, E., et al. (2023). Lattice Radiation Therapy in clinical practice: A systematic review. *Clin Transl Radiat Oncol*, **39:100569**

[Jäkel, 2020] Jäkel, O. (2020). Physical advantages of particles: protons and light ions. *Br J Radiol*, **93(1107):20190428**

[Jakubowska et al., 2016] Jakubowska, E. A., Gryziński, M., Golnik, N., et al. (2016). Ambient dose equivalent measurements in secondary radiation fields at proton therapy facility CCB IFJ PAN in Krakow using recombination chambers. *Nukleonika*, **61(1):23–28**

[Jan et al., 2011] Jan, S., Benoit, D., Becheva, E., et al. (2011). GATE V6: a major enhancement of the GATE simulation platform enabling modelling of CT and radiotherapy. *Phys Med Biol*, **56(4):881–901**

[Jay-Gerin, 2020] Jay-Gerin, J.-P. (2020). Ultra-high dose-rate (FLASH) radiotherapy: Generation of early, transient, strongly acidic spikes in the irradiated tumor environment. *Cancer/Radiothérapie*, **24(4):332–334**

[Jiang et al., 2020] Jiang, L., Li, X., Zhang, J., et al. (2020). Combined High-Dose LATTICE Radiation Therapy and Immune Checkpoint Blockade for Advanced Bulky Tumors: The Concept and a Case Report. *Front Oncol*, **10:548132**

[Johnsrud et al., 2023] Johnsrud, A. J., Jenkins, S. V., and Griffin, R. J. (2023). General principles of SFRT biology. In Zhang, H. and Mayr, N. A., editors of: *Spatially Fractionated, Microbeam and FLASH Radiation Therapy*. IOP Publishing, **2–1 to 2–18**

[Johnsrud et al., 2020] Johnsrud, A. J., Jenkins, S. V., Jamshidi-Parsian, A., et al. (2020). Evidence for Early Stage Anti-Tumor Immunity Elicited by Spatially Fractionated Radiotherapy-Immunotherapy Combinations. *Radiation Research*, **194(6):688–697**

[Joiner, 2018] Joiner, M. C. (2018). Linear energy transfer and relative biological effectiveness. In Joiner, M. C. and van der Kogel, A. J., editors of: *Basic Clinical Radiobiology (Fifth Edition)*. CRC Press, **68–77**

[Joiner et al., 2018] Joiner, M. C., van der Kogel, A. J., and Steel, G. G. (2018). Introduction: The significance of radiobiology and radiotherapy for cancer treatment. In Joiner, M. C. and van der Kogel, A. J., editors of: *Basic Clinical Radiobiology (Fifth Edition)*. CRC Press, **1–10**

[Kalholm et al., 2021] Kalholm, F., Grzanka, L., Traneus, E., and Bassler, N. (2021). A systematic review on the usage of averaged LET in radiation biology for particle therapy. *Radiotherapy and Oncology*, **161:211–221**

[Kanagavelu et al., 2014] Kanagavelu, S., Gupta, S., Wu, X., et al. (2014). In vivo effects of lattice radiation therapy on local and distant lung cancer: potential role of immunomodulation. *Radiat Res*, **182(2):149–162**

[Kanike et al., 2015] Kanike, V., Meesungnoen, J., and Jay-Gerin, J.-P. (2015). Acid spike effect in spurs/tracks of the low/high linear energy transfer radiolysis of water: potential implications for radiobiology. *RSC Adv.*, **5:43361–43370**

[Kanike et al., 2017] Kanike, V., Meesungnoen, J., Sanguanmith, S., et al. (2017). Generation of ultrafast transient acid spikes in high-temperature water irradiated with low linear energy transfer radiation. **6(1):31–40**

[Kaplan et al., 1990] Kaplan, I., Miterev, A., and Sukhonosov, V. (1990). Simulation of the primary stage of liquid water radiolysis. *International Journal of Radiation Applications and Instrumentation. Part C. Radiation Physics and Chemistry*, **36(3):493–498**

[Karamitros et al., 2014] Karamitros, M., Luan, S., Bernal, M., et al. (2014). Diffusion-controlled reactions modeling in Geant4-DNA. *Journal of Computational Physics*, **274:841–882**

[Kase et al., 2011] Kase, Y., Himukai, T., Nagano, A., et al. (2011). Preliminary calculation of RBE-weighted dose distribution for cerebral radionecrosis in carbon-ion treatment planning. *J Radiat Res*, **52(6):789–796**

[Kase et al., 2006] Kase, Y., Kanai, T., Matsumoto, Y., et al. (2006). Microdosimetric measurements and estimation of human cell survival for heavy-ion beams. *Radiat Res*, **166(4):629–638**

[Kase et al., 2013] Kase, Y., Yamashita, W., Matsufuji, N., et al. (2013). Microdosimetric calculation of relative biological effectiveness for design of therapeutic proton beams. *J Radiat Res*, **54(3):485–493**

[Khalifa et al., 2021] Khalifa, J., Mazieres, J., Gomez-Roca, C., et al. (2021). Radiotherapy in the Era of Immunotherapy With a Focus on Non-Small-Cell Lung Cancer: Time to Revisit Ancient Dogmas? *Front Oncol*, **11:662236**

[Khan and Gibbons, 2014a] Khan, F. and Gibbons, J. (2014). Chapter 2 - Nuclear Transformations. In *The Physics of Radiation Therapy (Fifth Edition)*. Lippincott Williams & Wilkins, **12–27**

[Khan and Gibbons, 2014b] Khan, F. and Gibbons, J. (2014). Chapter 26 - Image-Guided Radiation Therapy. In *The Physics of Radiation Therapy (Fifth Edition)*. Lippincott Williams & Wilkins, **510–523**

[Khan and Gibbons, 2014c] Khan, F. and Gibbons, J. (2014). Chapter 27 - Proton Beam Therapy. In *The Physics of Radiation Therapy (Fifth Edition)*. Lippincott Williams & Wilkins, **524–540**

[Khan and Gibbons, 2014d] Khan, F. and Gibbons, J. (2014). Chapter 4 - Clinical Radiation Generators. In *The Physics of Radiation Therapy (Fifth Edition)*. Lippincott Williams & Wilkins, **39–57**

[Khan and Gibbons, 2014e] Khan, F. and Gibbons, J. (2014). Chapter 5 - Interactions of Ionizing Radiation. In *The Physics of Radiation Therapy (Fifth Edition)*. Lippincott Williams & Wilkins, **58–74**

[Kim and Han, 2012] Kim, N. R. and Han, J. (2012). Pathologic review of cystic and cavitary lung diseases. *Korean J Pathol*, **46(5):407–414**

[Kim et al., 2019] Kim, W., Lee, S., Seo, D., et al. (2019). Cellular Stress Responses in Radiotherapy. *Cells*, **8(9):1105**

[Kłodowska et al., 2015] Kłodowska, M., Olko, P., and Waligórski, M. P. R. (2015). Proton microbeam radiotherapy with scanned pencil-beams–Monte Carlo simulations. *Phys Med*, **31(6):621–626**

[Knuth, 1997] Knuth, D. E. (1997). Chapter 4 - Arithmetic. In *The art of computer programming, volume 2 (3rd ed.): seminumerical algorithms*. Addison-Wesley Longman Publishing Co., Inc., **p232**

[Kokurewicz et al., 2021] Kokurewicz, K., Brunetti, E., Curcio, A., et al. (2021). An experimental study of focused very high energy electron beams for radiotherapy. *Communications Physics*, **4(1):33**

[Kokurewicz et al., 2019] Kokurewicz, K., Brunetti, E., Welsh, G. H., et al. (2019). Focused very high-energy electron beams as a novel radiotherapy modality for producing high-dose volumetric elements. *Scientific Reports*, **9(1):10837**

[Kreipl et al., 2009a] Kreipl, M. S., Friedland, W., and Paretzke, H. G. (2009). Interaction of ion tracks in spatial and temporal proximity. *Radiation and Environmental Biophysics*, **48(4):349–359**

[Kreipl et al., 2009b] Kreipl, M. S., Friedland, W., and Paretzke, H. G. (2009). Time- and space-resolved Monte Carlo study of water radiolysis for photon, electron and ion irradiation. *Radiat Environ Biophys*, **48(1):11–20**

[Kroemer et al., 2013] Kroemer, G., Galluzzi, L., Kepp, O., and Zitvogel, L. (2013). Immunogenic cell death in cancer therapy. *Annu Rev Immunol*, **31:51–72**

[Krupina et al., 2021] Krupina, K., Goginashvili, A., and Cleveland, D. W. (2021). Causes and consequences of micronuclei. *Curr Opin Cell Biol*, **70:91–99**

[Kundapur et al., 2022] Kundapur, V., Mayer, M., Auer, R. N., et al. (2022). Is Mini Beam Ready for Human Trials? Results of Randomized Study of Treating De-Novo Brain Tumors in Canines Using Linear Accelerator Generated Mini Beams. *Radiat Res*, **198(2):162–171**

[Kuo and Yang, 2008] Kuo, L. J. and Yang, L.-X. (2008). Gamma-H2AX - a novel biomarker for DNA double-strand breaks. *In Vivo*, **22(3):305–309**

[Kyriakou et al., 2019] Kyriakou, I., Ivanchenko, V., Sakata, D., et al. (2019). Influence of track structure and condensed history physics models of Geant4 to nanoscale electron transport in liquid water. *Phys Med*, **58:149–154**

[Kyriakou et al., 2022] Kyriakou, I., Sakata, D., Tran, H. N., et al. (2022). Review of the Geant4-DNA Simulation Toolkit for Radiobiological Applications at the Cellular and DNA Level. *Cancers*, **14(1)**

[Labate et al., 2020] Labate, L., Palla, D., Panetta, D., et al. (2020). Toward an effective use of laser-driven very high energy electrons for radiotherapy: Feasibility assessment of multi-field and intensity modulation irradiation schemes. *Sci Rep*, **10(1):17307**

[Lagzda, 2019] Lagzda, A. (2019). VHEE Radiotherapy Studies at CLARA and CLEAR facilities. *PhD thesis*, University of Manchester. **https://research.manchester.ac.uk/lagzda-vhee**

[Lagzda et al., 2020] Lagzda, A., Angal-Kalinin, D., Jones, J., et al. (2020). Influence of heterogeneous media on Very High Energy Electron (VHEE) dose penetration and a Monte Carlo-based comparison with existing radiotherapy modalities. *Nuclear Instruments and Methods in Physics Research Section B: Beam Interactions with Materials and Atoms*, **482:70–81**

[Laissue et al., 2013] Laissue, J. A., Bartzsch, S., Blattmann, H., et al. (2013). Response of the rat spinal cord to X-ray microbeams. *Radiother Oncol*, **106(1):106–111**

[Laissue et al., 2012] Laissue, J. A., Blattmann, H., and Slatkin, D. N. (2012). Alban Köhler (1874-1947): Inventor of grid therapy. *Zeitschrift für Medizinische Physik*, **22(2):90–99**

[Laissue et al., 1998] Laissue, J. A., Geiser, G., Spanne, P. O., et al. (1998). Neuropathology of ablation of rat gliosarcomas and contiguous brain tissues using a microplanar beam of synchrotron-wiggler-generated X rays. *Int J Cancer*, **78(5):654–660**

[Lam et al., 2015] Lam, R. K. K., Fung, Y. K., Han, W., and Yu, K. N. (2015). Rescue effects: irradiated cells helped by unirradiated bystander cells. *Int J Mol Sci*, **16(2):2591–2609**

[Lamirault et al., 2020a] Lamirault, C., Brisebard, E., Patriarca, A., et al. (2020). Spatially Modulated Proton Minibeams Results in the Same Increase of Lifespan as a Uniform Target Dose Coverage in F98-Glioma-Bearing Rats. *Radiat Res*, **194(6):715–723**

[Lamirault et al., 2020b] Lamirault, C., Doyère, V., Juchaux, M., et al. (2020). Short and long-term evaluation of the impact of proton minibeam radiation therapy on motor, emotional and cognitive functions. *Sci Rep*, **10(1):13511**

[Lansonneur et al., 2020] Lansonneur, P., Mammar, H., Nauraye, C., et al. (2020). First proton minibeam radiation therapy treatment plan evaluation. *Sci Rep*, **10(1):7025**

[LaVerne, 2004] LaVerne, J. A. (2004). Chapter 14 - Radiation Chemical Effects of Heavy Ions. In Mozumder, A. and Hatano, Y., editors of: *Charged Particle and Photon interactions with Matter: Chemical, Physiocochemical, and Biological Consequences with Applications (First Edition)*. CRC Press, **406–433**

[Le Caër, 2011] Le Caër, S. (2011). Water Radiolysis: Influence of Oxide Surfaces on H_2 Production under Ionizing Radiation. *Water*, **3(1):235–253**

[Ledo et al., 2022] Ledo, A., Fernandes, E., Salvador, A., et al. (2022). In vivo hydrogen peroxide diffusivity in brain tissue supports volume signaling activity. *Redox Biology*, **50:102250**

[Lee et al., 2016] Lee, E., Meyer, J., and Sandison, G. (2016). Collimator design for spatially-fractionated proton beams for radiobiology research. *Phys Med Biol*, **61(14):5378–5389**

[Lennicke et al., 2015] Lennicke, C., Rahn, J., Lichtenfels, R., et al. (2015). Hydrogen peroxide – production, fate and role in redox signaling of tumor cells. *Cell Communication and Signaling*, **13(1):39**

[Leo, 1994] Leo, W. R. (1994). 2. Passage of Radiation Through Matter. In *Techniques for Nuclear and Particle Physics Experiments*. Springer, **17–65**

[Liamsuwan et al., 2014] Liamsuwan, T., Hultqvist, M., Lindborg, L., et al. (2014). Microdosimetry of proton and carbon ions. *Med Phys*, **41(8):081721**

[Lim et al., 2015] Lim, J. B., Huang, B. K., Deen, W. M., and Sikes, H. D. (2015). Analysis of the lifetime and spatial localization of hydrogen peroxide generated in the cytosol using a reduced kinetic model. *Free Radic Biol Med*, **89:47–53**

[Liu et al., 2019] Liu, H., Li, Z., Slopsema, R., et al. (2019). TOPAS Monte Carlo simulation for double scattering proton therapy and dosimetric evaluation. *Phys Med*, **62:53–62**

[Lobachevsky et al., 2021] Lobachevsky, P., Forrester, H. B., Ivashkevich, A., et al. (2021). Synchrotron X-Ray Radiation-Induced Bystander Effect: An Impact of the Scattered Radiation, Distance From the Irradiated Site and p53 Cell Status. *Front Oncol*, **11:685598**

[Lobachevsky et al., 2015] Lobachevsky, P., Ivashkevich, A., Forrester, H. B., et al. (2015). Assessment and Implications of Scattered Microbeam and Broadbeam Synchrotron Radiation for Bystander Effect Studies. *Radiat Res*, **184(6):650–659**

[Lu and Flanz, 2020] Lu, H.-M. and Flanz, J. (2020). Chapter 4 - Characteristics of Clinical Proton Beams. In Paganetti, H., editor of: *Proton Therapy Physics*. CRC Press, **103–124**

[Ma et al., 2018] Ma, J., Wang, F., and Mostafavi, M. (2018). Ultrafast Chemistry of Water Radical Cation, $H_2O^{\bullet+}$, in Aqueous Solutions. *Molecules*, **23(2):244**

[Macchi et al., 2013] Macchi, A., Borghesi, M., and Passoni, M. (2013). Ion acceleration by superintense laser-plasma interaction. *Rev. Mod. Phys.*, **85:751–793**

[MacFadden et al., 2018] MacFadden, N., Peggs, S., and Gulliford, C. (2018). Development and validation of a Geant4 radiation shielding simulation framework. Technical report, Brookhaven National Laboratory

[Mackie, 2006] Mackie, T. R. (2006). History of tomotherapy. *Phys Med Biol*, **51(13):R427–53**

[Mairani et al., 2017] Mairani, A., Magro, G., Tessonnier, T., et al. (2017). Optimizing the modified microdosimetric kinetic model input parameters for proton and (4)He ion beam therapy application. *Phys Med Biol*, **62(11):N244–N256**

[Mairani et al., 2022] Mairani, A., Mein, S., Blakely, E., et al. (2022). Roadmap: helium ion therapy. *Phys Med Biol*, **67(15)**

[Malouff et al., 2020] Malouff, T. D., Mahajan, A., Krishnan, S., et al. (2020). Carbon Ion Therapy: A Modern Review of an Emerging Technology. *Front Oncol*, **10:00082**

[Manchado de Sola et al., 2018] Manchado de Sola, F., Vilches, M., Prezado, Y., and Lallena, A. M. (2018). Impact of cardiosynchronous brain pulsations on Monte Carlo calculated doses for synchrotron micro- and minibeam radiation therapy. *Med Phys*, **45(7):3379–3390**

[Mancusi et al., 2014] Mancusi, D., Boudard, A., Cugnon, J., et al. (2014). Extension of the Liège intranuclear-cascade model to reactions induced by light nuclei. *Phys. Rev. C*, **90:054602**

[Manti et al., 2017] Manti, L., Perozziello, F., Borghesi, M., et al. (2017). The radiobiology of laser-driven particle beams: focus on sub-lethal responses of normal human cells. *Journal of Instrumentation*, **12(03):C03084**

[Marks, 1952] Marks, H. (1952). Clinical Experience with Irradiation Through a Grid. *Radiology*, **58(3):338–342**

[Martínez-Rovira et al., 2015] Martínez-Rovira, I., Fois, G., and Prezado, Y. (2015). Dosimetric evaluation of new approaches in GRID therapy using nonconventional radiation sources. *Med Phys*, **42(2):685–693**

[Martínez-Rovira et al., 2017a] Martínez-Rovira, I., González, W., Brons, S., and Prezado, Y. (2017). Carbon and oxygen minibeam radiation therapy: An experimental dosimetric evaluation. *Med Phys*, **44(8):4223–4229**

[Martínez-Rovira et al., 2017b] Martínez-Rovira, I., Puxeu-Vaqué, J., and Prezado, Y. (2017). Dose evaluation of Grid Therapy using a 6 MV flattening filter-free (FFF) photon beam: A Monte Carlo study. *Med Phys*, **44(10):5378–5383**

[Masilela et al., 2021] Masilela, T. A. M., Delorme, R., and Prezado, Y. (2021). Dosimetry and radioprotection evaluations of very high energy electron beams. *Sci Rep*, **11(1):20184**

[Masilela and Prezado, 2023] Masilela, T. A. M. and Prezado, Y. (2023). Monte Carlo study of the free radical yields in minibeam radiation therapy. *Med Phys*, **50(8):5115–5134**

[Mattiuzzi and Lippi, 2019] Mattiuzzi, C. and Lippi, G. (2019). Current Cancer Epidemiology. *J Epidemiol Glob Health*, **9(4):217–222**

[Maxim et al., 2019] Maxim, P. G., Tantawi, S. G., and Loo, B. W. J. (2019). PHASER: A platform for clinical translation of FLASH cancer radiotherapy. *Radiother Oncol*, **139:28–33**

[Mayerhofer et al., 2021] Mayerhofer, M., Datzmann, G., Degiovanni, A., et al. (2021). Magnetically focused 70 MeV proton minibeams for preclinical experiments combining a tandem accelerator and a 3 GHz linear post-accelerator. *Med Phys*, **48(6):2733–2749**

[Mayr et al., 2023] Mayr, N. A., Mohiuddin, M., Snider, J. W., et al. (2023). Practice Patterns of Spatially Fractionated Radiation Therapy: A Clinical Practice Survey. *Advances in Radiation Oncology*, **101308**

[McMahon, 2018] McMahon, S. J. (2018). The linear quadratic model: usage, interpretation and challenges. *Phys Med Biol*, **64(1):01TR01**

[McMahon et al., 2018] McMahon, S. J., Paganetti, H., and Prise, K. M. (2018). LET-weighted doses effectively reduce biological variability in proton radiotherapy planning. *Phys Med Biol*, **63(22):225009**

[McManus et al., 2020] McManus, M., Romano, F., Lee, N. D., et al. (2020). The challenge of ionisation chamber dosimetry in ultra-short pulsed high dose-rate Very High Energy Electron beams. *Sci Rep*, **10(1):9089**

[Meesungnoen and Jay-Gerin, 2005] Meesungnoen, J. and Jay-Gerin, J.-P. (2005). High-LET radiolysis of liquid water with 1H+, 4He2+, 12C6+, and 20Ne9+ ions: effects of multiple ionization. *J Phys Chem A*, **109(29):6406–6419**

[Meesungnoen and Jay-Gerin, 2009] Meesungnoen, J. and Jay-Gerin, J.-P. (2009). High-LET ion radiolysis of water: oxygen production in tracks. *Radiat Res*, **171(3):379–386**

[Meesungnoen and Jay-Gerin, 2011] Meesungnoen, J. and Jay-Gerin, J. P. (2011). Chapter 14 - Radiation Chemistry of Liquid Water with Heavy Ions: Monte Carlo Simulation Studies. In Hatano, Y., Katsumura, Y., and Mozumder, A., editors of: *Charged Particle and Photon interactions with Matter: Recent Adcances, Applications, and Interfaces (First Edition)*. CRC Press, **355–400**

[Mehnati et al., 2005] Mehnati, P., Morimoto, S., Yatagai, F., et al. (2005). Exploration of "over kill effect" of high-LET Ar- and Fe-ions by evaluating the fraction of non-hit cell and interphase death. *J Radiat Res*, **46(3):343–350**

[Meigooni et al., 2006] Meigooni, A. S., Dou, K., Meigooni, N. J., et al. (2006). Dosimetric characteristics of a newly designed grid block for megavoltage photon radiation and its therapeutic advantage using a linear quadratic model. *Med Phys*, **33(9):3165–3173**

[Meng et al., 2018] Meng, L., Cheng, Y., Tong, X., et al. (2018). Tumor Oxygenation and Hypoxia Inducible Factor-1 Functional Inhibition via a Reactive Oxygen Species Responsive Nanoplatform for Enhancing Radiation Therapy and Abscopal Effects. *ACS Nano*, **12(8):8308–8322**

[Meyer et al., 2019] Meyer, J., Eley, J., Schmid, T. E., et al. (2019). Spatially fractionated proton minibeams. *Br J Radiol*, **92(1095):20180466**

[Meyer et al., 2023] Meyer, J., Prezado, Y., Zhang, H., and Mayr, N. A. (2023). Glossary of spatially fractionated and FLASH radiation therapy. In Zhang, H. and Mayr, N. A., editors of: *Spatially Fractionated, Microbeam and FLASH Radiation Therapy*. IOP Publishing, **25–1 to 25–5**

[Meyer et al., 2017] Meyer, J., Stewart, R. D., Smith, D., et al. (2017). Biological and dosimetric characterisation of spatially fractionated proton minibeams. *Phys Med Biol*, **62(24):9260–9281**

[Michalik et al., 1998] Michalik, V., Begusová, M., and Bigildeev, E. A. (1998). Computer-aided stochastic modeling of the radiolysis of liquid water. *Radiat Res*, **149(3):224–236**

[Miller et al., 2022] Miller, C. E., Xu, F., Zhao, Y., et al. (2022). Hydrogen Peroxide Promotes the Production of Radiation-Derived EVs Containing Mitochondrial Proteins. *Antioxidants*, **11(11)**

[Miller et al., 2010] Miller, E. W., Dickinson, B. C., and Chang, C. J. (2010). Aquaporin-3 mediates hydrogen peroxide uptake to regulate downstream intracellular signaling. *Proc Natl Acad Sci U S A*, **107(36):15681–15686**

[Miura et al., 2006] Miura, M., Blattmann, H., Bräuer-Krisch, E., et al. (2006). Radiosurgical palliation of aggressive murine SCCVII squamous cell carcinomas using synchrotron-generated X-ray microbeams. *Br J Radiol*, **79(937):71–75**

[Mohiuddin et al., 1990] Mohiuddin, M., Curtis, D. L., Grizos, W. T., and Komarnicky, L. (1990). Palliative treatment of advanced cancer using multiple nonconfluent pencil beam radiation. A pilot study. *Cancer*, **66(1):114–118**

[Mohiuddin et al., 1996] Mohiuddin, M., Stevens, J. H., Reiff, J. E., et al. (1996). Spatially fractionated (GRID) radiation for palliative treatment of advanced cancer. *Radiation Oncology Investigations*, **4(1):41–47**

[Montay-Gruel et al., 2019] Montay-Gruel, P., Acharya, M. M., Petersson, K., et al. (2019). Long-term neurocognitive benefits of FLASH radiotherapy driven by reduced reactive oxygen species. *Proc Natl Acad Sci U S A*, **116(22):10943–10951**

[Moorrees and Bezak, 2012] Moorrees, J. and Bezak, E. (2012). Four dimensional radiotherapy: a review of current technologies and modalities. *Australasian Physical & Engineering Sciences in Medicine*, **35(4):399–406**

[Moraru et al., 2008] Moraru, I. I., Schaff, J. C., Slepchenko, B. M., et al. (2008). Virtual Cell modelling and simulation software environment. *IET Syst Biol*, **2(5):352–362**

[Morgan and Liu, 2011] Morgan, M. J. and Liu, Z.-g. (2011). Crosstalk of reactive oxygen species and NF-κB signaling. *Cell Res*, **21(1):103–115**

[Moskvin et al., 2010] Moskvin, V., Salvat, F., Stewart, D. K., and DesRosiers, C. M. (2010). PENELOPE Monte Carlo engine for treatment planning in radiation therapy with Very High Energy Electrons (VHEE) of 150–250 MeV. In *IEEE Nuclear Science Symposuim Medical Imaging Conference*, 1961–1966

[Mothersill and Seymour, 1997] Mothersill, C. and Seymour, C. (1997). Medium from irradiated human epithelial cells but not human fibroblasts reduces the clonogenic survival of unirradiated cells. *Int J Radiat Biol*, **71(4):421–427**

[Mozumder and Magee, 1966] Mozumder, A. and Magee, J. L. (1966). Model of Tracks of Ionizing Radiations for Radical Reaction Mechanisms. *Radiation Research*, **28(2):203–214**

[Mueller et al., 2018] Mueller, S., Fix, M. K., Henzen, D., et al. (2018). Electron beam collimation with a photon MLC for standard electron treatments. *Physics in Medicine & Biology*, **63(2):025017**

[Munro and Gilbert, 1961] Munro, T. R. and Gilbert, C. W. (1961). The relation between tumour lethal doses and the radiosensitivity of tumour cells. *Br J Radiol*, **34(400):246–251**

[Muth et al., 1977] Muth, C. P., Salewski, D., Glaser, F. H., and Heider, K. M. (1977). Grid method in telecobalt therapy. *Radiobiol Radiother (Berl)*, **18(6):691–699**

[Nabrinsky et al., 2022] Nabrinsky, E., Macklis, J., and Bitran, J. (2022). A Review of the Abscopal Effect in the Era of Immunotherapy. *Cureus*, **14(9):e29620**

[Nagasawa and Little, 1992] Nagasawa, H. and Little, J. B. (1992). Induction of sister chromatid exchanges by extremely low doses of alpha-particles. *Cancer Res*, **52(22):6394–6396**

[Nakajima et al., 2015] Nakajima, K., Yuan, J., Chen, L., and Sheng, Z. (2015). Laser-Driven Very High Energy Electron/Photon Beam Radiation Therapy in Conjunction with a Robotic System. *Applied Sciences*, **5(1):1–20**

[Nakaoka et al., 2021] Nakaoka, A., Nakahana, M., Inubushi, S., et al. (2021). Exosome-mediated radiosensitizing effect on neighboring cancer cells via increase in intracellular levels of reactive oxygen species. *Oncol Rep*, **45(4)**

[Nardone et al., 2022] Nardone, V., D'Ippolito, E., Grassi, R., et al. (2022). Non-Oncological Radiotherapy: A Review of Modern Approaches. *Journal of Personalized Medicine*, **12(10):1677**

[Naseri and Mesbahi, 2010] Naseri, A. and Mesbahi, A. (2010). A review on photoneutrons characteristics in radiation therapy with high-energy photon beams. *Rep Pract Oncol Radiother*, **15(5):138–144**

[Neuner et al., 2012] Neuner, G., Mohiuddin, M. M., Vander Walde, N., et al. (2012). High-dose spatially fractionated GRID radiation therapy (SFGRT): a comparison of treatment outcomes with Cerrobend vs. MLC SFGRT. *Int J Radiat Oncol Biol Phys*, **82(5):1642–1649**

[Ng et al., 2013] Ng, W.-L., Huang, Q., Liu, X., et al. (2013). Molecular mechanisms involved in tumor repopulation after radiotherapy. *Transl Cancer Res*, **2(5):442–448**

[Ngwa et al., 2018] Ngwa, W., Irabor, O. C., Schoenfeld, J. D., et al. (2018). Using immunotherapy to boost the abscopal effect. *Nature Reviews Cancer*, **18(5):313–322**

[Nikjoo et al., 2006] Nikjoo, H., Uehara, S., Emfietzoglou, D., and Cucinotta, F. (2006). Track-structure codes in radiation research. *Radiation Measurements*, **41(9):1052–1074**

[Omran, 2005] Omran, A. R. (2005). The epidemiologic transition: a theory of the epidemiology of population change. 1971. *Milbank Q*, **83(4):731–757**

[OpenGATE Collaboration, 2023] OpenGATE Collaboration (2023). GATE documentation. **OpenGATE Collaboration**. Accessed August 14, 2023

[Orgogozo et al., 2016] Orgogozo, V., Peluffo, A., and Morizot, B. (2016). Chapter One - The "Mendelian Gene" and the "Molecular Gene": Two Relevant Concepts of Genetic Units. In Orgogozo, V., editor of: *Genes and Evolution*, volume 119 of *Current Topics in Developmental Biology*. Academic Press, **1–26**

[Ortiz, 2022] Ortiz, R. (2022). Dosimetric studies for proton minibeam radiation therapy. *PhD thesis*, Université Paris-Saclay. **https://theses.hal.science/tel-03957981**

[Ortiz et al., 2021] Ortiz, R., De Marzi, L., and Prezado, Y. (2021). Proton Minibeam Radiation Therapy and Arc Therapy: Proof of Concept of a Winning Alliance. *Cancers (Basel)*, **14(1):116**

[Ortiz et al., 2022] Ortiz, R., De Marzi, L., and Prezado, Y. (2022). Preclinical dosimetry in proton minibeam radiation therapy: Robustness analysis and guidelines. *Medical Physics*, **49(8):5551–5561**

[Padilla-Cabal et al., 2020] Padilla-Cabal, F., Alejandro Fragoso, J., Franz Resch, A., et al. (2020). Benchmarking a GATE/Geant4 Monte Carlo model for proton beams in magnetic fields. *Med Phys*, **47(1):223–233**

[Paganetti, 2020] Paganetti, H. (2020). Chapter 1 - Proton Therapy: History and Rationale. In Paganetti, H., editor of: *Proton Therapy Physics*. CRC Press, **1–18**

[Paganetti et al., 2002] Paganetti, H., Niemierko, A., Ancukiewicz, M., et al. (2002). Relative biological effectiveness (RBE) values for proton beam therapy. *Int J Radiat Oncol Biol Phys*, **53(2):407–421**

[Pajonk et al., 2010] Pajonk, F., Vlashi, E., and McBride, W. H. (2010). Radiation resistance of cancer stem cells: the 4 R's of radiobiology revisited. *Stem Cells*, **28(4):639–648**

[Pakniyat et al., 2020] Pakniyat, F., Nedaie, H. A., Mozdarani, H., et al. (2020). Enhanced response of radioresistant carcinoma cell line to heterogeneous dose distribution of grid; the role of high-dose bystander effect. *Int J Radiat Biol*, **96(12):1585–1596**

[Papiez et al., 2002] Papiez, L., DesRosiers, C., and Moskvin, V. (2002). Very high energy electrons (50-250 MeV) and radiation therapy. *Technol Cancer Res Treat*, **1(2):105–110**

[Pelliccioni, 2000] Pelliccioni, M. (2000). Overview of Fluence-to-Effective Dose and Fluence-to-Ambient Dose Equivalent Conversion Coefficients for High Energy Radiation Calculated Using the FLUKA Code. *Radiation Protection Dosimetry*, **88(4):279–297**

[Peñagarícano et al., 2010] Peñagarícano, J. A., Moros, E. G., Ratanatharathorn, V., et al. (2010). Evaluation of spatially fractionated radiotherapy (GRID) and definitive chemoradiotherapy with curative intent for locally advanced squamous cell carcinoma of the head and neck: initial response rates and toxicity. *Int J Radiat Oncol Biol Phys*, **76(5):1369–1375**

[Perl et al., 2012] Perl, J., Shin, J., Schümann, J., et al. (2012). TOPAS: An innovative proton Monte Carlo platform for research and clinical applications. *Med Phys*, **39(11):6818–6837**

[Peucelle, 2016] Peucelle, C. (2016). Spatial fractionation of the dose in charged particle therapy. *PhD thesis*, Université Paris-Saclay. **https://theses.hal.science/tel-01432875**

[Peucelle et al., 2015a] Peucelle, C., Martínez-Rovira, I., and Prezado, Y. (2015). Spatial fractionation of the dose using neon and heavier ions: A Monte Carlo study. *Med Phys*, **42(10):5928–5936**

[Peucelle et al., 2015b] Peucelle, C., Nauraye, C., Patriarca, A., et al. (2015). Proton minibeam radiation therapy: Experimental dosimetry evaluation. *Med Phys*, **42(12):7108–7113**

[Pham-Huy et al., 2008] Pham-Huy, L. A., He, H., and Pham-Huy, C. (2008). Free radicals, antioxidants in disease and health. *Int J Biomed Sci*, **4(2):89–96**

[Phillips, 2016] Phillips, D. (2016). A lifetime in photochemistry; some ultrafast measurements on singlet states. *Proceedings of the Royal Society A: Mathematical, Physical and Engineering Sciences*, **472(2190):20160102**

[Pimblott, 1992] Pimblott, S. M. (1992). Investigation of various factors influencing the effect of scavengers on the radiation chemistry following the high-energy electron radiolysis of water. *The Journal of Physical Chemistry*, **96(11):4485–4491**

[Plante, 2010] Plante, I. (2010). Radiation chemistry and oxidative stress. *The National Aeronqutics and Space Administration (NASA)*. **RadiationChemistry**. Accessed June 21, 2023

[Plante, 2011] Plante, I. (2011). A Monte-Carlo step-by-step simulation code of the non-homogeneous chemistry of the radiolysis of water and aqueous solutions. Part I: theoretical framework and implementation. *Radiat Environ Biophys*, **50(3):389–403**

[Plante and Cucinotta, 2009] Plante, I. and Cucinotta, F. A. (2009). Cross sections for the interactions of 1 eV-100 MeV electrons in liquid water and application to Monte-Carlo simulation of HZE radiation tracks. *New Journal of Physics*, **11(6):063047**

[Platzman, 1955] Platzman, R. L. (1955). Subexcitation Electrons. *Radiation Research*, **2(1):1–7**

[Podgorsak, 2005] Podgorsak, E. B. (2005). Chapter 5. Treatment Machines for External Beam Radiotherapy. In Podgorsak, E. B., editor of: *Radiation Oncology Physics: A Handbook for Teachers and Students*. International Atomic Energy Agency, Vienna, **123–160**

[Podgorsak and Podgorsak, 2005] Podgorsak, E. B. and Podgorsak, M. B. (2005). Chapter 15. Special Procedures and Techniques in Radiotherapy. In Podgorsak, E. B., editor of: *Radiation Oncology Physics: A Handbook for Teachers and Students*. International Atomic Energy Agency, Vienna, **505–548**

[Pollard et al., 2017] Pollard, T. D., Earnshaw, W. C., Lippincott-Schwartz, J., and Johnson, G. T. (2017). Chapter 1 - Introduction to Cells. In *Cell Biology (Third Edition)*. Elsevier, **3–14**

[Pommarel et al., 2017] Pommarel, L., Vauzour, B., Mégnin-Chanet, F., et al. (2017). Spectral and spatial shaping of a laser-produced ion beam for radiation-biology experiments. *Phys. Rev. Accel. Beams*, **20:032801**

[Potez et al., 2019] Potez, M., Fernandez-Palomo, C., Bouchet, A., et al. (2019). Synchrotron Microbeam Radiation Therapy as a New Approach for the Treatment of Radioresistant Melanoma: Potential Underlying Mechanisms. *Int J Radiat Oncol Biol Phys*, **105(5):1126–1136**

[Pouget et al., 2018] Pouget, J.-P., Georgakilas, A. G., and Ravanat, J.-L. (2018). Targeted and Off-Target (Bystander and Abscopal) Effects of Radiation Therapy: Redox Mechanisms and Risk/Benefit Analysis. *Antioxid Redox Signal*, **29(15):1447–1487**

[Prasanna et al., 2014] Prasanna, A., Ahmed, M. M., Mohiuddin, M., and Coleman, C. N. (2014). Exploiting sensitization windows of opportunity in hyper and hypo-fractionated radiation therapy. *J Thorac Dis*, **6(4):287–302**

[Prezado, 2022] Prezado, Y. (2022). Divide and conquer: spatially fractionated radiation therapy. *Expert Reviews in Molecular Medicine*, **24:e3**

[Prezado et al., 2015] Prezado, Y., Deman, P., Varlet, P., et al. (2015). Tolerance to Dose Escalation in Minibeam Radiation Therapy Applied to Normal Rat Brain: Long-Term Clinical, Radiological and Histopathological Analysis. *Radiat Res*, **184(3):314–321**

[Prezado et al., 2017a] Prezado, Y., Dos Santos, M., Gonzalez, W., et al. (2017). Transfer of Minibeam Radiation Therapy into a cost-effective equipment for radiobiological studies: a proof of concept. *Sci Rep*, **7(1):17295**

[Prezado and Fois, 2013] Prezado, Y. and Fois, G. R. (2013). Proton-minibeam radiation therapy: a proof of concept. *Med Phys*, **40(3):031712**

[Prezado et al., 2021] Prezado, Y., Hirayama, R., Matsufuji, N., et al. (2021). A Potential Renewed Use of Very Heavy Ions for Therapy: Neon Minibeam Radiation Therapy. *Cancers (Basel)*, **13(6):1356**

[Prezado et al., 2019] Prezado, Y., Jouvion, G., Guardiola, C., et al. (2019). Tumor Control in RG2 Glioma-Bearing Rats: A Comparison Between Proton Minibeam Therapy and Standard Proton Therapy. *International Journal of Radiation Oncology, Biology, Physics*, **104(2):266–271**

[Prezado et al., 2017b] Prezado, Y., Jouvion, G., Hardy, D., et al. (2017). Proton minibeam radiation therapy spares normal rat brain: Long-Term Clinical, Radiological and Histopathological Analysis. *Sci Rep*, **7(1):14403**

[Prezado et al., 2018] Prezado, Y., Jouvion, G., Patriarca, A., et al. (2018). Proton minibeam radiation therapy widens the therapeutic index for high-grade gliomas. *Scientific Reports*, **8(1):16479**

[Prezado et al., 2011] Prezado, Y., Martínez-Rovira, I., Thengumpallil, S., and Deman, P. (2011). Dosimetry protocol for the preclinical trials in white-beam minibeam radiation therapy. *Medical Physics*, **38(9):5012–5020**

[Prezado et al., 2012] Prezado, Y., Sarun, S., Gil, S., et al. (2012). Increase of lifespan for glioma-bearing rats by using minibeam radiation therapy. *J Synchrotron Radiat*, **19:60–65**

[Prezado et al., 2009] Prezado, Y., Thengumpallil, S., Renier, M., and Bravin, A. (2009). X-ray energy optimization in minibeam radiation therapy. *Med Phys*, **36(11):4897–4902**

[Price et al., 2021] Price, L. S. L., Rivera, J. N., Madden, A. J., et al. (2021). Minibeam radiation therapy enhanced tumor delivery of PEGylated liposomal doxorubicin in a triple-negative breast cancer mouse model. *Ther Adv Med Oncol*, **13:17588359211053700**

[Putnam, 2012] Putnam, R. W. (2012). Chapter 17 - Intracellular pH Regulation. In Sperelakis, N., editor of: *Cell Physiology Source Book (Fourth Edition)*. Academic Press, San Diego, **303–321**

[Ramos-Méndez et al., 2020a] Ramos-Méndez, J., Domínguez-Kondo, N., Schuemann, J., et al. (2020). LET-Dependent Intertrack Yields in Proton Irradiation at Ultra-High Dose Rates Relevant for FLASH Therapy. *Radiat Res*, **194(4):351–362**

[Ramos-Méndez et al., 2021] Ramos-Méndez, J., LaVerne, J. A., Domínguez-Kondo, N., et al. (2021). TOPAS-nBio validation for simulating water radiolysis and DNA damage under low-LET irradiation. *Phys Med Biol*, **66(17):175026**

[Ramos-Méndez et al., 2018] Ramos-Méndez, J., Perl, J., Schuemann, J., et al. (2018). Monte Carlo simulation of chemistry following radiolysis with TOPAS-nBio. *Phys Med Biol*, **63(10):105014**

[Ramos-Méndez et al., 2020b] Ramos-Méndez, J., Shin, W.-G., Karamitros, M., et al. (2020). Independent reaction times method in Geant4-DNA: Implementation and performance. *Med Phys*, **47(11):5919–5930**

[Ranji-Burachaloo et al., 2018] Ranji-Burachaloo, H., Gurr, P. A., Dunstan, D. E., and Qiao, G. G. (2018). Cancer Treatment through Nanoparticle-Facilitated Fenton Reaction. *ACS Nano*, **12(12):11819–11837**

[Reda et al., 2020] Reda, M., Bagley, A. F., Zaidan, H. Y., and Yantasee, W. (2020). Augmenting the therapeutic window of radiotherapy: A perspective on molecularly targeted therapies and nanomaterials. *Radiother Oncol*, **150:225–235**

[Regnard et al., 2008] Regnard, P., Duc, G. L., Bräuer-Krisch, E., et al. (2008). Irradiation of intracerebral 9L gliosarcoma by a single array of microplanar x-ray beams from a synchrotron: balance between curing and sparing. *Physics in Medicine & Biology*, **53(4):861**

[Risse, 1929] Risse, O. (1929). Mechanism of the chemical action of x-rays in aqueous solutions. *Strahlentherapie*, **34:578–581**

[Rivera et al., 2020] Rivera, J. N., Kierski, T. M., Kasoji, S. K., et al. (2020). Conventional dose rate spatially-fractionated radiation therapy (SFRT) treatment response and its association with dosimetric parameters-A preclinical study in a Fischer 344 rat model. *PLoS One*, **15(6):e0229053**

[Rockwell, 2003] Rockwell, S. (2003). The life and legacy of Marie Curie. *Yale J Biol Med*, **76(4-6):167–180**

[Ronga et al., 2021] Ronga, M. G., Cavallone, M., Patriarca, A., et al. (2021). Back to the Future: Very High-Energy Electrons (VHEEs) and Their Potential Application in Radiation Therapy. *Cancers (Basel)*, **13(19):4942**

[Roots and Okada, 1975] Roots, R. and Okada, S. (1975). Estimation of Life Times and Diffusion Distances of Radicals Involved in X-Ray-Induced DNA Strand Breaks or Killing of Mammalian Cells. **64(2):306–320**

[Rubini et al., 2014] Rubini, G., Nicoletti, A., Rubini, D., and Asabella, A. N. (2014). Radiometabolic Treatment of Bone-Metastasizing Cancer: From ^{186}Rhenium to ^{223}Radium. *Cancer Biotherapy and Radiopharmaceuticals*, **29(1):1–11**

[Rückert et al., 2021] Rückert, M., Flohr, A.-S., Hecht, M., and Gaipl, U. S. (2021). Radiotherapy and the immune system: More than just immune suppression. *Stem Cells*, **39(9):1155–1165**

[Ruddon, 2007] Ruddon, R. W. (2007). Characteristics of Human Cancer. In *Cancer Biology (Fourth Edition)*. Oxford University Press, USA, **3–16**

[Sabatasso et al., 2011] Sabatasso, S., Laissue, J. A., Hlushchuk, R., et al. (2011). Microbeam radiation-induced tissue damage depends on the stage of vascular maturation. *Int J Radiat Oncol Biol Phys*, **80(5):1522–1532**

[Saha, 2013] Saha, G. B. (2013). Chapter 15 - Radiation Biology. In *Physics and Radiobiology of Nuclear Medicine (Fourth Edition)*. Springer New York, New York, NY, **263–299**

[Sammer et al., 2021] Sammer, M., Girst, S., and Dollinger, G. (2021). Optimizing proton minibeam radiotherapy by interlacing and heterogeneous tumor dose on the basis of calculated clonogenic cell survival. *Scientific Reports*, **11(1):3533**

[Sammer et al., 2019] Sammer, M., Teiluf, K., Girst, S., et al. (2019). Beam size limit for pencil minibeam radiotherapy determined from side effects in an in-vivo mouse ear model. *PLoS One*, **14(9):e0221454**

[Sarrut et al., 2014] Sarrut, D., Bardiès, M., Boussion, N., et al. (2014). A review of the use and potential of the GATE Monte Carlo simulation code for radiation therapy and dosimetry applications. *Med Phys*, **41(6):064301**

[Sato et al., 2019] Sato, K., Shimokawa, T., and Imai, T. (2019). Difference in Acquired Radioresistance Induction Between Repeated Photon and Particle Irradiation. *Front Oncol*, **9:01213**

[Schippers, 2020] Schippers, M. (2020). Chapter 3 - Proton Accelerators. In Paganetti, H., editor of: *Proton Therapy Physics*. CRC Press, **62–102**

[Schmidtlein et al., 2006] Schmidtlein, C. R., Kirov, A. S., Nehmeh, S. A., et al. (2006). Validation of GATE Monte Carlo simulations of the GE Advance/Discovery LS PET scanners. *Med Phys*, **33(1):198–208**

[Schneider, 2020] Schneider, T. (2020). Advancing the generation of proton minibeams for radiation therapy. *PhD thesis*, Université Paris-Saclay. **https://theses.hal.science/tel-03105944**

[Schneider, 2022] Schneider, T. (2022). Technical aspects of proton minibeam radiation therapy: Minibeam generation and delivery. *Phys Med*, **100:64–71**

[Schneider et al., 2020] Schneider, T., De Marzi, L., Patriarca, A., and Prezado, Y. (2020). Advancing proton minibeam radiation therapy: magnetically focussed proton minibeams at a clinical centre. *Scientific Reports*, **10(1):1384**

[Schneider et al., 2021] Schneider, T., De Marzi, L., Patriarca, A., and Prezado, Y. (2021). Monte Carlo Comparison of Proton and Helium-ion Minibeam Generation Techniques. *Front Phys*, **9:595721**

[Schneider et al., 2022] Schneider, T., Fernandez-Palomo, C., Bertho, A., et al. (2022). Combining FLASH and spatially fractionated radiation therapy: The best of both worlds. *Radiotherapy and Oncology*, **175:169–177**

[Schneider et al., 2023] Schneider, T., Malaise, D., Pouzoulet, F., and Prezado, Y. (2023). Orthovoltage X-ray Minibeam Radiation Therapy for the Treatment of Ocular Tumours-An In Silico Evaluation. *Cancers (Basel)*, **15(3):679**

[Schneider et al., 2019] Schneider, T., Patriarca, A., and Prezado, Y. (2019). Improving the dose distributions in minibeam radiation therapy: Helium ions vs protons. *Med Phys*, **46(8):3640–3648**

[Schneider et al., 2002] Schneider, U., Agosteo, S., Pedroni, E., and Besserer, J. (2002). Secondary neutron dose during proton therapy using spot scanning. *Int J Radiat Oncol Biol Phys*, **53(1):244–251**

[Schuemann et al., 2018a] Schuemann, J., McNamara, A. L., Ramos-Méndez, J., et al. (2018). TOPAS-nBio: An Extension to the TOPAS Simulation Toolkit for Cellular and Sub-cellular Radiobiology. *Radiation Research*, **191(2):125 – 138**

[Schuemann et al., 2018b] Schuemann, J., McNamara, A. L., Warmenhoven, J. W., et al. (2018). A New Standard DNA Damage (SDD) Data Format. *Radiation Research*, **191(1):76–92**

[Schüler et al., 2017] Schüler, E., Eriksson, K., Hynning, E., et al. (2017). Very high-energy electron (VHEE) beams in radiation therapy; Treatment plan comparison between VHEE, VMAT, and PPBS. *Med Phys*, **44(6):2544–2555**

[Schüller et al., 2020] Schüller, A., Heinrich, S., Fouillade, C., et al. (2020). The European Joint Research Project UHDpulse - Metrology for advanced radiotherapy using particle beams with ultra-high pulse dose rates. *Phys Med*, **80:134–150**

[Schültke et al., 2018] Schültke, E., Bräuer-Krisch, E., Blattmann, H., et al. (2018). Survival of rats bearing advanced intracerebral F 98 tumors after glutathione depletion and microbeam radiation therapy: conclusions from a pilot project. *Radiation Oncology*, **13(1):89**

[Schwarz and Blower, 2016] Schwarz, D. S. and Blower, M. D. (2016). The endoplasmic reticulum: structure, function and response to cellular signaling. *Cell Mol Life Sci*, **73(1):79–94**

[Serduc et al., 2009a] Serduc, R., Bouchet, A., Bräuer-Krisch, E., et al. (2009). Synchrotron microbeam radiation therapy for rat brain tumor palliation—influence of the microbeam width at constant valley dose. *Physics in Medicine & Biology*, **54(21):6711**

[Serduc et al., 2009b] Serduc, R., Bräuer-Krisch, E., Bouchet, A., et al. (2009). First trial of spatial and temporal fractionations of the delivered dose using synchrotron microbeam radiation therapy. *J Synchrotron Radiat*, **16(Pt 4):587–590**

[Seyfried and Huysentruyt, 2013] Seyfried, T. N. and Huysentruyt, L. C. (2013). On the origin of cancer metastasis. *Crit Rev Oncog*, **18(1-2):43–73**

[Sgouros, 2019] Sgouros, G. (2019). Radiopharmaceutical Therapy. *Health Phys*, **116(2):175–178**

[Shahzad et al., 2017] Shahzad, A., Phatangare, A. B., Bharud, V. D., et al. (2017). Design and development of the 6–18 MeV electron beam system for medical and other applications. *Radiation Effects and Defects in Solids*, **172(11-12):931–951**

[Sharma, 2013] Sharma, R. (2013). Chapter 41 - Biochemical Mechanisms of Fatty Liver and Bioactive Foods: Fatty Liver, Diagnosis, Nutrition Therapy. In Watson, R. R. and Preedy, V. R., editors of: *Bioactive Food as Dietary Interventions for Liver and Gastrointestinal Disease*. Academic Press, San Diego, **623–655**

[Shin, 2020] Shin, W.-G. (2020). Development and application of the Geant4-DNA toolkit for the simulation of radiobiological effects at the sub-cellular scale. *PhD thesis*, Université de Bordeaux. **https://theses.hal.science/tel-03161030**

[Shin et al., 2017] Shin, W.-G., Testa, M., Kim, H. S., et al. (2017). Independent dose verification system with Monte Carlo simulations using TOPAS for passive scattering proton therapy at the National Cancer Center in Korea. *Phys Med Biol*, **62(19):7598–7616**

[Siegbahn et al., 2006] Siegbahn, E. A., Stepanek, J., Bräuer-Krisch, E., and Bravin, A. (2006). Determination of dosimetrical quantities used in microbeam radiation therapy (MRT) with Monte Carlo simulations. *Medical Physics*, **33(9):3248–3259**

[Slatkin et al., 1995] Slatkin, D. N., Spanne, P., Dilmanian, F. A., et al. (1995). Subacute neuropathological effects of microplanar beams of x-rays from a synchrotron wiggler. *Proc Natl Acad Sci U S A*, **92(19):8783–8787**

[Slatkin et al., 1992] Slatkin, D. N., Spanne, P., Dilmanian, F. A., and Sandborg, M. (1992). Microbeam radiation therapy. *Med Phys*, **19(6):1395–1400**

[Small et al., 2021] Small, K. L., Henthorn, N. T., Angal-Kalinin, D., et al. (2021). Evaluating very high energy electron RBE from nanodosimetric pBR322 plasmid DNA damage. *Sci Rep*, **11(1):3341**

[Smith et al., 2018] Smith, R., Wang, J., Seymour, C., et al. (2018). Homogenous and Microbeam X-Ray Radiation Induces Proteomic Changes in the Brains of Irradiated Rats and in the Brains of Nonirradiated Cage Mate Rats. *Dose Response*, **16(1):1559325817750068**

[Smolarz et al., 2022] Smolarz, M., Skoczylas, Ł., Gawin, M., et al. (2022). Radiation-Induced Bystander Effect Mediated by Exosomes Involves the Replication Stress in Recipient Cells. *Int J Mol Sci*, **23(8):4169**

[Smyth et al., 2019] Smyth, L. M. L., Day, L. R., Woodford, K., et al. (2019). Identifying optimal clinical scenarios for synchrotron microbeam radiation therapy: A treatment planning study. *Phys Med*, **60:111–119**

[Sorcini et al., 1996] Sorcini, B. B., Hyödynmaa, S., and Brahme, A. (1996). The role of phantom and treatment head generated bremsstrahlung in high-energy electron beam dosimetry. *Phys Med Biol*, **41(12):2657–2677**

[Sorrentino et al., 2022] Sorrentino, I., Galli, M., Medraño-Fernandez, I., and Sitia, R. (2022). Transfer of H_2O_2 from Mitochondria to the endoplasmic reticulum via Aquaporin-11. *Redox Biol*, **55:102410**

[Sotiropoulos et al., 2021] Sotiropoulos, M., Brisebard, E., Le Dudal, M., et al. (2021). X-rays minibeam radiation therapy at a conventional irradiator: Pilot evaluation in F98-glioma bearing rats and dose calculations in a human phantom. *Clinical and Translational Radiation Oncology*, **27:44–49**

[Sotiropoulos and Prezado, 2021] Sotiropoulos, M. and Prezado, Y. (2021). A scanning dynamic collimator for spot-scanning proton minibeam production. *Sci Rep*, **11(1):18321**

[Sousa et al., 2022] Sousa, T., Gouveia, M., Travasso, R. D. M., and Salvador, A. (2022). How abundant are superoxide and hydrogen peroxide in the vasculature lumen, how far can they reach? *Redox Biol*, **58:102527**

[Sprung et al., 2012] Sprung, C. N., Yang, Y., Forrester, H. B., et al. (2012). Genome-wide transcription responses to synchrotron microbeam radiotherapy. *Radiat Res*, **178(4):249–259**

[Steel et al., 1989] Steel, G. G., McMillan, T., and Peacock, J. (1989). The 5Rs of Radiobiology. *International Journal of Radiation Biology*, **56(6):1045–1048**

[Stucki and Jackson, 2006] Stucki, M. and Jackson, S. P. (2006). gammaH2AX and MDC1: anchoring the DNA-damage-response machinery to broken chromosomes. *DNA Repair (Amst)*, **5(5):534–543**

[Subiel et al., 2017] Subiel, A., Moskvin, V., Welsh, G. H., et al. (2017). Challenges of dosimetry of ultra-short pulsed very high energy electron beams. *Phys Med*, **42:327–331**

[Subiel et al., 2014] Subiel, A., Moskvin, V., Welsh, G. H., et al. (2014). Dosimetry of very high energy electrons (VHEE) for radiotherapy applications: using radiochromic film measurements and Monte Carlo simulations. *Phys Med Biol*, **59(19):5811–5829**

[Suchowerska et al., 2005] Suchowerska, N., Ebert, M. A., Zhang, M., and Jackson, M. (2005). In vitro response of tumour cells to non-uniform irradiation. *Phys Med Biol*, **50(13):3041–3051**

[Sultana et al., 2022] Sultana, A., Alanazi, A., Meesungnoen, J., and Jay-Gerin, J.-P. (2022). Generation of ultrafast, transient, highly acidic pH spikes in the radiolysis of water at very high dose rates: relevance for FLASH radiotherapy. *Canadian Journal of Chemistry*, **100(4):272–279**

[Sung et al., 2021a] Sung, B. H., Parent, C. A., and Weaver, A. M. (2021). Extracellular vesicles: Critical players during cell migration. *Developmental Cell*, **56(13):1861–1874**

[Sung et al., 2021b] Sung, H., Ferlay, J., Siegel, R. L., et al. (2021). Global Cancer Statistics 2020: GLOBOCAN Estimates of Incidence and Mortality Worldwide for 36 Cancers in 185 Countries. *CA Cancer J Clin*, **71(3):209–249**

[Suntharalingam et al., 2005] Suntharalingam, N., Podgorsak, E. B., and Hendry, J. H. (2005). Chapter 14. Basic Radiobiology. In Podgorsak, E. B., editor of: *Radiation Oncology Physics: A Handbook for Teachers and Students*. International Atomic Energy Agency, Vienna, **485–504**

[Svendsen et al., 2021] Svendsen, K., Guénot, D., Svensson, J. B., et al. (2021). A focused very high energy electron beam for fractionated stereotactic radiotherapy. *Scientific Reports*, **11(1):5844**

[Takam et al., 2011] Takam, R., Bezak, E., Marcu, L. G., and Yeoh, E. (2011). Out-of-field neutron and leakage photon exposures and the associated risk of second cancers in high-energy photon radiotherapy: current status. *Radiat Res*, **176(4):508–520**

[Testa et al., 2013] Testa, M., Schümann, J., Lu, H.-M., et al. (2013). Experimental validation of the TOPAS Monte Carlo system for passive scattering proton therapy. *Medical Physics*, **40(12):121719**

[Thiam et al., 2008] Thiam, C. O., Breton, V., Donnarieix, D., et al. (2008). Validation of a dose deposited by low-energy photons using GATE/GEANT4. *Phys Med Biol*, **53(11):3039–3055**

[Thwaites and Tuohy, 2006] Thwaites, D. I. and Tuohy, J. B. (2006). Back to the future: the history and development of the clinical linear accelerator. *Phys Med Biol*, **51(13):R343–62**

[Tilikidis et al., 1996] Tilikidis, A., Lind, B., Näfstadius, P., and Brahme, A. (1996). An estimation of the relative biological effectiveness of 50 MV bremsstrahlung beams by microdosimetric techniques. *Phys Med Biol*, **41(1):55–69**

[Tobola-Galus et al., 2018] Tobola-Galus, A., Swakon, J., and Olko, P. (2018). Dosimetric characterization of collimators for spatially fractionated proton therapy of the eye. *Radiat Prot Dosimetry*, **180(1-4):351–354**

[TOPAS MC Inc, 2023] TOPAS MC Inc (2023). TOPAS documentation. **TOPAS MC Inc**. Accessed August 15, 2023

[Tran et al., 2022] Tran, K. B., Lang, J. J., Compton, K., et al. (2022). The global burden of cancer attributable to risk factors, 2010–19: a systematic analysis for the Global Burden of Disease Study 2019. *The Lancet*, **400(10352):563–591**

[Trappetti et al., 2021] Trappetti, V., Fazzari, J. M., Fernandez-Palomo, C., et al. (2021). Microbeam Radiotherapy-A Novel Therapeutic Approach to Overcome Radioresistance and Enhance Anti-Tumour Response in Melanoma. *Int J Mol Sci*, **22(14):7755**

[Tubin et al., 2019] Tubin, S., Popper, H. H., and Brcic, L. (2019). Novel stereotactic body radiation therapy (SBRT)-based partial tumor irradiation targeting hypoxic segment of bulky tumors (SBRT-PATHY): improvement of the radiotherapy outcome by exploiting the bystander and abscopal effects. *Radiat Oncol*, **14(1):21**

[UNDP, 2019] UNDP (2019). Inequalities in human development in the 21st century. In *Human Development Report (2019) beyond income, beyond averages, beyond today: inequalities in human development in the 21st century*. United Nations Development Programme (UNDP), **1–366**

[van Battum et al., 2003] van Battum, L. J., van der Zee, W., and Huizenga, H. (2003). Scattered radiation from applicators in clinical electron beams. *Physics in Medicine and Biology*, **48(15):2493–2507**

[Verderi, 2023] Verderi, M. (2023). Physics Content of Geant4 "More on Physics". **Geant4 PHENIICS & IN2P3 Tutorial**. Accessed August 14, 2023

[Verhaegen and Seuntjens, 2003] Verhaegen, F. and Seuntjens, J. (2003). Monte Carlo modelling of external radiotherapy photon beams. *Phys Med Biol*, **48(21):R107–64**

[von Sonntag, 2006] von Sonntag, C. (2006). Chapter 2 - Formation of Reactive Free Radicals in an Aqueous Environment. In *Free-Radical-Induced DNA Damage and Its Repair: A Chemical Perspective*. Springer, **7–46**

[Štepán and Davídková, 2008] Štepán, V. and Davídková, M. (2008). Impact of oxygen concentration on yields of DNA damages caused by ionizing radiation. *Journal of Physics: Conference Series*, **101:012015**

[Wasselin-Trupin et al., 2002] Wasselin-Trupin, V., Baldacchino, G., Bouffard, S., and Hickel, B. (2002). Hydrogen peroxide yields in water radiolysis by high-energy ion beams at constant LET. *Radiation Physics and Chemistry*, **65(1):53–61**

[Weiss, 1944] Weiss, J. (1944). Radiochemistry of Aqueous Solutions. *Nature*, **153(3894):748–750**

[WHO, 2023] WHO (2023). Leading causes of death and disability. A visual summary of global and regional trends 2000-2019. **WHO**. Accessed May 12, 2023

[Widel et al., 2012] Widel, M., Przybyszewski, W. M., Cieslar-Pobuda, A., et al. (2012). Bystander normal human fibroblasts reduce damage response in radiation targeted cancer cells through intercellular ROS level modulation. *Mutat Res*, **731(1-2):117–124**

[Wilkens and Oelfke, 2003] Wilkens, J. J. and Oelfke, U. (2003). Analytical linear energy transfer calculations for proton therapy. *Med Phys*, **30(5):806–815**

[Wilkinson et al., 2023] Wilkinson, B., Hill, M. A., and Parsons, J. L. (2023). The Cellular Response to Complex DNA Damage Induced by Ionising Radiation. *International Journal of Molecular Sciences*, **24(5):4920**

[Winterbourn, 2013] Winterbourn, C. C. (2013). The biological chemistry of hydrogen peroxide. *Methods Enzymol*, **528:3–25**

[Withers, 1975] Withers, H. R. (1975). The Four R's of Radiotherapy. In Lett, J. T. and Adler, H., editors of: *Advances in Radiation Biology, volume 5*. Elsevier, **241–271**

[Withers et al., 1988] Withers, H. R., Taylor, J. M., and Maciejewski, B. (1988). Treatment volume and tissue tolerance. *Int J Radiat Oncol Biol Phys*, **14(4):751–759**

[Wong et al., 2008] Wong, J., Armour, E., Kazanzides, P., et al. (2008). High-resolution, small animal radiation research platform with x-ray tomographic guidance capabilities. *Int J Radiat Oncol Biol Phys*, **71(5):1591–1599**

[Wong-Ekkabut et al., 2007] Wong-Ekkabut, J., Xu, Z., Triampo, W., et al. (2007). Effect of lipid peroxidation on the properties of lipid bilayers: a molecular dynamics study. *Biophys J*, **93(12):4225–4236**

[Wouters, 2018] Wouters, B. G. (2018). Cell death after irradiation: how, when and why cells die. In Joiner, M. C. and van der Kogel, A. J., editors of: *Basic Clinical Radiobiology (Fifth Edition)*. CRC Press, **27–40**

[Wouters and Begg, 2018] Wouters, B. G. and Begg, A. C. (2018). Irradiation-induced damage and the DNA damage response. In Joiner, M. C. and van der Kogel, A. J., editors of: *Basic Clinical Radiobiology (Fifth Edition)*. CRC Press, **11–26**

[Wright et al., 2021] Wright, M. D., Romanelli, P., Bravin, A., et al. (2021). Non-conventional Ultra-High Dose Rate (FLASH) Microbeam Radiotherapy Provides Superior Normal Tissue Sparing in Rat Lung Compared to Non-conventional Ultra-High Dose Rate (FLASH) Radiotherapy. *Cureus*, **13(11):e19317**

[Wu et al., 2010] Wu, X., Ahmed, M. M., Wright, J., et al. (2010). On Modern Technical Approaches of Three-Dimensional High-Dose Lattice Radiotherapy (LRT). **2(3):e9**

[Wu et al., 2020] Wu, X., Perez, N. C., Zheng, Y., et al. (2020). The Technical and Clinical Implementation of LATTICE Radiation Therapy (LRT). *Radiat Res*, **194(6):737–746**

[Xstrahl, 2023] Xstrahl (2023). Xstrahl Limited. **https://xstrahl.com/**. Accessed August 10, 2023

[Yan et al., 2020] Yan, W., Khan, M. K., Wu, X., et al. (2020). Spatially fractionated radiation therapy: History, present and the future. *Clin Transl Radiat Oncol*, **20:30–38**

[Yang et al., 2022a] Yang, D., Wang, W., Hu, J., et al. (2022). Feasibility of lattice radiotherapy using proton and carbon-ion pencil beam for sinonasal malignancy. *Ann Transl Med*, **10(8):467**

[Yang et al., 2013] Yang, Y., Bazhin, A. V., Werner, J., and Karakhanova, S. (2013). Reactive oxygen species in the immune system. *Int Rev Immunol*, **32(3):249–270**

[Yang et al., 2022b] Yang, Z., Zhong, W., Yang, L., et al. (2022). The emerging role of exosomes in radiotherapy. *Cell Communication and Signaling*, **20(1):171**

[Yu and Chen, 2023] Yu, Y. and Chen, Z. (2023). Dose calculation of proton therapy based on Monte Carlo and empirical formula. *Radiat Prot Dosimetry*, **199(2):124–133**

[Yücel et al., 2016] Yücel, H., Çobanbaş, İ., Kolbaşı, A., et al. (2016). Measurement of Photo-Neutron Dose from an 18-MV Medical Linac Using a Foil Activation Method in View of Radiation Protection of Patients. *Nuclear Engineering and Technology*, **48(2):525–532**

[Zacharatou Jarlskog and Paganetti, 2008] Zacharatou Jarlskog, C. and Paganetti, H. (2008). Physics Settings for Using the Geant4 Toolkit in Proton Therapy. *IEEE Transactions on Nuclear Science*, **55(3):1018–1025**

[Zackrisson et al., 1991] Zackrisson, B., Johansson, B., and Östbergh, P. (1991). Relative Biological Effectiveness of High-Energy Photons (up to 50 MV) and Electrons (50 MeV). *Radiation Research*, **128(2):192–196**

[Zaorsky et al., 2017] Zaorsky, N. G., Davis, B. J., Nguyen, P. L., et al. (2017). The evolution of brachytherapy for prostate cancer. *Nat Rev Urol*, **14(7):415–439**

[Zeman, 2016] Zeman, E. M. (2016). Chapter 1 - The Biological Basis of Radiation Oncology. In Gunderson, L. L. and Tepper, J. E., editors of: *Clinical Radiation Oncology (Fourth Edition)*. Elsevier, Philadelphia, **2–40.e5**

[Zeman et al., 2020] Zeman, E. M., Schreiber, E. C., and Tepper, J. E. (2020). Basics of Radiation Therapy. In Niederhuber, J. E., Armitage, J. O., Doroshow, J. H., et al., editors of: *Abeloff's Clinical Oncology (Sixth Edition)*. Elsevier, Philadelphia, **431–460.e3**

[Zeman et al., 1961] Zeman, W., Curtis, H. J., and Baker, C. P. (1961). Histopathologic effect of high-energy-particle microbeams on the visual cortex of the mouse brain. *Radiat Res*, **15:496–514**

[Zeman et al., 1959] Zeman, W., Curtis, H. J., Gebhard, E. L., and Haymaker, W. (1959). Tolerance of Mouse-Brain Tissue to High-Energy Deuterons. *Science*, **130(3391):1760–1761**

[Zhang, 2023] Zhang, H. (2023). GRID-collimator-based and static-field SFRT. In Zhang, H. and Mayr, N. A., editors of: *Spatially Fractionated, Microbeam and FLASH Radiation Therapy*. IOP Publishing, **9–1 to 9–19**

[Zhang and Mayr, 2023] Zhang, H. and Mayr, N. A. (2023). Spatially Fractionated, Microbeam and FLASH Radiation Therapy. *IOP Publishing*, **2053–2563**

[Zhang et al., 2020] Zhang, P., Darmon, A., Marill, J., et al. (2020). Radiotherapy-Activated Hafnium Oxide Nanoparticles Produce Abscopal Effect in a Mouse Colorectal Cancer Model. *Int J Nanomedicine*, **15:3843–3850**

[Zhang et al., 2023] Zhang, T., García-Calderón, D., Molina-Hernández, M., et al. (2023). A theoretical study of H_2O_2 as the surrogate of dose in minibeam radiotherapy, with a diffusion model considering radical removal process. *Med Phys*, **50(8):5262–5272**

[Zhang et al., 2016] Zhang, X., Penagaricano, J., Yan, Y., et al. (2016). Spatially fractionated radiotherapy (GRID) using helical tomotherapy. *Journal of Applied Clinical Medical Physics*, **17(1):396–407**

[Zhang et al., 2022] Zhang, Z., Liu, X., Chen, D., and Yu, J. (2022). Radiotherapy combined with immunotherapy: the dawn of cancer treatment. *Signal Transduction and Targeted Therapy*, **7(1):258**

[Zheng et al., 2008] Zheng, Y., Fontenot, J., Taddei, P., et al. (2008). Monte Carlo simulations of neutron spectral fluence, radiation weighting factor and ambient dose equivalent for a passively scattered proton therapy unit. *Phys Med Biol*, **53(1):187–201**

[Zhou et al., 2013] Zhou, Y., Yan, H., Guo, M., et al. (2013). Reactive oxygen species in vascular formation and development. *Oxid Med Cell Longev*, **2013:374963**

[Zhu et al., 2020] Zhu, H., McNamara, A. L., McMahon, S. J., et al. (2020). Cellular Response to Proton Irradiation: A Simulation Study with TOPAS-nBio. *Radiat Res*, **194(1):9–21**

[Zlobinskaya et al., 2013] Zlobinskaya, O., Girst, S., Greubel, C., et al. (2013). Reduced side effects by proton microchannel radiotherapy: study in a human skin model. *Radiat Environ Biophys*, **52(1):123–133**